University of Southampton

Faculty of Engineering and Physical Sciences

School of Engineering

An experimental study on the effects of winglets on the performance of horizontal axis tidal turbines

by

Rodolfo Olvera Trejo

ORCID ID 0000-0002-8607-1138

Thesis for the degree of Doctor of Philosophy

February 2022

University of Southampton

Abstract

Faculty of Engineering and Physical Sciences

School of Engineering

Thesis for the degree of Doctor of Philosophy

An Experimental Study on the Effects of Winglets on the Performance of Horizontal Axis Tidal Turbines

by

Rodolfo Olvera Trejo

Horizontal Axis Tidal Turbines (HATT) currently have a lower power coefficient than commercially available wind turbines. This has meant that in recent years less funding goes towards developing such technology. Furthermore, some planned projects have not gone ahead, and there does not seem to be support from the government to promote its development. In the wind industry, turbines can have 5 times the rated power of a tidal turbine because the rotor size is not a problem. In the tidal industry, size is constrained due to technical and environmental factors. An approach to face this issue is to increase the power coefficient for a fixed rotor size.

An experimental study is presented to investigate the performance of winglets fitted to a 1:20th scaled 1 *m* in diameter HATT. Winglets have been extensively employed in the aviation industry to reduce the vortices generated at the end of aircraft wings decreasing drag and hence increasing fuel economy of civilian aircraft. For horizontal axis turbines, winglets facing backwards on the suction side of the blades have been the subject of extensive research almost exclusively based on computer-driven numerical simulations as a means to increase the power capture of the rotor.

With the use of oil-based paint flow visualisation, the mechanism behind the phenomenon affecting winglets facing the suction side has been identified as part of this work. Vortices form behind the blade/winglet interface when they are oriented towards the flow direction. These vortices reduce performance due to viscous effects. Power and thrust coefficients were measured from the scale HATT and together with numerical Blade Element Momentum simulations, the bending moments at the root could be calculated. A winglet facing downstream decreases the power coefficient by 12% in average and increases the thrust coefficient by an average 5%. On the other hand, a symmetrically mirrored winglet facing upstream can increase the power coefficient by around 1-2%, at the same time the thrust coefficient increases by 3-4%. Assuming that the increase in thrust is caused by fitting the winglets, their structural cost in the bending moment at the root of the blade is up to 40% more, 4.2-5.6% in this case.

Cost-data from industry has suggested that even marginal increases in power coefficients due to winglets can provide a return on investment given the relative costs of blade manufacture and the expected level of subsides awarded to new and developing forms of electricity generation. Therefore, further work to optimise pressure-side winglets should be conducted.

Table of Contents

Table of Tables

Table of Figures

Table of Figures

Table of Figures

Table of Figures

Table of Figures

List of Accompanying Materials

Winglets data DOI: https://doi.org/10.5258/SOTON/D2129

Research Thesis: Declaration of Authorship

Print name: Rodolfo Olvera Trejo

Title of thesis: An Experimental Study on the Effects of Winglets on the Performance of Horizontal Axis Tidal Turbines

I declare that this thesis and the work presented in it are my own and has been generated by me as the result of my own original research.

I confirm that:

1. This work was done wholly or mainly while in candidature for a research degree at this University;
2. Where any part of this thesis has previously been submitted for a degree or any other qualification at this University or any other institution, this has been clearly stated;
3. Where I have consulted the published work of others, this is always clearly attributed;
4. Where I have quoted from the work of others, the source is always given. With the exception of such quotations, this thesis is entirely my own work;
5. I have acknowledged all main sources of help;
6. Where the thesis is based on work done by myself jointly with others, I have made clear exactly what was done by others and what I have contributed myself;
7. Parts of this work have been published as:

    - An experimental study on the performance of blade winglets for horizontal axis tidal turbines (Under revision)

Signature: ..... Date: 10-Feb-22

Acknowledgements

The fees and maintenance for my PhD were paid by the scholarship SENER-CONACyT, other costs such as manufacturing and testing time were kindly paid by my supervisor, Dr. Luke Myers. He is one of the most patient persons I have ever came across. I have to thank him for many aspects, including his support, guidance, understanding, encouragement. It took me a good few weeks to fully understand what was discussed during our meetings, mainly because of his intellectual input, but also because it is also present in his humour! My family also supported me emotionally, financially, and overall, in my well-being. My father, Isidro; my mother, Elia; my sister, Lorena; my aunt, Silvia; and my brother, Eduardo. Their love, advice, words of encouragement, understanding, and unconditional support were the engine that kept me going. My friends too, with whom I have also laughed, enjoyed, cried, shared, argued, and because I have learnt a lot thanks to them. Most graphs produced with © OriginLab Corporation software.

At university I found people who gave me support beyond their responsibilities. In no order, and apologies in advance if I forget to mention someone. From the Sustainable Energy Research Group: Victoria Aragón, Sheila Stickland, Prof. 'Bakr, Leo Bourikas, Phillip Turner, Phil Wu, Maj Alam, Mikey Harper, and Luke Blunden. Academics: Prof. Stephen Turnock for pointing out key aspects to address in the project, Dr Roeland de Kat for his knowledge on flow visualisation, Dr. Poshak.Gandhi for statistics, and Dr. Dario Carugo. Building 21 laboratories: Karl Scammel (not only for his vast technical expertise, but because he was willing to help in any situation), Dr. Toru Tsuzaki, Pilar Pascual, David Lynock, Andrew Morgan, and Dominic Mann. Postgraduate Research Student Office: Jackie Graham, Jennifer Knight, Emma Stephenson, Stephen Wakeling, and Lee Chisman. At the Engineering, Design and Manufacturing Centre: Tim Woolman for his help with the blade design, John Young, Justin Gregory, and Mike Street and Maurice Jones for their help with the Computer Aided Design. Also, to my lecturers back at my home university: Dra. Olimpia Salas-Martínez, Dra. Sofia Faddeeva, Dr. Jorge Aguirre-Aguilar, Dr. Ulises Figueroa-López, and particularly Dr. Agustín Vázquez-Sánchez for his guidance and support in many aspects.

During these years, I have also enjoyed practicing sports and meeting different people from the groups and societies at the Student's Union. Fellow salsa dancers, amigos from the Mexican Society, and at the language exchange meetings. The university also allowed me to attend conferences where I met many interesting people in my field, get access to different training courses such as technical writing, research methodology, presenting skills, data management, wellbeing, and stress management. In addition to that, I had the opportunity of being involved in different demonstrating opportunities in various laboratories, workshops, university days, exam invigilations, inductions and other tasks at university.

Definitions and Abbreviations

[°]	degrees	
α, AoA	angle of attack	[°]
β	pitch angle	[°]
η	efficiency	[%]
μ	dynamic viscosity	[Pa-s]
ρ	density	[kg/m^3]
τ	torque	[*N-m*]
ϕ	local inflow angle	[°]
ω	rotational speed	[*rad/s*]
[Ω]	Ohms	
a	induction factor	
a’	axial induction factor	
A	Area	
[*bit*]	binary digit	
B	number of Blades	
$C_{P,T}$	C_P: Power coefficient, C_T: Thrust coefficient	[ ]
c	airfoil chord	[*m*]
F	Force	[N]
h	height	[*m*]
[*Hz*]	Hertz	
K	Constant	
[*m*]	metre	

M	Moment	[Nm]
[N]	Newtons	
r, R	radius, fixed radius	[*m*]
Re	Reynolds number	
[rad]	radians	
[*s*]	second	
TSR, λ	tip speed ratio	[ ]
u, U	flow velocity	[*m/s*]
x, y, z	axis of reference	

Sub- and super-scripts

$( )^{+}$	high value	
$( )^{-}$	low value	
$( )_{gen}$	generator	[%]
$( )_{0}$	initial condition	
$( )_{\infty}$	condition one: undisturbed flow	[*SI*]
$( )_{w}$	condition two: flow in the far wake	[*SI*]
$( )_{max}$	maximum value	
$( )_{r}$	reference value	[*SI*]
$( )_{(y)}$	function of	[*m/s*]
$( )^{\alpha}$	power index (velocity profile)	[ ]

Abbreviations

AEP	Annual Energy Production
Aim-TTi	Aim Thurlby Thandar Instruments
ANN	Artificial Neural Network

AoA	angle of attack
BEIS	Department for Business, Energy, and Industrial Strategy
BEMT	Blade Element Momentum TheoryCAD Computer-Aided Design
CapEx	Capital Costs, Capital Expenditure
CfD	Contracts for Difference (UK)
CFD	Computational Fluids Dynamics
CSD	Computational Structure dynamics
DAQ	Data AcQuisition
DUT	Delft University of Technology
EMEC	European Marine Energy Centre
ETS	European Union Emission Trading System
EU	European Union
FEA, FEM	Finite Element Analysis, Finite Element Method
FORCE	Fundy Ocean Research Center for Energy
FFT	Fast Fourier Transform
FSI	Fluid Structure Interaction
GA	Genetic Algorithm
GPL	General Public License
GUI	Graphical User Interface
HATT	Horizontal Axis Tidal Turbine
HATCT	Horizontal Axis Tidal Current Turbine
HATST	Horizontal Axis Tidal Stream Turbine
HKT	Hydro-Kinetic Turbine
MCT	Marine Current Turbine

TCT	Tidal Current Turbine
TEC	Tidal Energy Converter
TSG	Tidal Stream Generator
TST	Tidal Stream Turbine
HAWT	Horizontal Axis Wind Turbine
Interreg	Interregional European projects
LabView	Laboratory Virtual Instrument Engineering Workbench, visual programming program for National Instruments equipment
LCOE	Levelised Cost of Energy
NASA	National Aeronautics and Space Administration
NDA	Non-Disclosure Agreement
NI	National Instruments
OES	Ocean Energy Systems
QBlade	Software to simulate VAWT and HAWT rotors using BEM
RED	Renewable Energy Directive (EU)
RET	Renewable Energy Target (Australia)
ROCs	Renewable Obligation Certificates (UK)
SET Plan	Strategic Energy Technology Plan
TIGER	Tidal Stream Industry Energiser
UoS	University of Southampton
VAWT	Vertical Axis Wind Turbine
VLM	Vortex Lattice Method
XFOIL	Program to design and analyse airfoils

Chapter 1 Introduction

1.1 Tidal Energy

Marine energy provides two main sources of energy: wave and tidal. Waves range from surface fluctuations to transatlantic waves, but the ones from which energy can be harvested are generated by wind currents, and the latter are a by-product of the sun heating earth's surface. Wave energy converters have shown good results in controlled conditions like in the laboratory, but they have struggled to match the performance in real life conditions due to the unpredictable and severe weather in the sea surface environment. Tidal currents are generated by gravitational forces, density gradients and the Coriolis effect. Tidal energy is mostly associated with extracting energy from the height difference of the rise and fall of the sea surface. Other methods include tidal currents and salinity and temperature gradients (EMEC, 2012). In fact, tides and tidal currents occur simultaneously because the sea level is mainly influenced by gravitational forces, and water motion generates these currents. Many devices have been designed to convert tidal current kinetic energy into electricity: horizontal and vertical axis turbines, oscillating hydrofoil, enclosed turbines, Archimedes screw, tidal kite, and others (Aqua-RET Project ©, 2012). The most common tidal current device is the horizontal axis tidal turbine (HATT). These tidal turbines work similarly to wind turbines, with the difference that they are installed under the sea and they rotate due to the water flow. Most of the knowledge for this technology comes from wind industry, yet the same level of power capture efficiency has not yet been achieved.

Tidal potential has been estimated in several countries including the UK. The Carbon Trust estimated in 2011 that by 2050, in a moderate scenario, that 20-30 *TWh* of electricity per year could come from tidal energy, compared to UK electricity consumption for that year of 360 *TWh* (Low Carbon Innovation Coordination Group, 2012, p. 4). According to British Petroleum's Energy Outlook (2019, p. 53), renewables are set to account for two-thirds of the growth in world power generation, achieving a share of 30% by 2040, and becoming the primary source of energy in the global power sector, with power generation absorbing half of all primary energy. In this central scenario, renewable energy is the fastest growing source of primary energy, with half of global growth in energy supplies, to increase from 5% today (BP, 2020, p. 7), to around 15% by 2040 (BP, 2019, p. 79). Renewables reached 1% of global energy only in 2006, and are expected to make the fastest incursion than any fuel ever (BP, 2019, p. 105). The energy sector, and in particular electricity, played an important role in the Covid-19 crisis, emphasizing the need of more secure and resilient energy systems (IEA, 2020, p. 18). Europe has the highest share of renewable power generation at 20.9%, twice the global average of 10.4% (BP, 2020, p. 60). With an expected

increase in the power market to over 50% by 2040 in the region, intermittency is one of the main challenges to address (BP, 2019, p. 105).

In 2009 the European Union (EU) defined a Renewable Energy Directive (RED) in line with the EU Emission Trading System, that is focused on reducing greenhouse gas emissions (UK Government, 2010, p. 5). Taking the UK as an example, it promotes the development of renewable power by a mechanism named Contracts for Difference (CfD). Under this agreement, the government agrees to pay over a 15-year period the difference between the cost of a low carbon technology and the average market price for electricity. There have been 3 allocation rounds since 2015 every 2 years, with the fourth expected to occur in 2021. However, as predicted by Bahaj (2013, p. 13), tidal stream energy has not received the level of support seen before 2017 when a different scheme called Renewable Obligation Certificates (ROCs) was in place.

Australia and Mexico are two other examples where incentives for renewable sources have been adopted (del Razo, 2016, p. 88). These two countries have defined targets for renewable energy production in the mid-term. In Australia, the Renewable Energy Target (RET) required a minimum of 20% of renewable energy production by 2020 (del Razo, 2016, p. 87). The Clean Energy Regulator in Australia announced that the target had been met in September 2019 (Clean Energy Council, 2020). In 2020, 27.7% of electricity generation came from renewable sources (Clean Energy Council, 2021, p. 7). The Mexican government is pursuing a 35% of electricity generated from clean sources by 2024, with interim targets of 25% for 2018, and 30% for 2021. By the end of 2018, the gross power generation from renewable sources was 23.2%, around 8% less than expected (Secretaría de Energía, 2020, p. 22). The UK had a target of 30% of its electricity being produced from renewables by 2020 (UK Government, 2010, p. 4). The figures for 2019 showed that 35% of total electricity generation came from renewables, already meeting the target. There were two other targets in line with the RED, one for renewable heat of 12%, and a second for renewables in transport of 10%, as of 2019 figures were 7.9% for heat and 8.8% in transport, both still behind the targets by 2020 (BEIS, 2020, p. 106). In addition, the total renewable energy target was set at 15% by the end of 2020. The final generation for the RED in 2020 was 13.6% overall, 6.6% for heat (revised), and 10.3% for transport (BEIS, 2021, p. 43).

Tidal energy has the unique characteristic of being completely predictable ahead of time, even over several years in advance (Fraenkel, 2002, p. 8). This is occurs because the main tidal currents are driven by the interaction of the earth with the gravitational forces of the sun and the moon (Bryans *et al.*, 2005, p. 2035). For such reason, if there were an array of tidal turbines (namely tidal farm), the renewable energy supply from that turbine arrangement could be predicted in advance of the forecasted electricity demand. The main challenge for most renewable sources like

solar and wind is that the local available power varies over days, hours and even minutes. In addition to this, resource availability does not match the real time demand (Delucchi and Jacobson, 2011, p. 1171).

There is a global effort to decarbonise the electrical grid for many reasons broadly discussed. Modernisation and increasing energy efficiency are two of the key factors to improve security by diminishing the chances of outages, improving flexibility, reducing losses, and allowing the integration of intermittent renewables like wind and solar. This would allow the system to overcome natural occurring disasters, extreme weather conditions and other unexpected events (IEA, 2020, p. 15).

Wind turbine developers are manufacturing larger rotors to achieve a higher energy extraction; tidal turbine developers cannot do the same. Wind turbines with rotor diameters of 150 *m* or more are built now by the largest companies (Kumar *et al.*, 2016, p. 212), with rated power close to 10 *MW*. On the other hand, tidal turbines have constrictions that prevent the technology to use the same approach. Recently, real size prototypes have rotor diameters under 20 *m* (Zhou *et al.*, 2017, p. 857), with rated power of around 2 *MW*. The main restrictions faced by tidal turbine developers include: turbulence in the seabed caused by the natural bathymetry, circular motion near the surface created by waves, and the vertical velocity profile (Myers and Bahaj, 2008, p. 1, 2010, p. 219). This interaction is illustrated by Allmark, Martinez, *et al.* (2021) in Figure 1.1.

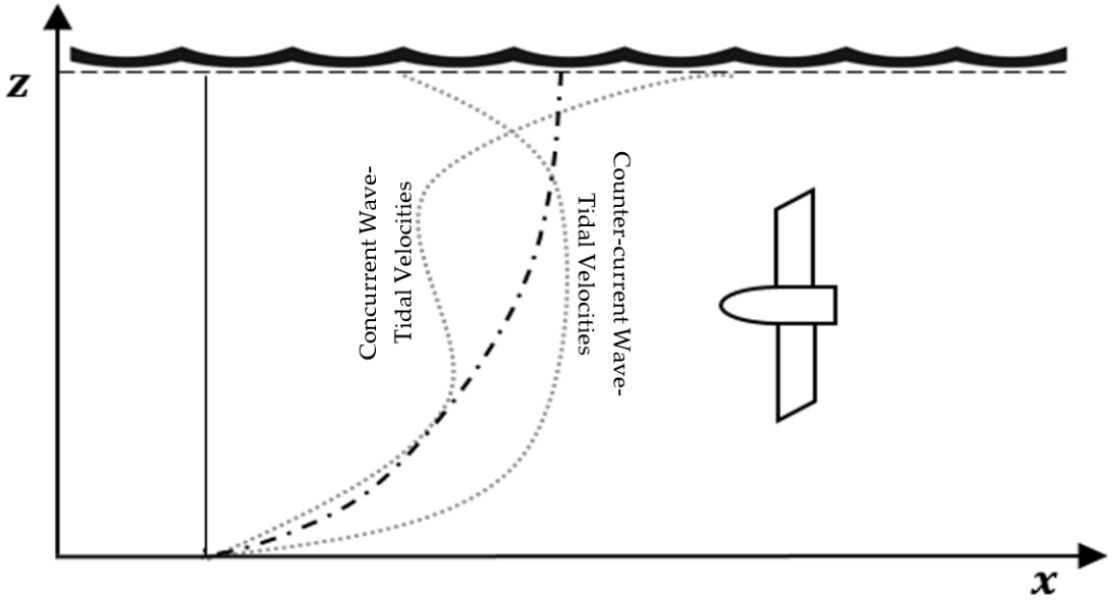

Figure 1.1 Velocity profile under current-wave interaction (Encarnacion, Johnstone and Ordonez-Sanchez, 2019, p. 9).

The velocity profile shifts towards the left when waves are travelling in the same direction as the current because the lower part of the circular motion of the waves moves to the opposite

direction, while at the surface there is a more pronounced profile towards the current direction. Similarly, when waves are travelling opposite to the current, the velocity profile shifts to the direction of the current below the surface, and opposite at the surface.

Tidal turbines encounter three main differences with wind turbines: Reynolds numbers (inherent to the environment), possible cavitation and other stall characteristics (Batten et al., 2006, p.249). There are other limitations to the blade length regarding capital costs and modern material properties, because compared to wind turbines, thrust forces per unit area are around 30 times higher for tidal turbines compared to wind turbines at their typical rated flow velocities. Ebdon *et al.* calculated the thrust to be only 6 times higher per unit area, but their calculations were based using wind speeds of 40 *m/s* (144 km/hr) (2021, p. 15). The thrust force due to the incoming flow to the turbine is given by $\frac{1}{2}\rho A U^2$, where ρ is the density of the fluid and U its speed. The rated wind speed for a typical wind turbine is around 15 *m/s* (Office of Energy Efficiency & Renewable Energy, 2017), and the density of air is 1.225 *kg/m^3*, resulting in 173.18 kN for a 20-m wind turbine. Similarly, a typical value for the rated speed of a conventional tidal turbine is 3 *m/s* (Encarnacion, Johnstone and Ordonez-Sanchez, 2019, pp. 1–2), and the density of sea water is 1025 *kg/m^3*, producing 5.79 MN for a tidal turbine of same size. Figure 2.10 compares two turbines with these characteristics. Additionally, there is a perceived limit of 25-26 m in diamater for horizontal axis tidal turbines. Such a limit is determined by mechanical properties of currently available materials (Johnstone, 2021).

1.2 Project Overview

Tidal turbines are currently tested full scale and are at a stage just before deployment of commercially viable arrays. One of the main factors holding the technology back is the high capital cost. There are financial incentives for this type of technology albeit less than some years ago. Wind power and solar photovoltaic panels are benefiting from most of these incentives. Tidal turbines still have room for improvement regarding power capture efficiency. This means that increasing such efficiency, will translate into a reduction in the Levelised Cost of Energy (LCOE). Most of the available knowledge from the wind energy sector has been applied to designing and developing modern tidal turbines, but there is still a gap between efficiencies. Horizontal axis turbines have root and tip losses that could be reduced by slightly modifying blade designs and measures such as these are seen as lower risk than, for example, manufacturing slender more efficient blades when operating in such a harsh and high force environment. The research herein is centred about experimental tests using a 1:20th scale horizontal axis tidal turbine and improving efficiency of the primary power capture system which in this case is the rotor/blades.

SIMEC Atlantis is a company with some history in the tidal industry. They provided the blade geometry of their AR2000 tidal turbine for this research. In the year 2000, Marine Current Turbines Ltd. was founded, and in 2003 installed the first offshore tidal turbine 'Seaflow' with a rated power of 300 *kW*. In 2008, they installed the first commercial-scale turbine 'SeaGen S' in Northern Ireland, it was rated at 1.2 *MW* and connected to the electrical grid. In 2010 Siemens became a shareholder of the company and in 2012 acquired the majority of the shares in the company. Atlantis Resources Ltd. acquired the company in 2015, after securing funding the previous year for the first multi-MW turbine project MeyGen. In 2017, GFG Alliance acquired almost half of the company to become SIMEC Atlantis Energy.

With the current gap in power capture efficiencies between tidal turbines and wind turbines, every 0.01 increase in power coefficient justifies up to a £50,000 capital cost for a 2 *MW* device (Bray, 2017) based on present device costs and revenue for the sale of electricity. The aim of this project is to study available techniques to increase energy capture efficiency through modification of an existing blade set. These methods are detailed further in the following chapter and broadly function by reducing losses due to flow separation and turbulence. Research conducted herein will investigate previous work to increase the capture efficiency of horizontal axis turbine blades and will aim to select one of those methods for further investigation.

Chapter 2 Tidal Energy Review

Tidal current generation in the UK has a technically extractable resource of 18 *TWh/y*, or around 4.8% of its annual electricity demand (Metoc Ltd. for the Sustainable Development Commission, 2007, pp. 9–12). Figure 2.1 shows a map of the resource, 60% of which is located in the Pentland Firth (where the EMEC is located), other sites include: Casquets (Channel Islands), Rathlin Island and other sites in Northern Ireland, Mull of Galloway, Islay, Carmel Head (Anglesey), Bill of Portland, The Bristol Channel, Pembrokeshire (St David's Head, Ramsey Island), and Lleyn peninsula (2007, p. 25).

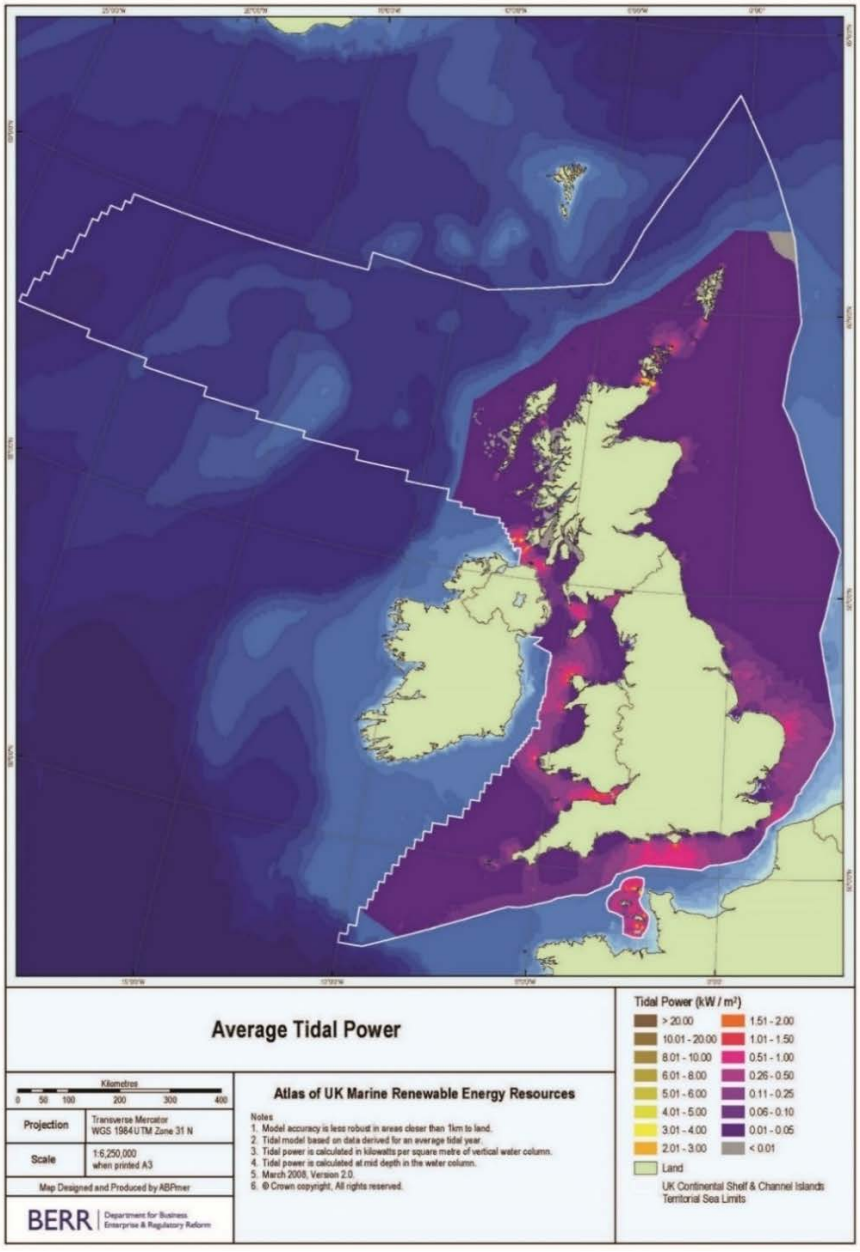

Figure 2.1 Average Tidal Power in the UK (Reproduced from http://www.renewables-atlas.info/ © Crown Copyright).

Worldwide there is a potential annual energy available of tidal current estimated at 800 *TWh/y*, which represents around 3.5% of global electricity demand (Breeze, 2014, p. 288). Figure 2.2 shows tidal current projects around the world. Sites marked on grey are early concepts, yellow means they are not operational, and green fully operational.

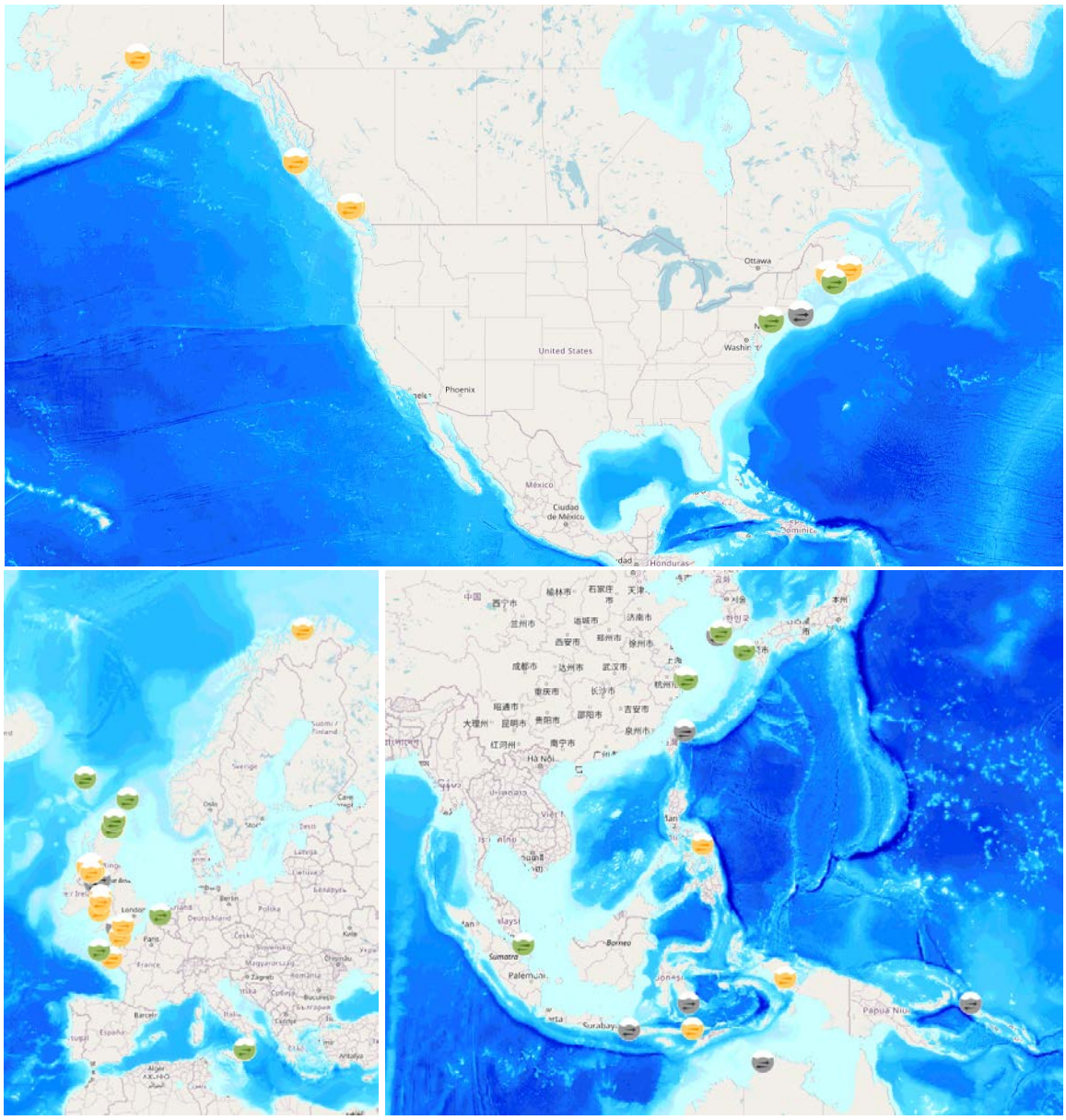

Figure 2.2 Tidal current projects around the world (Ocean Energy Systems, 2021).

In North America, the USA has a demonstration project on the East Channel of the East River (0.105 *MW*). Most projects in Canada are on the coast of Nova Scotia (0.5 *MW* installed). In Europe most projects are located at the European Marine Energy Centre in the Pentland Firth, UK (6 *MW*), and some further North (0.4 *MW*). In mainland Europe there is a single project at the Eastern Scheldt in the Netherlands (1.25 *MW*). One off the island of Ouessant, Brittany in France (0.5 *MW*) and a small turbine at the Strait of Messina in Italy (55 *kW*). In Asia, China has a couple of projects on their east coast (1.5 *MW*), Singapore has one in the Singapore Strait (62 *kW*), South

Korea has one in the Yellow Sea (0.15 *MW*), and Japan one in the straits of Naru Island, Goto island chain (0.5 *MW*).

Tidal currents are predictable, they can be decomposed into harmonic functions, but they vary from site to site. Tides are generated from the gravitational pull of the celestial bodies governed by Newton's law of universal gravitation $F = \frac{GMm}{D^2}$, where G is the gravitational constant (6.67 x $10^{-11}\ Nm^2/kg^2$), M and m are the masses of the bodies, and D is the distance between the centres of the masses. Evidently, tides are mainly affected by the influence of the sun and the moon. The sun is much larger than the earth, but considerably further than the moon, so the sun's effect is only 46% of the one from the moon (Baker, 1991, p. 3).

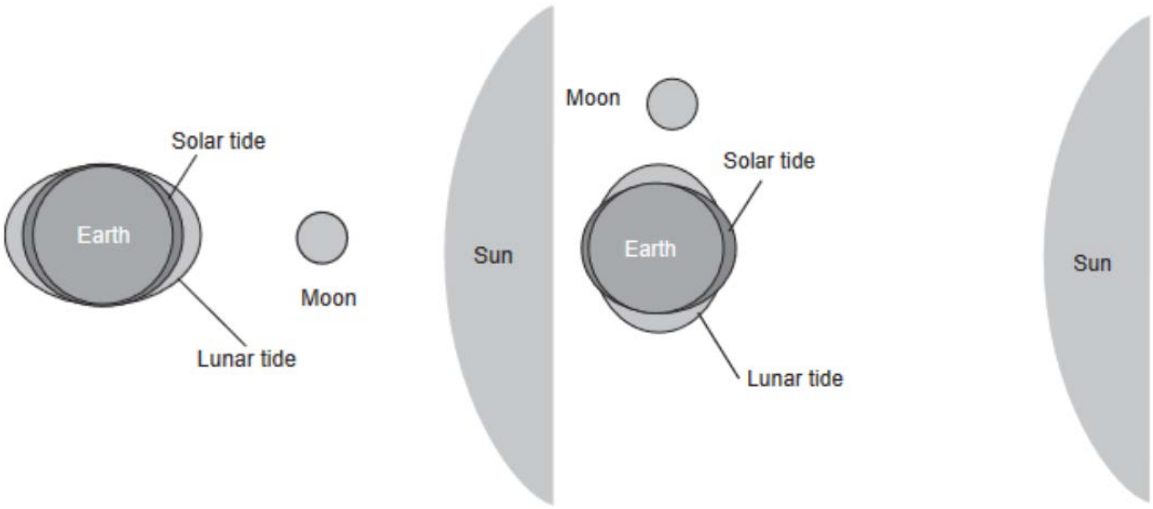

Figure 2.3 Position of the moon along the earth-sun axis during spring tides (Left) and neap tides (Right) (Bryden, 2004, p. 141).

The rise and fall of the sea level produce the sea current, which can be decomposed into harmonic equations of the form:

$$U(t) = U_0 + \sum \left[U_A \cos\left(\frac{2\pi t}{T_A} + \rho_A \right) \right] \qquad \text{Equation 2.1}$$

Where $U(t)$ is the current speed at any time t, U_0 is the mean current speed (usually 0), U_A is the mean current of any constituent, T_A is tidal period of the constituent, and ρ_A is the phase difference of the constituent when $t = 0$ (Hardisty, 2009, p. 24).

The main constituents of the currents are the lunar diurnal constituent (O_1), the principal lunar semi-diurnal constituent (M_2), the lunar quarter diurnal (M_4), and the principal solar semi-diurnal constituent (S_2), where U corresponds to the current, so O_{U1} is from O_1 (Hardisty, 2009, p. 48).

$$U(t) = U_0 + U_{O_{U_1}} \cos\left[\frac{2\pi t}{T_{O_{U_1}}} + \rho_{O_{U1}} \right] + U_{M_{U_2}} \cos\left[\frac{2\pi t}{T_{M_{U_2}}} + \rho_{M_{U2}} \right]$$

$$+U_{M_{U4}} \cos\left[\frac{2\pi t}{T_{M_{U4}}} + \rho_{M_{U4}}\right] + U_{S_{U2}} \cos\left[\frac{2\pi t}{T_{S_{U2}}} + \rho_{S_{U2}}\right] + \cdots$$

The faster speeds occur during spring tides, and the lower peak speeds happen during neap tides as illustrated in Figure 2.4. On the left a yearly variation can be appreciated, and on the right a monthly range is shown.

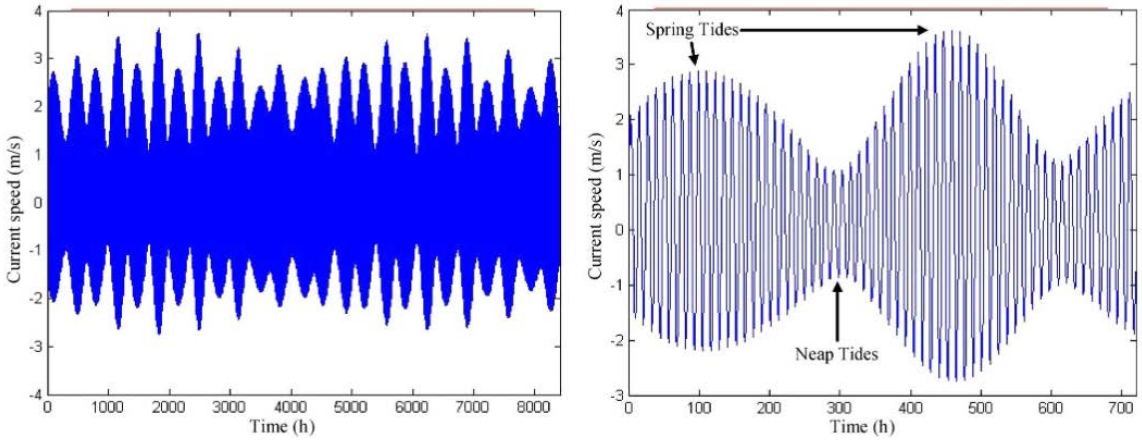

Figure 2.4 Example of tidal current speed variation over a year (Left) and over a month (Right) (Ben Elghali *et al.*, 2007, p. 788) ©[2007].

2.1 State of the industry

According to the Ocean Energy Systems (OES) annual report (2019, pp. 10–17), the following projects have an overall capacity of more than 1 *MW*. In Canada, in the province of Nova Scotia Big Moon Power was allocated a 5-MW project in 2018, 2 *MW* for Jupiter Hydro in 2019, and 1.5 *MW* for Nova Innovation in 2019. Sustainable Marine Energy Ltd. Will deliver a 9-MW project in a joint venture with Minas Tidal Ltd. DP energy is progressing with a 9-MW project at the Fundy Ocean Research Center for Energy (FORCE) with 6 Andritz Hammerfest Hydro AH1000 MK1 turbines. Tocardo has been operating a 1.25 *MW* tidal power plant in the Eastern Scheldt, in the Netherlands. Magallanes Renovables, a Spanish-based company, has a 1.7 *MW* power platform deployed since February 2019 in Orkney. In the UK, SIMEC Atlantis Energy has generated more than 30 *GWh* with their 6-*MW* project called MeyGen, consisting of 4 turbines (SIMEC Atlantis Energy, 2020c). Nova Innovation is also a UK based company with $3\ x\ 100\ kW$ turbines in the Shetland Islands. It was recently granted licence to install a 1.5-MW tidal array in the Bay of Fundy, Nova Scotia, starting in 2020. Orbital Marine Power keeps the site where the SR2000 was at EMEC, a 2-MW floating device deployed when the company was called Scotrenewables Tidal Power, that achieved over 3 *GWh* of generation in a period of comprising from 2016 to 2018. The

second-generation device, under the new company rebranding, will still be a floating 2-MW device called the O2.

During the tidal energy industry development, there have been various concepts proposed for horizontal axis tidal turbines (HATTs), but the ones widely manufactured are the regular 3 bladed horizontal axis devices. Lunar Energy Tidal was working with a ducted prototype [Figure 2.5 (Left)]. In March 2008, the company had signed a Memorandum of Understanding with Korea Midland Power, to develop a 300-MW tidal array in South Korea by 2015 (Bahaj, 2011, p. 3414). Unfortunately, they we not able to secure the remaining funding for the project, and it had to be terminated (Bahaj, 2013, p. 5). Another company with a unique prototype that a similar outcome was OpenHydro. At some point this company was acquired by DCNS as a subsidiary, but that was finally liquidated in July 2018. It started operations in 2005, and as the name of the company name suggests, they had developed a turbine with an open centre. One of their biggest and latest turbines was an 8^{th} generation, 2-MW, 16-m open-centre tidal turbine [Figure 2.5 (Right)]. This devices was generating power in Cape Sharp, Nova Scotia (Naval Group, 2016).

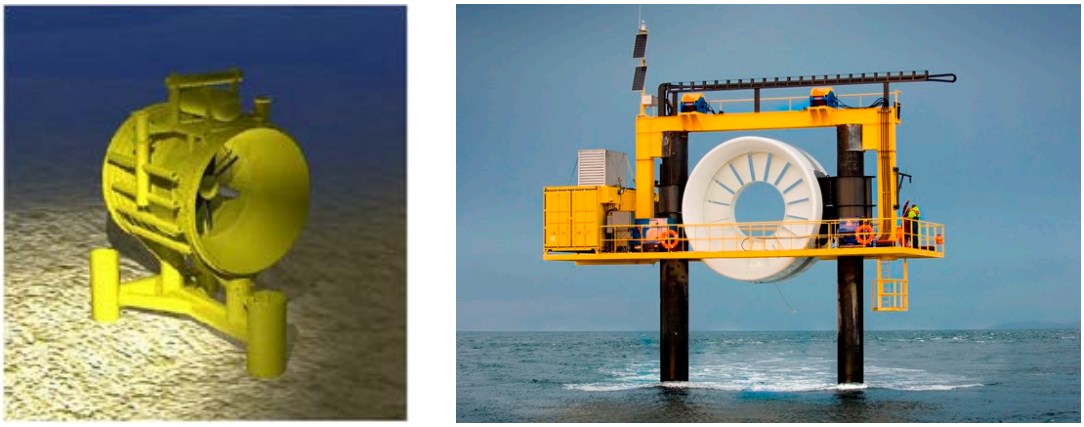

Figure 2.5 Lunar Energy turbine (Lunar Energy, 2020) (Left). OpenHydro turbine (Right) (EMEC, 2022) (Photo by Mike Brookes-Roper).

There are no commercial tidal farms up to this date. The main reason is the huge initial capital cost required to build a tidal farm. The technology is still at its early stages of maturity. Wind turbines and solar PV panels were at this stage too, but the difference is that they had more support for being one of the first big scale renewables with a large potential worldwide. It is true that the tidal sector gets most of the know-how from wind industry, but it still has not achieved the same level of competitiveness needed in the market. One way of closing that gap is by improving the efficiency of the turbines, to bring them closer to the levels of wind turbines. Having done that, tidal developers will also probably recur to the expertise that has been acquired in the last years in offshore wind for the deployment of their own turbines.

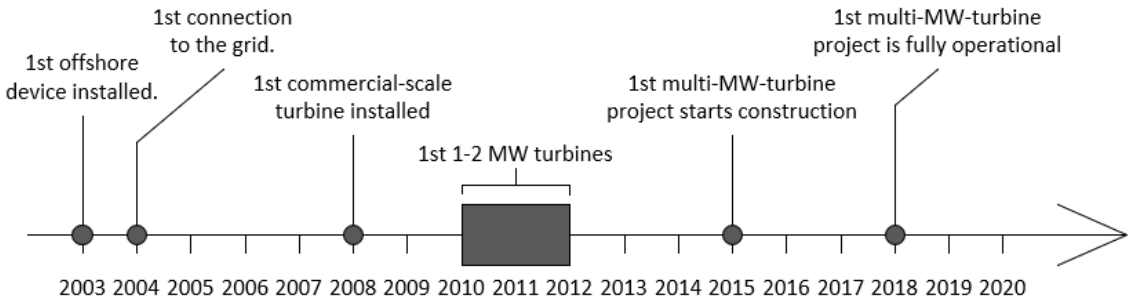

Figure 2.6 Milestones of tidal energy in the last decades.

As it can be seen in Figure 2.6, in the last couple of decades, Marine Current Turbine (MCT) developers have accomplished a series of milestones that have brought them to a stage where they are very close to developing commercial tidal projects. In 2003, Marine Current Turbines Ltd. installed the world's first offshore tidal turbine 'Seaflow' with a rated power of 300 kW. In 2008, the world's first commercial scale turbine was installed, the 'SeaGen S' (Figure 2.7), a two-bladed twin turbine with a rated power of 1.2 *MW* and a total cost of around £10m (MacGillivray *et al.*, 2014, p. 119). Siemens became a shareholder of the company in 2010 and acquired the remaining shares in 2012. In 2015, the company was purchased by Atlantis Resources Ltd. (2015). In 2017 after an acquisition, it became SIMEC Atlantis Energy (SIMEC Atlantis Energy, 2020a).

Figure 2.7 Seagen S turbine (SIMEC Atlantis Energy, 2016).

In 2004 ANDRITZ HYDRO Hammerfest connected the world's first tidal turbine prototype to the grid in Norway. The 'HS300' had a rated power of 300 *kW* and accumulated more than 16,000 *hr* of operation. The next model, the 'HS1000', was the first 1 *MW* pre-commercial device installed at the EMEC in 2011(ANDRITZ HYDRO Hammerfest, 2012, p. 7).

Tidal Generation Ltd. deployed in 2010 a 500-kW device, called 'Deepgen', at the EMEC. From 2011 to 2012, the company became a subsidiary of Rolls-Royce, it was acquired subsequently by Alstom and in 2013 a 1-MW turbine was installed at the same centre. Finally, in 2016 GE completed the acquisition of Alstom, ended the tests at the centre and started developing a 1.4-MW turbine, denominated 'Oceade' (EMEC, 2016a).

Figure 2.8 AR1500 turbine (Lockheed Martin, 2017)

In 2014, MeyGen Ltd., 86% owned by SIMEC Atlantis, secured funding for the first multi-MW turbine project, that started construction in 2015. Phase 1A was fully operational in 2018. It consists of one 1.5-MW Atlantis 'AR1500' (Figure 2.8) and three 1.5-MW ANDRITZ HYDRO Hammerfest turbines. The project consists of 3 Phases, with a permit of up to 398 *MW* of installed capacity, with a present grid capacity of 252 *MW* (SIMEC Atlantis Energy, 2020b).

Other small companies are Voith Hydro and Tocardo. The German company Voith Hydro developed a 1-MW turbine 'HyTide 1000' with a rotor diameter of 13 m and it was installed at the EMEC in 2013. Tocardo is a Dutch company with integrated floating platforms. For example, their Universal Foundation System can consist of five 300 *kW* 'T2' turbines to add up a capacity of 1.5 *MW* in a single structure. In October 2019 Tocardo was declared bankrupt (EMEC, 2016b). Subsequently in January 2020 it was announced that QED Naval and HydroWing had acquired Tocardo Tidal Power (van Unen, 2020).

Some small devices are worth of mention. The company Sabella developed the 'D10', a 10-m rotor with a power capacity of 0.5-1.1 *MW* (Zhou *et al.*, 2017, p. 855). Nautricity Ltd. has a 500-kW contra–rotating turbine 'CoRMaT' that was installed at the EMEC in April 2017 (EMEC, 2017).

As of summer 2020, there are two companies still testing their devices at the EMEC, they are Magallanes Renovables SL, and Orbital Marine Power Ltd which is the rebranded company previously known as Scotrenewables Tidal Power Limited (EMEC, 2020). What both have in common are their floating structures for the turbines. This setup promises to reduce installation costs (Magallanes Renovables, 2020; Orbital Marine Power, 2020).

2.2 Issues Faced by Industry

In 2016, the European Commission published a review of the state of the industry of wave and tidal current energy producers. The report was produced by the Institute for Energy and Transport, part of the Joint Research Centre. The purpose of this centre is to provide independent evidence to support EU policies. The authors Uihlein and Magagna cover the following aspects: resource assessment and forecasting; environmental impacts; socio-economic impacts; grid integration; installation, operation and maintenance; and regulatory affairs, together with existing gaps in knowledge and some recommendations on where future research should focus (2016).

Resource assessments of tidal currents have been made for several years now; forecasts are also readily available. The main environmental impacts include changes in water flows, composition of substrate, and sediment dynamics which also affect sea life directly. Life Cycle Assessments have also been carried out for devices that were ready for deployment. Such is the case for the 'Seagen', made by Douglas, Harrison and Chick (2008). In the case of tidal arrays, it gets more complicated, because until now there is no tidal farm of sufficient scale to evaluate. The approach is to make an estimate, which varies with the size and factors such as turbine efficiency, transmission and power losses (Domenech, Eveleigh and Tanju, 2018, p. 725). Other costs must be considered as well, such as operational costs, grid connection and installation costs. Social impacts include job creation, CO_2 reductions, impacts on other marine users, energy security, health and quality of life. There is only one cost-benefit analysis, available online, of a hypothetical tidal array by Houde (2012). In the analysis a 300 MW array was assumed, at present value it was estimated to yield negative numbers due to the high initial costs. Grid connection involves difficulties with high costs too, as subsea electrical components can be very expensive. Another issue regarding grid connection is the resource availability because the grid would have to be extended to allow integration from the coasts. It is estimated that the installation, operation, and maintenance can be around 3.4–5.8% of capital expenditure, compared to 2.3–3.7% for offshore wind (Lacal Arantegui *et al.*, 2014). Lastly, the current legal framework needs to be revised as not much attention is given to ocean energy and the legal barriers it may encounter.

Vazquez and Iglesias investigated the effects of the input values on a Levelised Cost of Energy analysis for hypothetical tidal stream projects. The assessment proposed six tidal farms with different number of turbines, rows and spacing. The device interaction was modelled numerically, and the impact of the economic and financial variables was also considered. In addition to that, sensitivity and multivariable analyses were performed. The result showed that increasing the power coefficient C_P from 0.35 to 0.50 reduced the LCOE by 20% (2016, p. 95).

$$C_P = \frac{\tau\Omega}{\frac{1}{2}\rho A U_{max}^3} \qquad \text{Equation 2.2}$$

The power generated by a turbine can be calculated multiplying the torque (τ) times the rotational speed (Ω). The denominator is the available power in the fluid, where ρ is the density, A the area of the rotor, and U_{max} the maximum flow velocity. The power coefficient is the proportion of energy that can be extracted from the total available to the swept area of the rotor.

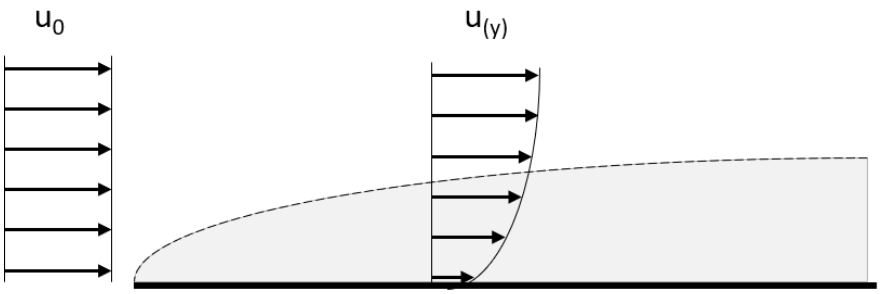

Figure 2.9 Velocity profile developed over a surface.

Tidal turbines are constrained in size by their proximity to the seabed and the water surface. Onshore wind turbines have tall towers to see a relatively uniform wind velocity profile across the turbine. The velocity profile shown in Figure 2.9 is well approximated by a 1/7th power law (α), $u_y=u_r(h/h_r)^{\alpha}$ (Myers and Bahaj, 2010, p. 220), where h is the height and r the reference measurement. In the case of tidal turbines, the velocity seen at the top of the turbine can be 50% higher than the one at the bottom in an example from Mason-Jones *et al.*(2013, p. 24). Ideally, the turbine should be positioned close to the water surface, but that is not always possible due to maritime traffic. In the same example, a 10-m diameter turbine is proposed to be positioned 10 m from the seabed, and it was modelled using CFD. The cyclic torque, power and thrust resulted in an asymmetric loading due to the high velocity shearing flow, that have to be considered in the design process (Mason-Jones *et al.*, 2013, p. 29).

In the third auction of CfD in the UK, there was a record-breaking price of around £40/*MWh* for offshore wind farms that could start operating in 2023. Those prices could be cheaper than existing combined-cycle gas plants. The first auction in 2014 awarded projects with prices of £150/*MWh* (Simon, 2019). The strike price is a fixed price payable for the electricity generation

that new technology developers can receive usually for first of a kind or new technology. CfDs pay the difference between the reference price (market price) and the strike price. Strike prices for tidal stream have been from £305/*MWh* (2014-2019) to £217/*MWh* (2024/25) for the first three rounds, with no projects awarded so far. The reference price of electricity for the financial year 2020/21 was £55.20/*MWh.*

In comparison, the European Strategic Energy Technology Plan (SET Plan) projects that tidal energy could achieve a LCOE of £135/*MWh* by 2025 and £90/*MWh* by 2030 (OES, 2019, p. 32)[1]. At the same time, for tidal stream, the BEIS estimates a LCOE for 2025 of £169 to £338 per *MWh*. Being optimistic, if offshore wind projects that started in 2016 were awarded a strike price of £150/*MWh*, and an optimistic scenario places the LCOE of tidal stream energy at £169/*MWh,* that implies that tidal energy is still behind offshore wind by around 10 years. A recent 2 *MW* floating tidal stream device was estimated at a LCOE of under £200/*MWh*, comparing to the same offshore wind projects mentioned above, where 3 *GW* of installed capacity benefit from prices at 2019 of £165 to £180 per *MWh*, could mean that the gap could come narrower than 10 years between both technologies (Orbital Marine Power, 2021). Considering all the investment being put in wind energy, and the lack of same attention to tidal, the gap could increase. It is understandable that the government allocates most of the funding on more mature (thus cheaper) technologies, but it slows down the development of new ones. The tidal energy industry acquired a significant proportion of its knowledge from the wind industry, but that does not mean that at some point the wind sector could not benefit from new developments on tidal generators.

Onshore wind power does not require support from government anymore as it is a mature and competitive technology. Offshore wind energy seems to have taken the same route too. In Germany and The Netherlands, there are already subsidy-free offshore wind turbine projects. It seems that in 2019 The UK may have awarded the world's first offshore windfarm that would have to pay money back to the government during the lifetime of the project if the wholesale prices keep going up at a growth of 0.3% per year (even below historical rates) (Jansen *et al.*, no date, p. 618).As it has been previously mentioned, tidal turbine developers cannot just increase the rotor diameter of the devices to get higher power performance, because a higher tip speed ratio increases the possibility of cavitation. Cavitation is a phenomenon that occurs when water pressure drops below vapour pressure forming bubbles that later implode, this could erode the blades and reduces the turbine performance. Bahaj *et al.* found that the decrease in power capture could be up to 5% (2007, p. 419). In shallow water, seabed and the water surface represent additional constraints to rotor sizes. There is another reason not to increase

[1] Exchange rate of £0.9/€ (Aug 2020)

indiscriminately the rotor size, and that is thrust force. The maximum axial thrust force ($T_{max}[N]$) acts in the direction of the flow, given by:

$$T_{max} = \frac{1}{2} C_T \rho A V_{max}^2 \qquad \text{Equation 2.3}$$

Where C_T is the thrust coefficient, typically around 0.9 (Bahaj and Myers, 2003, p. 2209) , ρ is water density, A is the turbine cross sectional area, and V_{max} is the undisturbed flow speed.. The higher the thrust, the more expensive the structure must be to withstand it. A device with a high power coefficient, and a relatively low thrust coefficient would be ideal in terms of cost-effectiveness. Water density is 800 times higher than air, outweighing the reduction of tidal turbines swept area and flow velocity, compared to wind turbines conditions, as seen next.

The Office of Energy Efficiency and Renewable Energy of the United States of America Department of Energy, shows a power curve for a typical wind turbine where it can be appreciated that the rated speed is 15 *m/s* (2017). Two of the most powerful tidal turbines to date, the SR2000 (Scotrenewables), and the AR2000 (SIMEC Atlantis), have a rated current speed of 3.0 *m/s* (Encarnacion, Johnstone and Ordonez-Sanchez, 2019, pp. 1–2). Taking the densities for air and sea water of 1.225 *kg/m³* and 1025 *kg/m³*, respectively, Figure 2.10 shows that a tidal turbine of 25 *m* in diameter receives the same amount of axial thrust as a 145-m wind turbine. A factor of around 5.8 could be used for other values using this comparison. The rated power for the turbines is in the range of 10 *MW* for wind and 2 *MW* for tidal.

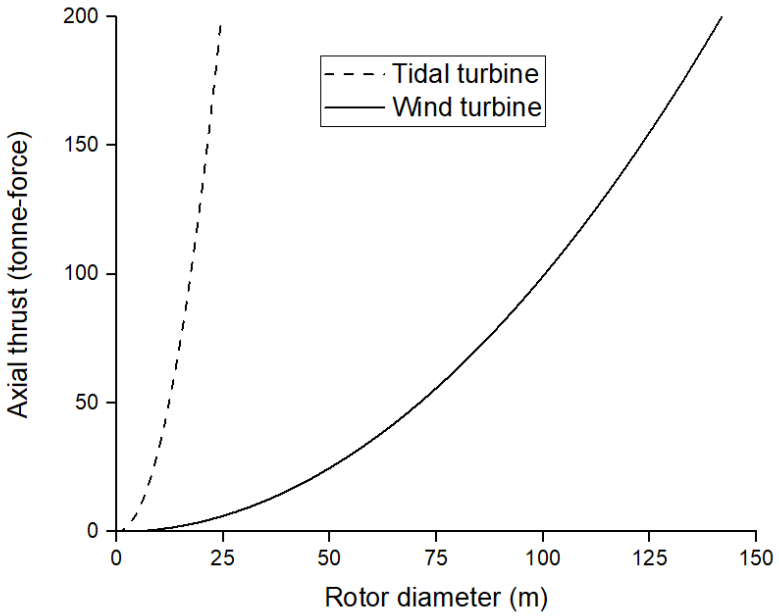

Figure 2.10 Thrust comparison for tidal and wind turbines.

In 2016, the UK Government removed funding support for marine energy for CfDs. The second auction in 2017 was dominated by offshore wind and gas projects, with a small amount support to energy from waste. In the same year, the construction of a pilot tidal array in Normandy was authorized, and even though almost half of the CapEx was funded, the project did not go through. The TIGER project, funded by Interreg, has the aim to reduce tidal industry costs from £270/*MWh* to £135/*MWh* by 2025 (OES, 2019, p. 32)[2]. The UK Offshore Renewable Energy Catapult reported in 2018 that tidal has the potential to reach £90/*MWh* by 1 *GW* installed and £80/*MWh* by 2 *GW*. As it will be seen in the next section, tidal turbines have a power coefficient close to wind turbines and have similar levels of power coefficient for equally rated turbines (Bahaj and Myers, 2003, p. 2207).

2.3 Energy costs

In the previous section we compared technologies based on their LCOE. As its name suggests, it is a measure that weights different variables for the duration of the project, resulting in a simple cost per unit of electricity that allows comparisons between different technologies. The main input variables for the calculation are the capital costs, operation and maintenance, discount rate, expected lifetime and depending on the technology some others like fuel for fossil-fuel-dependent technologies, or efficiency for renewable energy. Vazquez and Iglesias realised a single and multiple variable analysis, both key studies in Multi-criteria Decision Making, for tidal stream energy projects. They found that the three factors, in order of importance, that affected the LCOE were the power coefficient, the discount rate and the capital costs (Vazquez and Iglesias, 2016, p. 99).

In the introduction it was briefly discussed that offshore energy-harvesting farms should be as close to the shore as possible to reduce costs, in addition, the water depth can increase the costs significantly as well. The 2015 Cost of Wind Energy Review calculated a LCOE for onshore wind energy at £46/*MWh*, and £138/*MWh* for bottom-fixed offshore wind farms, 3 times more expensive (Moné *et al.*, 2015, p. 74)[3]. The same report in 2018 places the LCOE for onshore wind at £32/*MWh*, 30% cheaper in only 3 years. Bottom fixed turbines were £68/*MWh*, coming down to cost just above 2 times the price on-land. Wind farms with floating structures still being the most expensive at £100/*MWh* with a sensitivity range for offshore wind turbines of £63-£124/*MWh*. The variation is mostly influenced by the fluctuation in CapEx (£1882-£4954/*kW*) that depends mostly on water depth and proximity to shore (Stehly and Beiter, 2018, p. 37)[3].

[2] Exchange rate of £0.9/€ (Aug 2020).
[3] At a exchange rate of £0.76/$ (Aug 2020)

Modern wind turbines achieve a power coefficient of around 0.50 (Porté-Agel, Bastankhah and Shamsoddin, 2020, p. 2), while tidal turbines range from 0.39 to 0.45 (Rosli and Dimla, 2018, p. 36). Both are governed by the Betz limit of 0.59 for the maximum power that can be extracted by these types of devices in an open flow. For this first parameter, there is more room for improvement for tidal turbines, so it makes sense that it is the most important factor affecting the calculation of the LCOE. The discount rate is the second value considered, and because it is calculated for projects ranging 20 or 30 years, it works in a similar way as the compound interest, but in this case is the amount of value that the initial investment will lose over time. Project developers tend to use high discount rates, of around 10% (Vazquez and Iglesias, 2016, p. 91), because they generally expect to get profit at the middle of the project, between 10 and 15 years from start. According to WindEurope, the average lifetime of a wind turbine ranges between 20 and 25 years, with some reaching up to 35 years by repowering them (WindEurope, 2020, p. 9). Tidal turbines lifespan is in the same range, as it is the case for the one sold by Andritz Hydro, with a lifetime of 25 years and 5 periods of servicing (2012, p. 9). Rotor blades are the most expensive parts of a tidal turbine as can be seen in the costs breakdown (Coles *et al.*, 2021, pp. 2139–3) in Figure 2.11. The rotor blades represent the 43% of the cost of a single turbine, in this example, £5M each.

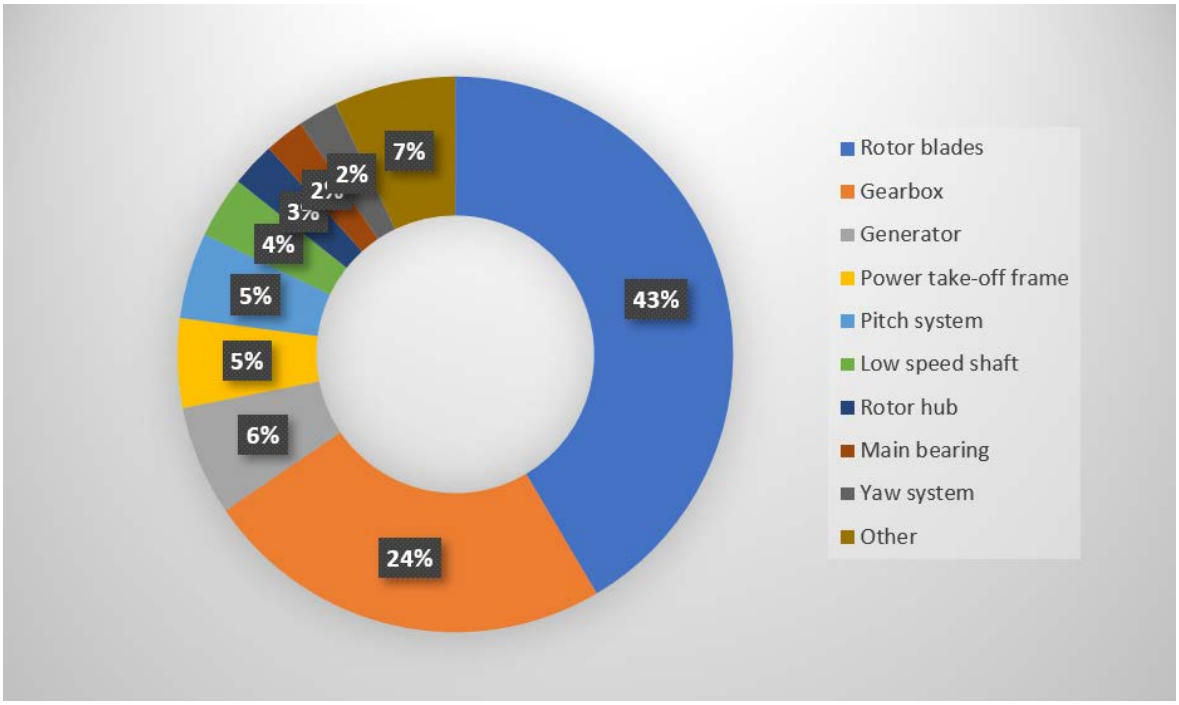

Figure 2.11 Capital costs breakdown for a single tidal turbine.

For the case of a tidal array, the costs can be observed by category (Black & Veatch for BEIS, 2020, p. 23) in Figure 2.12. Turbines represent 39% of the CapEx. Modern manufacturing processes use composite materials, so the blades are built with a spar (also called 'skeleton') (Lin, Lee and Lwin,

2011, p. 237). Redesigning the blades would incur in a minimum extra manufacturing cost (included in other costs), so it seems like a feasible course of action to improve the power output of a tidal turbine. Increased power coefficients in tidal turbines can come from better control systems, forecasting, maintenance strategies and improved blade hydrodynamics. Offshore wind turbines are expected to be rated at 12-15 *MW* for projects from 2023, tidal current turbines are limited in size because of the environmental factors previously discussed (CATAPULT Offshore Renewable Energy, 2018, p. 11). In the next section, the different options to increase energy production in tidal turbines will be discussed.

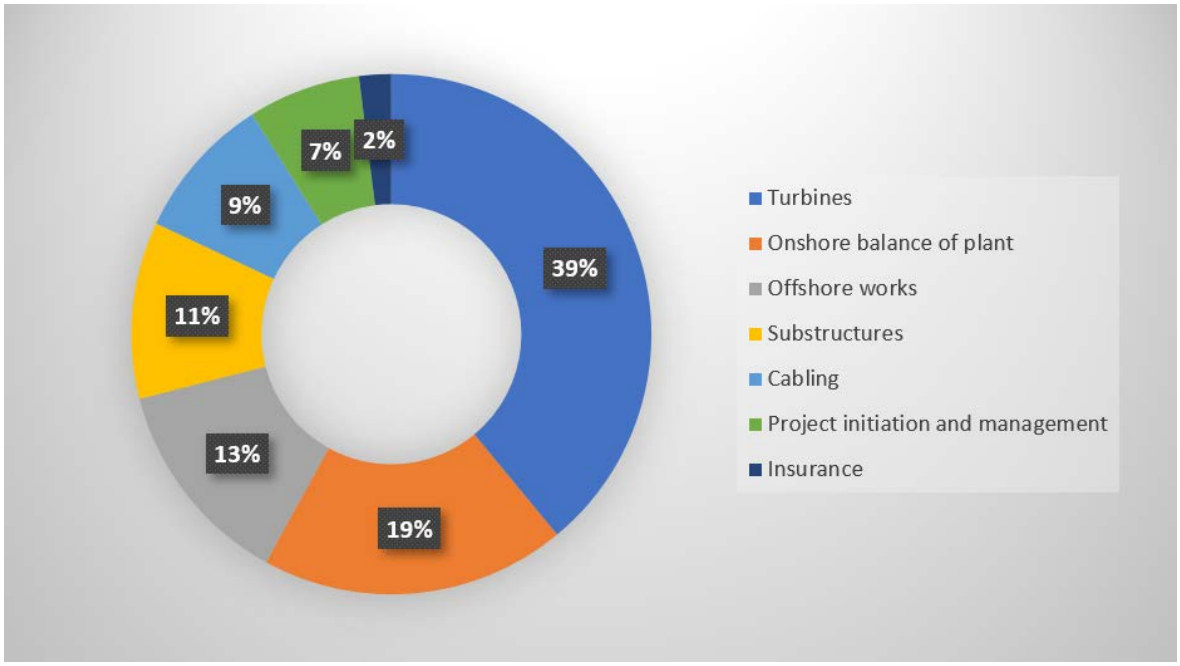

Figure 2.12 Capital costs of a case study tidal stream farm.

2.4 Methods studied to increase power output

There have been various methods studied both by simulations and experimentally to try to improve power capture from horizontal axis wind turbines. Bach et al. (2014) investigated experimentally the use of micro-tabs that alleviated the overall load to the blade, improving the lift to drag ratio, but no measurement wad made to the power or thrust coefficients. In 2015, Ibrahim et al. introduced slots and tubercles to the blades and tested their performance for different wind speeds. The average power coefficient for the slotted blades was 0.39, compared to 0.36 for the straight blade, and 0.13 for the one with tubercles (Ibrahim *et al.*, 2015). Non-straight blades also have been studied by Shen *et al.*, finding an optimised shape for a specific blade that resulted in an increase in the AEP of their model by 5.9%, while keeping the same level of thrust for the turbine (2016). The most widely studied, and probably the ones that have given better results are winglets, and they will be discussed in depth in the following section.

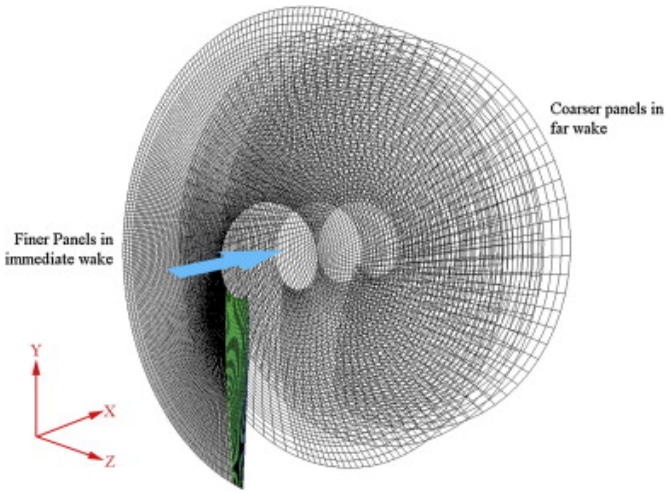

Figure 2.13 Fluid dynamics simulation for bend-twist coupled HATT blades (Nicholls-Lee, Turnock and Boyd, 2013, p. 543).

In the case of tidal turbines, there have been few simulations and fewer experimental studies performed. Nicholls-Lee, Turnock and Boyd made a fluid dynamics analysis of passively adaptive tidal turbine blades, estimating an increase of up to 5% in the C_P and a decrease of up to 12% in the C_T (2013, p. 549) (Figure 2.13). Experiments performed by J. Giles were focused on a technique that did not modify the design of the turbine but added a ramp on the seabed to produce a more even velocity profile at the rotor, that could result in an increased thrust and 5% more power (2013, p. 132).

2.5 Winglets on Airplane Wings

In 1897, English engineer Frederick W. Lanchester, obtained a patent for vertical surfaces at the wing tips. In 1976 an aeronautical engineer, Richard Whitcomb, carried out his research at NASA using the term winglet to refer to a nearly vertical wing extension to reduce the induced drag on wings (Whitcomb, 1976). In principle, their main function is to prevent the interaction of the fluid from the high to the low-pressure side, diminishing the tip vortex, decreasing the spanwise flow, therefore reducing the induced drag (Maughmer, 2003, p. 1100). Winglets are evolving in aviation towards active systems that can respond to flight conditions (Jeffrey, 2020, p. 37). Figure 2.14 (L) shows the vortex formed at the edge of a wing where the flow from the high-pressure side travels towards the low-pressure side, as a result from the pressure difference. Figure 2.14 (R) illustrates the same vortices occurring at the current turbine blade tips. In contrast to an airplane wing, where vortices are perpendicular to the stream flow, in the case of current turbines, the vortices travel relatively in the same direction of the fluid.

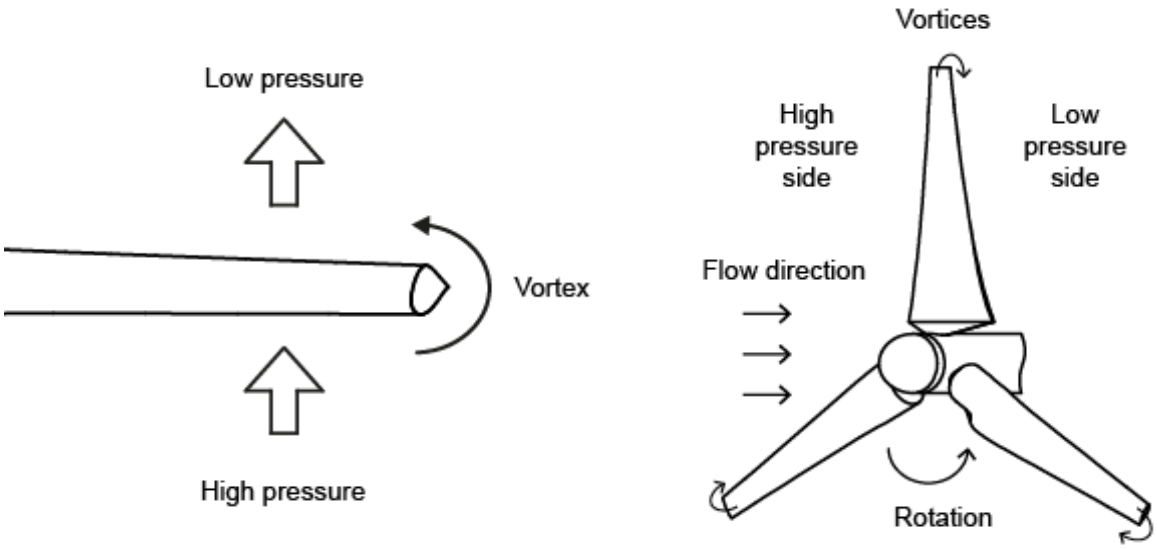

Figure 2.14 Left: Vortex direction in an airplane wing. Right: Vortices in a turbine blade.

There are different types of winglets, such as multi-tip, blended, fins, spiroid, raked, c-type and winglet fence (Sweety *et al.*, 2019, pp. 220–224). The present study is focused mainly on bent wing extensions (blended winglets) because their construction is straightforward, and they can be defined with 8 key parameters that will be detailed in the next section. Such specification can help determine the effect of each variable in the overall performance, but it does not necessarily mean that the result will be the addition of such changes, rather an overall outcome.

2.6 Winglets on wind and tidal turbines

In 1985, Gyatt and Lissaman tested tip devices in HAWTs, finding no apparent improvement over the regular wing performance, but emphasizing that 'The promising results obtained on nonrotating wings make it difficult to accept that tip devices could not improve wind turbine performance'. During that time, the most cost-effective method was experimental, both either out on the field or in wind tunnels (Gyatt and Lissaman, 1985, pp. 61–63).

2.6.1 Winglets on wind turbines

At the beginning of the 1990s, a Japanese researcher, Yukimaru Shimizu from Mie University, in collaboration with the Delft University of Technology (DUT), carried out a series of experiments on "Mie-type" winglets. These winglets have a height of around 20% the blade length, and are dual, this means that there is a section pointing upwind and downwind, with the latter being bigger. Additionally, some theories were developed on how winglets might affect tip vortices, and numerical models were applied (Shimizu *et al.*, 1990). Around the year 2000, the increased

capability and availability of computers made Computational Fluid Dynamics (CFD) replace physical experiments and simulating the use of winglets on wind turbines became the standard.

Shimizu et al. started testing the “Mie-type” vanes of approximately 20% the height of the blade. They reported an increase in the power coefficient of around 27% for a tip speed ratio (TSR) of 4, no effect on thrust is presented. After that, Prof. van Bussel from the DUT in The Netherlands, developed a momentum theory for a blade-winglet configuration. The main assumption was that the increase in power happened by the shift in the vorticity of the wake downstream (van Bussel, 1990, p. 1). A couple of years later, further experiments and an adjusted theoretical model was presented, announcing an augmentation of 17% in the power coefficient, instead of the 27% previously stated, for a TSR of 5 (Shimizu *et al.*, 1992, p. 122). In 2003 more studies were carried out the power augmentation reported was 8.75% (Shimizu *et al.*, 2003a, p. 187).

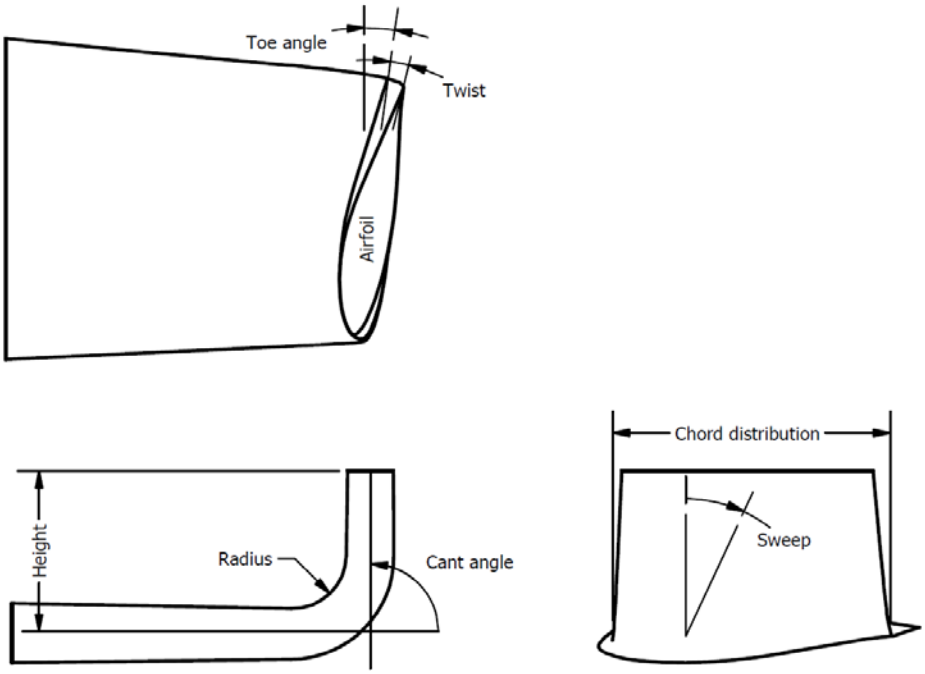

Figure 2.15 Design variables for winglets facing the suction side.

In 2006 Johansen and Sørensen used CFD to investigate the possible increase in C_P by using winglets on wind turbines at Risø National Laboratory, Denmark. A key aspect from their studies is that they used the geometry explained by Maughmer (2003) that defines 8 key parameters of winglets: the airfoil, chord distribution, height, radius, twist, sweep, cant and toe angle (Figure 2.15), the cant angle is measured from the plane of the blade towards the suction side. A cant angle of 90° means towards the suction side and pointing the pressure side would be -90°. The height is represented as a percentage of the blade length. The radius is also represented as a percentage of the winglet height. The sweep as well as the other angles, is measured from a normal view of the turbine and if applicable, following the flow direction. A positive sweep angle

is looking backwards the axial rotation and vice versa. Their simulations focused on different configurations of winglets facing the pressure side for wind speeds from 6 *m/s* to 12 *m/s*. The one with the best overall power performance had a height of just 1.5% the size of the blade at 90°, obtaining a 1.3% increase in power and 1.6% in thrust (Johansen and Sørensen, 2006, p. 8). According to their simulations, the winglet affects approximately 14% of the end part of the blade (2006, p. 9). Finally, the effect of pointing the winglet to the opposite side, the suction side, was analysed with slightly better results (2006, p. 16).

In the following year, Gaunaa and Johansen presented their theoretical work where they explain that the increase in power is derived to a reduction of tip effects rather than the downwind vorticity shift as believed until that date (2007a, p. 5). They evaluated the effect on a winglet with 25% of radius, and the results from their code placed downwind winglets as superior in performance compared to upwind ones (2007a, p. 8). In their article, a reduction in the total drag is also achieved. The total drag is the addition of the drag induced by the winglet minus the reduction of the induced drag of the blade (2007a, p. 2). It is pointed out that compared to the work seen on winglets for airplanes, few has been done on winglets for rotors (2007b, p. 48; Gertz, Johnson and Swytink-Binnema, 2012, p. 390). In another paper, Johansen and Sørensen estimated an increased power of 1.0% to 2.8% and additional thrust of 1.2% to 3.6%. The winglet configuration yielding the best results had a height of 2%, a radius of 20%, and a twist of 4° with an increase of 1.74% in power and 2.13% in thrust (Johansen and Sørensen, 2007).

Over the past 10 years more simulations have been carried out with the use of CFD, incorporating winglets of less than 10% of relative height with respect to the blade length, resulting in power coefficient increases ranged from 2% to 8%. Prof. Chattot studied the effects of blade tip modifications on wind turbine performance using an optimization code, based on Golden vortex model (2009). The results favoured a backward sweep, and forward dihedral and winglet (facing upstream), each one analysed independently. Lawton and Crawford used a wake vortex method and concluded that a winglet facing downwind of a 5% height would result in a power increase of 2% with a similar increase in thrust (2014). Elfarra, Sezer-Uzol and Akmandor pointed out that winglets add aerodynamic forces and bending moment due to their weight too (2014, p. 136), and used a genetic algorithm to optimize a winglet design and estimated the power capture increase in 9% (2015).

In 2019, *Mourad et al.* found through simulations that winglets performed better to the opposite side of what was commonly found, and cited 6 authors that supported winglets pointing upwind for better rotor performance (2020, p. 3). Maughmer wrote that *"…, the downward-oriented winglet produces a spanwise contraction of the wake and is less effective…"* in his paper regarding

the design of winglets for sailplanes (2003, p. 1100). As it was discussed in section 2.5, the pressure and the suction side for an airplane wing and a turbine blade are almost perpendicular to the flow direction from each other. In this case, an upward-oriented winglet, would correspond to the suction side of a wind turbine, *i.e.* pointing downwind. The experiments performed by Ali *et al.* are for a non-rotating blade mounted on a base (2015, pp. 760, Fig. 2), and it makes sense that their results compare to what is a standard in airplane industry, that is winglets pointing upwards. Zhu's *et al.* simulations determined that winglets facing the pressure side were more effective than the ones facing the opposite direction in some conditions and vice versa. Their conclusion was that a design with winglets facing both directions was more effective in all conditions (Zhu *et al.*, 2017, p. 7). Khaled *et al.* performed a series of experiments and simulations with winglets from 1-7% of height and cant angles from 15-90° (pointing downwind), finding with an Artificial neural Network that the longest performed better at around 48.3°. Their simulations were compared to experiments with five winglets at 90°, and the winglets in their simulations went out of the original rotor size as it can be deducted from their graph of C_P vs. cant angle (Khaled *et al.*, 2019, pp. 10, Fig. 15), where all winglets should have the same coefficient as the normal blade at an angle of 0°. Khalafallah, Ahmed and Emam carried out simulations of wind turbine blades with winglets facing both directions, finding that the best configuration was for the ones pointng upstream, in addition to downstream swept blades (2019, p. 9). It was is interesting to find the former and the latter simulations suggesting that winglets perform better in the opposite direction to what previous studies had shown.

A fewer number of experiments have been carried out in the academia recently. Gertz and Johnson set a baseline case for a wind turbine with exchangeable tips of the outer 10% of the blade. The evaluation testbed included a model based on Blade Element Momentum (BEM) theory. The blades had a length of 1.6 m and the rotor was tested at a 10-m × 12-m open-jet wind tunnel with a capability of producing winds up to 11 *m/s* (2011, p. 1361). The next year, Gertz, Johnson and Swytink-Binnema presented their results with a power increase of 5% to 7% for wind speeds between 6.5 m/s and 9.5 m/s. In the same article, a report is mentioned where it is suggested that winglets can only be optimized for one operating point (2012, p. 392) as their effect has a bell-shaped power curve, and their own results were in agreement (2012, p. 406).

If a tidal turbine were to be optimised for an operating point, the percentual increment would not reflect on its entirety to the annual energy production. Due to the variation in speeds of tidal currents, it would be less than that, and it would be site specific. Taking as an example Figure 2.16 showing a case study for a site with a maximum speed of 4 m/s, using the product specifications for first commercial scale turbine, the SeaGen-S 2000, with a rate speed of 2.5 *m/s*. In this case,

roughly half of the yearly production is extracted above rated speed. This means that if the maximum power were to be incremented by 2%, the AEP would only increase by 1%.

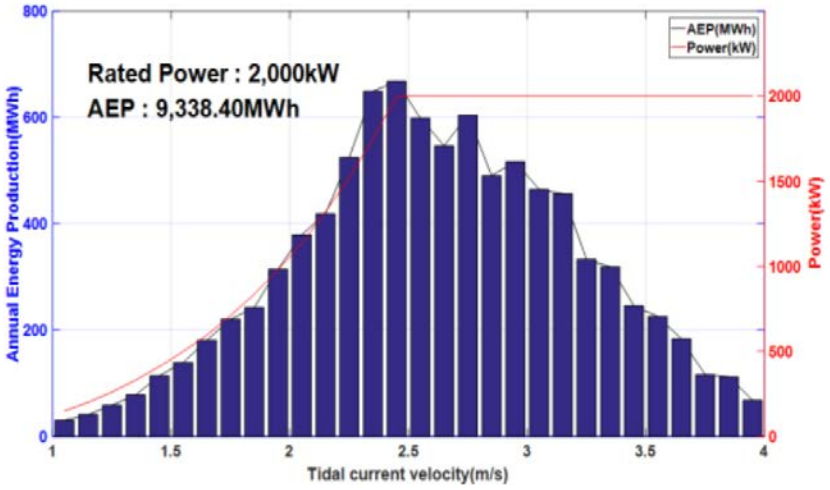

Figure 2.16 Average Energy Production for a case study with a SeaGen-S turbine (Ko, Park and Lee, 2018, p. 1305) (Reproduced and modified with permission from the Coastal Education and Research Foundation, Inc.).

In 2012 and 2013 Saravanan, Parammasivam and Rajan, from India, presented their results on the effect of winglets on pressure difference. In their first study, the rotor had a diameter of 340 *mm* and the two variables of the winglets taken into consideration for the study were the height and radius, bent to the suction side with a cant angle of 75° (2012, pp. 425, 426). The wind speed was kept constant for all tests at 5 *m/s*. The presence of the winglets seemed to have an increased pressure at 0.3c with a maximum pressure difference at 0.95R (2012, p. 427). In the suction side the pressure dropped up to 10% (2012, p. 425). Then, in 2013 a small rotor was tested for low wind speeds with the same winglets used previously. This time, in addition to the fact that they measured an improvement in the power coefficient for low wind speeds, they observed that the starting velocities were lower for all setups with winglets (2013, p. 162). Aravindkumar, from India as well, measured a noise reduction of 25% (in logarithmic scale) in addition to a power increase of 2.01% (2014, p. 243).

Another experimental investigation was found on a small scale HAWT for domestic purposes. Results indicate a lift-to-drag ratio increase of 26%, but it has to be pointed out that the experiment involved a non-rotating blade (Ali *et al.*, 2015). Tobin, Hamed and Chamorro obtained an 8.2% power increase and 15% added thrust for a turbine with winglets (2015, p. 11955). Similarly, a radial increase in length of the blade would result in a bigger rotor area with a corresponding power output increase of 7.8% (2015, p. 11969). In addition to that, the higher thrust coefficient generated a region of higher mean shear and turbulence outside of the rotor (2015, p. 11963).

In a different experiment, the interaction between two wind turbines fitted with winglets was studied. The wind turbine located downstream saw a decrease in power capture, however the added power extraction for both was higher (Ostovan and Uzol, 2016). Mühle et al. studied the effect of winglets on the tip vortex and the near wake, finding that for wake regions larger than x/D=4.0, the wake's mean recovered faster due to the tip vortex interaction stimulated by the winglets, in addition to a higher power extraction (2020).

ENERCON is probably the only large manufacturer that has exploited the potential of winglets. Figure 2.17 shows a rotor blade from the E–101 wind turbine with winglets. The company has been using them for their turbines since the early 2000's. Some versions of the E–66 (Hau, 2013) and E–70 turbine models include them. Their winglets point towards the pressure side to allow tower clearance (Hansen, 2017, p. 19; Johnson *et al.*, 2019, p. 16). The upgraded 2010 version of the 2007 E–126 model achieved an enhancement of 12% to 15% was by the refinement of the airflow around the nacelle and the addition of winglets (de Vries, 2010).

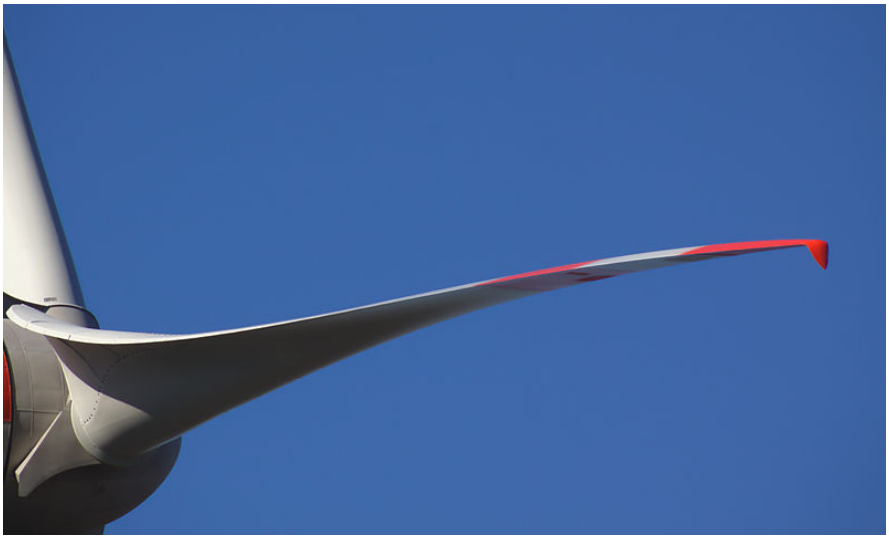

Figure 2.17 ENERCON E-101 turbine with winglets (Aßbrock, 2013).

2.6.2 Winglets on Tidal Turbines

Studies on winglets for tidal turbines are scarce, the ones published are mostly numerical, and the majority produced suggest they should face the suction side. Zhu et al. took power and thrust measurements from an experimental study on a horizontal axis marine current turbine, carried out at the University of Southampton (Bahaj *et al.*, 2007) to adjust their baseline for the simulation. Their best design produced a power increase of 3.96% at a higher tip speed ratio (Zhu *et al.*, 2017, p. 7). Ren, Liu and Zhang presented a triangular winglet bent downstream that increased the power coefficient by 4.34% and the thrust coefficient by 3.97% at an optimal TSR of 5 (2017). In 2019, the same authors compared the effect of facing the winglets in both directions,

finding that the best design achieved a 4.66% power increase when facing downstream (Ren, Liu and Zhang, 2019).

To the time of this project, only one experimental study was found. Young et al. evaluated four different winglets, consisting of a linear extension of the tidal turbine blade, varying the main parameter of cant angle. In their study, the power coefficient, the hydrodynamic efficiency, and the structural efficiency were considered. After initial simulations using a modified vortex-lattice method, three winglets were designed to face upstream, and one downstream. Even though all of them were expected to perform better than the regular blade, only the ones facing upstream did. It was proposed that viscous effects (i.e. a separation at the corner of the blade-winglet junction) play a role in the drop in power coefficient for the winglet facing downstream (Young et al., 2019).

Table 2-2 on page 40 summarizes the main studies carried out on winglets (bent wing extension ones) design parameters and its effect on different numerical, CFD, and experimental studies of HATs with winglets, from its beginning and its evolution to date.

2.7 Material selection for tidal turbines

Blades are the most expensive components of the turbines and are expected to last for as long as 10 to 20 years of operation (Li *et al.*, 2014, p. 230). Tidal turbines face additional issues to wind turbines. Due to the high density of water, high cyclic hydrodynamic loads can cause fatigue and failure. Corrosion is another challenge inherent to the marine environment. Material selection plays an important role when mitigating such demands. From materials used in ship propellers, to more advanced composites which performance has not been tested for long periods of times under water, new technologies are applied in the manufacturing process to make the blades cost-effective as well as strong, stiff, and durable.

Metal alloys such as nickel-aluminium bronze have been widely used in the ship industry to manufacture propellers. Ship propellers have a different geometry than tidal turbine blades, and their purpose is to give a ship propulsion rather than harvesting the kinetic energy from the current as a tidal turbine does. Metallic tidal turbine blades would add weight, which in consequence would require a thicker shaft, and it can be seen how the additional weight translates into a heavier (and more expensive) turbine. In that sense, composite materials are the preferred choice of tidal turbine developers due to the complex shape of the blades (Li *et al.*, 2016, p. 418).

Standard turbine blades consist of a foam core, shear web and facesheet. Fibre glass/epoxy composites are used for the shear web and facesheet as they can withstand cyclic hydrodynamic

loads and corrosion. The core foam serves as the inner structure in the manufacturing process, in operation it can provide neutral buoyance for the rotor and provides water permeability. The shear web is responsible for carrying out the shear loading during operation (Anyi and Kirke, 2010, p. 111).

Carbon fibre/epoxy blades provide more strength and lightness, but they are normally 10 to 20 times more expensive than glass fibres (Li *et al.*, 2014, p. 231). Up until 2020, only around 10 published results were published in the previous 40 years on the effect of aging by sea water on facture of carbon fibre laminates for marine applications (Le Guen-Geffroy *et al.*, 2020, p. 199). An option is to use fibre glass composites with carbon fibre reinforcements in key components like the spar. The larger the wind turbine, the more efficient and cost effective it is, as the size increases, more carbon fibre reinforcement is used to compensate the high stress and fatigue on the blades (Golfman, 2016, pp. 3–11).In recent years, additive manufacturing has brought the opportunity of replacing moulds with parts produced using this technique, reducing time and costs. It could also be part of the structure to bear the cyclic loads. Even the shear web could be integrated into the design together with the root fasteners (Murdy *et al.*, 2021, p. 1).

Passively adaptive tidal turbine blades have the capability of changing pitch, on a fixed pitch turbine, depending on the load. Murray *et al.* (2018) constructed a bent twist turbine blade with graphite epoxy composite. The induced bent twist coupling was achieved by orienting the composite fibres at 30° from the axis along the blade. A FEA-BEMT tool was developed for the iteration between the structural response and the hydrodynamic performance of the passive adaptive blades. CFD can also be coupled with the FEA as done by (Nicholls-Lee, Turnock and Boyd (2013). Particle swarm optimisation (PSO) can also be used iteratively after the hydrodynamic modelling, in conjunction with the structural analysis to find the optimum number of layers, ply thickness and orientations (Li and Chandrashekhara, 2015, p. 1191).

2.8 Computational Fluid Structure Interaction (FSI)

FSI couples CFD with Computational Structure Dynamics (CDS) to give a more realistic solution to simulations. CDS uses a Finite Element Method (FEM) to evaluate the forces and stresses on the structure, to predict potential material failure. Some authors consider that a full scale fluid-structure interaction is essential to model wind turbines performance accurately (Korobenko *et al.*, 2018, p. 255).

One example is the work carried out at the Sustainable & Resilient Structures Research Group at the National University of Ireland Galway. With the aid of an in-house structural analysis software called BladeComp and their state-of-the-art Large Structures Testing Laboratory, different

projects within the wind and tidal industry, regarding turbine blades, have been carried out (Finnegan *et al.*, 2020, p. 260). In 2019 they analysed the structure for manufacture of an Orbital Marine Power tidal turbine, determining that the impact on blade deflection using a single shear web instead of two was minimal (Fagan *et al.*, 2019, p. 9). The internal structure of a tidal turbine can be seen in Figure 2.18. The blade structure was designed and optimised using their in-house software BladeComp which carries out multi-objective optimisation to minimise the blade mass and flapwise tip deflection (Jiang, Fagan and Goggins, 2019, p. 3). The material analysed was Glass-fibre with a powder epoxy resin. The software uses a genetic algorithm to determine the optimum number of layers and their orientation (Jiang, Fagan and Goggins, 2019, p. 4).

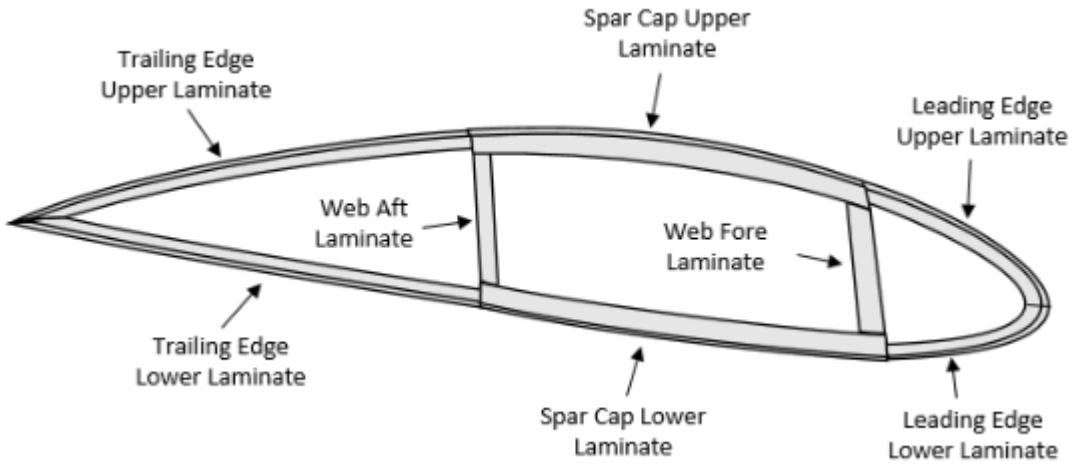

Figure 2.18 Tidal turbine internal structure (Fagan *et al.*, 2019, p. 5).

Another example of these types of studies is the one carried out by Lothodé *et al.* (2020, p. 4) on the blade-mast fluid-structure interaction, validating their results with the experimental results of one of the tidal turbines of the University of Southampton. The blade was modeled with three different Young's moduli E=69 *GPa* corresponding to the original value of aluminium, a second one with a value of E/2, and the third one with E/4. In the simulation it was found that the blades with the lowest Young's modulus bent so much that the performance was seriously compromise. For instance, if the same turbine had purely wooden blades, it would have a lower power capture purely from a wrong selection of materials.

2.9 Computational Fluid Dynamics

Computational Fluid Dynamics aim to model the physical properties of conservation of mass, momentum (Navier-Stokes equations), and energy, together with turbulence modelling (Rodriguez, 2019, p. 11). The Reynolds number (*Re*) plays an important role, as it describes laminar and turbulent flows. There are methods that disregard the viscous effects and others that take them into consideration. The most common used methods are explained next.

2.9.1 Vortex Lattice Method (VLM)

VLMs are surface panel methods that represent thickness effects with source panels and lift effects with vortex ones. They rely on numerical techniques to generate a solution. It is assumed that the vortex strength varies both chordwise and spanwise. For each point in the lattice, the velocities induced by other sections are summed. The result is a set of linear equations expressing the boundary condition of flow tangency on the surface. The local velocities are used to calculate the static pressure on each panel. With these pressures, the forces and moments can be obtained. They are inviscid codes, meaning that they do not simulate the boundary layer, thus, the drag coefficient from the skin friction is not accounted for (Bertin and Cummings, 2014, pp. 788–789).

Laß *et al.* performed an analysis using a VLM and verifying their model agains experimental results publised by Bahaj *et al.* (2007), finding a good agreement of the power and thrust coefficients in uniform flow with a yaw angle of 25° and a uniform flow of $1.8\ m/s$ (2019). Young *et al.* carried out a numerical and experimental study on tidal turbines using a software called Tornado. It is a vortex lattice code used for wing applications, so it had to be modified to model the motion of the tidal turbine wake. In order to verify the numeric results and to understand viscous effects, experimental tests were carried out using a $700\ mm$ tidal turbine. Experiments showed that the discrepancy between the inviscid model relied on a combination of viscous and inviscid effects (2019).

2.9.2 Reynolds-averaged Navier-Stokes (RANS)

Predicts the average result of turbulent flows. It includes transport equations to simulate effects of Reynolds stresses generated or dissipated withing the flow, representing the transport momentum in the mainstream direction, caused by disturbances in the other two perpendicular directions. Average stress models are adjusted to semi-empirical models, dependent of experimentally obtained constants. These values are very frequently obtained where the fluid is air or water, and in the experimental setup there is a flat plate (Alonzo-García, Gutiérrez-Torres

and Jiménez-Bernal, 2016, p. 320). It is a numerical method that solves the timed-averaged Navier-Stokes equations, where the velocity has two components, one for the average velocity and another one for the fluctuations. They are turbulence models, and the most common ones use two variables, the first being the turbulent kinetic energy, and the second either frequency, dissipation, time, enstrophy, acceleration, or another. As long as both form a mathematical expression with units of length squared per unit of time, the same units as the turbulent kinematic viscosity. The most commonly used turbulence models and its main characteristics are next described (Rodriguez, 2019, p. 148).

2.9.2.1 Kolmogorov 1942 *k-ω*

It was the first two-equation transport model developed. Kolmogorov noted that turbulence consists of eddies that range from large to small. He realised that energy was taken from the flow by large eddies and passed to the smaller ones until energy was dissipated by the viscous force of the fluid. This process is now referred as “cascading”. Large eddies (called integral eddies) contain 4/5 of the energy. Small eddies where energy dissipation occurs are named Kolmogorov eddies, and the ones in between are defined as Taylor eddies. This second transport variable (ω) applies to the three eddy scales. Together they form a self-consistent combination of variables for the two-equation models (Rodriguez, 2019, p. 149).

2.9.2.2 Wilcox *k-ω*

In 1988, David Wilcox combined the Prandtl’s *k* transport turbulence partial differential equations (PDE), Kolmogorov’s ω transport PDE, and Saffman’s upgrades to produce a model. In 1998, he made some advances to his model, and in 2006 it was further improved. The latter is a good model for turbulence near the wall conditions as well as free stream, placing this model as one of the best two-equation RANS model of the three (Rodriguez, 2019, p. 153).

2.9.2.3 Standard *k-ε* (SKE) Model

During the 1940s, Pei Yuan Chou associated the dissipation model, based on ω, for Taylor eddies. For the author, Taylor scale eddies played an important role in the dissipation of turbulence, so he deemed necessary to find an equation to describe the behaviour of this length. It is defined by the equation of decay of vorticity. The original model went into different modifications, until in the early 1970s, Jones, Launder, and Sharma came with the standard *k-ε* (SKE) Model (Rodriguez, 2019, p. 159).

2.9.2.4 Menter 2003 SST Model

Florian Menter realised that the SKE model simulated reasonably flows at high Re numbers in free streams, while the 1988 *k-ω* model worked well at low Re numbers and near the wall. He combined both models to act on the regions that they performed better and blends them at intermediate regions. In 1992 he created the shear stress transport (SST) model, which was improved later in 2003. This model is considered as good as the 2006 *k-ω* model, and even performs better in the transonic regime (Rodriguez, 2019, p. 172).

Batten, Harrison and Bahaj measured the accuracy of the actuator disc-RANS approach for predicting the performance of a scaled tidal turbine. Their model had a minor tendency to underpredict the power coefficient, and over-predict the thrust coefficient, which is considered to be a conservative model in the sense that it underpredicted the amount of energy that could be extracted by the turbine, and at the same time over-predicted the thrust force exerted on the turbine (2013, p. 10)**.**Another comparative study with used a RANS model to predict the performance of a 700-mm tidal turbine, finding good agreement at the rated TSR of 4, but a discrepancy at lower and higher TSR. The difference at lower speeds was attributed to the fact that the CFD simulation does not capture the stall characteristics of the airfoil accurately. At higher angles of attack, the flow is assumed to remain attached, which consequently over-predicted the torque. There was also an over prediction at higher TSR, but there was no clear reason found. It is explained that the lack of the turbine nacelle in the simulation was the one responsible for underpredicting the losses caused by the latter (Smyth, 2020, p. 67).

2.9.3 Large Eddy Simulation (LES)

LES modelling focuses on simulating large eddies, the ones containing around 80% of the turbulent kinetic energy and using a model to approximate the smaller eddies. LES is considered an intermediate methodology in terms of resolution, cost and speed between RANS and DNS. Generally speaking, LES is an order of magnitude more time consuming than RANS, but two, three, or more orders of magnitude computationally cheaper than DNS. Due to its effectiveness in engineering, there are dozens of LES models available.

Ahmed *et al.* (2017) performed a computer simulated study based on a tidal stream turbine deployed at EMEC by Alstom. Load fluctuations were studied: power, thrust, and bending moments at the blades. These loads are produced by the inflow velocity profile, support structure, rotor, turbulence and waves. The cyclic fluctuations were simulated with RANS solvers, and the full spectrum of turbulent fluctuations using a LES model. The average loads were succesfully reproduced using the SST *k-ω* model, and the full range of loads with the LES

model (2017, pp. 236, 246)**.**A full scaled tidal turbine was simulated (including 3 blades, nacelle and pile) with RANS and LES by Afgan *et al.* (2013). The geometry and experimental setup is from Bahaj *et al.* (2005) for their deep tip inmersion case with the optimum pitch angle of 20°. LES simulations were in good agreement with the experimental results, RANS simulations under predicted the performance at low rotational speeds (TSR=5) by around 10%, but were closer to LES simulations at the design operating conditions (TSR≈6), within 3% (2013, p. 100). LES provides a detailed description of tip vortices, which are not captured by RANS models, the next step is to include wafe motion to simulate the flow cyclic variation (2013, p. 108).

Hybrid computer models have been developed to overcome the difficulties of LES models to solve near-wall regions. These models combine the easiness and power of RANS models near the wall, and the resolution of the rest of the flow using LES methods. An example is the detached-eddy simulation (DES) (Nicholls-Lee and Turnock, 2007, p. 4). Gajardo Orellana (2017) successfully applied a coupled DES-BEM model that was validated agains work from Stallard *et al.* (2013) on interaction of scaled tidal turbines in a flume.

2.9.4 Direct Numerical Simulation (DNS)

DNS solves all time and spatial scales of the Navier-Stokes equations, so it does not model, average or approximate any variable, function, or geometry. It is extremely accurate, but at the same time it requires tens of millions to billions of computational nodes (Day *et al.*, 2012). To be able to use DNS for very large systems (nuclear plants, cruises, jets), faster computers with multiple cores and many core processors might be required, or even the nano and quantum computers to be developed in the next decades.

Jing *et al.* (2020) performed direct numerical simulations on a horizontal axis wind turbine (HAWT) to study the effect of the Coriolis and centrifugal forces (generated from the rotating turbine) on the flow detachment from the blades, showing that the laminar to turbulent transition on rotating blades is caused by the Tollmien–Schlichting wave (2020, p. 10).Table 2-1 provides a high-level comparison of different CFD methods applied to most engineering applications, excluding large systems, in terms of resources needed and its output.

Table 2-1 Comparative table for different CFD methods in engineering applications.

	Inviscid methods	**RANS**	**LES**	**DNS**
Time consuming	Minutes-hours on a personal computer	Hours to days on a personal computer	10s-100s times more than RANS	Hundreds plus hours on a supercomputer
Cost	Low	Accessible for most engineering applications	Expensive for most engineering applications	100s-1000s times more than LES
Computational resources	Hundreds of sections analysed	Thousands to millions of nodes	Up to 10^7 nodes required	10^7-10^9 nodes required
Level of output	Does not predict viscous effects	Models all turbulent scales	Resolves large eddies, models smaller scales	Solves all turbulent scales

2.10 Testing sites for tidal turbines

There are three main ways where a scaled turbine can be tested: in a current circulating flume, at a towing tank or in-situ. Each has different characteristics, advantages and disadvantages.

2.10.1 Current Circulating Tanks

As the name suggests, it is a water tank with the capability of recirculating water to generate a current, some can even generate waves like IFREMER at Boulogne-sur-Mer, France. The turbulence intensity at this facility for a speed of 0.8 *m/s* has been measured to be 1.85% (Porter *et al.*, 2020, p. 7). These types of facilities tend to be expensive due to the amount of electricity needed to recirculate the water. The flume is 18 *m* long, 4 *m* wide, and 2 *m* deep Figure 2.19.

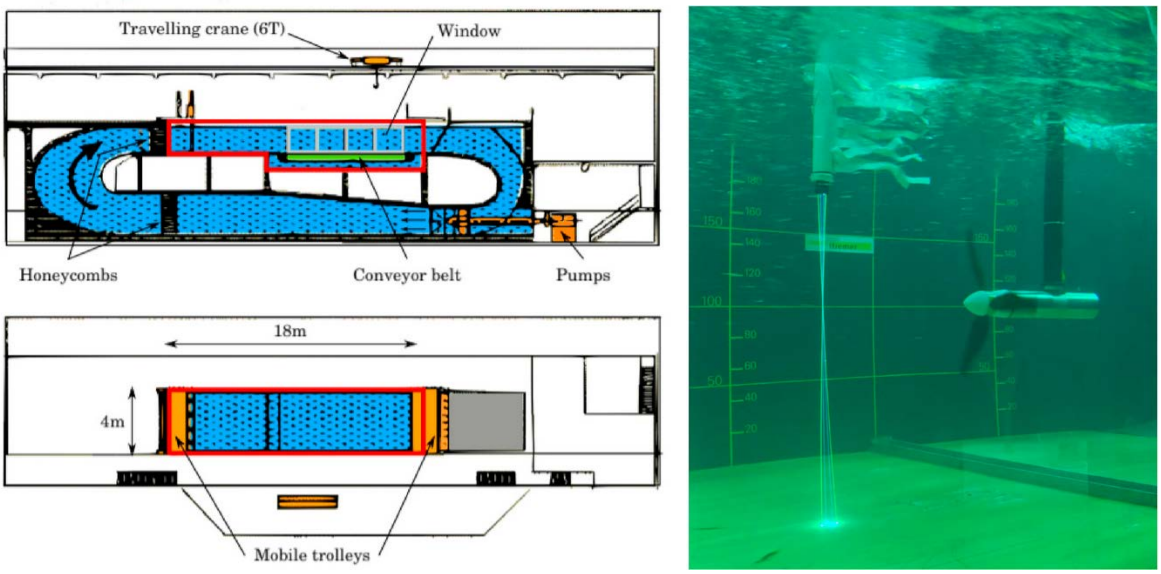

Figure 2.19 Schematic of IFREMER flume (Left). Scaled turbine being tested (Right) (Allmark, Ellis, *et al.*, 2021, p. 1423).

Another option is the round recirculating current and wave tank FloWave at the University of Edinburgh, with turbulence intensity values between 5%-11% across the test area for typical tidal turbine test velocities between 0.9-1.1 *m/s* (Figure 2.20).

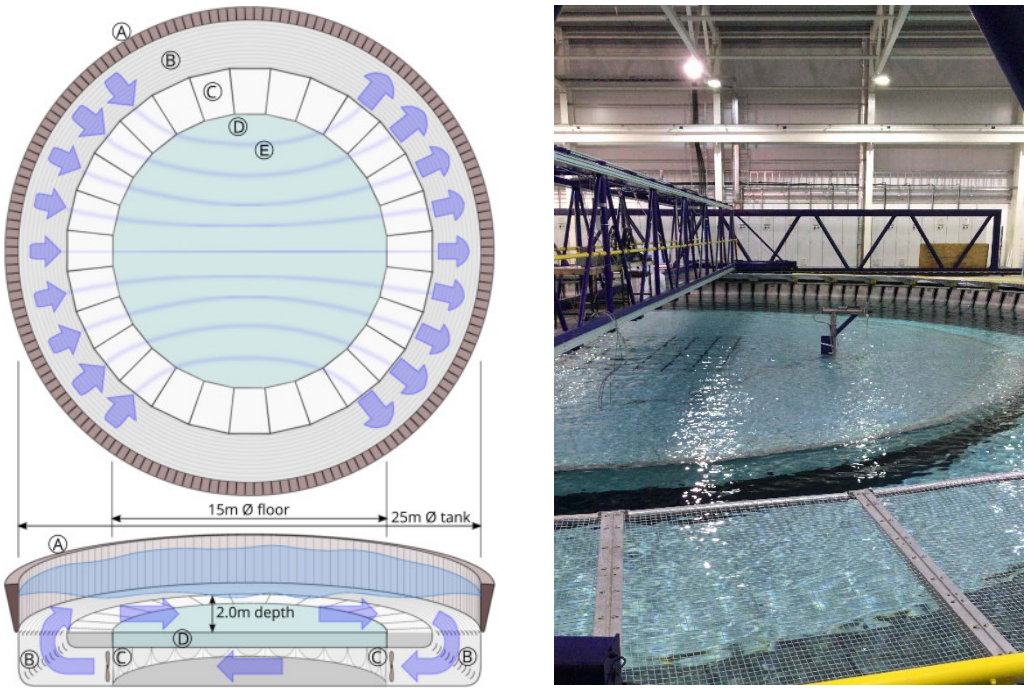

Figure 2.20 FloWave diagram (Left) (Sutherland *et al.*, 2017, p. 104). Example of installed turbine with raised floor (Right).

2.10.2 Towing tank

A towing tank is a large construction containing hundreds of thousands to millions of litres of water. With the use of a carriage, any device attached to it can be towed along the tank through still water to generate an apparent flow towards the moving object. Some facilities have wave making capabilities as well. They were mainly designed for ship applications, but they can be used to study submerged bodies and sporting fluid dynamics too. Figure 2.21 shows the schematic of a 76-m towing tank (Kelvin Hydrodynamics Laboratory at the University of Strathclyde), and a tidal turbine being tested at the Umberto Pugliese towing tank in Italy. The turbulence in the undisturbed flow at these facilities is practically zero, the downside of it is that measurements length is dependent on the size of the tank, and there has to be a waiting time between towing runs to allow the water in the tank to settle and thus achieve repeatable conditions.

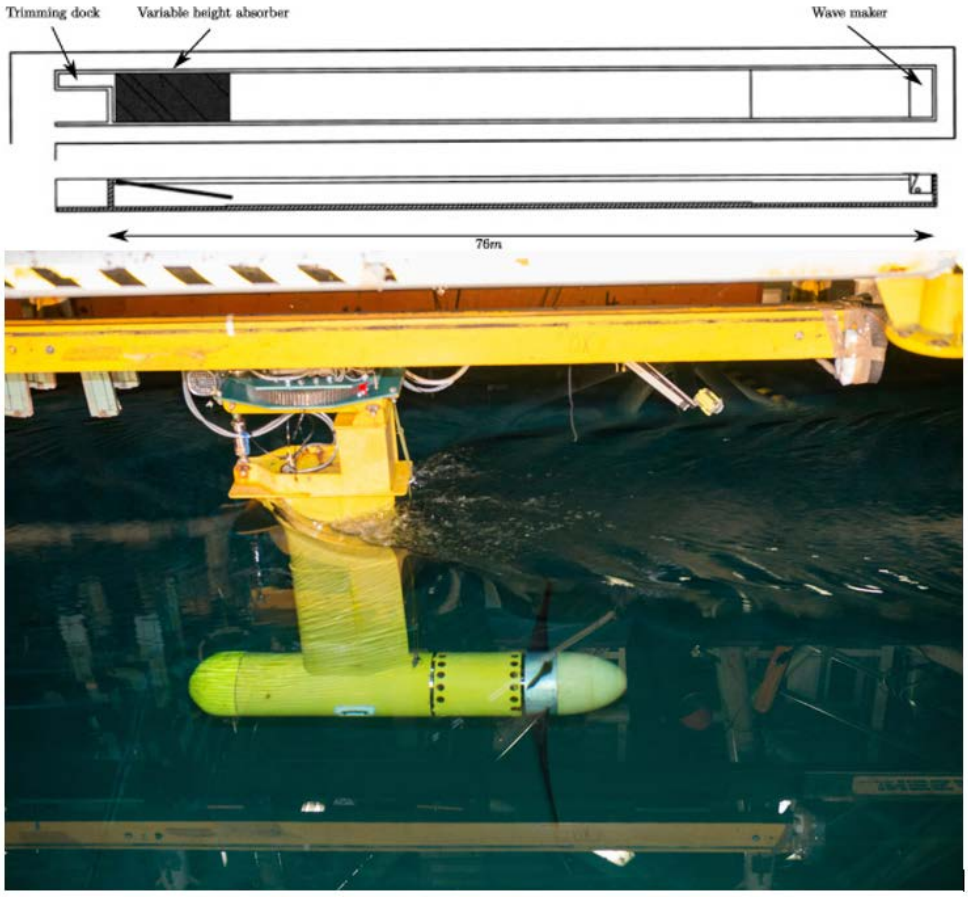

Figure 2.21 Towing tank diagram (Up) (Gaurier *et al.*, 2015, p. 90). Turbine fixed to the carriage (Down) (Institute of Marine Engineering, 2021).

2.10.3 In-situ

There is always the option to test the devices in a river or the coast. Accessibility would be the first issue, including access to facilities and instrumentation. Turbulence intensities can be vary between 3-24% (Gaurier *et al.*, 2020, p. 1158). The advantage is having more realistic environmental conditions. Figure 2.22 shows the deployment of a turbine close to the mouth of a river.

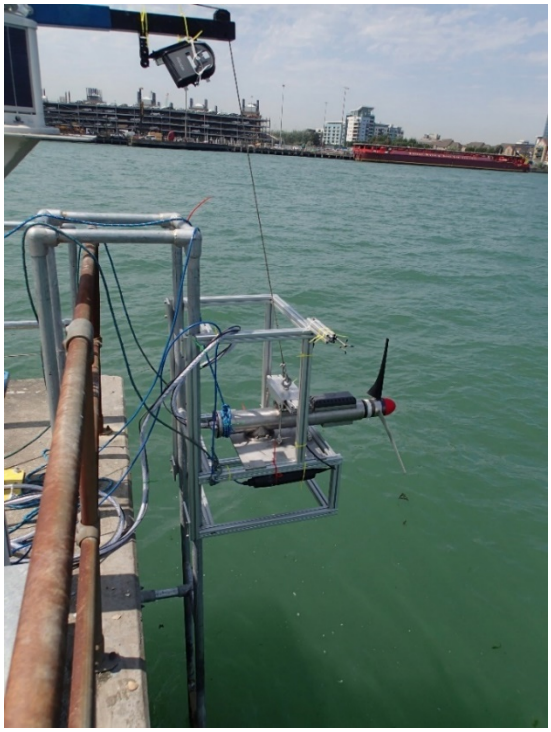

Figure 2.22 Pre-test measuring instrumentation deployment at Weston jetty (University of Southampton).

2.11 Research needs

The power coefficient of tidal turbines is similar to the ones seen in the wind industry. The difference is that to close that gap, tidal developers have a limit in size due to the environment and capabilities of materials used these days. Optimising the blades by making them slimmer is not a solution either because of the large thrust forces seen in the marine environment. Economically speaking, and as a matter of public perception, it is not worth the risk jeopardizing the structural integrity of tidal turbines to make the optimisation. As the technology matures, more governmental support can be expected, just as it happened with the wind energy industry. New methods to increase power output can achieve this task without changing the original blade design. Winglets have shown a good performance in the aviation sector and have also been used commercially on wind turbines. Due to the characteristics of the flow around the areas of interest,

it would be better suited for this project to evaluate experimentally the impact of fitting winglets to a scaled tidal turbine.

There is a need to measure how winglets affect the power and thrust coefficient on tidal turbines. Also, there is no methodology on how to design winglets for low speed rotating applications as there are for high subsonic speeds (Whitcomb, 1976), and low speeds (Chattot, 2006) for non-rotating applications. A better understanding between the winglet/flow interaction would be ideal. 80% of the previous simulations studied in this research suggest that winglets for horizontal axis turbines could increase the power coefficient between 1.3-10% while increasing the thrust coefficient by similar values.

2.12 Research aim

The aim of this project is to quantify the effect of adding winglets to a tidal turbine on the power and thrust coefficient through a series of experiments in a towing tank. It is expected that the flow around flow enhancement devices on a rotating blade might include regions of stalled or highly rotational flow which might not be accurately simulated computationally or modelled numerically therefore an experimental work that can be visually analysed in this case seems appropriate.

2.13 Research objectives

- Review techniques previously suggested or tested to improve power capture on horizontal axis wind/tidal turbines.
- Identify the design parameters for winglets
- Design and commission the manufacturing of the blades and winglets
    - Design the blade/winglet interface
- Measure the effect of different winglets designs on the power and thrust coefficients
- Analyse and interpret the results
- Identify the source of any change detected
- Make suggestions for further improvement

2.14 Research limitations

- Few experiments have been carried out using winglets on wind turbines, and less on tidal.
- Variations on power and thrust coefficients could be small, in the range of 1-2%.
- There is no hi-tech equipment available for flow visualisation.

Table 2-2. Main studies on HATs with winglets and their design parameters

Research Paper				Parameters						Results		
Source	Type	Country	Method	Height [%R]	Radius [%H]	Cant [°]	T, t[4] [°]	Sweep [°]	Airfoil	TSR (λ)	$P_{aug.}$ [%]	$T_{aug.}$ [%]
(Mühle *et al.*, 2020)	Wind	Norway	Exp.	10.76	3.09	90		17.86		6	10.68	12.64
(Mourad *et al.*, 2020)	Wind	Egypt	CFD	0.8		-90	20t	0	SD8000	7	2.4	2.9
(Young *et al.*, 2019)	Tidal	UK	VLM+Exp.	10, 20	(10*mm*)	-90-90				4	10	
(Khaled *et al.*, 2019)	Wind	Egypt	Exp.+CFD	1-7	(1*mm*)	90			NACA4412	5	8.28	8.74
(Khalafallah, Ahmed and Emam, 2019)	Wind	Egypt	CFD			-40	10T		Swept blade	6	4.39	
(Zhu *et al.*, 2017)	Tidal	China	CFD	2.5	48	90, -90	-	45	NACA 63-812	3 - 10	3.96	
(Ostovan and Uzol, 2016)	Wind	Turkey	Exp.	6	(0)	90	1T	-0.5	PSU 94-097	≈6	4.2	6.5
(Tobin, Hamed and Chamorro, 2015)	Wind	USA	Exp.	6.7	100	90				5.4	8.2	15.0
(Elfarra, Sezer-Uzol and Akmandor, 2015)	Wind	Turkey	CFD+GA	1.5	(0)	45, 90	0, 2T	+ -	S809	1.5-7.5	3.2-4.6	0.8-1.5
(Lawton and Crawford, 2014)	Wind	Canada	CFD	5		90	6.73T	0	NACA 64		≈2	2.8
(Elfarra, Sezer-Uzol and Akmandor, 2014)	Wind	Turkey	CFD+GA	1.5	(0)	84	2T		S809		≈9	≈1.3

[4] T: twist, t: toe

(Saravanan, Parammasivam and S, 2013)	Wind	India	Exp.	4	12.5	75			NACA 4412	2-3	2-6	
(Gertz, Johnson and Swytink-Binnema, 2012)	Wind	Canada	Exp.	8	(0)	90	-0.5T	0	PSU 94–097	6.7	5-7	
(Chattot, 2009)	Wind	USA	Num.	10	(0)	-90			S809	5.39	3.5	
(Gaunaa and Johansen, 2007b) (Gaunaa and Johansen, 2007a)	Wind Wind	Denmark Denmark	CFD Num.	2	25	90			Risø B1-15	8	1.74 2.47	2.80 2.61
(Johansen and Sørensen, 2007)	Wind	Denmark	CFD	2	20	90	4T	0			1.0-1.8	1.2-3.6
(Johansen and Sørensen, 2006)	Wind	Denmark	CFD	1.5		90		0	NACA 64-518		1.3	1.6
(Shimizu *et al.*, 2003b)	Wind	Japan	Exp.	9		Mie-type			NACA 4418	5.5	14.5	
(Shimizu *et al.*, 2003a)	Wind	Japan	Exp.	9		Mie-type			NACA 4418	5.42	8.75	
(Imamura, Hasegawa and Kikuyama, 1998)	Wind	Japan	Num.	10		10-80		0	NACA 0012			
(Shimizu *et al.*, 1992)	Wind	Japan	Exp.	20		Mie-type			NACA 4412	5	17	
(van Bussel, 1990)	Wind	Netherlands	Num.	20		Mie-type			NACA 4412	8	=	
(Shimizu *et al.*, 1990)	Wind	Japan	Exp.	≈20		Mie-type			FX74-CL6-140	4	27	
(Gyatt and Lissaman, 1985)	Wind	USA	Exp.	5		Single, fin, and double			NACA 23012,21		–	

Chapter 3 Theory

In 1919 the German physicist Albert Betz concluded that the highest kinetic energy that could be extracted from a free flow passing through a planar disc is nearly 60% of the total energy available (Betz, 1927, p.911). Evidently, this is an ideal value considering some assumptions including the following:

- There is a uniform thrust throughout the entire disc.
- The flow is non compressible and it is perpendicular to the axis of rotation.
- Comparing it to a Horizontal Axis Turbines (HATs) the rotor would not have a hub and extracts energy as if it had infinite number of blades and without losses.

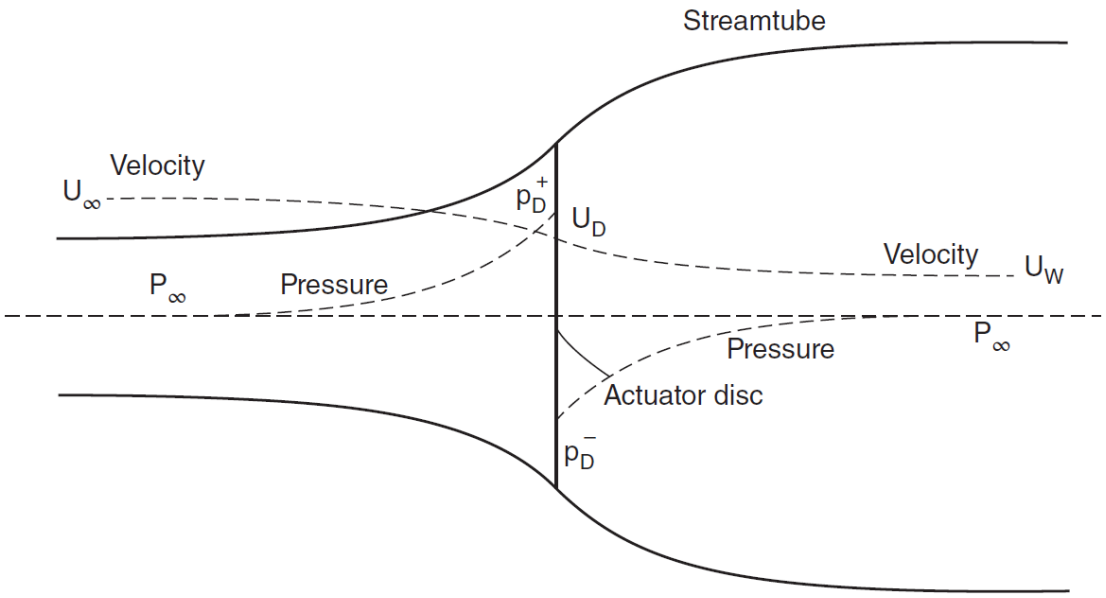

Figure 3.1 Ideal energy-extracting actuator disc (T. L. Burton *et al.*, 2021, p. 41).

Figure 3.1 is a schematic of the actuator disc that represents the behaviour of the flow as it passes through and energy is extracted. It can be seen that the flow has an initial velocity u_∞ and a velocity after energy is extracted u_w. The power coefficient C_P of the optimal amount of power P that can be extracted, when the $\frac{u_w}{u_\infty}$ ratio is $\frac{1}{3}$, is equal to $\frac{16}{27}$:

$$C_{Pmax} = \frac{P_{max}}{P_{wind}} = \frac{16}{27} \approx 0.593 \qquad \text{Equation 3.1}$$

$\frac{1}{3}$ represents the ratio of the flow speed after and before the turbine. The flow experiences a change of momentum, caused due to the pressure difference. The peak power is extracted when the velocity in the far wake is a third of the ambient flow speed. Beyond this point, the flow

velocity at the disc starts to reduce and the power capture decreases. If there was a hypothetical situation where you could take all of the energy out of the flow, the velocity behind the disc would be 0 m/s $\left(\frac{u_w}{u_\infty} = 0\right)$, there is no more energy in the flow to convert into useful energy. In fact, as it can be seen in the Simple Momentum Theory that follows, the total speed reduction is equal before and after the rotor to achieve maximum power extraction.

Such power coefficient can be surpassed in an enclosed-device situation, where a Venturi-like nozzle would accelerate the flow and increase the rotational speed. Ideally, tidal arrays would be deployed as close to the coasts as possible, to reduce costs, and in locations with strong tidal currents. That is the case for narrow channels. In this scenario, the turbines placed in a line would act as a tidal fence that would 'block' a considerable cross-section of the channel. Such blockage would cause an increased speed of the water surrounding the turbines by the flow upstream as only a small amount of water could divert around the turbines (It is also true for hydropower, where turbines are ducted) (Twidell, 2015, p. 463).

Tidal turbines encounter three main differences with wind turbines: Reynolds numbers (inherent to the environment), possible cavitation and other stall characteristics (Batten et al., 2006, p.249). Most commercial wind turbines operate with Reynolds numbers on the range of 10^6 and 10^7 (Ge, Tian and Deng, 2016, p. 1). Tidal turbines operate around Reynolds numbers of 10^6 as well (SIMEC Atlantis Energy, 2018). The difference between the two relies on how such Reynolds numbers result from the calculations. The Reynolds number is defined as:

$$Re = \frac{\rho u L}{\mu} \qquad \text{Equation 3.2}$$

Where $\rho$is the density, u is the flow speed, L is the section length, and μ is the dynamic viscosity. On wind turbines the Reynolds number is product of higher flow speeds and a less viscous environment. In the case of tidal turbines, the Reynolds number is the result of the water density and higher viscosity. Table 3-1 shows a worked example for a tidal and wind turbine. The ratio of the Reynolds numbers is around 1:10.

Table 3-1 Re number for two example turbines.

	$\rho\ [kg/m^3]$	TSR	$u\ [m/s]$	$\mu\ [kg/(m \cdot s)]$	Chord [m]	Re [ ]
Tidal	1025	5.0	3	$1.002x10^{-3}$	0.4	$6.017x10^6$
Wind*	1.225	5.0	15	$1.825x10^{-5}$	0.1	$5.034x10^5$

* For a small wind turbine

Cavitation appears when water pressure is reduced below the vapour pressure, forming bubbles that subsequently implode in regions of higher pressure. It has erosive effects on the blades, reduces hydrodynamic performance, and produces noise and vibration (Carlton, 2019, p. 13). Cavitation is more likely to occur at the tip of the blade during the highest point of its rotation (Myers and Bahaj, 2006, p.2209). Considering that tidal turbines need to be installed in shallow waters (less than 50 m), the tip speed should be limited to 10 m/s–15 m/s, as shown in a cavitation diagram as a function of depth by Fraenkel (2002, pp. 3–6). Power control by means of stall regulation might be a better cost–effective solution rather than pitch regulation due to the complications implicated in the last one (Batten et al., 2008, p.1095). Stall regulation occurs when the hydrodynamic performance of the airfoil decreases as the angle of attack increases in high flow speeds, pitch regulation relies on an active pitch control for the blades. Nearly all present designs of large wind turbines are pitch-regulated as the addition of active power control across all operating conditions is seen as beneficial for the additional cost and complexity. Additionally, Horizontal Axis Wind and Tidal Turbines (HAWTs and HATTs) have losses from the tips of around 5-10% (Wood, Okulov and Bhattacharjee, 2016, p. 269), and there is also a small percentage of unused energy at the centre of the rotor. It is estimated that by redirecting that flow to the edges of the turbine, there could be a increment of 3% in power (Peters, 2015).

3.1 Aerodynamics of HAWTs

The Wind Energy Handbook (T Burton *et al.*, 2011, pp. 39–92) dedicates a chapter on the Aerodynamics for Horizontal Axis Wind Turbines. For the present project it is important to recall two main theories: the actuator disc theory and the rotor blade theory. This section presents a summary of the underlying theory for HAWTs that can be applied for Horizontal Axis Tidal Turbines (HATTs).

3.1.1 Actuator Disc Theory

It can be assumed that in an ideal wind turbine, the stream flow affected by it is surrounded by a boundary layer, and that the air does not cross it. As the speed upstream is higher than the one downstream, consequently, the stream-tubular section is smaller upstream and bigger downstream. The mass of air at any cross-section of this "tube" is given by ρAU, where ρ is the density of air, A the cross-section area and U the air velocity. With this,

$$\rho A_{\infty} U_{\infty} = \rho A U = \rho A_w U_w \qquad \text{Equation 3.3}$$

where 1 refers to upstream, no sub-script at the actuator disc, and 2 downstream. Refer to Figure 3.1 for the evolution of the flow as it passes through the actuator disc.

There is a drop in the static pressure at the disc. It is also considered that the actuator disc will decrease the upstream velocity by $-aU_\infty$. a is defined as the axial flow induction factor. Leaving a velocity at the disc of

$$U = U_\infty(1 - a) \qquad \text{Equation 3.4}$$

3.1.1.1 Simple Momentum Theory

The air passing through the disc varies its velocity, thus a change of momentum defined by

$$Change\ of\ momentum = (U_\infty - U_w)\rho AU \qquad \text{Equation 3.5}$$

The change of momentum is caused by the pressure difference before and after the disc. The high pressure, represented by the *"+"* sign, is facing the flow and the side with low pressure, represented with the *"–"* sign, is in the same direction of the flow. So,

$$(P^+ - P^-)A = (U_\infty - U_w)\rho AU_\infty(1 - a) \qquad \text{Equation 3.6}$$

To get the pressure difference, Bernoulli's equation can be applied upstream and downstream. Under steady conditions, the total mechanical energy is constant

$$\frac{1}{2}\rho U^2 + P + \rho gh = K \qquad \text{Equation 3.7}$$

The equation represents the total energy in the flow. From left to right: kinetic energy, static pressure, and potential energy. Where:

- ρ is the density [kg/m^3],
- U is the flow speed [m/s],
- P is the static pressure [Pa],
- g is the gravitational constant [9.81 m/s^2], and
- h is the height from a point of reference [m].

Applying upstream and downstream, considering that the flow is incompressible and horizontal

$$(P^+ - P^-)A = \frac{1}{2}\rho(U_\infty^2 - U_w^2) \qquad \text{Equation 3.8}$$

Substituting in equation 2.5 and solving the quadratic equation for U_2 gives

$$U_w = U_\infty(1 - 2a) \qquad \text{Equation 3.9}$$

From Equation 3.4, it can be seen that half of the speed is lost upstream of the actuator disc and the other half downstream. The second solution to the quadratic equation is when U_2 is the same as U_∞, when $a = 0$, as if the disc had no effect on the flow.

3.1.1.2 The Power Coefficient

From Equation 3.6 the force can be calculated as:

$$F = (P^+ - P^-)A = 2\rho A U_\infty^2 a(1-a) \quad \text{Equation 3.10}$$

The power is *FU*

$$Power = FU = 2\rho A U_\infty^3 a(1-a)^2 \quad \text{Equation 3.11}$$

The power coefficient is the Power as defined previously, divided by the available power at the actuator disc, with the same conditions, but as if the disc had no effect on the flow

$$C_P = \frac{Power}{\frac{1}{2}\rho A U_\infty^3} \quad \text{Equation 3.12}$$

Then

$$C_P = 4a(1-a)^2 \quad \text{Equation 3.13}$$

3.1.1.3 The Lanchester-Betz limit

CP has a maximum value when

$$\frac{dC_P}{da} = 4(1-a)(1-3a) = 0 \quad \text{Equation 3.14}$$

And $a = \frac{1}{3}$

As stated at the beginning of the chapter,

$$\mathrm{C_{Pmax}} = \frac{16}{27} \approx 0.593 \quad \text{Equation 3.15}$$

3.1.1.4 The Thrust Coefficient

Similarly, the thrust coefficient becomes

$$C_T = \frac{Thrust}{\frac{1}{2}\rho U_\infty^2 A} \quad \text{Equation 3.16}$$

$$C_T = 4a(1-a) \quad \text{Equation 3.17}$$

This is valid for values of $a < \frac{1}{2}$, because when $a = \frac{1}{2}$, $U_w = (1-2a)U_\infty$ becomes zero, then the previously mentioned momentum theory no longer applies, as shown in Figure 3.2. The theoretical and experimental values for the thrust coefficient are compared in Figure 3.3, where it

can be appreciated that around the optimum value of $a_T = \frac{1}{3}$, the coefficient keeps increasing without reaching an evident peak.

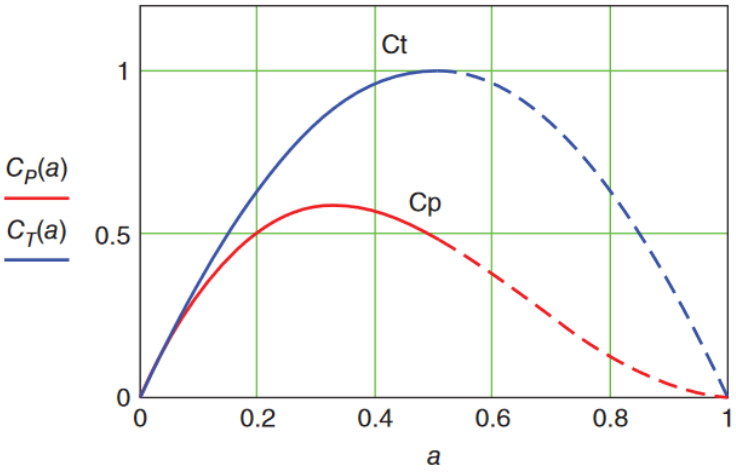

Figure 3.2 Theoretical variation of CP and CT with the induction factor (T. Burton *et al.*, 2021, p. 44).

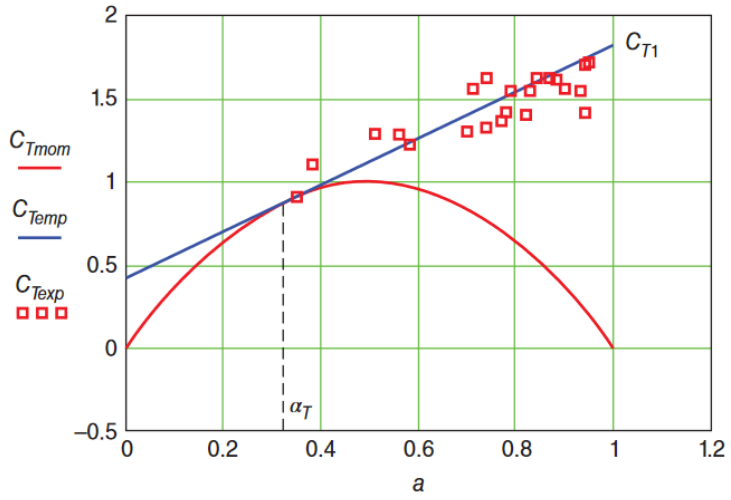

Figure 3.3 Theoretical and measured values of the thrust coefficient (T. Burton *et al.*, 2021, p. 67).

3.1.2 Rotor disc theory

Wind turbines consist of a rotor with n number of blades rotating at an angular velocity Ω. As the rotor spins, it sweeps out a disc, creating a pressure difference across it. This creates a loss of axial momentum in the wake. Together with that loss, there is a "loss" of energy that could be collected by an electrical generator connected to the shaft. Together with the thrust, the rotor sees a torque in the direction of rotation, opposite to the resistance exerted by the generator.

3.1.2.1 Wake rotation

The torque on the rotor disc produced by the flow produces a torque of equal magnitude and opposite direction on such flow. This causes the flow to rotate in opposite direction of the rotor. The flow gains a velocity factor tangent to the rotation, together with the axial one.

3.1.2.2 Angular momentum theory

The tangential and axial velocities are different for every section of the disc, called annular rings.

$$\delta\tau = \rho\delta A U_\infty (1-a) 2\Omega a' r^2 \qquad \text{Equation 3.18}$$

Where δA is the area of an annular ring.

$$\delta P = \delta\tau\Omega$$

Making equal to Equation 3.11,

$$2\rho\delta A U_\infty^3 a(1-a)^2 = \rho\delta A U_\infty (1-a) 2\Omega^2 a' r^2$$

simplifying

$$U_\infty^2 a(1-a) = \Omega^2 r^2 a'$$

Ωr is the tangential velocity of the ring. $\lambda_r = \Omega r/U_\infty$ is the *local tip speed ratio*. At the edge $r = R$, and $\lambda = \Omega R/U_\infty$ is called the *tip speed ratio*.

Then,

$$a(1-a) = \lambda_r^2 a' \qquad \text{Equation 3.19}$$

From Equation 3.18, considering that the area of the ring is $\delta A = 2\pi r \delta r$,

$$\delta P = \delta\tau\Omega = \left(\frac{1}{2}\rho U_\infty^3 2\pi r \delta r\right) 4a'(1-a)\lambda_r^2$$

Where the term in parenthesis is the available power passing through, then, the remaining component is the section efficiency

$$\eta_r = 4a'(1-a)\lambda_r^2 \qquad \text{Equation 3.20}$$

For the power coefficient:

$$\frac{\delta C_P}{dr} = \frac{4\pi\rho U_\infty^3 (1-a) a' \lambda_r^2 r}{\frac{1}{2}\rho U_\infty^3 \pi R^2} = \frac{8(1-a)a'\lambda_r^2 r}{R^2}$$

$$\frac{\delta C_P}{\delta \mu} = 8(1-a)a'\lambda^2\mu^3 \qquad \text{Equation 3.21}$$

$\mu = r/R$.

Bernoulli's theorem can be applied at the disc to give

$$\frac{1}{2}\rho U_\infty^2(1-a)^2 + \frac{1}{2}\rho\Omega^2 r^2 + \frac{1}{2}\rho w^2 + p^+$$
$$= \frac{1}{2}\rho U_\infty^2((1-a)^2 + \frac{1}{2}\rho\Omega^2(1+2\mathrm{a}')^2 r^2 + \frac{1}{2}\rho w^2 + p^-$$

Then

$$\Delta p = 2\rho\Omega^2(1+a')a'r^2$$

There are two components to this pressure drop. One

$$\Delta p_1 = 2\rho\Omega^2 a' r^2 \qquad \text{Equation 3.22}$$

and the second

$$\Delta p_2 = 2\rho\Omega^2 a'^2 r^2 \qquad \text{Equation 3.23}$$

which is caused by a radial, static pressure gradient in the wake, balancing the centrifugal force.

$$\frac{\mathrm{dp}}{\mathrm{dr}} = \rho(2\Omega a')^2 r$$

3.1.2.3 Maximum power

Differentiating Equation 3.20

$$\frac{da}{da'} = \frac{1-a}{a'} \qquad \text{Equation 3.24}$$

Doing the same for Equation 3.19

$$\frac{da}{da'} = \frac{\lambda_r^2}{1-2a}$$

making them both equal

$$a'\lambda_r^2 = (1-a)(1-2a) \qquad \text{Equation 3.25}$$

Solving Equation 3.19 for a', and substituting in Equation 3.25 gives the optimum values for a and a' that give the maximum power coefficient

$$a = \frac{1}{3}$$

and

$$a' = \frac{a(1-a)}{\lambda_r^2}$$ Equation 3.26

Substituting Equation 3.30 in Equation 3.21

$$C_P = 8\int_0^1 (1-a)\frac{a(1-a)}{\lambda^2\mu^2}\lambda^2\mu^3 d\mu = 4a(1-a)^2 = \frac{16}{27}$$ Equation 3.27

3.1.3 Rotor blade theory (blade-element/momentum theory)

The forces on the blade elements with radius r and length δr for multiple blades of a wind turbine, produce a rate of change of axial and angular momentum passing through the rotor. Additionally, the force on the elements induced by the change in pressure related to the rotational velocity in the wake is also produced by the lift and drag forces.

3.1.3.1 Blade element theory

It starts with the assumption that the forces mentioned above can be calculated as it would be done in a two-dimension airfoil, with an angle of attack α from the incident velocity at the 2-D plane of the blade, ignoring the spanwise velocity and 3D effects.

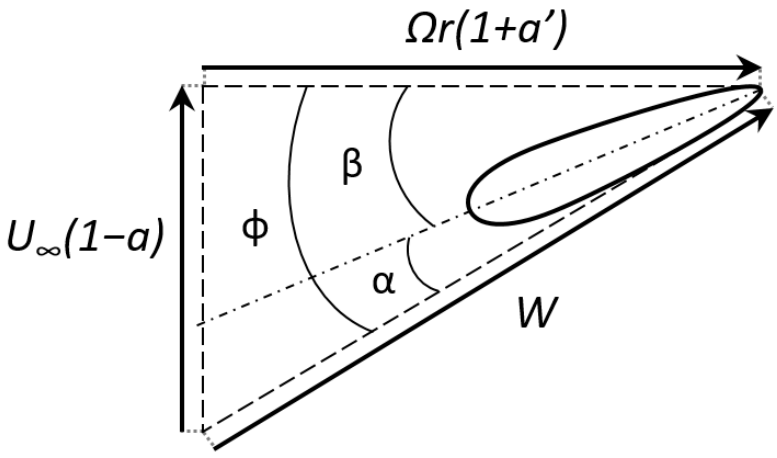

Figure 3.4 Blade element diagram.

Considering a turbine with *B* blades, radius *R*, chord *c*, and a pitch angle *β*. Where the chord and pitch angle vary along the blade. Blades rotating at angular velocity *Ω*. The tangential velocity is *rΩ*, and the one of the wake is *a'rΩ*. Combined, the tangential flow is *(1 + a')rΩ*. The resultant relative velocity at the blade is *W*

$$W = \sqrt{U_\infty^2(1-a)^2 + r^2\Omega^2(1+a')^2}$$ Equation 3.28

Acting at an angle ϕ. Then

$$sin\phi = \frac{U_\infty(1-a)}{W}\ and\ cos\phi = \frac{r\Omega(1+a')}{W} \quad \text{Equation 3.29}$$

The angle of attack is

$$\alpha = \phi - \beta \quad \text{Equation 3.30}$$

The main assumption of this theory is that the lift and drag forces are the same as in an element facing a 2-D flow. The lift force is defined by

$$\delta L = \frac{1}{2}\rho W^2 c C_l \delta r \quad \text{Equation 3.31}$$

and the drag

$$\delta D = \frac{1}{2}\rho W^2 c C_d \delta r \quad \text{Equation 3.32}$$

Where C_l and C_d are the corresponding lift and drag coefficients.

3.1.3.2 The blade-element/momentum (BEM) theory

In the BEM theory, it is assumed that the forces of the blade are the only ones responsible for the change in axial momentum of the air passing through the swept area and that the axial induction factor does not change at different radii. In practice, this factor is rarely uniform, but assuming it does not change has been experimentally proven to be acceptable (Lock, Bateman and Townend, 1924).

The thrust on the turbine equals the rate of change of axial momentum from Equation 3.10, with $A = 2\pi r\delta r$

$$\delta T = \frac{1}{2}\rho W^2 Bc(C_l cos\phi + C_d sin\phi)\delta r = 2\pi r\delta r\rho U_\infty(1-a)2aU_1 \quad \text{Equation 3.33}$$

The torque equals the rate of change of angular momentum

$$\delta\tau = \frac{1}{2}\rho W^2 Bcr(\delta L sin\phi - \delta D cos\phi)\delta r = 2\pi r\delta r\rho U_\infty(1-a)2a'r^2\Omega \quad \text{Equation 3.34}$$

If drag is disregarded from the equations, ϕ can be calculated from

$$\tan\phi = \frac{a'r\Omega}{aU_\infty} = \frac{a'}{a}\frac{r}{R}\lambda \quad \text{Equation 3.35}$$

λ is the tip speed ratio $R\Omega/U_\infty$.

From geometry, the inflow angle is also

$$\tan\phi = \frac{1-\mathrm{a}}{\lambda_r(1+a')} \qquad \text{Equation 3.36}$$

and λ_r is the local speed ratio $r\Omega/U_\infty$.

Equating both formulas

$$\frac{\mathrm{a}'}{\mathrm{a}}\frac{\mathrm{r}}{\mathrm{R}}\lambda = \frac{1-\mathrm{a}}{\lambda_r(1+a')}$$

$$\mathrm{a}(1-\mathrm{a}) = \lambda_\mathrm{r}^2 a'(1+a') \qquad \text{Equation 3.37}$$

$\mu = r/R$ and at the edge of the blade $\mu = 1$ and $a' = a'_t$, then

$$\mathrm{a}(1-\mathrm{a}) = \lambda^2 a'_t(1+a'_t) \qquad \text{Equation 3.37b}$$

Including the drag, Equation 3.33 can be simplified to

$$\frac{\mathrm{W}^2}{U_\infty^2} B\frac{c}{R}(C_l cos\phi + C_d sin\phi) = 8\pi a(1-a)\mu \qquad \text{Equation 3.38}$$

The torque in Equation 3.34 becomes

$$\frac{\mathrm{W}^2}{U_\infty^2} B\frac{c}{R}(C_l sin\phi - C_d cos\phi) = 8\pi\lambda\mu^2 a'(1-a) \qquad \text{Equation 3.39}$$

For convenience

$$C_x = C_l cos\phi + C_d sin\phi \qquad \text{Equation 3.40}$$

and

$$C_y = C_l sin\phi - C_d cos\phi \qquad \text{Equation 3.40b}$$

Equations Equation 3.38 and Equation 3.39 are solved for a and a' in an iterative process, considering a 2-D airfoil. The following equations, derived from Equation 3.38, Equation 3.39, Equation 3.40, and Equation 3.40b are more convenient to use. The right-hand side of the equations are initially evaluated with some approximated values, leaving easier equations to solve for the next iteration.

$$\frac{a}{1-a} = \frac{\sigma_r}{4\sin^2\phi} C_x \qquad \text{Equation 3.41}$$

$$\frac{a'}{1-a'} = \frac{\sigma_r}{4\sin\phi cos\phi} C_y \qquad \text{Equation 3.42}$$

σ is the blade solidity, and it is defined as the blade front area divided by the total rotor area. σ_r is the chord solidity, and it is the blade chord length at a given radius divided by its respective circumferential length.

$$\sigma_r = \frac{Bc}{2\pi r} = \frac{Bc}{2\pi\mu R} \qquad \text{Equation 3.43}$$

In practice *a* is not uniform along the blade, the error involved assuming that it is, is small for tip speed ratios greater than 3. The blade-element/momentum theory is summarized in Figure 3.5.

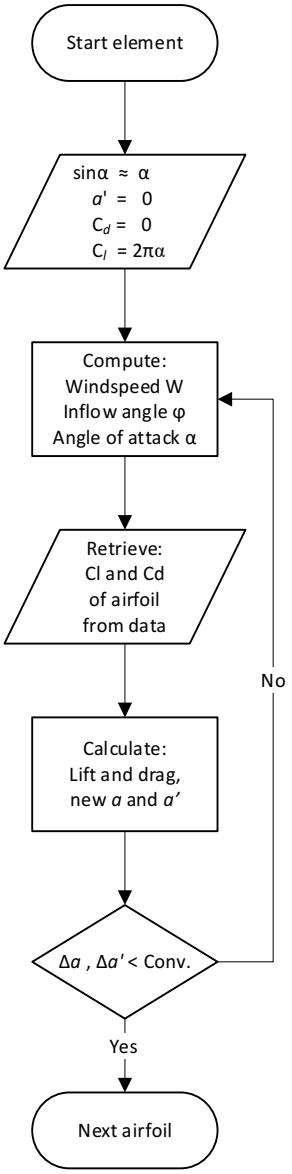

Figure 3.5 Flow chart of the blade-element/momentum theory.

The iteration process starts by making the following assumptions: the angle of attack (α) is very small, so that $\sin(\alpha) \approx \alpha$; the tangential induction factor (a') is zero; and the drag coefficient (C_d) is zero too. This simplifies the calculation of the lift coefficient (C_l). From there, an inflow angle and new angle of attack are calculated. With information of the lift and drag coefficients for the

specific airfoil, the lift and drag forces are calculated. New axial and tangential induction factors are obtained from the forces and compared with the previous factors. When the difference between the new induction factors, and the previously calculated ones is within the convergence criterion, the process for this annular ring is complete, and the process is repeated for the next section until the forces for all the blade sections have been calculated.

3.1.3.3 Determining the rotor power and torque

To calculate the performance of a rotor, an iterative process is also needed. It starts by assuming that *a* and *a'* are initially zero, obtaining ϕ, C_l, and C_d, then calculate new factors using Equation 3.41 and Equation 3.42, until values converge.

From Equation 3.34, the torque at each blade section with length δr is

$$\delta\tau = 4\pi\rho U_\infty \Omega r a'(1-a) r^2 \delta r$$

including the drag

$$\delta\tau = 4\pi\rho U_\infty \Omega r a'(1-a) r^2 \delta r - \frac{1}{2}\rho W^2 B c C_d cos\phi r \delta r$$

The whole rotor develops a torque

$$\tau = \frac{1}{2}\rho U_\infty^2 \pi R^3 \lambda \int_0^R \mu^2 \left(8a'(1-a)\mu - \frac{W}{U_\infty}\frac{B\frac{c}{R}}{\pi} C_d (1+a') \right) \delta\mu \qquad \text{Equation 3.44}$$

The power developed is

$$P = \tau\Omega$$

The power coefficient is

$$C_P = \frac{P}{\frac{1}{2}\rho U_\infty^3 \pi R^2}$$

It is an iterative solution because the airfoil characteristics are a non-linear function of the AoA. The process is summarized in Figure 3.6.

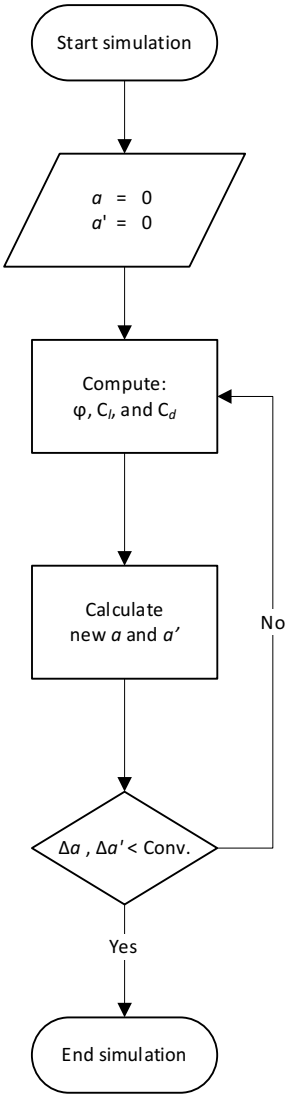

Figure 3.6 Flowchart of the calculation of the rotor performance.

The performance of a rotor is calculated over a range of tip speed ratios. From the blade-element/momentum method previously described, the lift and drag as a function of the angle of attack and Reynolds numbers are interpolated to determine the coefficients of the rotor at a certain angle of attack.

3.1.4 Blade geometry

3.1.4.1 Optimum design for variable speed

For a given tip speed ratio, the torque at each section is maximised when

$$8\pi\lambda\mu^2 \frac{d}{da'} a'(1-a) = 0$$

so that

$$\frac{da}{da'} = \frac{1-a}{a'} \qquad \text{Equation 3.45}$$

Dividing Equation 3.39 over Equation 3.38

$$\frac{\frac{C_l}{C_d}tan\phi - 1}{\frac{C_l}{C_d} + tan\phi} = \frac{\lambda\mu a'(1-a)}{a(1-a) + (a'\lambda\mu)^2} \qquad \text{Equation 3.46}$$

The inflow angle ϕ is

$$tan\phi = \frac{1-a}{\lambda\mu(1+a')} \qquad \text{Equation 3.47}$$

Substituting Equation 3.47 in Equation 3.46

$$\frac{\frac{C_l}{C_d}\frac{1-a}{\lambda\mu(1+a')} - 1}{\frac{C_l}{C_d} + \frac{1-a}{\lambda\mu(1+a')}} = \frac{\lambda\mu a'(1-a)}{a(1-a) + (a'\lambda\mu)^2}$$

Simplifying

$$\left[\frac{C_l}{C_d}(1-a) - \lambda\mu(1+a')\right][a(1-a) + (a'\lambda\mu)^2] = \left[\lambda\mu(1+a')\frac{C_l}{C_d} + (1-a)\right]\lambda\mu a'(1-a) \qquad \text{Equation 3.48}$$

Ignoring drag, Equation 3.48 reduces to

$$a(1-a) - \lambda^2\mu^2 a' = 0 \qquad \text{Equation 3.48b}$$

Differentiating Equation 3.48b with respect to a'

$$(1-2a)\frac{da}{da'} - \lambda^2\mu^2 = 0 \qquad \text{Equation 3.49}$$

Substituting Equation 3.45 into Equation 3.49

$$(1-2a)(1-a) - \lambda^2\mu^2 a' = 0 \qquad \text{Equation 3.50}$$

Solving Equation 3.48b for $a'$and substituting in Equation 3.50, the flow induction factors are obtained for optimum operation

$$a = \frac{1}{3} \quad \text{and} \quad a' = \frac{a(1-a)}{\lambda^2\mu^2} \qquad \text{Equation 3.51}$$

To determine blade geometry, and necessary pitch angle β, substitute $sin\phi$ in Equation 3.39 (still disregarding the drag)

$$\frac{\mathrm{W}}{U_\infty} B \frac{c}{R} C_l (1-a) = 8\pi\lambda\mu^2 a'(1-a) \qquad \text{Equation 3.52}$$

From where

$$\frac{B}{2\pi}\frac{c}{R} = \frac{4\lambda\mu^2 a'}{\frac{W}{U_\infty} C_l}$$

Then

$$\sigma_r \lambda C_l = \frac{B}{2\pi}\frac{c}{R}\,\lambda C_l = \frac{4\lambda^2\mu^2 a'}{\sqrt{(1-a)^2 + \left(\lambda\mu(1+a')\right)^2}} \qquad \text{Equation 3.53}$$

Including the optimum values of Equation 3.51

$$\sigma_r \lambda C_l = \frac{\frac{8}{9}}{\sqrt{\left(1-\frac{1}{3}\right)^2 + \lambda^2\mu^2\left(1+\frac{2}{9\lambda^2\mu^2}\right)^2}} \qquad \text{Equation 3.53b}$$

The left-hand side of Equation 3.53b includes the chord solidity σ_r and the lift coefficient C_l as the blade geometry parameter.

Turbines operate at variable speeds and can still maintain a constant tip speed ratio to obtain a maximum power coefficient. The torque has to be maximised at each station for a chosen tip speed ratio. The drag is disregarded at first and only the lift component is calculated, which gives the induction factors in Equation 3.51 ($a = \frac{1}{3}$ in agreement with the momentum theory).

For the blade geometry (how the chord varies along the blade) and pitch angle β distribution, the lift coefficient can be defined as the value that corresponds to the maximum lift to drag ratio, even though the drag has been disregarded. If for a specific design, C_l is kept constant, Figure 3.7 shows how the geometry needs to be for higher tip speed ratios. A high tip speed ratio needs a thin long blade, and a low tip speed requires a thick short one.

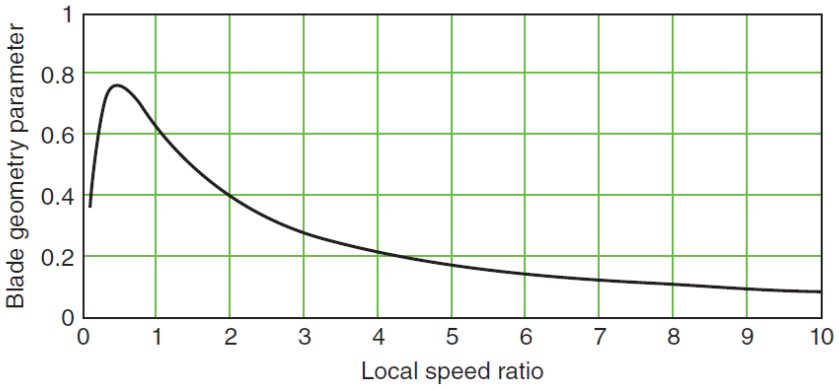

Figure 3.7 Blade geometry parameter versus local tip speed ratio (T. L. Burton *et al.*, 2021, p. 71).

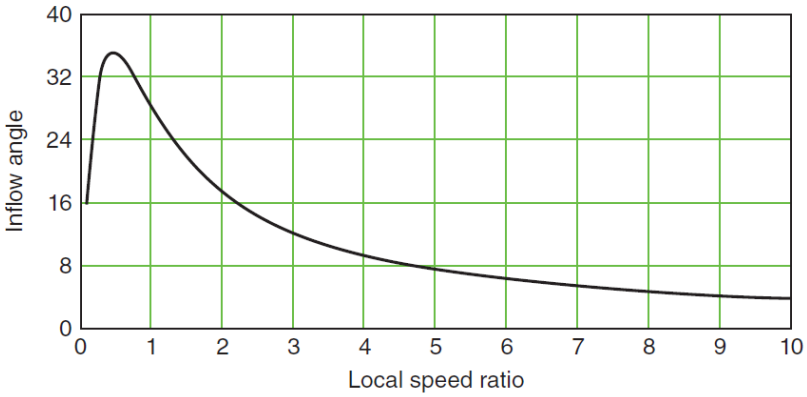

Figure 3.8 Inflow angle versus local tip speed ratio (T. L. Burton *et al.*, 2021, p. 72).

Similarly, the inflow angle varies as shown in Figure 3.8 and Equation 3.54. As with the blade geometry, close to the root, the inflow angle is larger.

$$\tan\phi = \left[\frac{1-a}{\lambda\mu(1+a')}\right] \qquad \text{Equation 3.54}$$

For optimum operation (when $a = \frac{1}{3}$):

$$\tan\phi = \left[\frac{1-\frac{1}{3}}{\lambda\mu\left(1+\frac{2}{9\lambda^2\mu^2}\right)}\right] \qquad \text{Equation 3.54a}$$

3.1.4.2 A blade design

Taking the NACA 4412 airfoil as an example (a common choice for hand-made wind turbines due to its bottom side being almost flat, which makes it easy to manufacture), at a Reynolds number of around 5 x 10^5, the maximum lift to drag ratio happens at a lift coefficient of approximately 0.7 and an angle of attack of around 3°. Keeping C_l and α constant at those values, on a three-blade

rotor operating at a tip speed ratio of 6, the blade chord to radius ratio and the twist vary as shown in Figure 3.9.

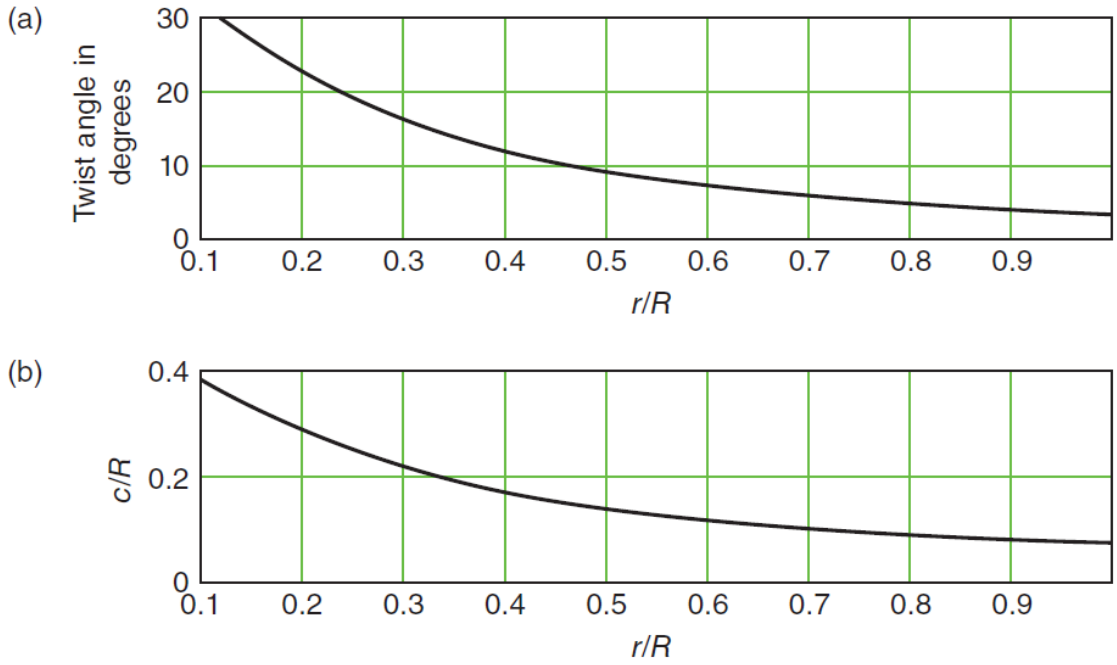

Figure 3.9 Optimum blade twist and chord to radius ratio (T. L. Burton *et al.*, 2021, p. 73).

It can be seen in Figure 3.9b that the blade does not have a uniform taper, which would make it difficult to manufacture. At optimum tip speed ratio, most of the torque comes from the outer part of the blade (T Burton *et al.*, 2011, p. 72). At the same time, the tip losses occur at the blade tip as it will be seen in the following sections. To make the manufacturing process simple, a straight line can be drawn passing through the outer 70% to 90% section of the blade, at the same time a lot of material is removed from the root as can be observed in Figure 3.10.

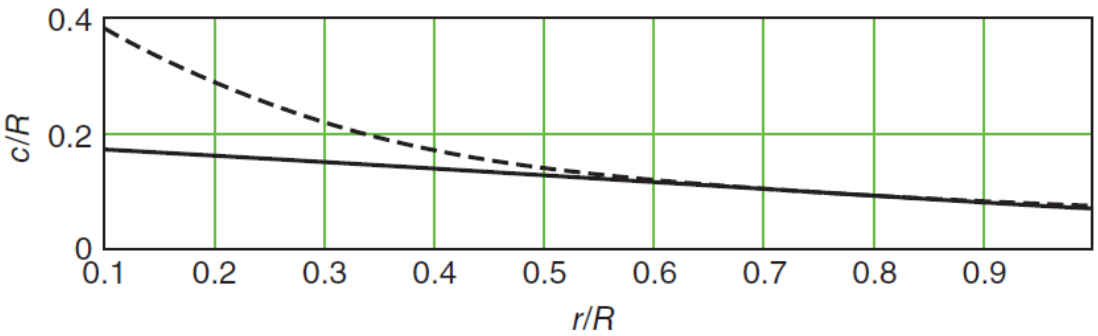

Figure 3.10 Linear tapper for optimal blade design (T Burton *et al.*, 2011, p. 71).

The new chord to radius ratio is:

$$\frac{c}{R} = \frac{8}{9(0.8\lambda)}\left(2 - \frac{\lambda\mu}{0.8\lambda}\right)\frac{2\pi}{C_l \lambda B} \qquad \text{Equation 3.55}$$

0.8 in Equation 3.55 refers to the point at 80% of the blade, midpoint between the chosen values. Equation 3.53b and Equation 3.55 can be combined to calculate the C_l along the blade (Figure 3.11).

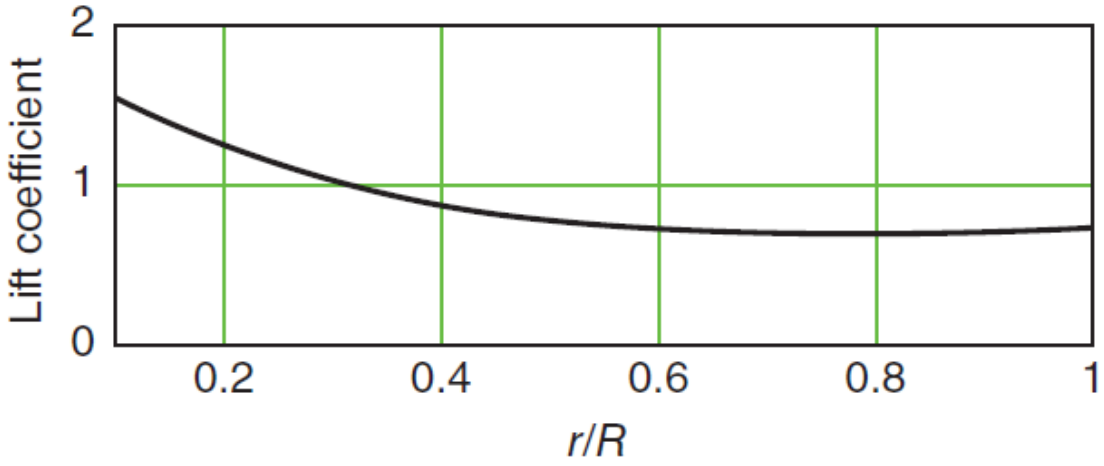

Figure 3.11 Lift coefficient along the linear tapered blade (T. L. Burton *et al.*, 2021, p. 74).

3.1.4.3 Effect of drag on optimum blade design

The same procedure followed in section 3.1.3.2 for Equation 3.33 can be done including the drag. Equation 3.39 becomes

$$\frac{B}{2\pi}\frac{c}{R}\lambda C_l = \frac{4\lambda^2\mu^2 a'(1-a)}{\frac{W}{U_\infty}\sqrt{(1-a) - \frac{C_l}{C_d}\lambda\mu(1+a')}} \qquad \text{Equation 3.56}$$

Figure 3.12 shows the results of Equation 3.44 with maximum power coefficients for different TSRs and lift to drag ratios. Induction factors have been calculated without considering drag (Equations Equation 3.41 and Equation 3.42) the torque is the one that includes drag from Equation 3.44.

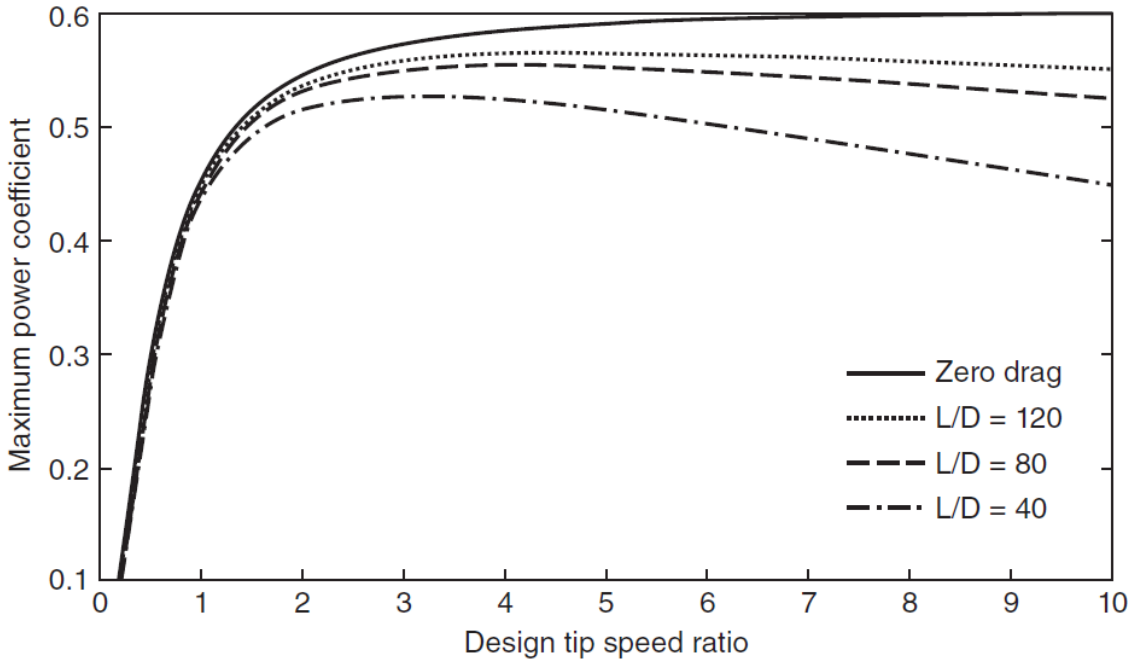

Figure 3.12 Variation of C_P versus TSR for different lift/drag ratios (T. L. Burton *et al.*, 2021, p. 76).

3.1.4.4 Tip losses

To be able to quantify tip losses, it would be necessary to know how the axial induction factor varies azimuthally, but it is not possible to calculate using the blade element-momentum theory. In 1919, Ludwig Prandtl developed an approximation for the tip-loss factor.

3.1.4.5 Prandtl's approximation

In 1919 Ludwig Prandtl developed an approximate solution for the tip-loss factor $f(r)$

$$f(r) = \frac{2}{\pi}\cos^{-1}\left(e^{-\pi\left(\frac{R_w - r}{d}\right)}\right) \qquad \text{Equation 3.57}$$

$R_w - r$ is measured from the edge of the wake. d is the distance between discs. The angle of the vortex sheets is ϕ_s

$$d = \frac{2\pi R_w}{B} sin\phi_s = \frac{2\pi R_w}{B}\frac{U_1(1-a)}{W_s} \qquad \text{Equation 3.58}$$

Figure 3.13 shows the variation of the tip loss factor from the root to the tip of a blade.

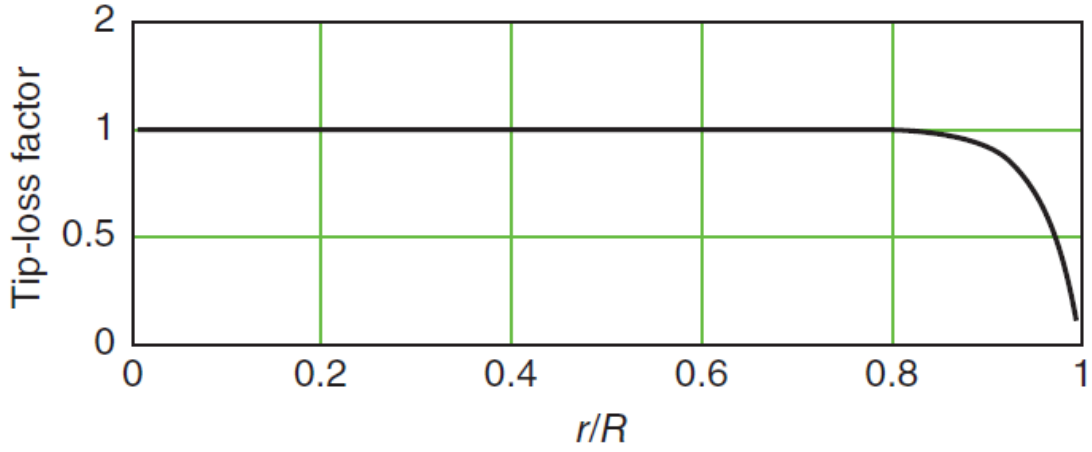

Figure 3.13 Variation of the tip-loss factor along the span (T. L. Burton *et al.*, 2021, p. 79).

3.1.4.6 Effect of tip losses on optimum blade design

Without tip losses, the optimum axial induction factor is constant at $\frac{1}{3}$. Considering tip losses, a becomes zero at the end of the wake and increases as it approaches the tip of the blade. If $a(r)$ varies with the radius, the flow factor is $a(r)/f(r)$. From Equation 3.47, the inflow angle becomes

$$tan\phi = \frac{1}{\lambda\mu}\left(\frac{1-\frac{a}{f}}{1+\frac{a'}{f}}\right) \qquad \text{Equation 3.59}$$

If drag is disregarded, Equation 3.47 becomes

$$tan\phi = \frac{\lambda\mu a'(1-a)}{a(1-a)+(a'\lambda\mu)^2} \qquad \text{Equation 3.60}$$

Therefore,

$$\frac{\lambda\mu a'(1-a)}{a(1-a)+(a'\lambda\mu)^2} = \frac{\left(1-\frac{a}{f}\right)}{\lambda\mu\left(1+\frac{a'}{f}\right)}$$

Expanding

$$\lambda^2\mu^2\frac{(f-1)}{f}a'^2 - \lambda^2\mu^2(1-a)a' + a(1-a)\left(1-\frac{a}{f}\right) = 0 \qquad \text{Equation 3.61}$$

The first term of the previous equation can be ignored because it is zero for most part of the blade where $f = 1$, and in the tip region a'^2 is very small. For tip speed ratios of more than three, such assumption makes a negligible difference.

$$\lambda^2\mu^2 a' = a\left(1-\frac{a}{f}\right) \qquad \text{Equation 3.62}$$

Equation 3.45 is still valid

$$\frac{da}{da'} = \frac{1-a}{a'}$$

Equation 3.62 becomes

$$\frac{da}{da'} = \frac{1}{\lambda^2\mu^2}\left(1-2\frac{a}{f}\right)$$

Then

$$(1-a)\left(1-2\frac{a}{f}\right) = \lambda^2\mu^2 a'$$

Equating it to Equation 3.62

$$a^2 - \frac{2}{3}(f+1)a + \frac{1}{3}f = 0$$

giving

$$a = \frac{1}{3} + \frac{1}{3}f - \frac{1}{3}\sqrt{1-f+f^2} \qquad \text{Equation 3.63}$$

Where a is the radial variation.

The power coefficient is still determined by Equation 3.21

$$C_P = \frac{P}{\frac{1}{2}\rho U_\infty^3 \pi R^2} = 8\lambda^2 \int_0^1 a'(1-a)\mu^3 d\mu$$

Figure 3.14 shows the difference in power coefficient, including tip losses. The effect of tip-losses is more significant at lower TSRs because the separation between helicoidal vortex sheets is large, on the other hand, at high tip speed ratios drag reduces the power coefficient.

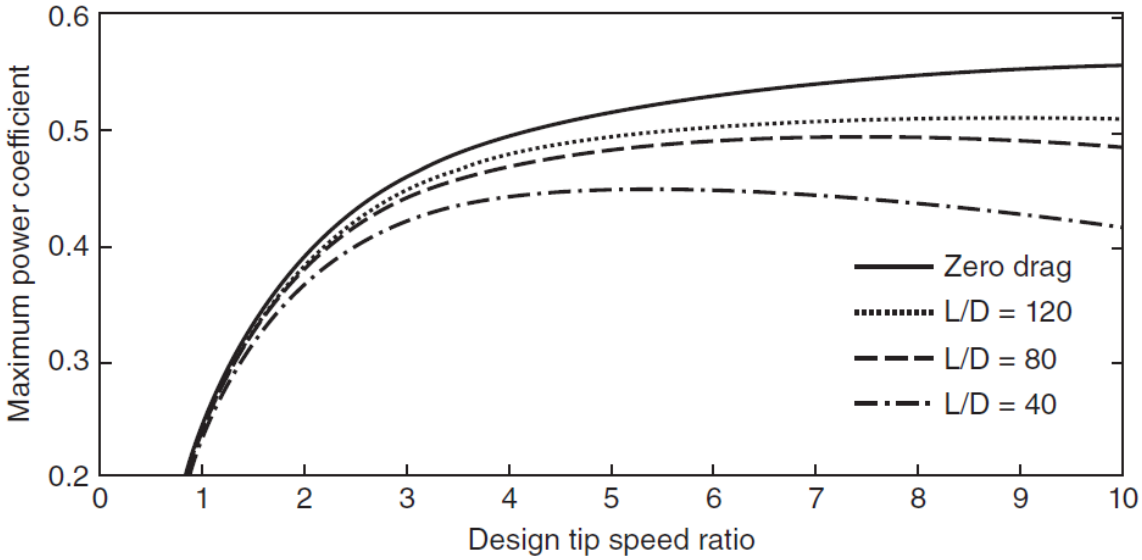

Figure 3.14 Variation of C_P versus TSR for different lift/drag ratios, including tip-losses (T Burton *et al.*, 2011, p. 90)

Prandtl 's tip-loss correction has been used since Glauert refined the BEM theory (1929). Wilson and Lissaman (1974) improved the tip-loss model, and subsequently de Vreis (1979). Mikkelsen, Sørensen and Shen (2001) proposed an updated technique, very shortly upgraded (Shen *et al.*, 2005), in good agreement with experimental results for a NREL rotor and a Swedish WG 500 turbine. Nowadays, Prandtl's and Shen *et al.* tip-loss corrections are found in BEM software.

Tornado is a vortex lattice code developed by Melin (2000) capable of modelling the interaction of airplane wing's spanwise sections unlike BEM models. Young *et al.* modified the code to use it in rotational applications (2019). Still, the code is not capable of simulating viscous effect (like most simulations) and an experimental study was carried out to test four winglet designs on tidal turbines. In all cases, winglets facing the pressure side increased the performance of the turbine.

3.1.5 Bending moment on the blade

The moment of the blade can be calculated from the torque and the thrust as follows:

$$\Delta T = \Delta L cos(\phi) - \Delta \mathrm{D} \sin(\phi) \qquad \text{Equation 3.64}$$

$$\frac{\Delta \tau}{r} = \Delta L sin(\phi) + \Delta \mathrm{D} \cos(\phi) \qquad \text{Equation 3.65}$$

Where L and D are the lift and drag forces, the other elements have been previously defined.

$$\Delta L = C_L \frac{1}{2} \rho W^2 c \cdot dr \qquad \text{Equation 3.66}$$

$$\Delta D = C_D \frac{1}{2} \rho W^2 c \cdot dr \qquad \text{Equation 3.67}$$

$c \cdot dr$ is the area of the blade element producing the lift and drag forces.

All calculations are for one blade, so for the whole rotor it would have to be multiplied by the number of blades (B).

Each component of the torque and thrust along the blade produce a maximum bending moment at the root as shown in Figure 3.15. The resulting moment can be calculated as:

$$M = \sqrt{\left(\sum_{i=1}^{n} \tau_i\right)^2 + \left(\sum_{r>0}^{R} r \times T_r\right)^2} \qquad \text{Equation 3.68}$$

Where τ_i is the local torque, r the radial position, and T_r the local thrust.

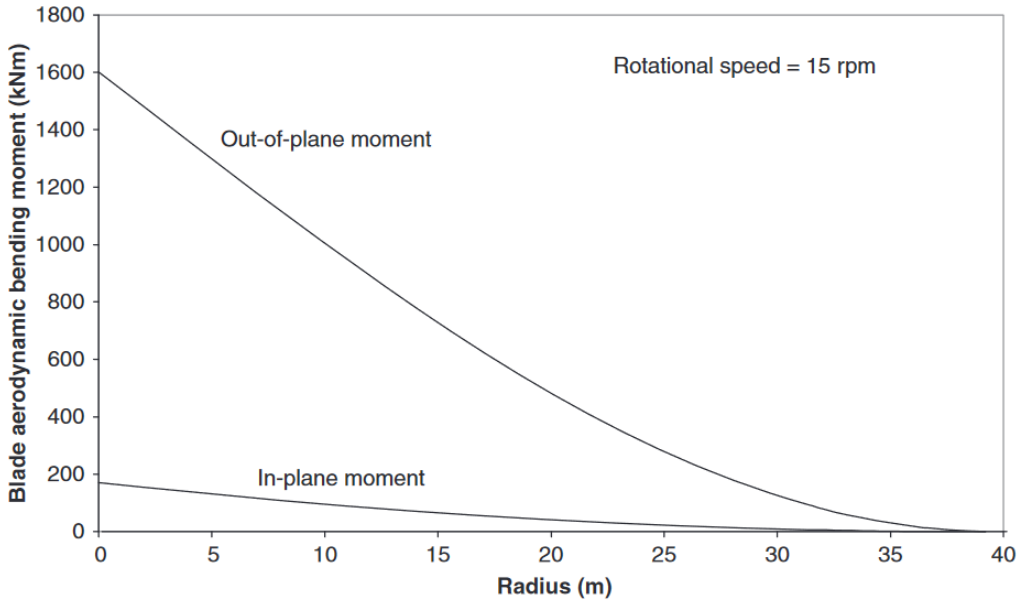

Figure 3.15 Bending moment along the blade of an 80 m diameter wind turbine in operation (Tony Burton *et al.*, 2011, p. 216).

The torque is the in-plane moment, the one that rotates the blades around the axis. The out-of-plane moment is the thrust, and in the case of this turbine goes towards the opposite direction of the hub cone. Figure 3.16 shows the contribution from each airfoil to the bending

moments, and the axes where they act on. The moment in x corresponds to the torque, the moment in y is product of the thrust, and the y' axis is where resulting moment acts upon.

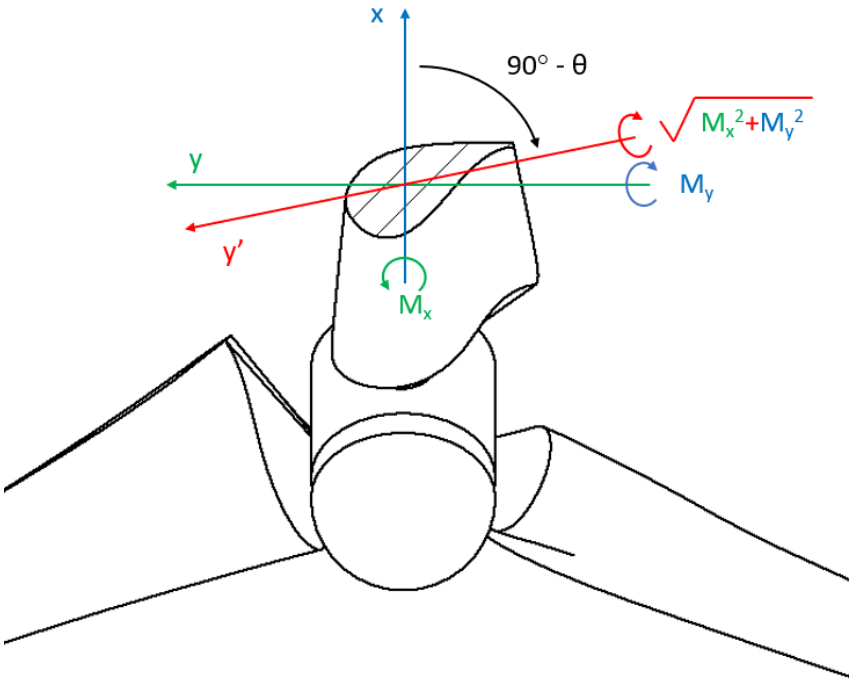

Figure 3.16 Schematic of the axes for each airfoil section, the moments generated at the root of the blade, and the combined moment along the prime axis.

Just as the thrust and torque coefficients, the moment coefficients along the axes can be calculated proportionally to the energy available through the rotor area:

$$C_{M_x} = \frac{M_x}{\frac{1}{2}\rho U_\infty^2 AR}$$

$$C_{M_y} = \frac{M_y}{\frac{1}{2}\rho U_\infty^2 AR}$$

$$C_M = \sqrt{\left(C_{M_x}\right)^2 + \left(C_{M_y}\right)^2}$$

3.2 Summary

Actuator disc theory is an analytical method to quantify rotor performance. The rotor is represented by a porous disc that allows the flow through the swept area, while being subject to surface forces. It is based on conservation of mass, momentum, and energy. The main limitation is that forces are equally distributed along the disc (Sørensen, 2012, p. 255).

Rotor disc theory models the turbine as a rotor with n number of blades rotating at an angular speed Ω, creating a pressure difference across the disc. This generates a loss of axial momentum in the wake, together with a "loss" of energy that could be extracted by and electrical generator connected to the shaft. The rotor perceives a torque in the direction of rotation, together with a thrust force in the same direction as the flow (T. L. Burton *et al.*, 2021, p. 45).

Blade-element/momentum theory (rotor blade theory) combines blade element theory, which discretises the blade into small sections to calculate the forces in those elements and integrates them along the blade over one revolution to determine the forces and moments for the entire rotor, with momentum theory (actuator disc theory) to determine the power and torque of the rotor. In addition, it can be applied to obtain the induction factor along the blades(Agelin-Chaab, 2018, p. 502).

It assumes that each section accounts independently for the convergence of the solution, rather than the actual interaction of them. It does not take into consideration the wake expansion. Hub and tip losses are not taken into account, but those corrections can be incorporated. The yaw of the turbine is not considered. Turbulent flow, flow detachment, 3D-flow, and spanwise flow cannot be modelled with this method. BEMT is still a powerful numerical method, very efficient computationally speaking, that *"has been the mainstay of the wind turbine industry for predicting wind turbine performance"* (Dixon and Hall, 2013, p. 475).

Chapter 4 Experimental method

4.1 Turbine design and operation

The turbine used in this work is a 3-bladed 'upwind' horizontal axis device with blade diameter of 1 *m* scaled to 1:20 from the AR2000 turbine from SIMEC Atlantis Energy. The blade geometry data was provided under an NDA, for such reason the specifications are not presented in detail, but there is an effort put to give specific examples with commonly available airfoils.
Non-dimensionalised details are specified in section 4.3.1. Approximately the outer 10% of the blade is interchangeable as detailed in section 4.3.2. The blade pitch angle was kept at 0°, but the design allowed pitch angles from -5° to 5° in increments of 1° by the use of different root pieces. An image is shown in section 4.3.3.

It is equipped with a dynamometer that measures rotor torque and thrust at the hub. It utilises full strain gauge bridges and runs 'wet' upstream of all seals and bearings. Rotor speed and blade radial position is quantified via a rotary encoder mounted on the main shaft within the nacelle. A 2-stage planetary gearbox and a synchronous generator convert mechanical energy to electrical and the rotor speed is controlled either by a wire-wound resistor bank or an electrical variable load. All data travelling out from the turbine is sampled and amplified using a wireless telemetry system to transmit data from the shaft to cables that join into a main umbilical cord that also convey the generated power out and low voltage DC power in to power the onboard systems. Further details of the turbine design and general set up can be found in (Bahaj and Myers, 2013; Galloway, Myers and Bahaj, 2014).

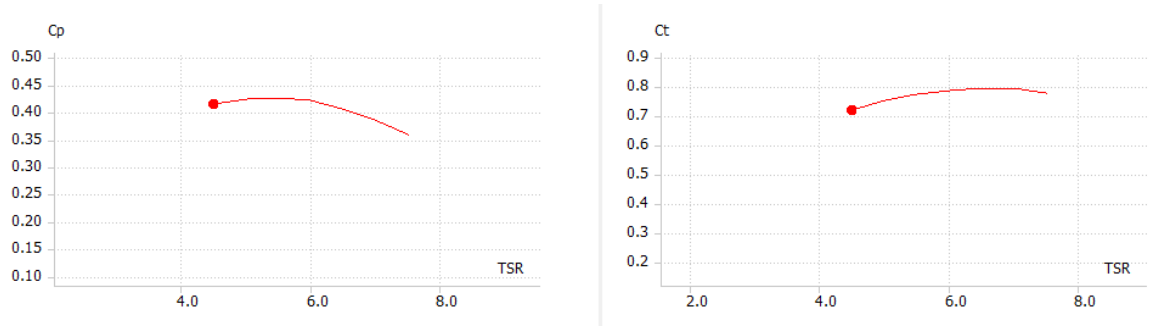

Figure 4.1 Cp and Ct curves from the BEM software simulation.

Before manufactured, the turbine performance was simulated with a BEM software (Figure 4.1), and compared against the full-scale turbine, then the blade design was sent to the Engineering Design and Manufacturing Centre (University of Southampton) to be milled on a 5-axis CNC machine from T6082-T6 aluminium alloy, with a precision of ± 50 microns (Figure 4.2). The

winglets were 3D printed in aluminium as well with at a precision of ±0.1 mm (Figure 4.3), subsequently hand polished and finished to fit the blades.

Figure 4.2 CNC machining of a blade from a block of aluminium.

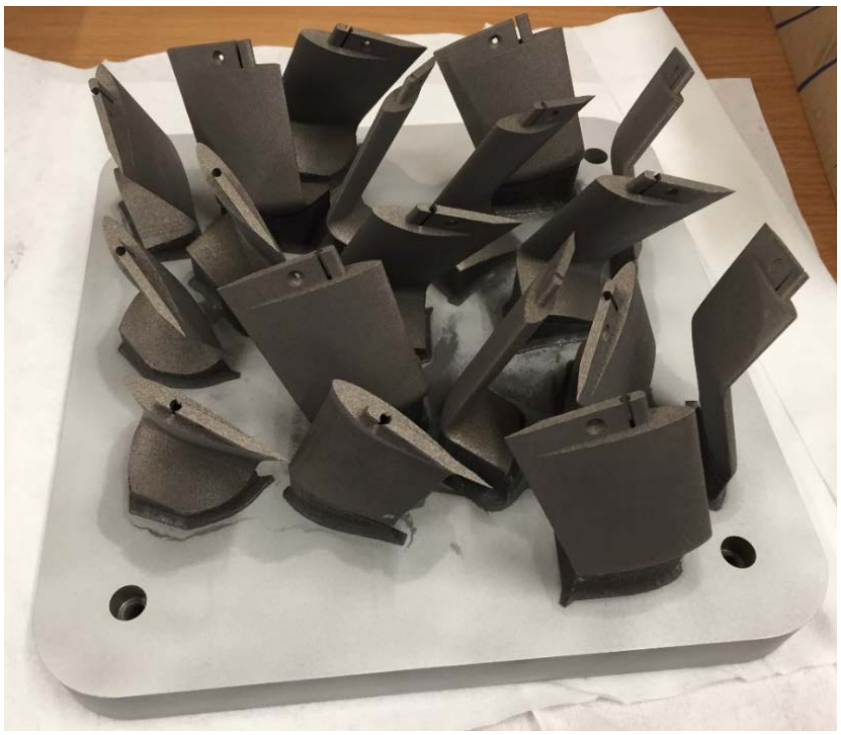

Figure 4.3 Several winglets 3D printed in aluminium on a 30x30-mm plate.

QBlade is a software developed by the Institute for Fluid Dynamics and Technical Acoustics of the Technical University of Berlin, released under a General Public License. The program integrates XFOIL, which is a very well-known program for the design and analysis of airfoils, to analyse their performance and include them into the simulation of HAWT and VAWT (QBlade Team, 2014).

The functions used are shown in Figure 4.4.

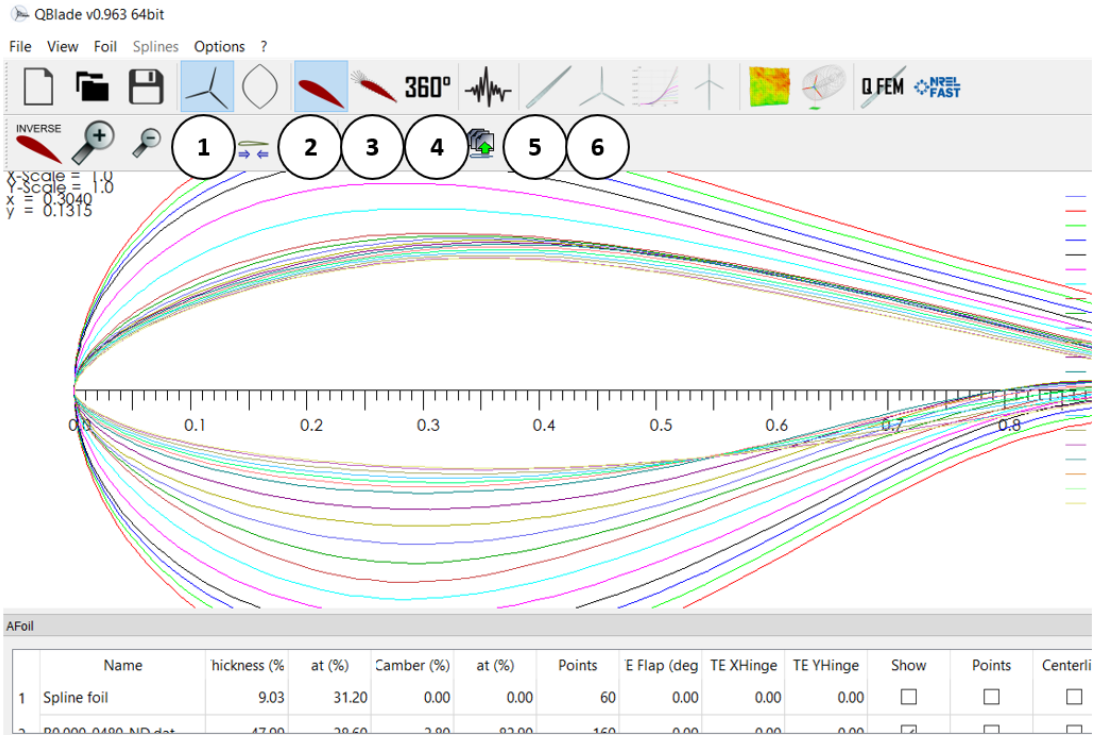

Figure 4.4 Qblade user interface.

1. HAWT Mode
2. Airfoil design
3. XFOIL Direct Analysis
4. Polar Extrapolation to 360
5. HAWT Rotorblade Design
6. Rotor BEM Simulation

The first step is to select the HAWT mode and load an airfoil profile into the software. Following the airfoil used as example in Section 3.1.4.2, the NACA 4412 profile can be seen in Figure 4.5.

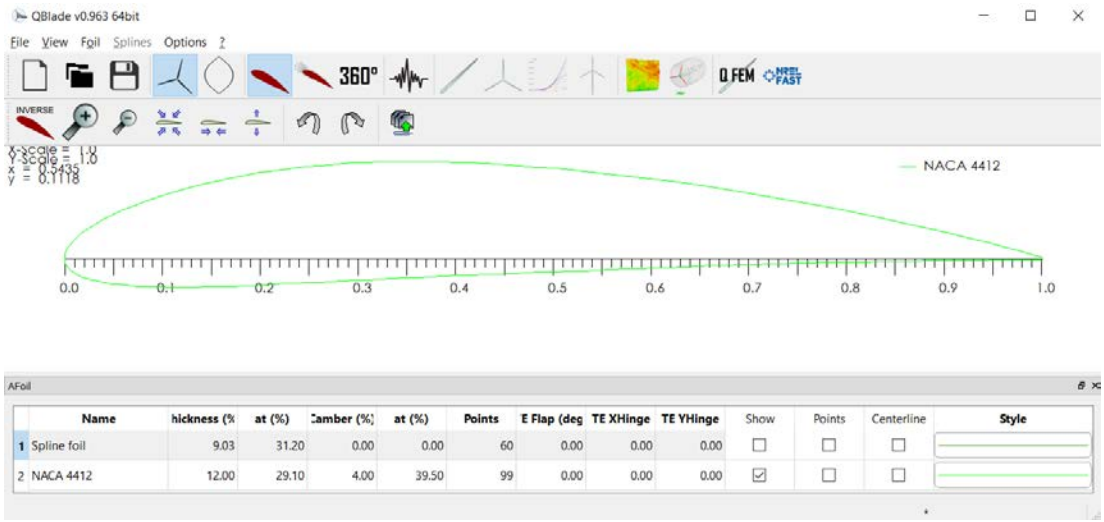

Figure 4.5 NACA 4412 airfoil loaded in the Airfoil design section in QBlade.

Next, the airfoil is analysed using the integrated XFOIL routine. XFOIL is a program written by Mark Drela in 1986 to compute the flow around subsonic foils in 2D. It calculates the pressure distribution around the airfoil, thus the lift and drag coefficients. To calculate a new polar, it is necessary to define the parameters shown in Figure 4.6.

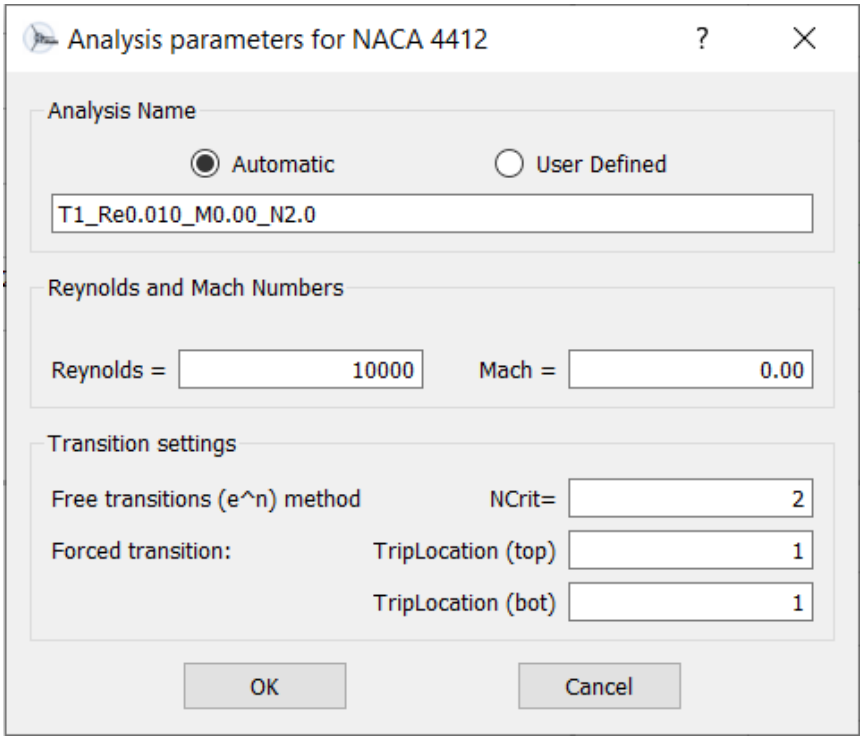

Figure 4.6 Analysis parameters.

The first field is the name, which can be determined automatically from the airfoil number, Reynolds, Mach and NCrit numbers, or defined by the user. Then the Mach number can be specified because this is a program developed initially to use on aircraft wings, and according to the XFOIL manual, reasonably accurate solutions can be expected for Mach numbers below 1.05 (Drela and Youngren, 2001). The Reynolds number has to be specified too. For the first estimate, the resultant from the flow speed and the rotational speed versus the blade twist helped group the chord-based Reynolds numbers from 6.67×10^4 to 2.67×10^5 in increments of 16,667 as shown in Figure 4.7.

A tip-speed-ratio range from 4 to 8 would cover the speeds allowed by the experiments. The lowest Reynolds number of 6.67×10^4, in fact corresponds to the scaled Reynolds number as it will be seen in the next section. The numbers are grouped and filled in different shades of grey for easiness of visualisation.

TSR	4	4.5	5	5.5	6	6.5	7	7.5	8
Hydrofoil	1.33E+05	1.50E+05	1.67E+05	1.83E+05	2.00E+05	2.17E+05	2.33E+05	2.50E+05	2.67E+05
0	6.67E+04	6.67E+04	6.67E+04	8.33E+04	8.33E+04	1.00E+05	1.00E+05	1.00E+05	1.17E+05
1	6.67E+04	6.67E+04	8.33E+04	8.33E+04	1.00E+05	1.00E+05	1.17E+05	1.17E+05	1.33E+05
2	8.33E+04	8.33E+04	1.00E+05	1.00E+05	1.17E+05	1.17E+05	1.33E+05	1.50E+05	1.50E+05
3	8.33E+04	1.00E+05	1.17E+05	1.17E+05	1.33E+05	1.50E+05	1.50E+05	1.67E+05	1.67E+05
4	1.00E+05	1.17E+05	1.17E+05	1.33E+05	1.50E+05	1.67E+05	1.67E+05	1.83E+05	2.00E+05
5	1.17E+05	1.17E+05	1.33E+05	1.50E+05	1.67E+05	1.67E+05	1.83E+05	2.00E+05	2.17E+05
6	1.17E+05	1.33E+05	1.50E+05	1.50E+05	1.67E+05	1.83E+05	2.00E+05	2.17E+05	2.33E+05
7	1.17E+05	1.33E+05	1.50E+05	1.67E+05	1.83E+05	2.00E+05	2.17E+05	2.17E+05	2.33E+05
8	1.33E+05	1.50E+05	1.67E+05	1.67E+05	1.83E+05	2.00E+05	2.17E+05	2.33E+05	2.50E+05
9	1.33E+05	1.50E+05	1.67E+05	1.83E+05	2.00E+05	2.17E+05	2.33E+05	2.50E+05	2.67E+05
10	1.33E+05	1.50E+05	1.67E+05	1.83E+05	2.00E+05	2.17E+05	2.33E+05	2.50E+05	2.67E+05
11	1.33E+05	1.50E+05	1.67E+05	1.83E+05	2.00E+05	2.17E+05	2.33E+05	2.50E+05	2.67E+05
12	1.33E+05	1.50E+05	1.67E+05	1.83E+05	2.00E+05	2.17E+05	2.33E+05	2.50E+05	2.67E+05
13	1.33E+05	1.50E+05	1.67E+05	1.83E+05	2.00E+05	2.17E+05	2.33E+05	2.50E+05	2.67E+05
14	1.33E+05	1.50E+05	1.67E+05	1.83E+05	2.00E+05	2.17E+05	2.33E+05	2.50E+05	2.67E+05
15	1.33E+05	1.50E+05	1.67E+05	1.83E+05	2.00E+05	2.17E+05	2.33E+05	2.50E+05	2.67E+05
16	1.33E+05	1.50E+05	1.67E+05	1.83E+05	2.00E+05	2.17E+05	2.33E+05	2.50E+05	2.67E+05
17	1.33E+05	1.50E+05	1.67E+05	1.83E+05	2.00E+05	2.17E+05	2.33E+05	2.50E+05	2.67E+05
18	1.33E+05	1.50E+05	1.67E+05	1.83E+05	2.00E+05	2.17E+05	2.33E+05	2.50E+05	2.67E+05
19	1.33E+05	1.50E+05	1.67E+05	1.83E+05	2.00E+05	2.17E+05	2.33E+05	2.33E+05	2.50E+05
20	1.33E+05	1.50E+05	1.67E+05	1.67E+05	1.83E+05	2.00E+05	2.17E+05	2.33E+05	2.50E+05
21	1.33E+05	1.50E+05	1.67E+05	1.67E+05	1.83E+05	2.00E+05	2.17E+05	2.33E+05	2.50E+05

Figure 4.7 First estimation of Reynolds numbers for all sections on tip speed ratios from 4 to 8.

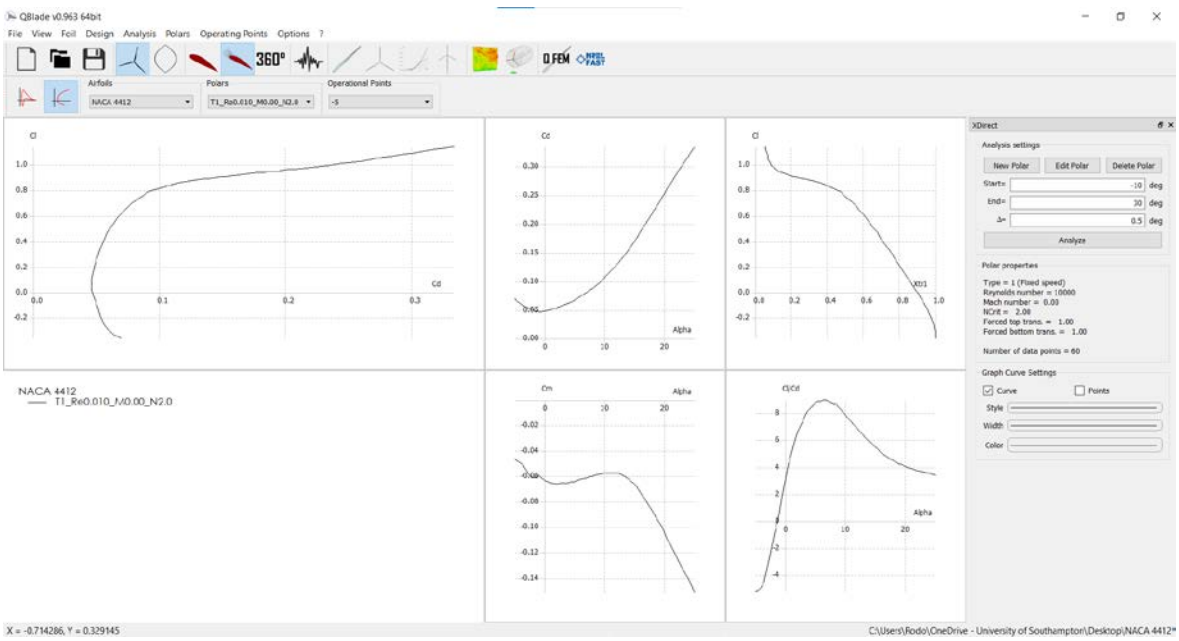

Figure 4.8 XFOIL computation for the NACA 4412 airfoil.

Figure 4.8 shows an output example for the NACA 4412 airfoil from -5° to 25° angles of attack in increments of 0.5°. Again, these angles were estimated from the geometry analysis of the resultant of the flow speed and the rotational speed versus its projection on the airfoil considering the twist angle.

To check the initial selection of angles of attack and Reynolds numbers, Figure 4.9 and Figure 4.10 were taken from the actual rotor simulation for tip speed ratios from 4 to 8.

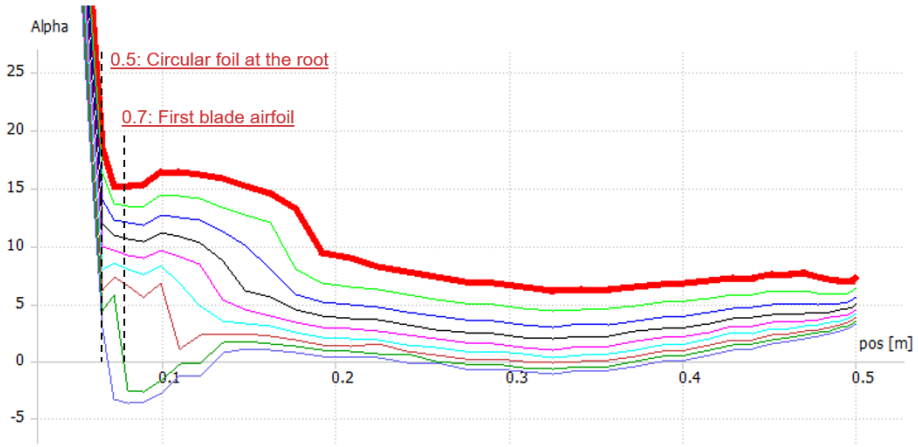

Figure 4.9 Alpha angles for the rotor for tip speed ratios from 4 to 8.

In Figure 4.9 it can be seen that for the slowest tip speed ratio (4) in red, the largest angle of attack is at 0.1 m from the centre of the axis with a value of 16.6°. At the same time, the smallest angle of attack at a tip speed ratio of 8 is -3.35° again just before 0.1 m from the centre, so the range chosen from -5° to 25° covers all the angles. The first straight lines correspond to the joint between the root (a circular foil) and the first airfoil.

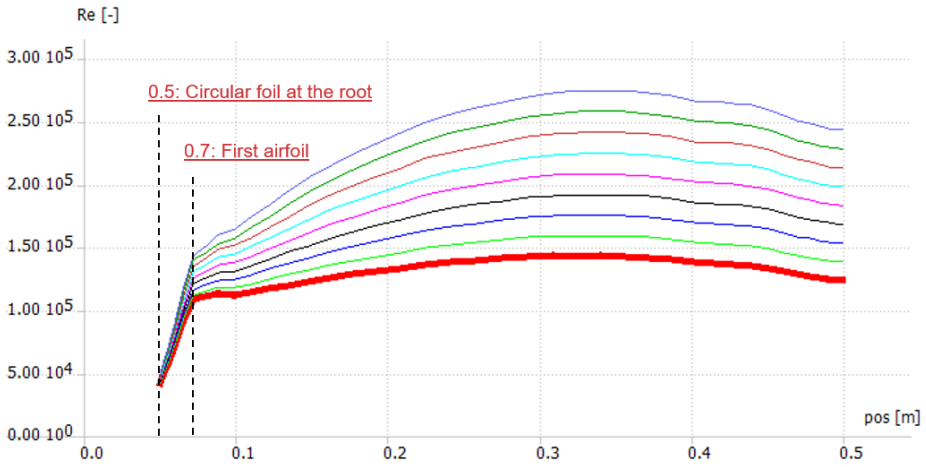

Figure 4.10 Reynolds numbers for the rotor simulation for tip speed ratios from 4 to 8.

In the case of the Reynolds numbers, Figure 4.10 shows the Reynolds numbers for the lowest tip speed ratio of 4 in red up until a tip speed ratio of 8. The lowest value where the blade starts at a position of 0.7 m is around 1.08 x 10^5, and the highest point is for a tip speed ratio of 8 located between 0.3 and 0.4 m on the blade with a value close to 2.74 x 10^5. The range estimated initially of 6.67 x 10^4 to 2.67 x 10^5 close to the high end of the values very and the lowest. As it will be seen later, the airfoil values are extrapolated to a range from -180° to 180°.

NCrit corresponds to the turbulence level for the coefficient to use in the e^n criterion for the transition of the flow from laminar to turbulent. Table 4-1 shows some values with the corresponding turbulence level and an example situation (Drela and Youngren, 2001, p. Transition criterion).

Table 4-1 Ncrit values for different situations.

Ncrit	turb. Level (%)	Situation
1	1.966%	
2	1.296%	
3	0.854%	
4	0.563%	dirty wind tunnel
5	0.371%	
6	0.245%	
7	0.161%	
8	0.106%	
9	0.070%	average wind tunnel standard "e^9 method"
10-12		clear wind tunnel
11-13		motor glider
12-14		sailplane

Murray *et al.* carried out towing tank experiments on tidal turbines, finding that an Ncrit value of 2 reflected the behaviour of the environment (Murray *et al.*, 2018, p. 209).

The next step is the polar extrapolation. There are two methods to choose from, Montgomerie and Viterna. The first was used as the second is for large HAWTs (Marten and Wendler, 2013, p. 75). Figure 4.11 shows the lift and drag coefficients extrapolation for the NACA 4412 airfoil.

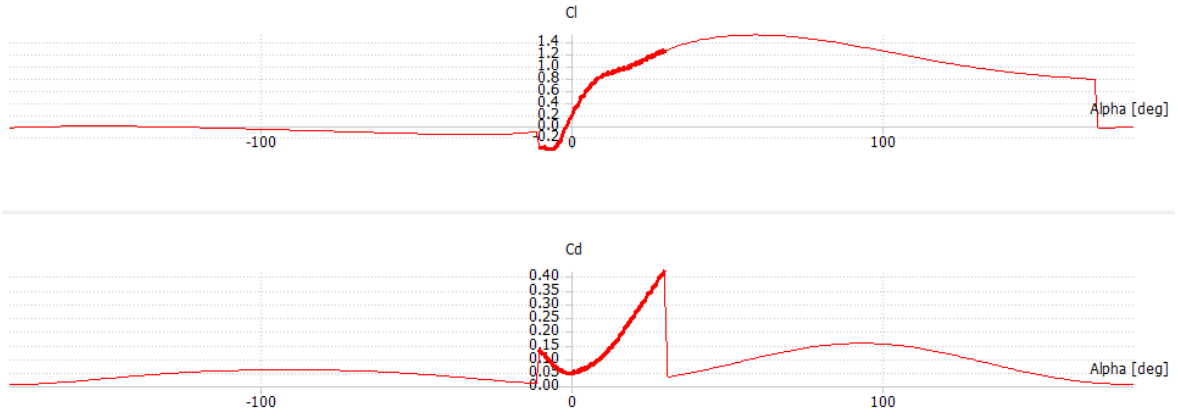

Figure 4.11 Lift and drag coefficients extrapolation from -180° to 180°.

The next section is for the blade design, as can be seen in Figure 4.12. (All design details hidden).

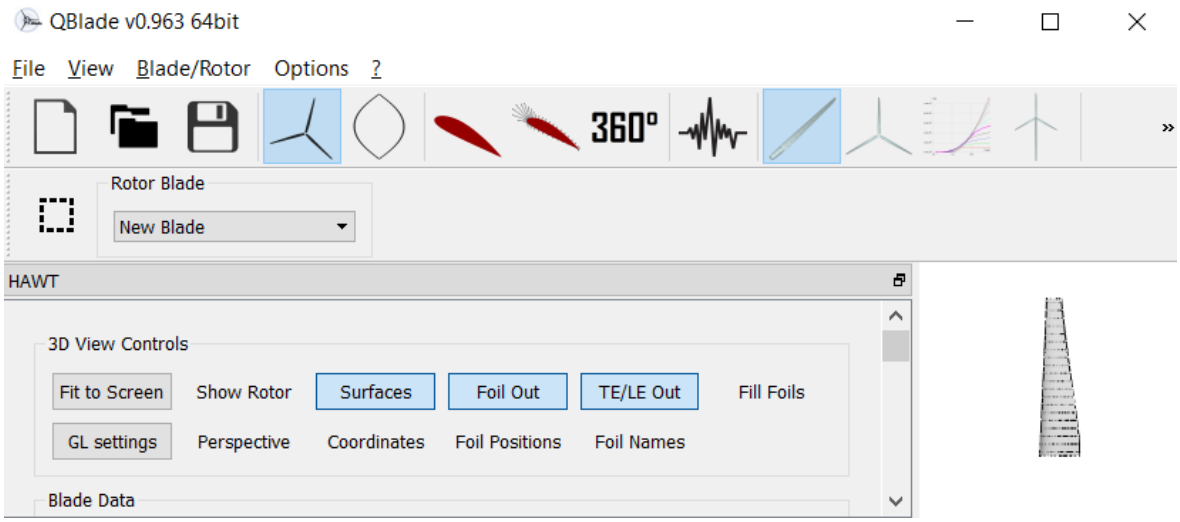

Figure 4.12 Blade design section.

The BEM theory combines the actuator disc theory (Section 3.1.1) and the rotor blade theory (Section 3.1.3). The blade is sectioned into a number of elements, each defined by their position with respect to the radius, airfoil profile, chord, twist and width. The windspeed W (relative to each section) and the angle of attack α are calculated. Then, from the previous step the lift and drag coefficients for each profile are extracted. With that information and the area of an airfoil the normal and tangential forces can be calculated, hence the thrust and torque. Each element's contribution is added to find the thrust and torque for the rotor (Marten and Wendler, 2013, p. 33) (Figure 4.13).

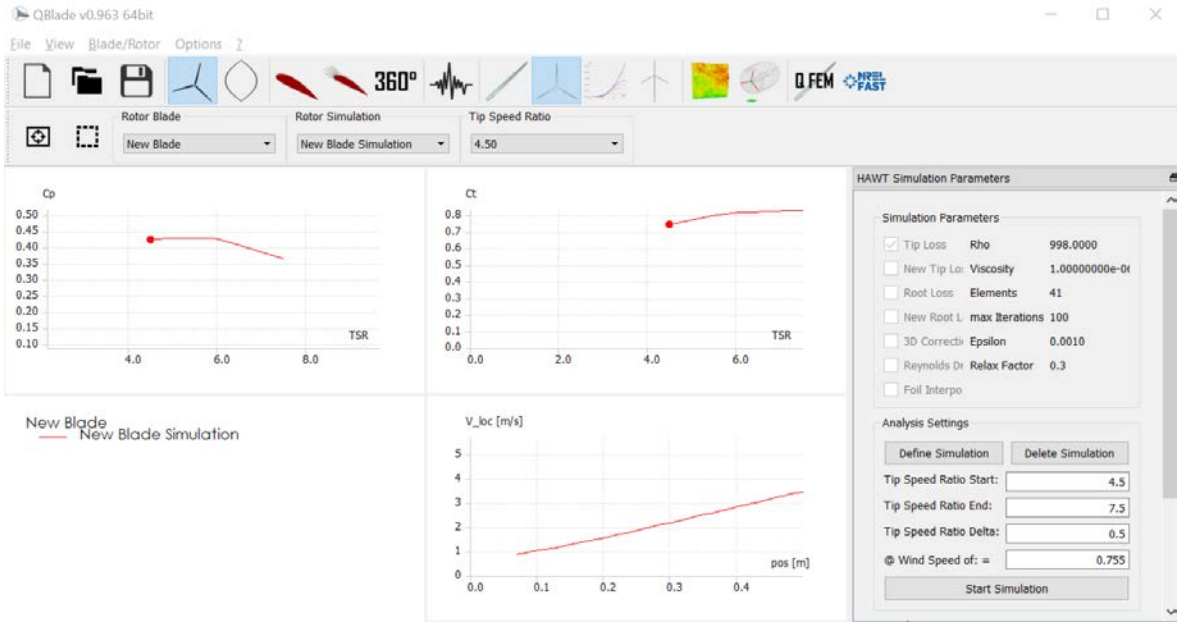

Figure 4.13 Rotor BEM simulation

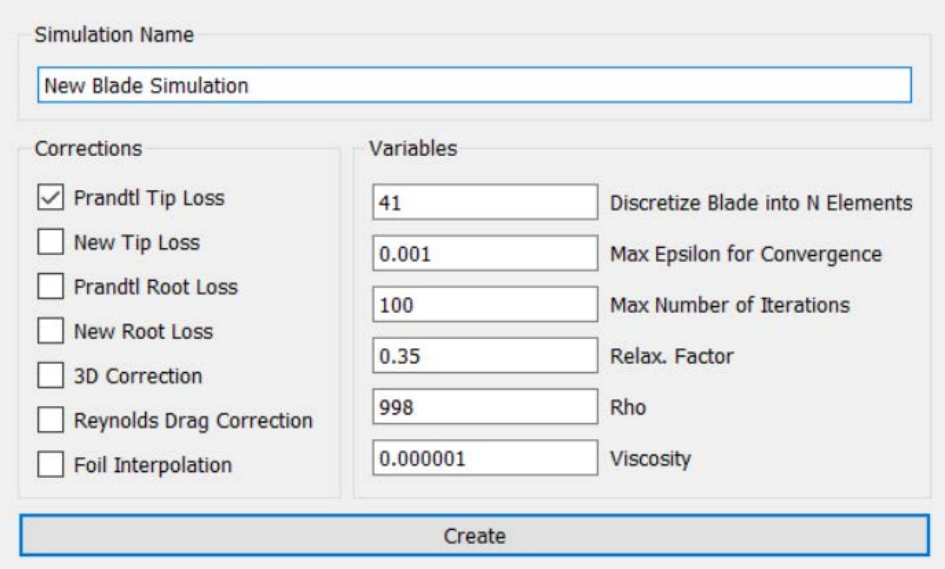

Figure 4.14 BEM parameters.

Figure 4.14 shows the different parameters that can be chosen for the simulation. In the right-hand side, has values than can be defined arbitrarily such as the number of blade elements or the number of iterations. Others such as density or viscosity vary with temperature. Values were chosen for 20°C at atmospheric pressure. Epsilon is either the difference in the induction factor or the axial induction factor before the program determines that the calculation of the convergence of forces and angles before passing to the next calculation. The relaxation factor is introduced to overcome the fluctuation of the induction factor, it can take a value from 0 to 1 and helps the software be more robust when making the calculations.

Figure 4.15 shows the problem at the root when asking the program to account for root losses.

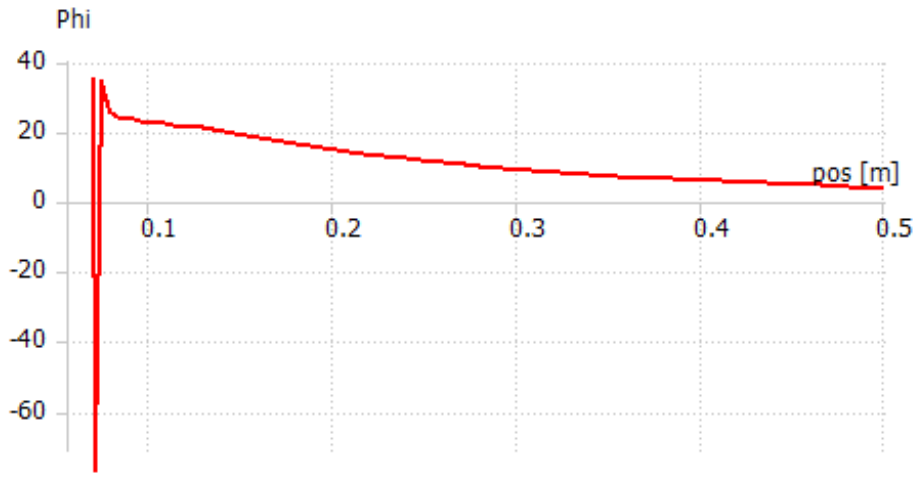

Figure 4.15 Inflow angle with root corrections.

The rotor was simulated for a full range of tip speed ratios so that the power and thrust curves could be better appreciated as seen on Figure 4.16. The dot along the line indicates the peak power at a tip speed ratio of 5.

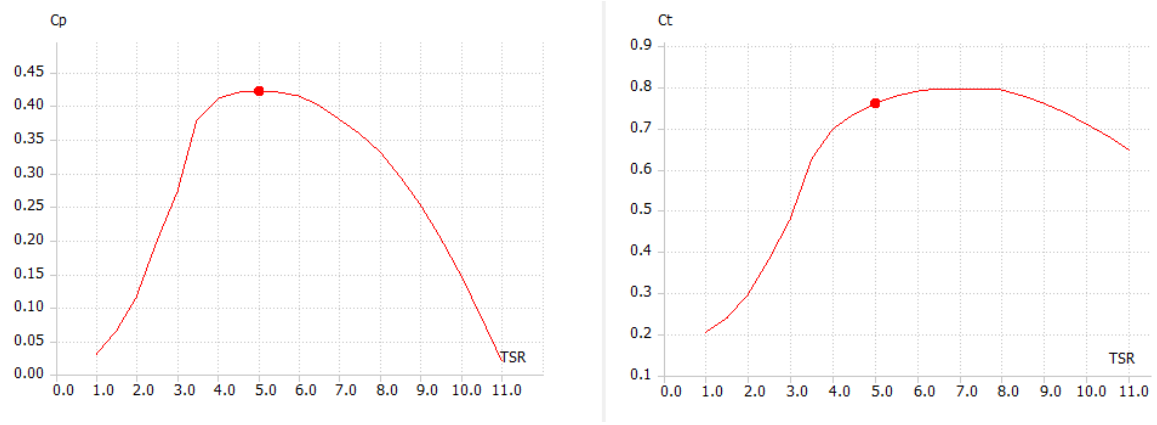

Figure 4.16 Full power and thrust curves for the rotor simulation, indicating peak power.

In order to simulate the curves, all polars had to be calculated from 4 x 10^4 to 4 x 10^5 Reynolds numbers in increments of 10,000. Figure 4.17 shows the Reynolds numbers along the blade for tip speed ratios from 1 to 11 in increments of 0.5. The thicker line shows the variation for maximum estimated power output. At that tip speed ratio of 5, the tip of the blade experiences Reynolds numbers of 1.5 x 10^5, and as it is explained in the next section it corresponds to the expected values at peak power compared to the full-scale turbine.

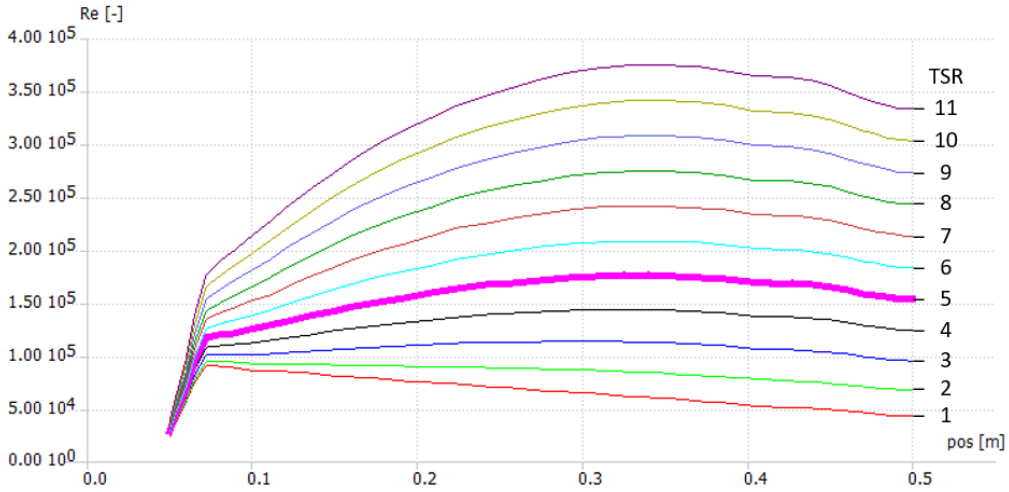

Figure 4.17 Reynolds numbers at each length of the blade for different TSRs.

The performance of the rotor was simulated before manufacturing the blades. Once it was checked that the simulation showed a performance curve above 0.4 of C_P, the blade designs were sent to be manufactured., Neither an extension of the blade nor the winglets were analysed. Winglets were 3D printed and subsequently tested in the towing tank.

After exporting the Drag coefficient, inflow angle, and inflow velocity, Figure 4.18 (Top) shows the Force per unit of length simulated along the blade, and Figure 4.18 (Bottom) when the tip losses are considered. A rotor simulation to compare the power curves with and without considering losses is shown in Figure 4.19. When 3D correction or Foil interpolation were chosen, the program crashed. There was no change seen when choosing the Reynolds correction option. For those reasons, the only option considered was the Tip Loss correction.

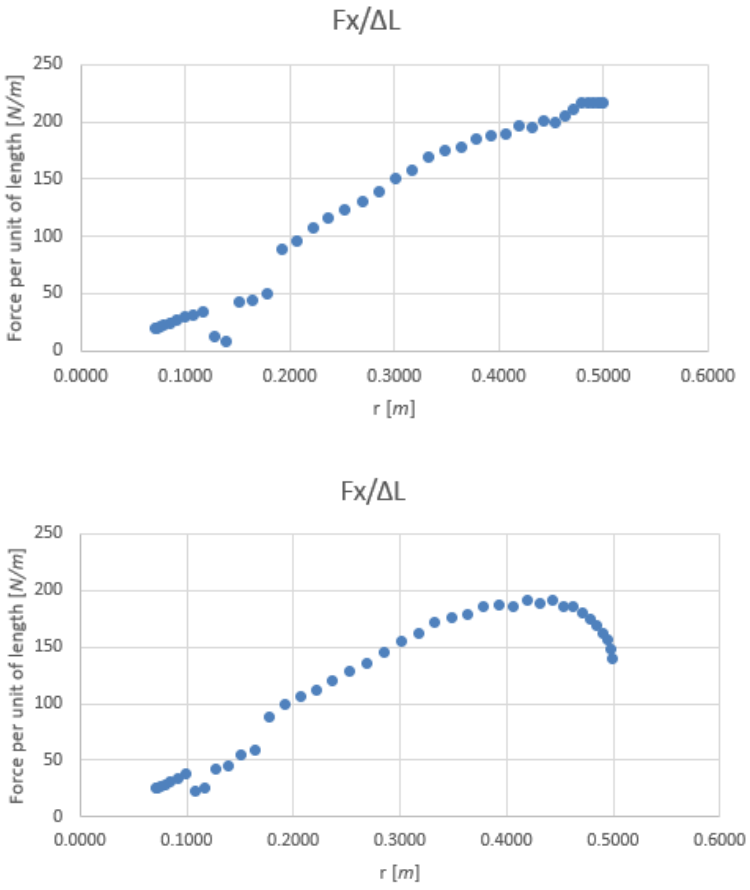

Figure 4.18 (Top) Simulation without tip losses. (Bottom) Tip losses accounted for (Used with permission from Microsoft).

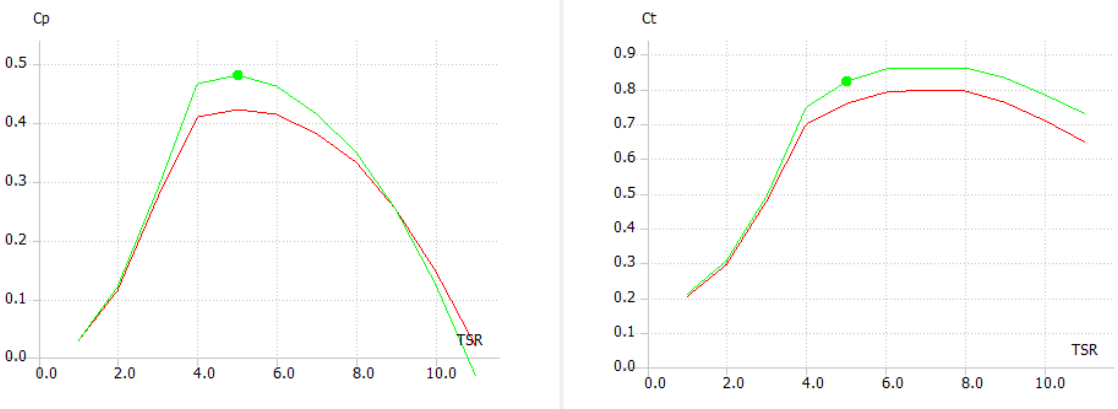

Figure 4.19 Rotor simulation with tip losses (red line) and disregarding tip losses (green line).

4.2 Turbine Scaling

All dimensions follow an isotropic scaling. The speeds using the Froude scaling to keep dynamic similarity, as both are influenced by inertia and gravity forces, and the Re numbers are shown in the following table:

Table 4-2 Scaling factors.

	AR2000	Scale, factor	1:20 prototype
Diameter [m]	20	Isotropic, 1/20	1
Operational speed [m/s]	2.8	Froude, 1/√20	0.626
Rotor speed [rpm]	14.3	Froude, √20	64
Angular speed [rad/s]	1.47	Froude, √20	6.69
TSR [ ]	5.35	1	5.35
Re number	6E6	$(1/20)^{3/2}$	6.7E4, 1.5E5*

*Expected experimental value

In practice, a towing speed of 0.76m/s was chosen to get a range of rotational speeds from 60 to 120 rpm, given the generator efficiency. An optimum operational TSR of 5 was found under such conditions. The result of the power scaling is presented in the following table:

Table 4-3 Power scale.

	AR2000	Scaling factor	1:20 prototype
Power	2 *MW*	1/(20^2*(2.8/0.76)^3)≈1/20,003	≈ 99.9 *W*

Canet, Bortolotti and Bottasso published in the European Academy for Wind energy scaling factors for a geometrically scaled model like the one used in this project (2020, p. 15). That approach gives a scaled Reynolds number of 6.7 x 10^4, and the experimental value can be calculated for the optimal operating speed at the tip of the blade with $\alpha \approx 0$, so that $\cos(\alpha) \approx 1$:

$$\frac{TSR * flow\ speed * chord}{dynamic\ viscosoty} = \frac{5 * 0.76 * 0.04}{1x10^{-6}} = 1.52x10^5$$

The simulation calculated a value of 1.53381 x 10^5.

One of the most sensitive parameters is the Reynolds number, because at low Reynolds numbers the viscosity plays a high role on the boundary layers and flow detachment from the airfoil. At higher Reynolds numbers the turbulence generates conditions for better flow attachment and the viscous effects become less influential. A representative airfoil operating between Re numbers of 1 x 10^4 to 5 x 10^4 experiences flow separation at very low angles of attack. Between Re numbers

of 5 x 10^4 to 1 x 10^5 there is flow separation at the back of the blades, and it is not until above values of 5 x 10^5 that the airfoils operate in ideal conditions (Winslow *et al.*, 2017) (Figure 4.20).

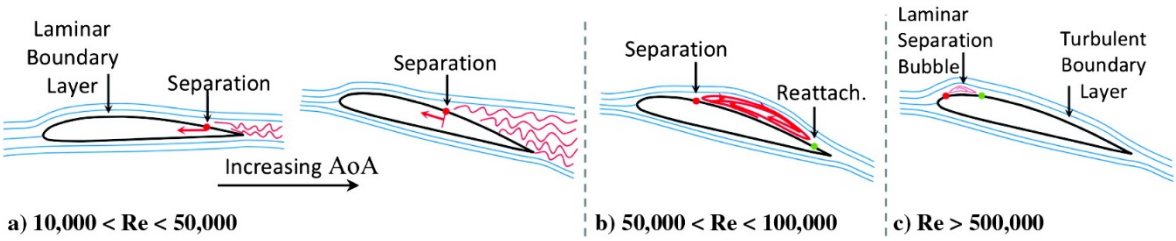

Figure 4.20 Airfoil behaviour at Reynolds numbers below 1 x 10^6 (Winslow *et al.*, 2017, p. 1051).

Table 4-4 shows the calculation of the rotor size for a scaled model of a 20-m rotor diameter operating at maximum power output and Re numbers in the range of 6 x 10^6 at the tip of the blade. Any model smaller than 0.8 m would be operating at conditions with a strong influence of viscous effects. On the other hand, it would require a scale no less than 1:8 to achieve Re numbers above 5 x 10^5, that is a diameter of 2.5 m for a geometrically scaled model.

Table 4-4 Rotor scaling for a 20-m tidal turbine operating at Re numbers of 6 x 10^6.

Re number	5 x 10^4	1 x 10^5	5 x 10^5
Rotor diameter	0.5 m	0.8 m	2.5 m
Flow speed	0.48 *m/s*	0.61 *m/s*	1.08 *m/s*

4.3 Blade design

4.3.1 Non-dimensionalised parameters

The data provided included the hydrofoils profiles, hub radius, position, twist and chord. The blade was divided into 20 sections, and the position given was the one at the middle of each section as it can be seen in Figure 4.21. The normalised twist can be appreciated in Figure 4.22. A normalised value of 1 for the twist corresponds to the maximum twist of the blade at the root. The other angles are a proportion of it, and they are plotted so that the curve can be visualised. The first and last points were defined so that they kept the same slope of the curve. The foils at the beginning and at the end of the blade were scaled appropriately from the adjacent ones. The centreline was chosen at $\frac{1}{3}$ of the leading edge as it was approximately the location of the thickest section for each airfoil.

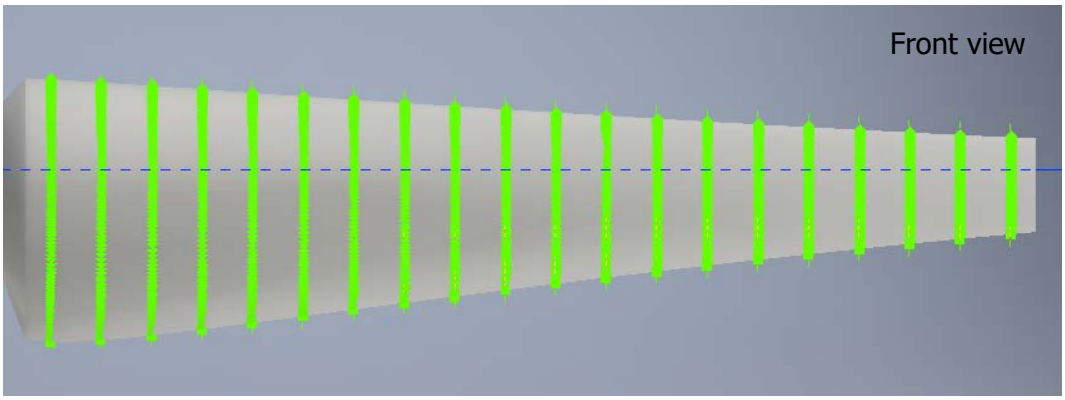

Figure 4.21 Blade hydrofoils positions (Autodesk screen shot reprinted courtesy of Autodesk, Inc.).

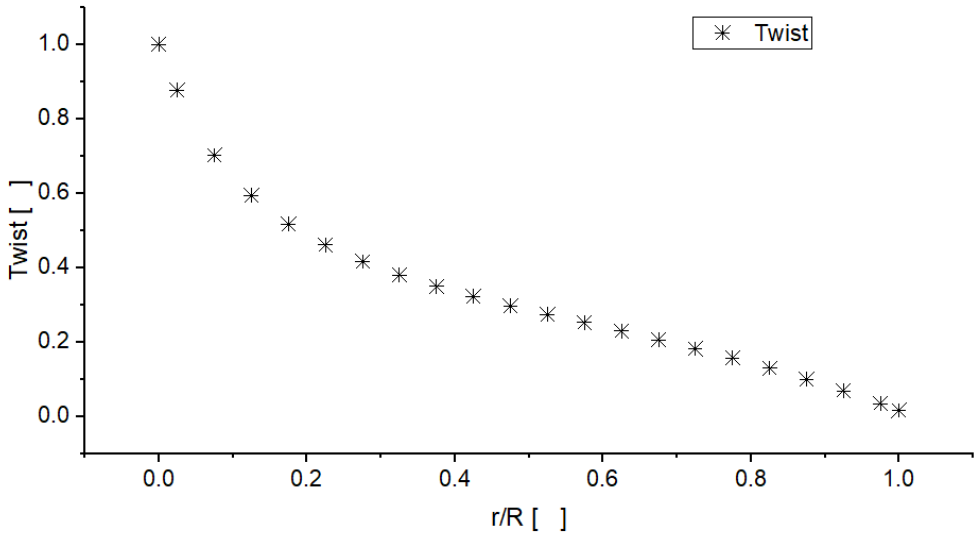

Figure 4.22 Blade pre-twist for each section.

4.3.2 Tip attachments

The middle part of the 18th section of the blade was used for the fitting design, giving an interchangeable 10.75% outer part of the blade as seen in Figure 4.23.

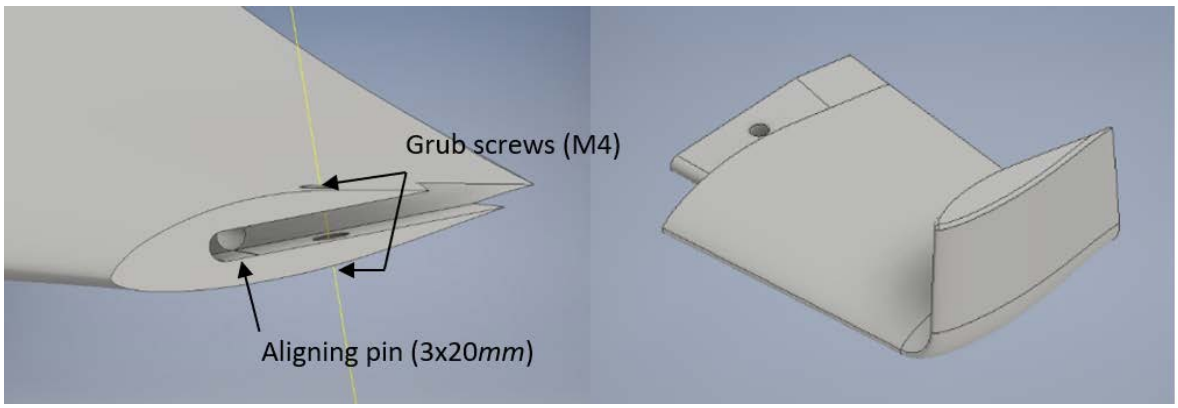

Figure 4.23 Interchangeable section of the blades (Autodesk screen shots reprinted courtesy of Autodesk, Inc.).

4.3.3 Blade alignment

Previous root designs had an issue with the alignment, as it was difficult to make the three blades be aligned when placing them in the hub. With the aligning root shown in Figure 4.24, the blades could be aligned in increments of 1° from -5° to 5° with different root tips. The precision was measured to 0.5°.

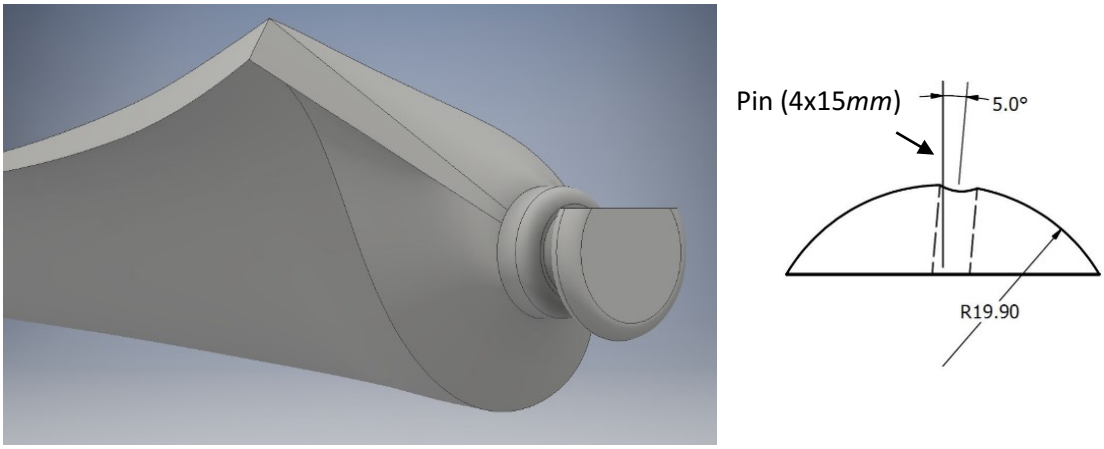

Figure 4.24 Root alignment (Autodesk screen shots reprinted courtesy of Autodesk, Inc.).

4.4 Winglets

Out of the winglets listed in Section 2.5, the present study focuses on bent wing extensions. These winglets are achieved by extending the blade past the radius, maintaining the airfoil shape and twist proportional to the distance from the centre, to maintain its 'triangular' appearance and bending them to keep the original rotor size. That way, the bent section forms the winglet. Figure 4.25 shows isometric views of the 20 different winglets finished. They had to be hand polished and fitted with the aligning pins. Table 4-5 shows the detailed specification of the 20 winglets designed and 3D printed for this project. They are numbered in order of design, varying the most relevant parameters first such as height, radius, cant, airfoil and toe angle. The height is calculated relative to the blade length, and the radius relative to the winglet height. It was found that to keep the same curvature radius, it might be more appropriate to relate it to the blade length. The cant angle is considered positive towards the pressure side and negative towards the suction side. Fillet is the curvature radius at the top of the winglet. The Loft feature was used in the CAD program and it determines how the winglet connects to the blade before being bent. Some airfoil shapes were changed for half the chord, a line, half a line, a point and inverted airfoils. The toe angle is measured seeing the rotor from the front, towards the direction of the flow, and using the normal convention of positive clockwise and negative counterclockwise.

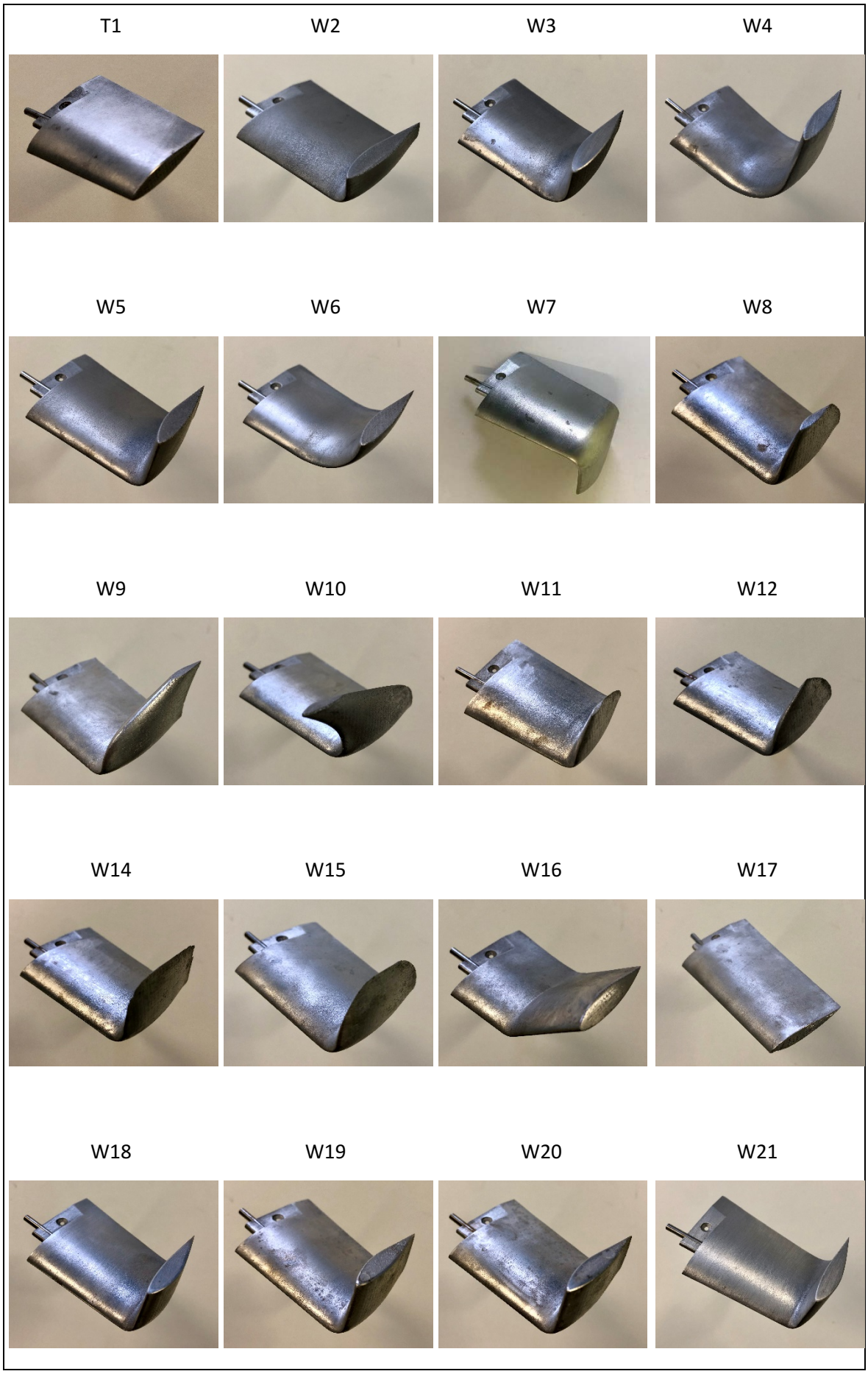

Figure 4.25 Isometric views of the 20 hand-finished winglets.

Table 4-5 Detail of the 20 different winglets and extensions designed.

No.	Height	Radius	Cant	Fillet	Loft	Shape	Centre	Toe
T1	0 mm (0.0%)	0%	0°	0.6 mm	Free	Foil	Yes	0°
W2	12.5mm (2.5%)	50%	90°	0.6 mm	Free	Foil	Yes	0°
W3	25 mm (5.0%)	50%	90°	0.6 mm	Free	Foil	Yes	0°
W4	50 mm (10.0%)	50%	90°	0.563 mm	Free	Foil	Yes	0°
W5	25 mm (5.0%)	25%	90°	0.6 mm	Free	Foil	Yes	0°
W6	25 mm (5.0%)	100%	90°	0.6 mm	Free	Foil	Yes	0°
W7	25 mm (5.0%)	25%	-90°	0.6 mm	Free	Foil	Yes	0°
W8	25 mm (5.0%)	25%	90°	0.6 mm	Tangent	½ c	Yes	0°
W9	25 mm (5.0%)	25%	90°	0.0 mm	Tangent	½ c	+45°	0°
W10	25 mm (5.0%)	25%	90°	0.6 mm	Tangent	½ c	-45°	0°
W11	25 mm (5.0%)	25%	90°	0.6 mm	Tangent	¼ c	Yes	0°
W12	25 mm (5.0%)	25%	90°	N/A	Tangent	Point	Yes	0°
W14	25 mm (5.0%)	25%	90°	N/A	Tangent	Line	Yes	0°
W15	25 mm (5.0%)	25%	90°	N/A	Tangent	Line ½c	Yes	0°
W16	25 mm (5.0%)	25%	45°	0.6 mm	Free	Foil	Yes	0°
E17	25 mm (5.0%)	0%	0°	0.6 mm	Free	Foil	Yes	0°
W18	25 mm (5.0%)	25%	90°	0.6 mm	Free	Inv. Foil	Yes	0°
W19	25 mm (5.0%)	25%	90°	0.6 mm	Free	Foil	Yes	3.5°
W20	25 mm (5.0%)	25%	90°	0.6 mm	Free	Foil	Yes	-3.5°
W21	25 mm (5.0%)	25%	90°	0.6 mm	Free	Inv. Foil	Yes	-3.5°

The first tip is labelled as T1 (Figure 4.26) because it is not a winglet *per se*, it is in fact the tip of the normal blade which section was split with the design to attach the winglets. In other words, when the blade has this tip attached, it looks like a normal blade. The blade with this configuration serves as baseline for the rest of the winglets which are mostly grouped in threes to try to see a trend in any variation.

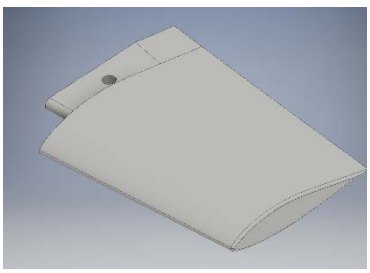

Isometric view

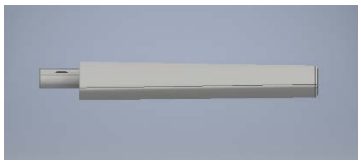

Left view

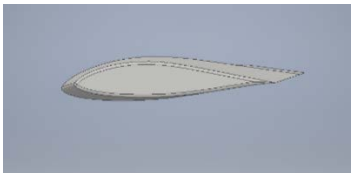

Front view

No.	Height	Radius	Cant	Fillet	Loft	Shape	Centre	Toe
T1	0 mm (0.0%)	0%	0°	0.6 mm	Free	Foil	Yes	0°

Figure 4.26 Tip 1 (T1): Tip for the normal blade (Autodesk screen shots reprinted courtesy of Autodesk, Inc.).

Winglets 2-4 were designed to compare the first design parameter that makes a winglet, which is the height. All other values were fixed, but because the radius is relative to the height, so it changes too. It was an issue addressed after their design during the experimental results

comparisons. Different views of the winglets, together with their specifications can be seen in Figure 4.27, Figure 4.28, and Figure 4.29.

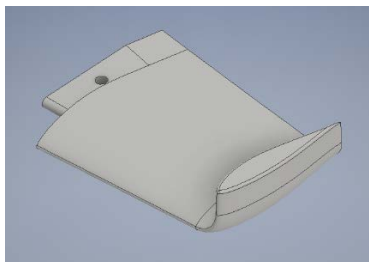
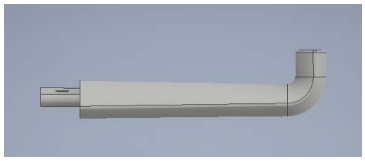
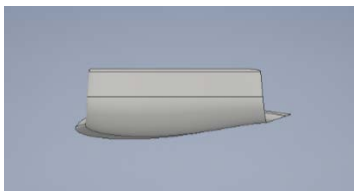

Isometric view Left view Front view

No.	Height	Radius	Cant	Fillet	Loft	Shape	Centre	Toe
W2	12.5mm (2.5%)	50%	90°	0.6 mm	Free	Foil	Yes	0°

Figure 4.27 Winglet 2 (W2): 2.5% height (Autodesk screen shots reprinted courtesy of Autodesk, Inc.).

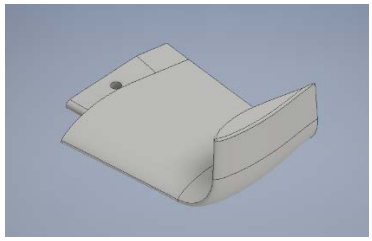
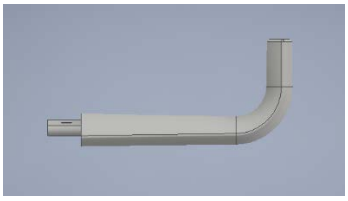
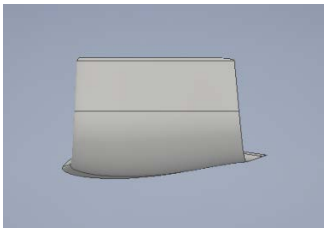

Isometric view Left view Front view

No.	Height	Radius	Cant	Fillet	Loft	Shape	Centre	Toe
W3	25 mm (5.0%)	50%	90°	0.6 mm	Free	Foil	Yes	0°

Figure 4.28 Winglet 3 (W3): 5.0% height (Autodesk screen shots reprinted courtesy of Autodesk, Inc.).

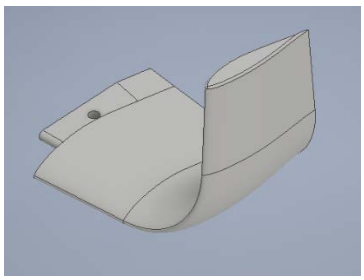
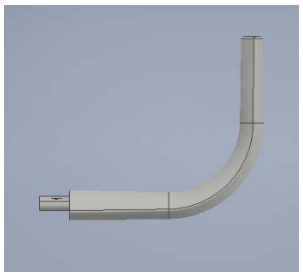
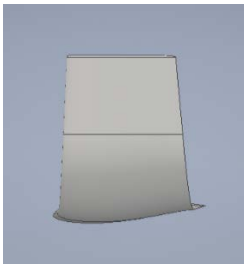

Isometric view Left view Front view

No.	Height	Radius	Cant	Fillet	Loft	Shape	Centre	Toe
W4	50 mm (10.0%)	50%	90°	0.563 mm	Free	Foil	Yes	0°

Figure 4.29 Winglet 4 (W4): 10.0% height (Autodesk screen shots reprinted courtesy of Autodesk, Inc.).

Winglets 5 and 6 compare the curvature radius versus winglet 3. The values are 25%, 50% and 100%. The height is kept constant at 5% (Figure 4.28, Figure 4.30, and Figure 4.31).

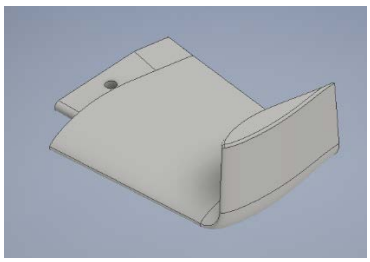

Isometric view

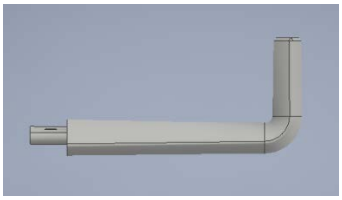

Left view

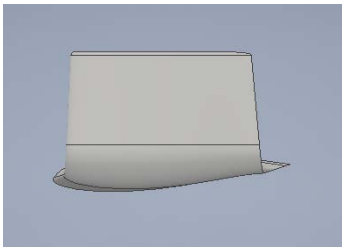

Front view

No.	Height	Radius	Cant	Fillet	Loft	Shape	Centre	Toe
W5	25 mm (5.0%)	25%	90°	0.6 mm	Free	Foil	Yes	0°

Figure 4.30 Winglet 5 (W5): 5.0% height, 25% radius (Autodesk screen shots reprinted courtesy of Autodesk, Inc.).

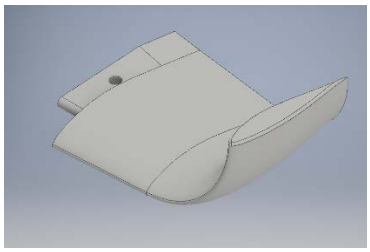

Isometric view

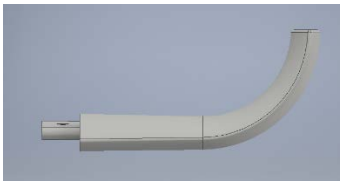

Left view

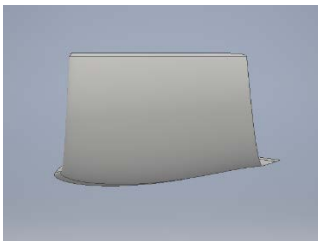

Front view

No.	Height	Radius	Cant	Fillet	Loft	Shape	Centre	Toe
W6	25 mm (5.0%)	100%	90°	0.6 mm	Free	Foil	Yes	0°

Figure 4.31 Winglet 6 (W6): 5.0% height, 100% radius (Autodesk screen shots reprinted courtesy of Autodesk, Inc.).

Winglet 7 (Figure 4.32) compares cant angle versus winglet 5 (Figure 4.30).

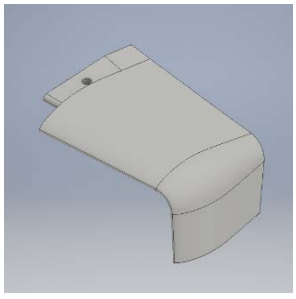

Isometric view

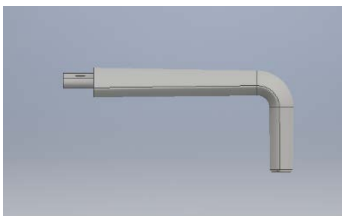

Left view

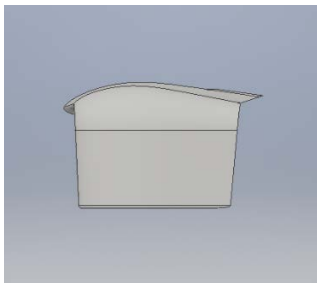

Front view

No.	Height	Radius	Cant	Fillet	Loft	Shape	Centre	Toe
W7	25 mm (5.0%)	25%	-90°	0.6 mm	Free	Foil	Yes	0°

Figure 4.32 Winglet 7 (W7): 5.0% height, 25% radius, -90° cant (Autodesk screen shots reprinted courtesy of Autodesk, Inc.).

Winglet 8 (W8) varies the size of the end airfoil to half of it, positioned at the central axis (Figure 4.33, everything else is the same as winglet 5 (Figure 4.30).

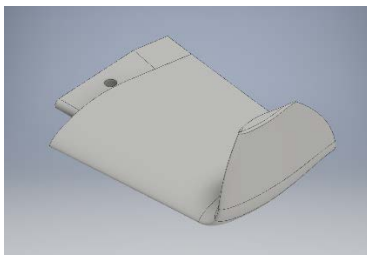

Isometric view

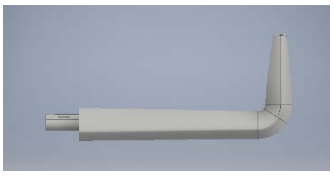

Left view

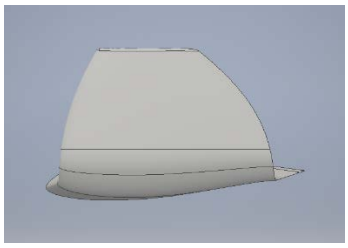

Front view

No.	Height	Radius	Cant	Fillet	Loft	Shape	Centre	Toe
W8	25 mm (5.0%)	25%	90°	0.6 mm	Tangent	½ c	Yes	0°

Figure 4.33 Winglet 8 (W8). Half airfoil at the central axis (Autodesk screen shots reprinted courtesy of Autodesk, Inc.).

Winglet 9 and 10 are similar to the previous winglet, with the difference that the airfoil is moved back and forward by 45° (Figure 4.34 and Figure 4.35).

(Autodesk screen shots reprinted courtesy of Autodesk, Inc.)

Isometric view

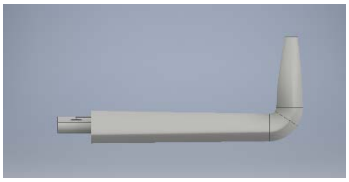

Left view

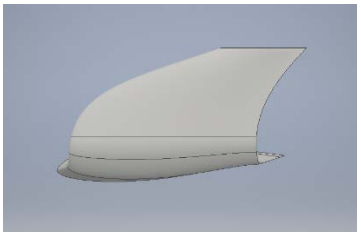

Front view

No.	Height	Radius	Cant	Fillet	Loft	Shape	Centre	Toe
W9	25 mm (5.0%)	25%	90°	0.0 mm	Tangent	½ c	+45°	0°

Figure 4.34 Winglet 9 (W9). Half airfoil +45° from the central axis (Autodesk screen shots reprinted courtesy of Autodesk, Inc.).

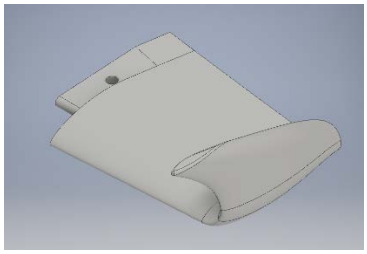

Isometric view

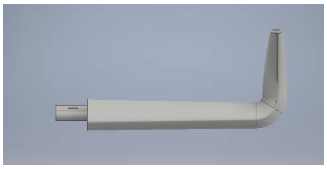

Left view

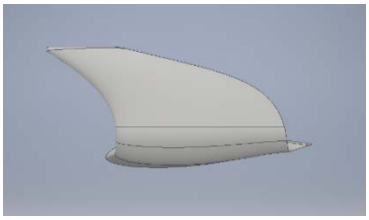

Front view

No.	Height	Radius	Cant	Fillet	Loft	Shape	Centre	Toe
W9	25 mm (5.0%)	25%	90°	0.0 mm	Tangent	½ c	+45°	0°

Figure 4.35 Winglet 10 (W10): Half airfoil -45° from the central axis (Autodesk screen shots reprinted courtesy of Autodesk, Inc.).

Winglets 11 and 12 were designed to further explore the reduction in size of the tip airfoil. Winglet 12 (Figure 4.37) is very similar to winglets used by Enercon (Figure 2.17, p. 27). As mentioned before, for obvious reasons, there are no published results about them, and it is thought that they are oriented towards the pressure side for tower clearance concerns. Winglet 11 (Figure 4.36) has a tip airfoil half the size of winglet 8.

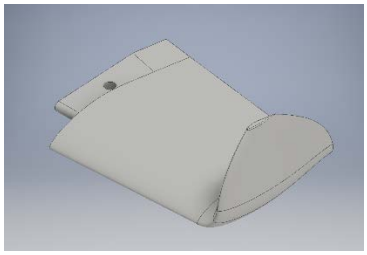

Isometric view

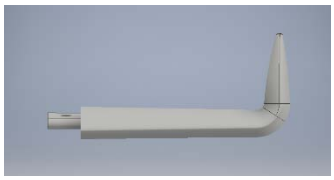

Left view

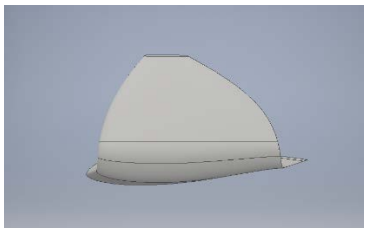

Front view

No.	Height	Radius	Cant	Fillet	Loft	Shape	Centre	Toe
W11	25 mm (5.0%)	25%	90°	0.6 mm	Tangent	¼ c	Yes	0°

Figure 4.36 Winglet 11 (W11): A quarter airfoil at the central axis (Autodesk screen shots reprinted courtesy of Autodesk, Inc.).

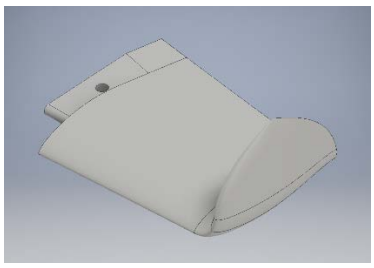

Isometric view

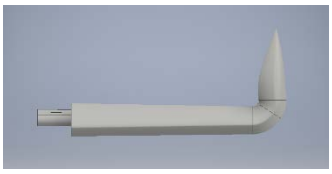

Left view

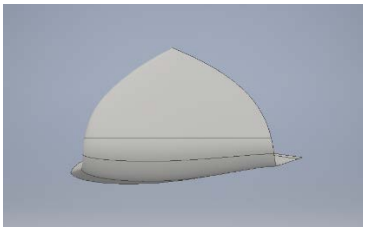

Front view

No.	Height	Radius	Cant	Fillet	Loft	Shape	Centre	Toe
W12	25 mm (5.0%)	25%	90°	N/A	Tangent	Point	Yes	0°

Figure 4.37 Winglet 12 (W12): Endpoint located at the central axis (Autodesk screen shots reprinted courtesy of Autodesk, Inc.).

Winglets 14 and 15 (Figure 4.38 and Figure 4.39) were designed to explore the effect of reducing the airfoil thickness. Winglet 14 has two sharp edges that do not seem aerodynamic or stable. Winglet 15 has half the chord of winglet 14 so that the edges are rounded, and it seems to have a more aerodynamic shape.

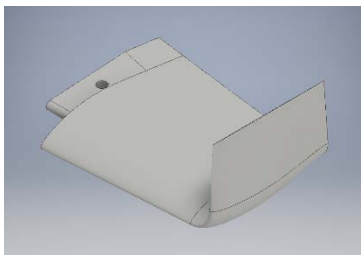

Isometric view

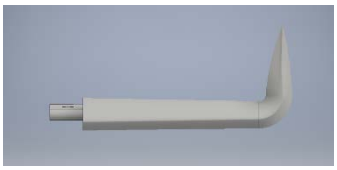

Left view

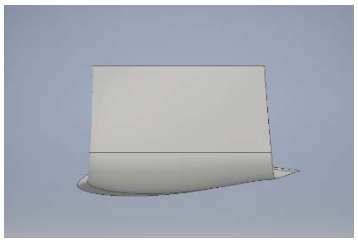

Front view

No.	Height	Radius	Cant	Fillet	Loft	Shape	Centre	Toe
W14	25 mm (5.0%)	25%	90°	N/A	Tangent	Line	Yes	0°

Figure 4.38 Winglet 14 (W14): Airfoil of 1mm thickness to resemble a line (Autodesk screen shots reprinted courtesy of Autodesk, Inc.).

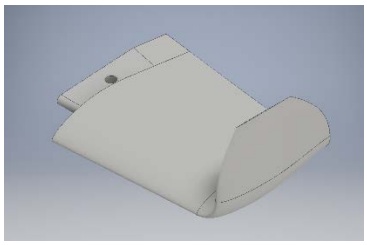

Isometric view

Left view

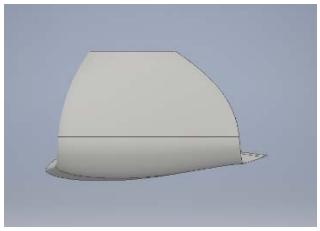

Front view

No.	Height	Radius	Cant	Fillet	Loft	Shape	Centre	Toe
W15	25 mm (5.0%)	25%	90°	N/A	Tangent	Line ½c	Yes	0°

Figure 4.39 Winglet 15 (W15): Half airfoil 1 *mm* thick positioned in line with the central axis (Autodesk screen shots reprinted courtesy of Autodesk, Inc.).

Winglet 16 (Figure 4.40) has a cant angle of 45° towards the suction side, keeping the same rotor diameter, to compare it with winglet 5 (90° cant angle) and the baseline tip 1 (T1), so that there was a middle point between no cant angle and a 'full' cant angle.

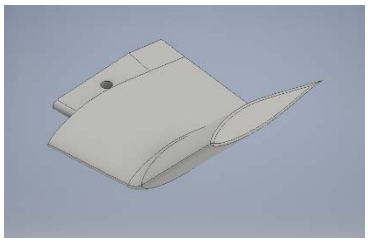

Isometric view

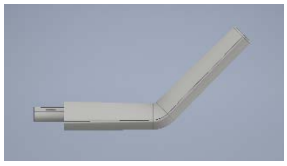

Left view

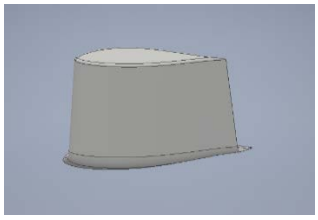

Front view

No.	Height	Radius	Cant	Fillet	Loft	Shape	Centre	Toe
W16	25 mm (5.0%)	25%	45°	0.6 mm	Free	Foil	Yes	0°

Figure 4.40 Winglet 16 (W16): 45° cant angle (Autodesk screen shots reprinted courtesy of Autodesk, Inc.).

Extension 17 (Figure 4.41) is simply a rotor extension. In principle, a bigger rotor generates more power. For this to be completely true, the whole blade should have been scaled, but to manufacture another 3 sets of blades just to prove this is not practical. Instead, the effect of extending the blade by keeping the same blade aspect ratio and parameters such as twist, is explored.

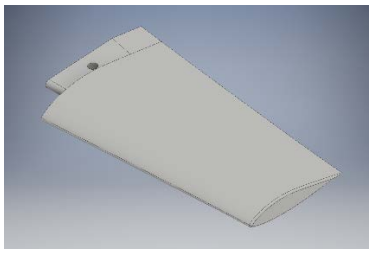

Isometric view

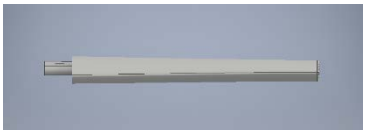

Left view

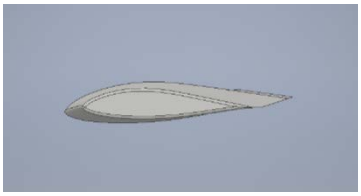

Front view

No.	Height	Radius	Cant	Fillet	Loft	Shape	Centre	Toe
E17	25 mm (5.0%)	0%	0°	0.6 mm	Free	Foil	Yes	0°

Figure 4.41 Tip extension (E17): 5.0% blade extension (Autodesk screen shots reprinted courtesy of Autodesk, Inc.).

Winglet 18 has the same characteristics as the base winglet (W5) but an inverted profile. The way it was flipped is detailed in the next section.

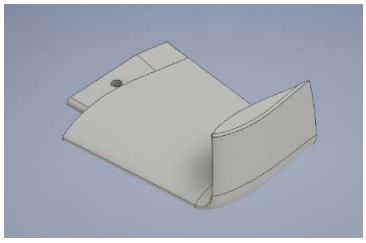

Isometric view

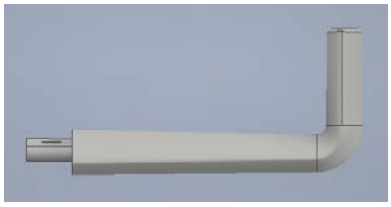

Left view

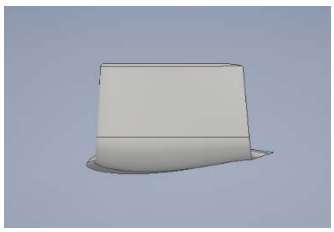

Front view

No.	Height	Radius	Cant	Fillet	Loft	Shape	Centre	Toe
W18	25 mm (5.0%)	25%	90°	0.6 mm	Free	Inv. Foil	Yes	0°

Figure 4.42 Winglet 18 (W18): Inverted airfoil (Autodesk screen shots reprinted courtesy of Autodesk, Inc.).

Winglets 19 and 20 were designed to measure the effect of the toe angle in winglets. The toe angle would be similar to a blade pitch, and it changes the angle of attack perpendicular to the flow that passes through the turbine as it rotates (Figure 4.43 and Figure 4.44). Winglet 21

incorporates an inverted airfoil shape and a toe angle, again to try and measure any effect of the airfoil orientation.

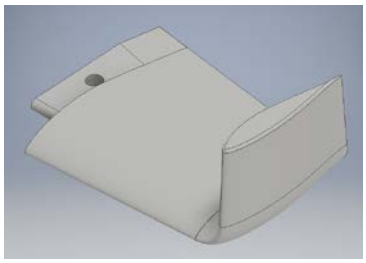

Isometric view

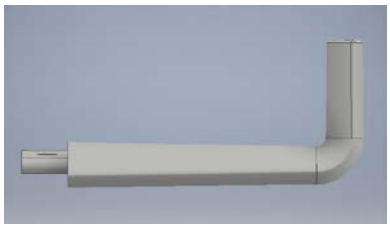

Left view

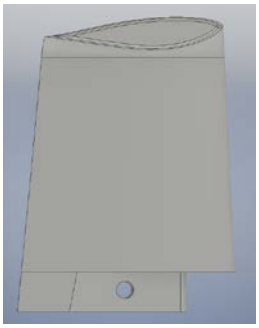

Top view

No.	Height	Radius	Cant	Fillet	Loft	Shape	Centre	Toe
W19	25 mm (5.0%)	25%	90°	0.6 mm	Free	Foil	Yes	3.5°

Figure 4.43 Winglet 19 (W19): Winglet with a 3.5° toe angle towards the centre of the turbine (Autodesk screen shots reprinted courtesy of Autodesk, Inc.).

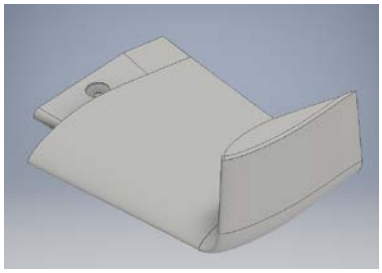

Isometric view

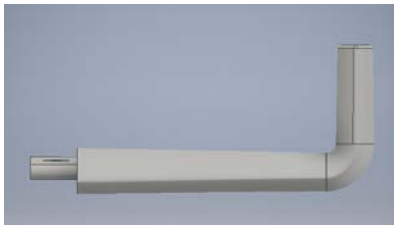

Left view

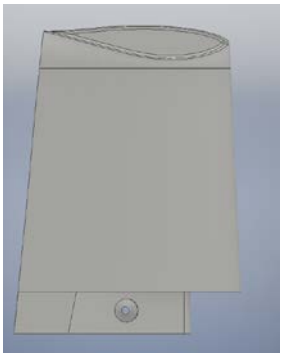

Top view

No.	Height	Radius	Cant	Fillet	Loft	Shape	Centre	Toe
W20	25 mm (5.0%)	25%	90°	0.6 mm	Free	Foil	Yes	-3.5°

Figure 4.44 Winglet 20 (W20): Winglet with a 3.5 toe angle away from the centre of the turbine (Autodesk screen shots reprinted courtesy of Autodesk, Inc.).

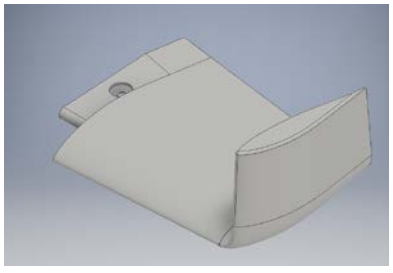

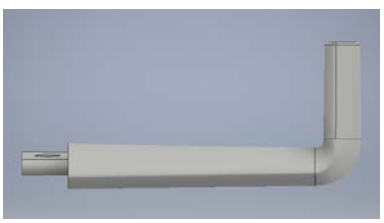

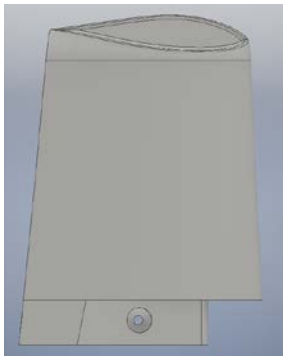

Isometric view		Left view			Top view			
No.	Height	Radius	Cant	Fillet	Loft	Shape	Centre	Toe
W21	25 mm (5.0%)	25%	90°	0.6 mm	Free	Inv. Foil	Yes	-3.5°

Figure 4.45 Winglet 21 (W21): Winglet with an inverted foil and a 3.5 toe angle out (Autodesk screen shots reprinted courtesy of Autodesk, Inc.).

4.4.1 Airfoil alignment for the inverted profile

There were two options to flip the airfoil profile for the extension of the blade that would be bent into a winglet. If the blade is bent towards the suction side, the winglet ends up with an 'inverted' profile, as seen from behind the blade. Considering that the direction of rotation, an inverted airfoil is less aerodynamic and produces more drag than if it was flipped. A solution to this is to invert the profile just at the end of the blade before bending it to produce the winglet. Figure 4.46 shows winglet 5 (W5), which is a normal extension of the blade bent towards the suction side, the airfoil is upside down. In the same figure is winglet 18 (W18) that has been flipped to correct this matter. The procedure is detailed next.

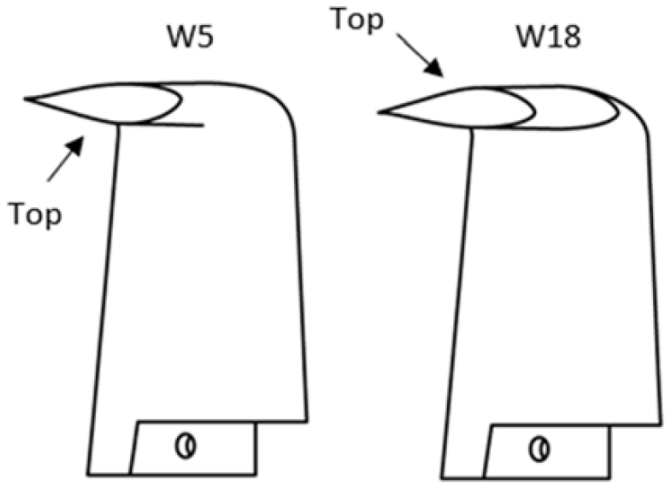

Figure 4.46 Normal and inverted airfoil bent towards the suction side to create a winglet.

Figure 4.47 shows the airfoil shape at the tip of the blade, with its centre point located at the axes' intersection. Option 1 is to align the trailing and leading edges, flipping the airfoil along the chord line and centring their inner points as shown in Figure 4.48. When the sections are joined, there is a misalignment shown in Figure 4.49.

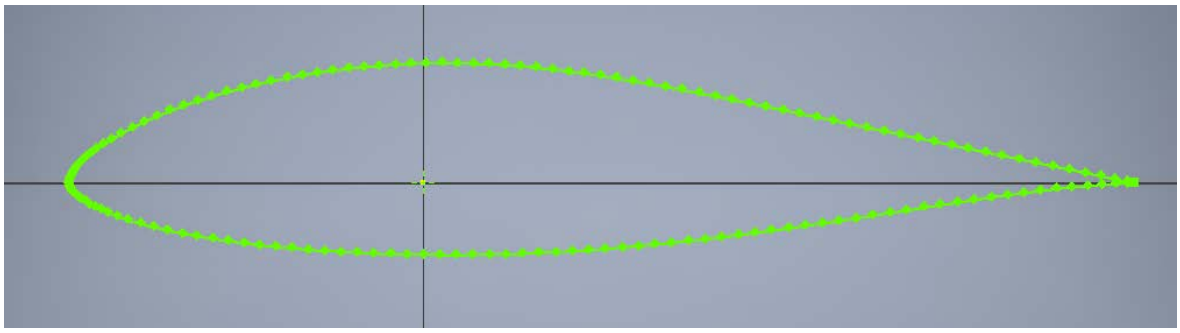

Figure 4.47 Tip profile with the centre point along the leading and trailing edge line (Autodesk screen shot reprinted courtesy of Autodesk, Inc.).

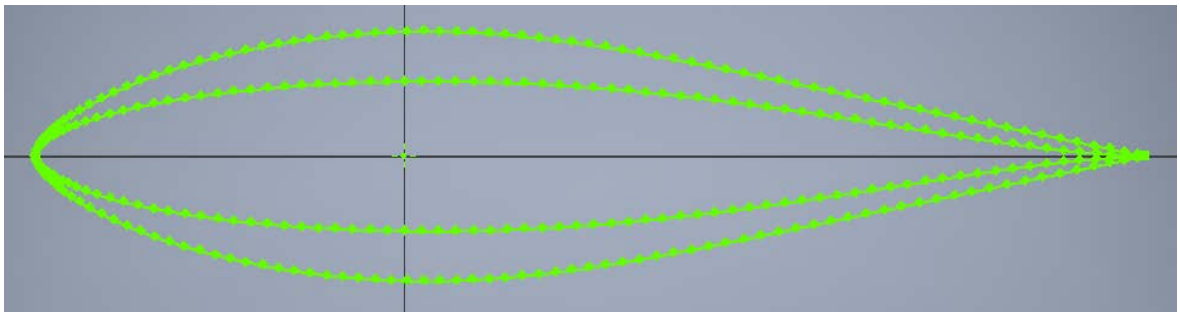

Figure 4.48 Inverted airfoils with aligned centre points (Autodesk screen shot reprinted courtesy of Autodesk, Inc.).

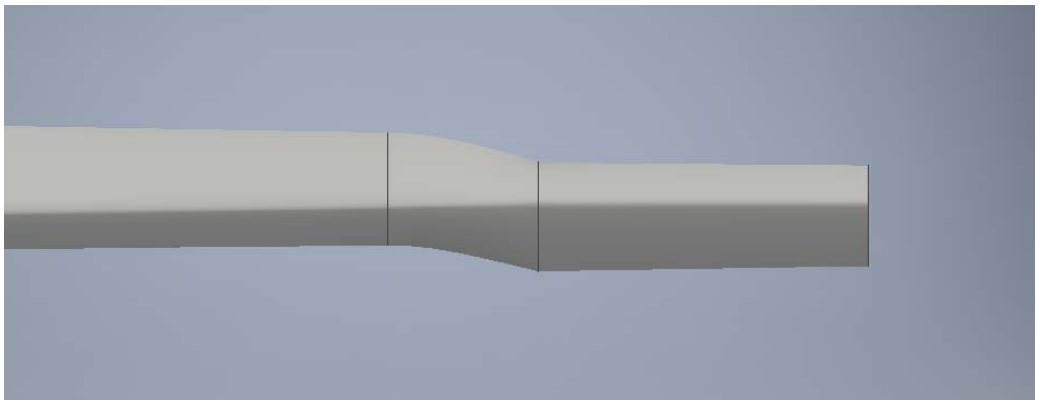

Figure 4.49 Blade extension for inverted airfoils with aligned centre points (Autodesk screen shot reprinted courtesy of Autodesk, Inc.).

The second option is to keep a fixed height along the span of the blade as shown in Figure 4.50. When both sections are joined, there is a jump from one leading edge to the other, as shown in Figure 4.51. After being bent, the joined section ends up between the beginning and the end of the curve, with the difference that a fixed height keeps the curvature radius in place as can be

observed in Figure 4.52 (Right), contrary to what happens if the centre points are aligned, resulting in what can be observed in Figure 4.52 (Left).

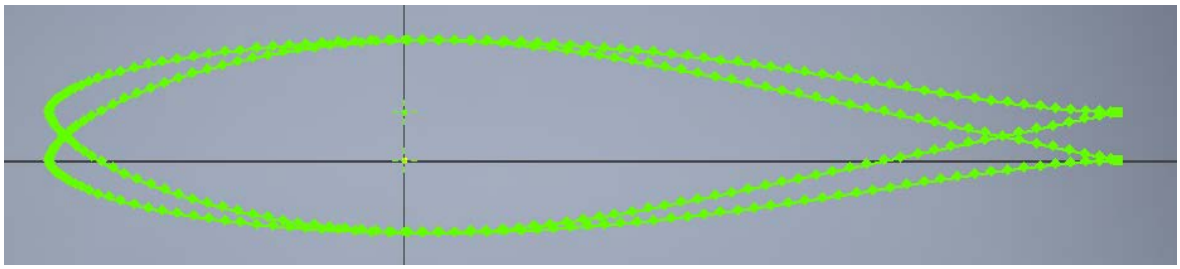

Figure 4.50 Inverted airfoils with fixed height (Autodesk screen shot reprinted courtesy of Autodesk, Inc.).

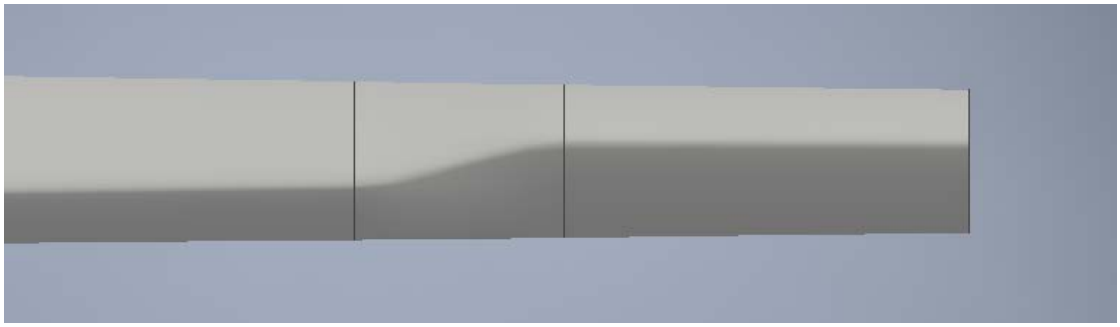

Figure 4.51 Blade extension for inverted airfoils with fixed height (Autodesk screen shot reprinted courtesy of Autodesk, Inc.).

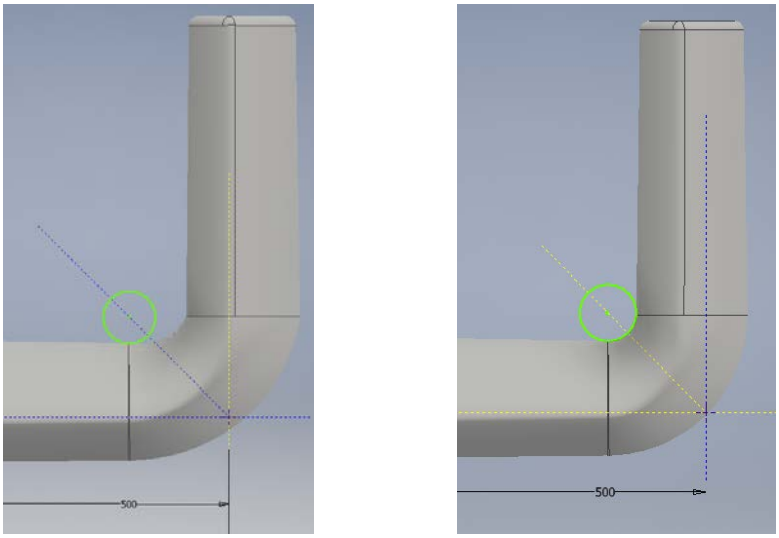

Figure 4.52 Curvature radius for aligned centre points (Left), and for fixed height (Right) (Autodesk screen shots reprinted courtesy of Autodesk, Inc.).

4.5 Gearbox and DC-motor generator efficiencies

The gearbox has a step-up ratio of 1:10 and the efficiency is estimated to be constant at 97% (Bahaj, 2013). The generator is a DC motor rated at 24 *V* and a speed of 3,000 *rpm* with an internal resistance of 50 *mΩ*. The efficiency of the generator varies as shown in Figure 4.53, with values for the straight blade at different tip speed ratios in Table 4-6. This is key to identify the peak in the power curve, although the instrumentation does not allow to record the instantaneous current and voltage delivered by the turbine during an entire run.

Table 4-6. Generator efficiency for the straight blade at given TSRs.

TSR	4.6	4.8	5.1	5.5	5.9	6.2	6.4	6.9	7.3
η_{gen}	-	38%	67%	80%	86%	90%	92%	95%	97%

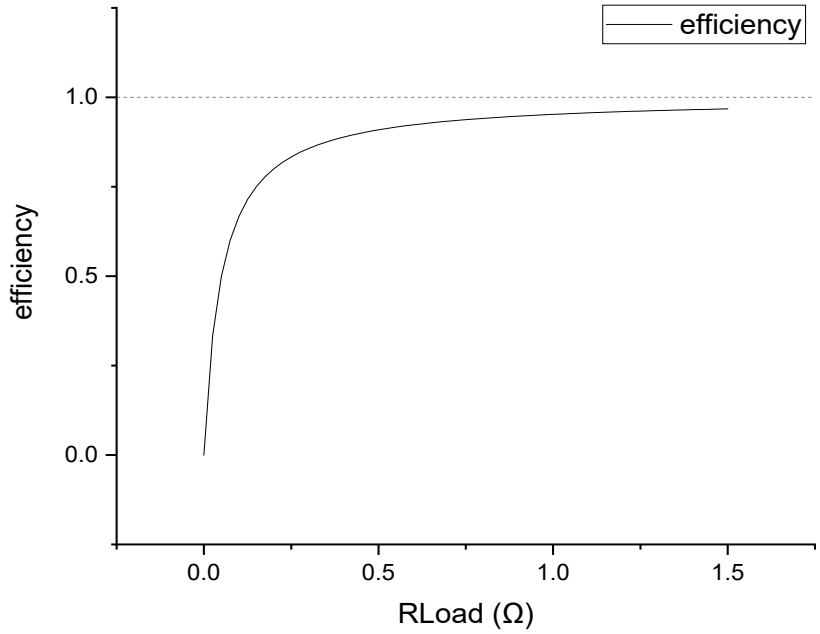

Figure 4.53 Generator efficiency vs. load resistance.

According to the maximum power transfer theorem (Figure 4.54), as the name states, for a Thevenin equivalent circuit, the maximum power dissipated in a system occurs when the load resistance matches the internal resistance of the generator, and the efficiency is of 50%. For this case, it is at around a tip speed ratio of 5.0.

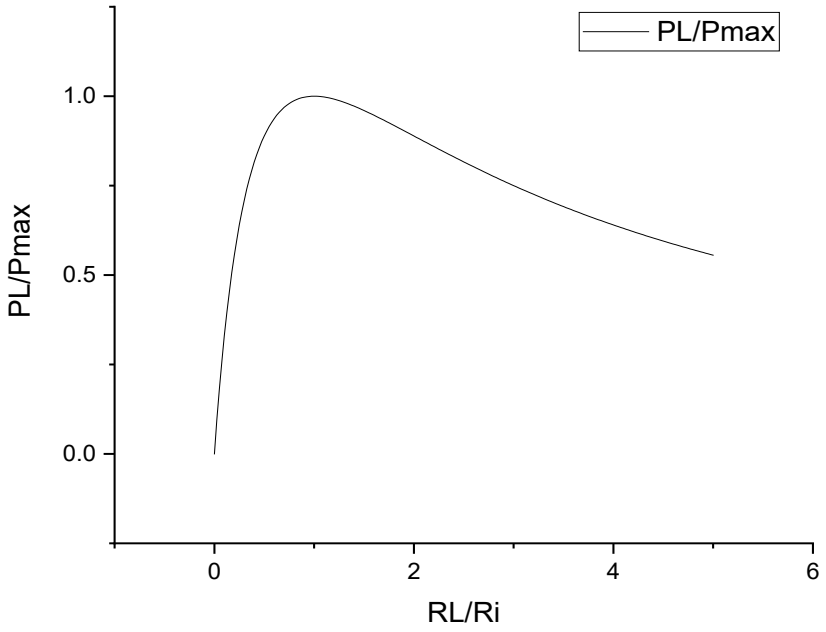

Figure 4.54 Maximum power transfer theorem.

When the load is disconnected, the turbine output is zero, because it is in short circuit, as shown in Figure 4.55 (Left). At this state, power is dissipated as heat by the internal resistance, and the turbine rotates at its lowest speed. The turbine operation occurs when the load is connected [Figure 4.55 (Centre)]. Lastly, the turbine rotates freely with an open circuit [Figure 4.55 (Right)] and reaches its maximum rotational speed when it is in equilibrium with the drag force.

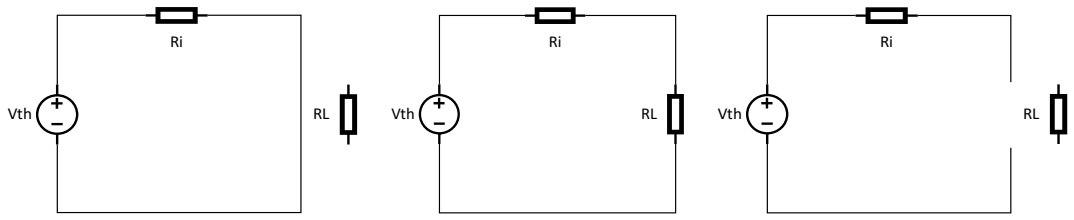

Figure 4.55 Turbine equivalent circuits. Short (Left), connected (centre), and open (Right).

4.6 Software

The thrust and torque signals were collected, filtered and amplified via a wireless telemetry system located inside the nacelle. A National Instruments® data acquisition (DAQ) box, model NI USB-6210, received the analogue signals, and passed them to a LabVIEW® program for a real-time viewing (Figure 4.56), and saved the raw data for post-processing. The power was

dissipated using a 300-W Aim-TTi LD300 Electronic Load, with a range from 0.04 to 10 Ω (0.01 Ω resolution), and a regulation of less than 2% for 90% load power change.

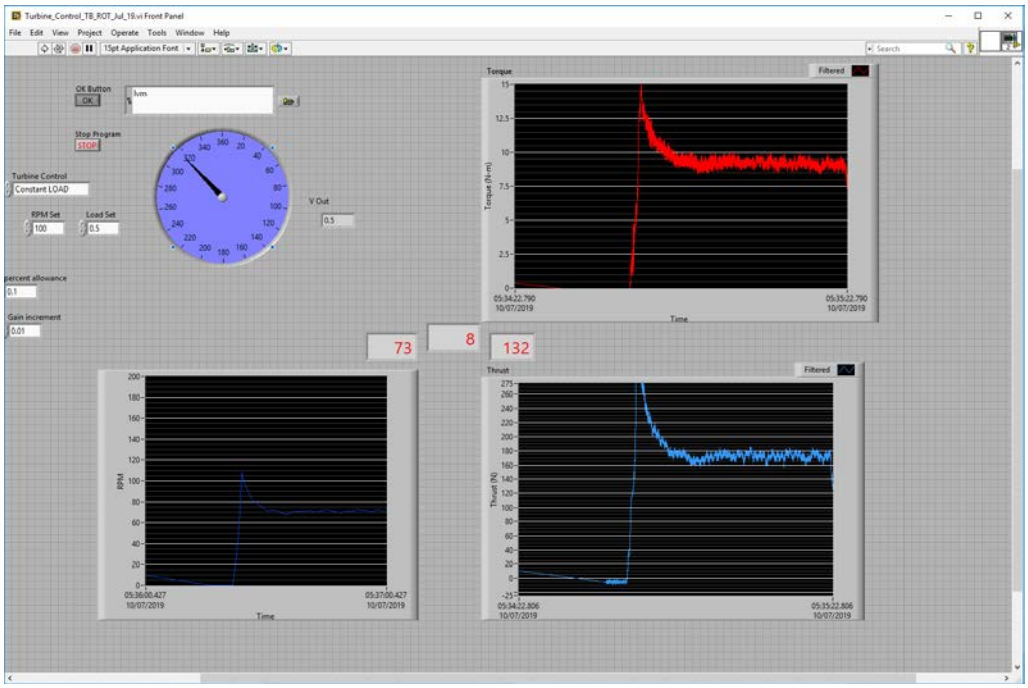

Figure 4.56 LabView screen preview of experimental runs (© 2022 National Instruments Corp.).

4.7 Calibration and uncertainty analysis

The thrust dynamometer was calibrated in the laboratory from 0 to 150 *N* at intervals of 30 *N* with a precision of 3.4 *mN*. The torque dynamometer calibration ranged from 0 to 11 *N-m* using intervals of 2.2 *N-m* measured to 0.26 *mN-m*, by hanging 0.5 *kg* weights at 0.442 ±0.001 *m* from the centre of the shaft at 0 ±1 *deg* at the plane of rotation. The zero reading for the thrust has scattered noise with a normal distribution as shown in the perpendicular histogram of Figure 4.57, with a standard deviation of ±5.77 *mV*, which represents around 1.03% of the average signal. The linear correlation has a value of 0.9999938 as shown in Figure 4.58, with a slope 227.893 *N/V*.

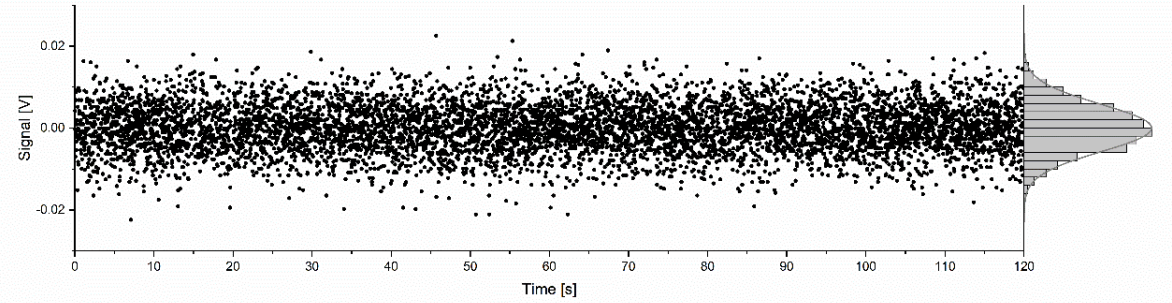

Figure 4.57 Noise in the acquisition signal.

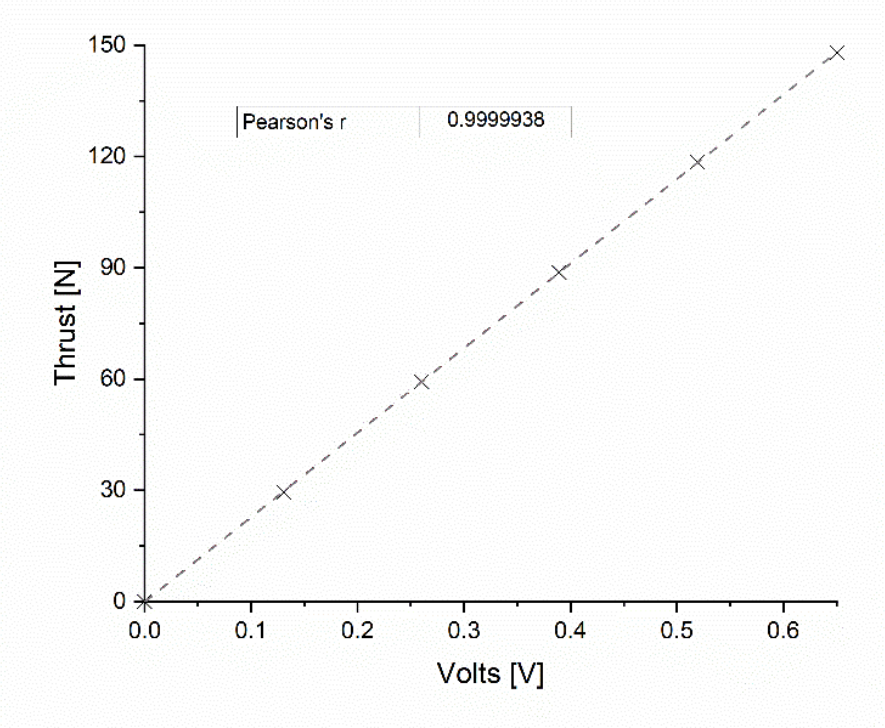

Figure 4.58 Thrust calibration.

The tank has been measured to have a velocity variation of ±0.002 m/s at 0.46 m/s (Galloway, 2013, p. 71). Additionally, the system of the carriage compensates for any additional load to keep the speed at the selected value. The variability in the angular speed at constant load for a speed of 0.85 *m/s* and 85 *rpm* was estimated by measuring 7 repeat runs (Table 4-7) with a standard deviation of 0.48 *rpm.* The variation of 0.5% agrees with the variation in the carriage speed.

Table 4-7. Repeatability runs.

Run	1	2	3	4	5	6	7
Mean rpm	84.89	83.97	85.10	85.13	85.37	84.99	85.44
Std. dev [*rpm*]	5.18	5.28	5.14	5.01	4.88	5.09	4.99
C_P	0.47	0.48	0.49	0.48	0.48	0.47	0.48
Std. dev [ ]	0.014	0.014	0.013	0.012	0.011	0.012	0.015
C_T	0.81	0.83	0.83	0.82	0.82	0.81	0.81
Std. dev [ ]	0.020	0.025	0.022	0.024	0.020	0.018	0.023

The standard deviation for the power and thrust coefficients are 1.4% and 1.2% of the mean, respectively. Precision uncertainties are added in quadrature (Gandhi *et al.*, 2019, pp. 22–24). The power is a product of the torque and angular velocity; thus, the percentage uncertainties have been added arithmetically as shown in Table 4-8.

Table 4-8 Measurement uncertainties.

	Thrust (N)	Torque (N·m)	Ω (rmp)	Power (W)
Precision uncertainty	0.8538	0.0327	0.48	0.49

Regression uncertainty	0.4311	0.0257	-	-
Total uncertainty	0.9564	0.0416	0.48	0.49
Percentage of the mean	1.29%	0.77%	0.53%	1.30%

Averaging the signal over a period of 120 s and plotting the error under a minute, the mean and the standard deviation converge with an error of less than 0.1% in just under five seconds as it can be seen in Figure 4.59. After performing the repeatability runs, it was found that the revolutions per minute (rpm) can be replicated around a predefined value with an accuracy of ±0.48(02) *rpm*.

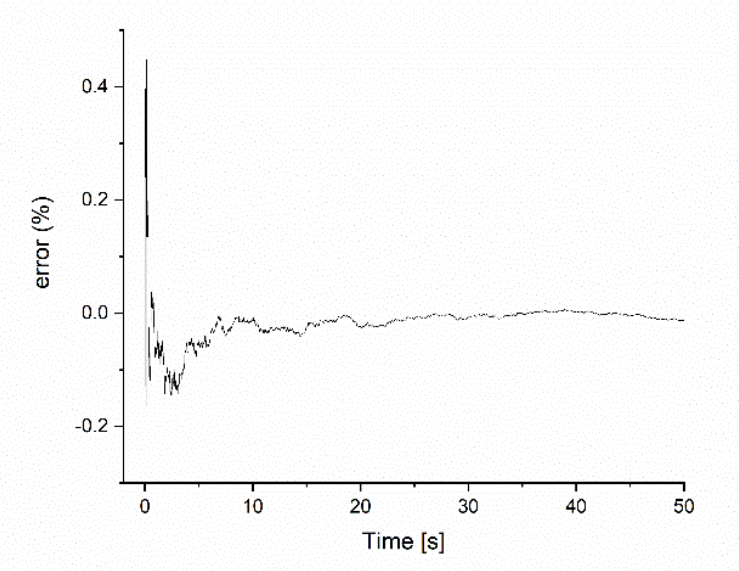

Figure 4.59 Percentage error for a sample time of 2 minutes.

4.8 Experimental set-up

Experiments were conducted at the wave/towing tank at Solent University in Southampton, UK. The tank has dimensions of 60*m* long, 3.7*m* wide and 1.8*m* deep, and a maximum carriage speed of 4 *m/s* (Figure 4.60).

Figure 4.60 View from the end of the towing tank (Solent University, 2017).

According to Du Buat's paradoxon, thrust forces can be 30% higher in a naturally turbulent environment such as a river (Muller, 2020, p. 2). The turbulence intensity in a towing tank can be considered to be close to zero (Blackmore, Batten and Bahaj, 2014, p. 9). Conditions with almost no turbulence are encountered after a long waiting time, such as at the beginning of the day when the water has been still for hours. It was seen empirically that after a waiting time of 10-15 minutes still conditions were achieved. Due to time and cost constraints, a waiting time of 4 minutes was determined as appropriate, by monitoring the fluctuations in the rotor speed. A 1-minute wait gave visible fluctuations in the speed, 2 minutes was determined to be the minimum waiting time before other corrections had to be made to the data. It took around 5 minutes per run (each data point recorded), 7 to 8 operating points were evaluated per winglet, and it took around 15 minutes to change the tips of the blades, no repeat runs were performed unless an anomaly was observed such as excessive noise on a run, equipment malfunction or significant deviation from an observed trend. To this end an inspection of all points on the performance curves for each winglet was analysed once acquired and any points of interest (for example peaks, unusual high or low values) were checked and repeated. Setting up the turbine and lowering it down took around 2-3 hours at the beginning and end of each experimental period. The turbine was towed a few runs at the beginning of the day to bring all components to an operating temperature. Under the chosen conditions, it took around 1 week per set of experiments, waiting

10-15 minutes for the tank to settle down would have meant increasing the total time of experiments 2-3 times more. One week is manageable because even though it is an intense task, it can be carried out *'non-stop'*. A usual week of experiments starts by transporting the hundreds of kilograms of devices and equipment on site which have to be assembled and disassembled at the end of the experiments. An early start of the day is mandatory, so that experiments can start as early in the day as possible, finishing late. Evenings are usually spent post processing data, debugging files or fixing technical problems. It is a very demanding endeavour both physically and mentally. It is also a very exciting and fulfilling experience, that invariably ends up depleting energy and resources. A day at one of such facilities costs thousands of pounds, and like any resource it must be optimised. The five rounds of experiments carried out would have taken months to complete, and the tank and project availability would not have been sufficient.

Another factor that was kept in mind was the blockage correction. There does not seem to be general agreement between different blockage correction models (Galloway, 2013, p. 143). A blockage correction method was used for a tidal turbine of 7.5% the cross-sectional area of the same towing tank used in this study. Finding that for a thrust coefficient of 0.8, the corrections accounted for a decrease of 8% and 5% of the power and thrust coefficient respectively (Bahaj *et al.*, 2007, p. 416).

In a towing tank environment, conditions can be controlled and measured more precisely than in real life conditions. Results will generally be ideal, and power coefficients will be higher than in normal operational conditions. On the other hand, it should be considered that higher forces can be seen by the turbine in a turbulent environment and keep that in mind for structural integrity when designing full scale devices. Towing tank experiments are practical because they allow making comparisons with slightly different conditions and identify minor changes in the results.

As seen in Section 4.2, the airfoil profiles are operating under Re numbers where the flow should have very similar conditions to the non-scaled turbine. The only other option would be to increase the rotor size (impractical as it has been seen already), because unlike for wind tunnels, it would not be possible to have a pressurised circulating flume. Operating the turbine at higher speeds could also bring Re numbers higher, but it would defy the purpose of the Froude scale. In Section 5.9, the Reynolds effect is discussed.

The turbine was placed at mid depth (Figure 4.61), in the middle of the tank (Figure 4.62).

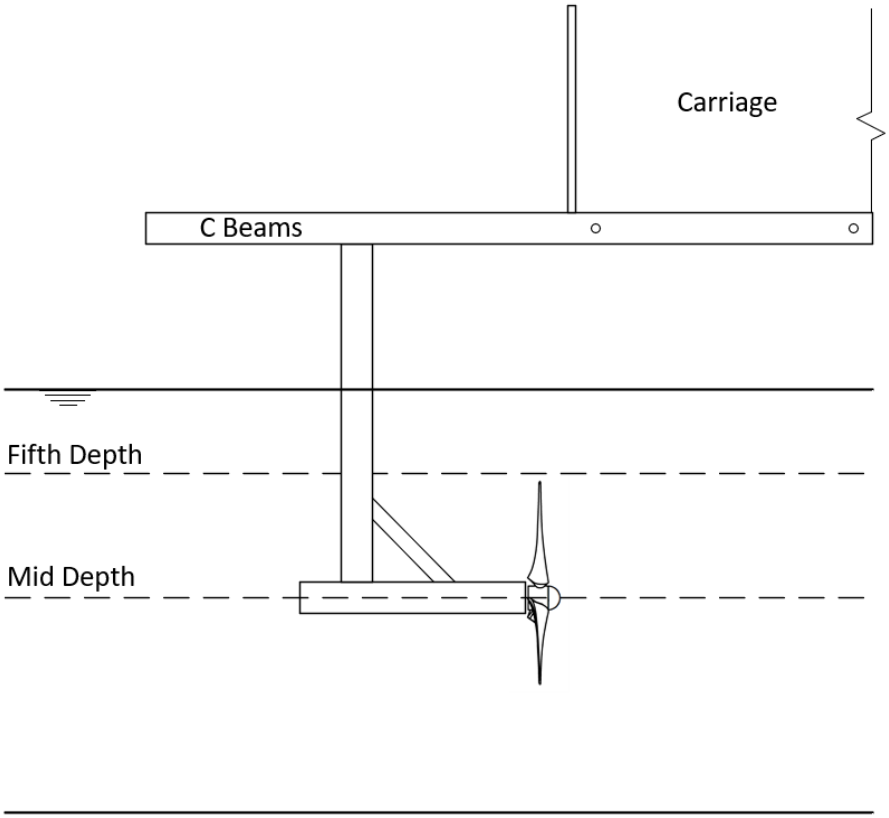

Figure 4.61 Side view of tidal turbine deployment.

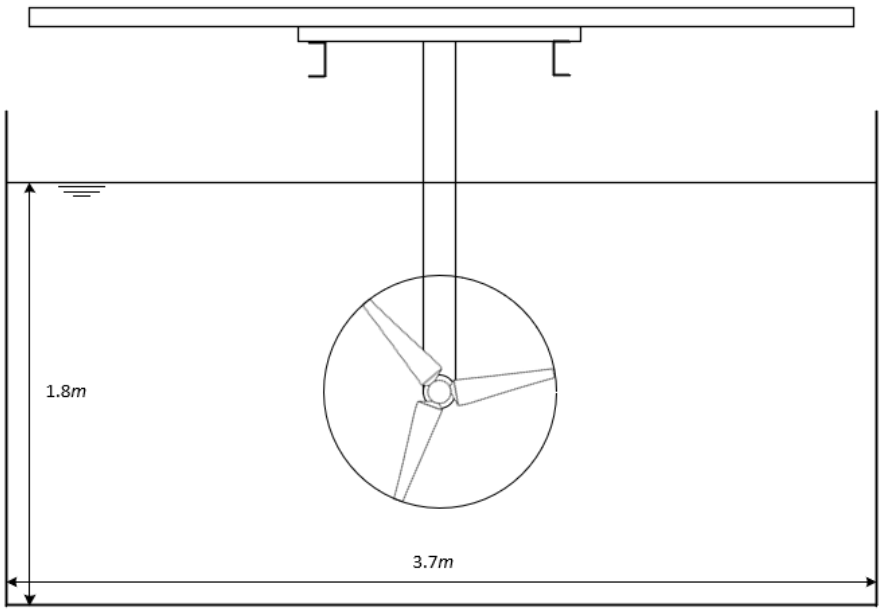

Figure 4.62 Front view of tidal turbine in the tank.

The electronic equipment was operated from the carriage with a similar layout as the one presented in Figure 4.63, consisting of the following items connected to the turbine via the umbilical cord:

1) Telemetry system: Receiving the data wirelessly directly from the shaft.
2) DAQ box: Receiving the amplified signal and feeding it to the personal computer.
3) Laptop: To visualise, record, store and process the data.
4) Electronic load: The front connection of the Aim-TTi LD300 was used with a maximum current input value of 30 *A*, maximum voltage of 80 *V*, and power of 320 *W*.
5) Power supply: Available in case the turbine did not self started, but it was not needed.
6) Compressor: To keep the turbine pressurised at 0.2 *bar* and prevent water infiltration.

Additionally, the carriage controls are located to the right of the setup, on a different bench facing the towing direction.

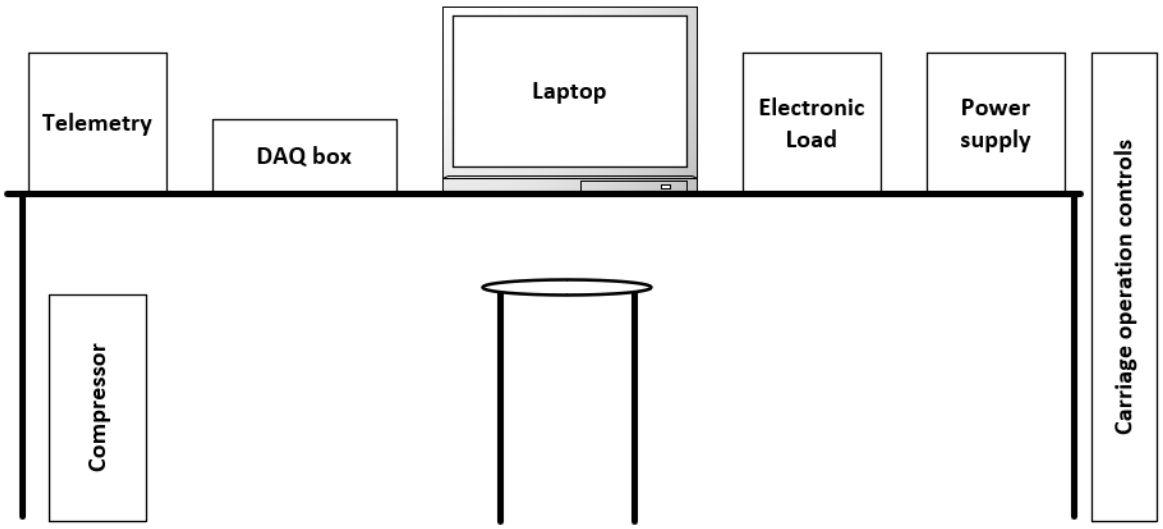

Figure 4.63 Equipment layout.

The turbine was deployed at the beginning of the day and lifted by the end of using a winch. The turbine fully assembled and ready to be deployed is shown in Figure 4.64. Each time, it took around 30 minutes to put the turbine in place. The blade and winglet interface made it easier only to pull the turbine up towards the front of the carriage just enough for the blades to come out of the water and be able to interchange the tips. This way, it was possible to change a whole set of winglets in around 15 minutes, rather than the hour it took to lift and lower the turbine completely. Pictures of the turbine with (Figure 4.65a) and without winglets (Figure 4.65b); the blade and winglet interface (Figure 4.65c); and some 3D printed winglets (Figure 4.65d).

Figure 4.64 Turbine ready to be deployed.

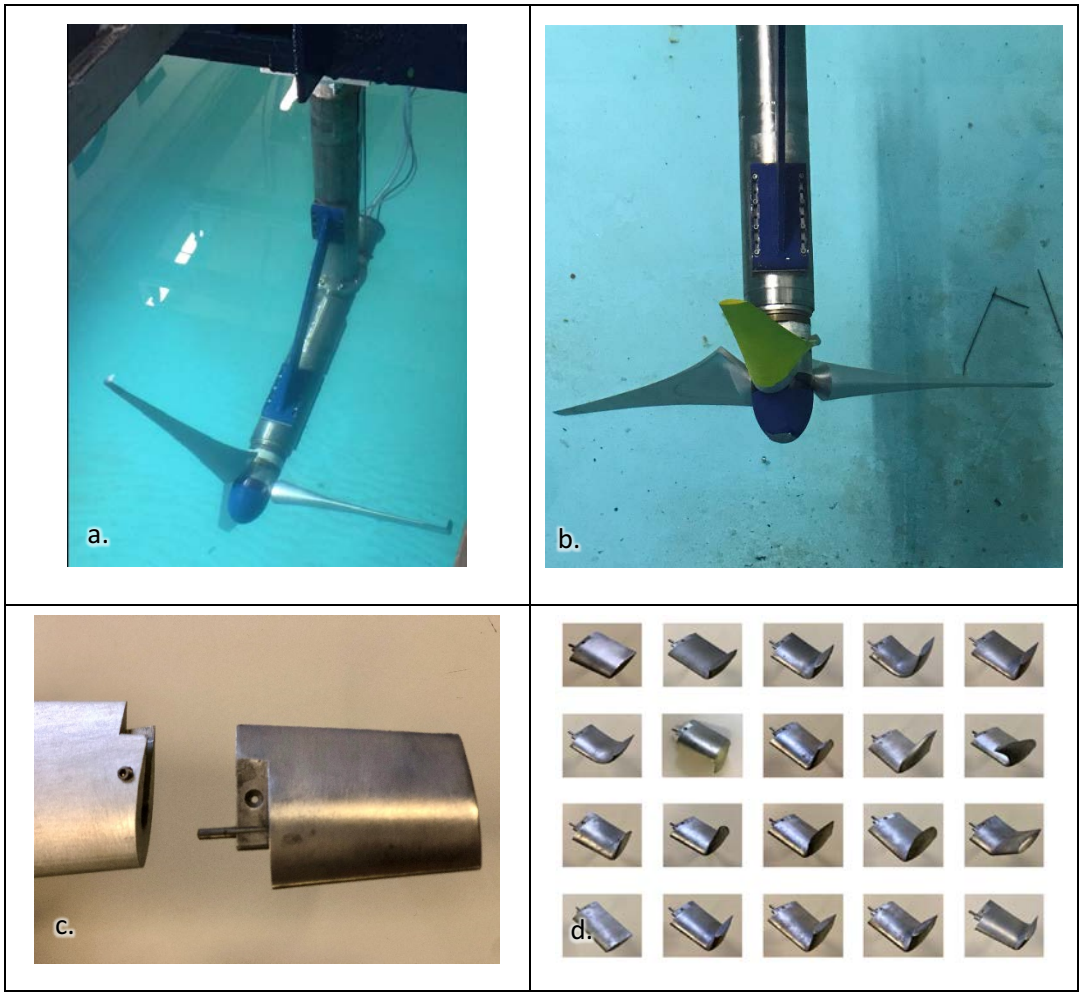

Figure 4.65 a) Turbine installed in towing tank with winglets. b) Main rotor. (c) Blade and winglet interface. (d) 3D printed winglets.

Chapter 5 Results and discussion

The experiments presented in this section are the result of 5 sets of experiments carried out both at the Solent University towing tank and at FloWave in the University of Edinburgh. Part of these results were shared as a collaborative work with two other projects. The complete details of the experimental runs can be found in Appendix B, and turbine specifications in Section 4.1. All measurements were taken with a fixed pitch angle of 0°.

5.1 Experimental process

The thrust measurement for W14 is presented as an example run. The data is unfiltered but has been calibrated as shown in Figure 5.1 with around 30 *s* of useful data per run (2,000 readings).

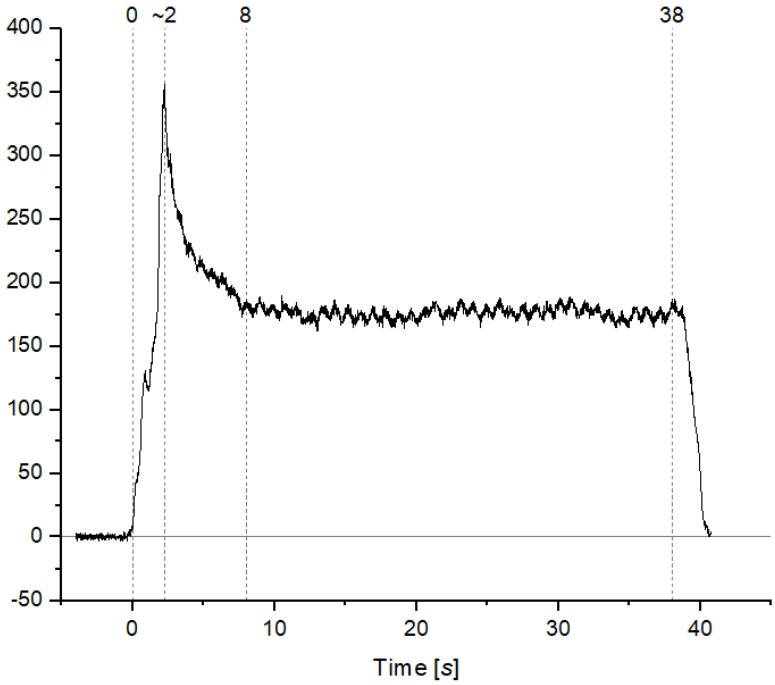

Figure 5.1 Example of a thrust recording for W14.

The run can be divided into four stages:

1. [0 to 2 *s*] Carriage starts up. Load disconnected, so the turbine starts rotating freely.
2. [2 to 8 *s*] Load is connected. The carriage reaches constant speed by that time.
3. [8 to 38 *s*] Carriage runs at desired speed. The turbine operates at constant load.
4. [38 to 40 *s*] Carriage reaches the end of the operating length and it is slowed down.

Small fluctuations can be observed during the recording, they are correlated to the turbine rotational speed as shown in Figure 5.2. If the mean is taken for both values from seconds 8 to 38,

and values are normalised with respect to each mean, the relationship can be seen in Figure 5.3. It is expected to see the thrust and torque fluctuate proportionally to the speed, as they depend on it and it is the only varying factor. The zoomed section is presented in Figure 5.4, the rpm data has been smoothed for ease of visualisation.

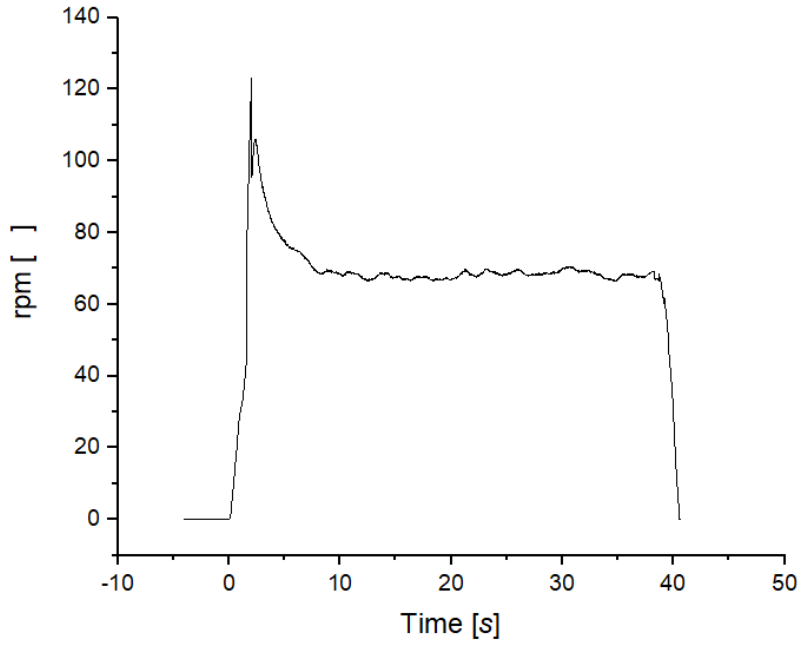

Figure 5.2 Rotational speed at around 68 rpm for W14.

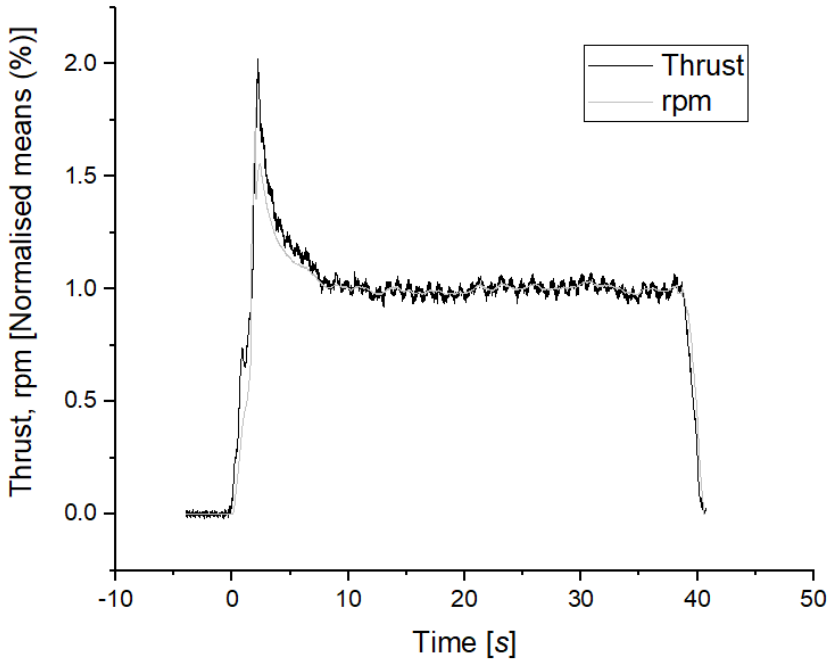

Figure 5.3 Superimposed thrust and rpm measurements with normalised means from 8 to 38 *s*.

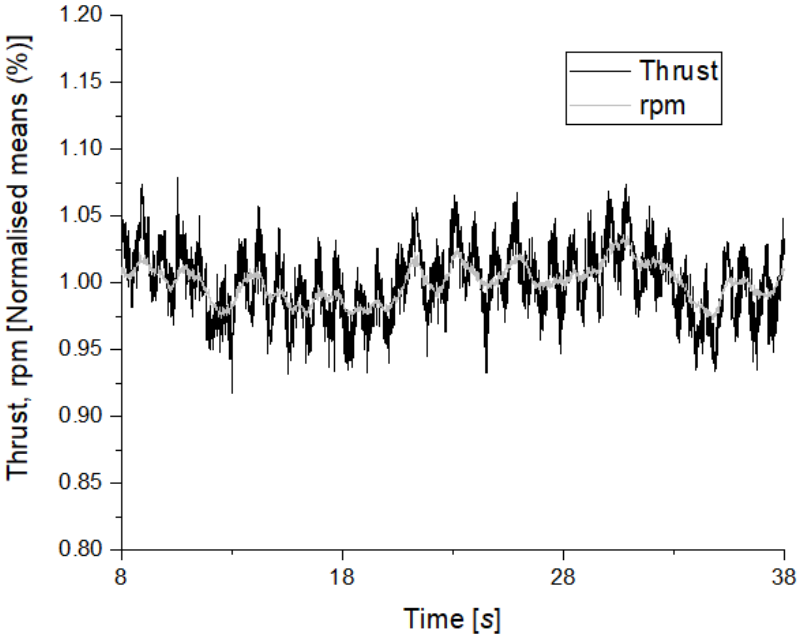

Figure 5.4 Close up of the visual correlation between the thrust and the turbine rotational speed.

5.1.1 Thrust vibration

When the fluctuations of the rotational speed are eliminated and the voltage of the thrust normalised, the variations can be seen in Figure 5.5. It is possible to identify these small fluctuations because the turbine is being towed and turbulence is almost null.

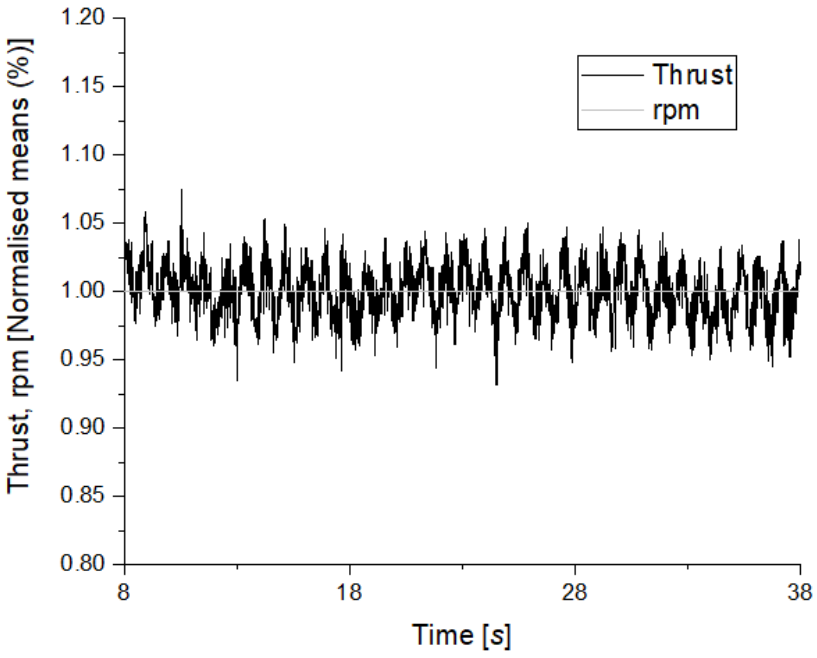

Figure 5.5 Variation of thrust with respect to constant rpm, both normalised.

Frequency is 68/60 *Hz*, corresponding to the rotational speed, and it presents a normal distribution as it can be observed in Figure 5.6. The average is 1+1.12E-15 *V* with a standard deviation of 15.7 *mV*. This vibration could be caused from the blades being unbalanced, as the manufacturing process included machining, cutting, and drilling at different stations. All from a block of aluminium which width was chosen to be the thinnest possible so that the CNC-machine time was minimum. That could have compromised precision in the alignment of the blades.

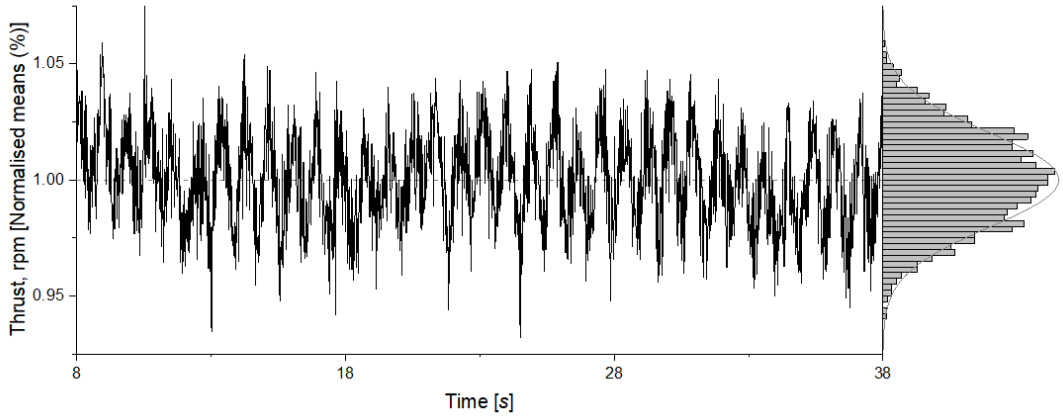

Figure 5.6 Distribution of thrust oscillations around constant rpm.

The spectral analysis of the signal shows a frequency 1.13 *Hz* present in the recording (Figure 5.7). It corresponds to the same rotational frequency of the system: $\frac{68\,rpm}{60\,sec} = 1.13\,Hz$. Such vibration is most likely product of an unbalance in the system, because that is the main cause of synchronous vibration (matching vibrating and rotational frequencies) (Adams, 2010, p. 330).

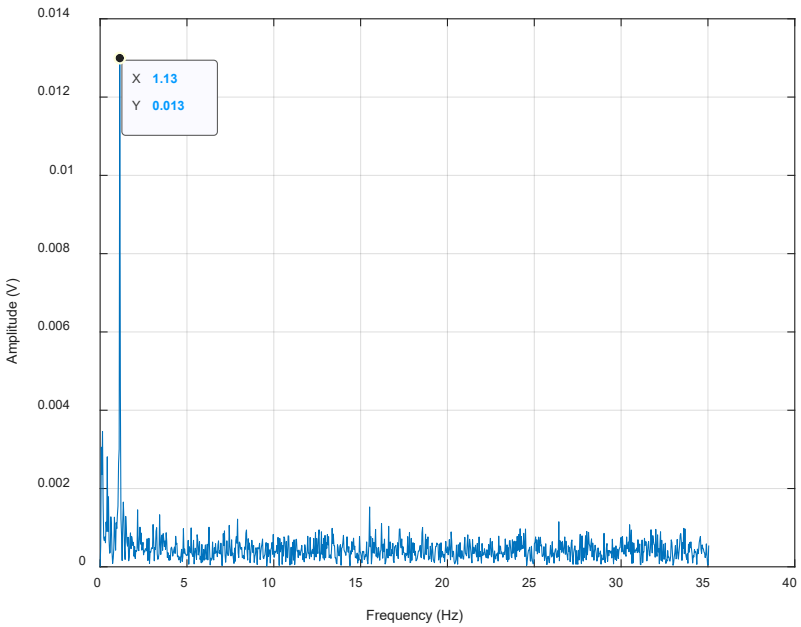

Figure 5.7 FFT of turbine thrust vibration at 68 *rpm* (© 1994-2022 The MathWorks, Inc.).

The same behaviour is found at all rotational speeds. The straight blade is chosen as it has the clearest readings, it will be evident by section 5.7 why winglets generate additional fluctuations. Figure 5.8 shows slightly more than 20 cycles equally spaced in a 15-s interval for T1 at 80.6 rpm. Normalised fluctuation here means that in addition to normalising the means, the fluctuation of the rotational speed has been eliminated to leave a clear view of the thrust variation around the rotor speed.

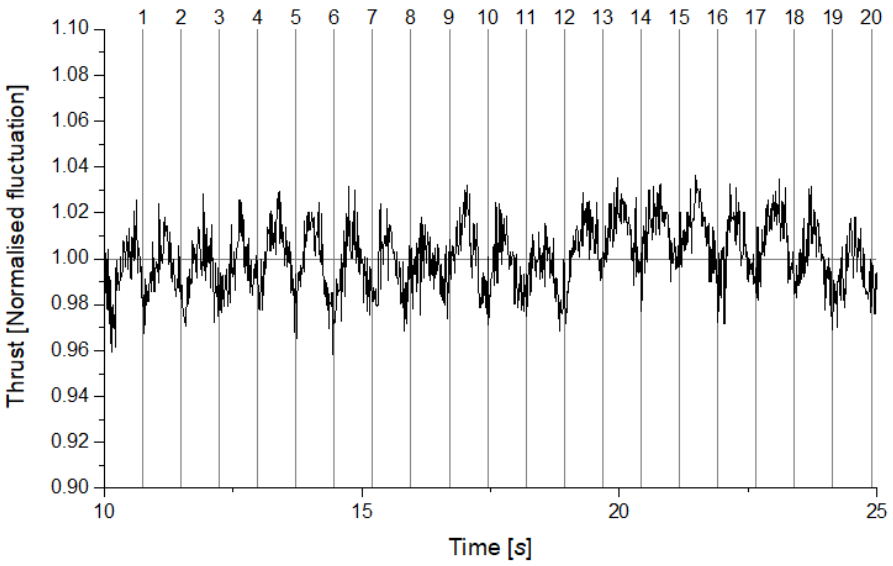

Figure 5.8 Normalised thrust fluctuation for T1 at 80.6 rpm.

The spectral analysis yields a frequency of 1.336 *Hz* (Figure 5.9), correspondent to the rotational frequency of $\frac{80.6}{60} = 1.34\ Hz$.

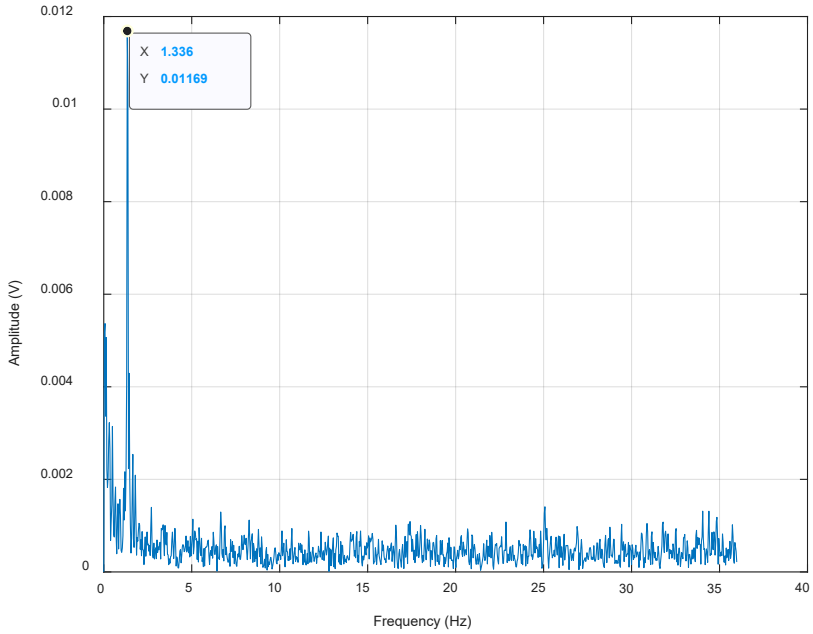

Figure 5.9 FFT of turbine thrust vibration at 80.6 *rpm* (© 1994-2022 The MathWorks, Inc.).

Readings at faster revolutions per minute have some fluctuations in rotational speed, which makes that spacing between each cycle of vibration have a different length. Figure 5.10 shows 23 cycles in a period of 15 *s* (Top) for a rotational speed of nearly 92 *rpm* and 25 fluctuations in the same period for an average speed of 100 *rpm* (Bottom).

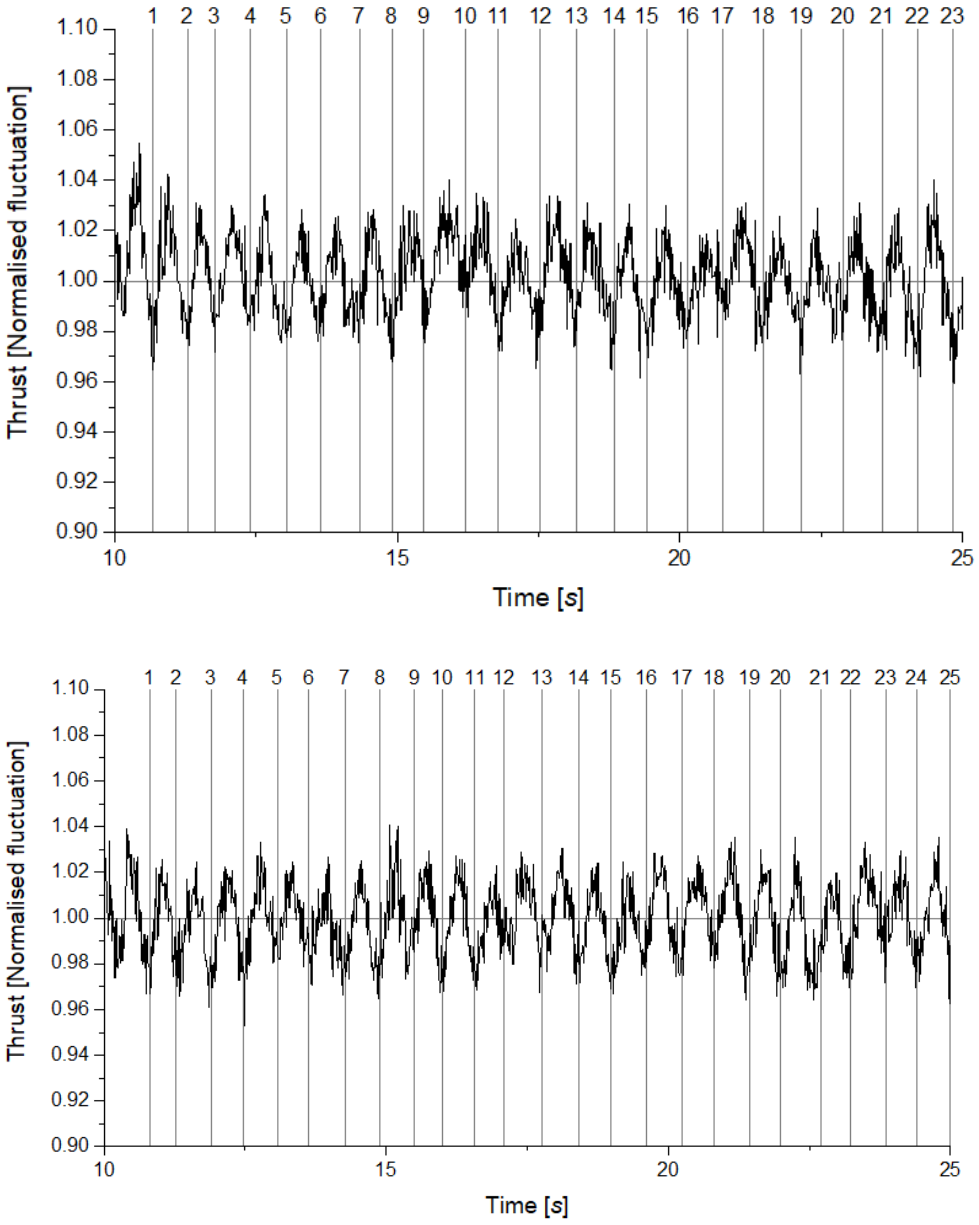

Figure 5.10 Normalised thrust fluctuations for T1 at speeds of 91.5 (Top) and 101 *rpm* (Bottom).

Figure 5.11 and Figure 5.12 show corresponding vibration frequency to rotational speeds of $\frac{91.5\ rpm}{60\ sec} = 1.52\ Hz$ and $\frac{101\ rpm}{60\ sec} = 1.68\ Hz$ respectively.

The blade position reading is taken around every 5 or 6 degrees (360°/~67 *Hz*). All torque and thrust readings are averaged to the closest full rotational speed, and in the case of the latter, that small difference is considered for the calculation.

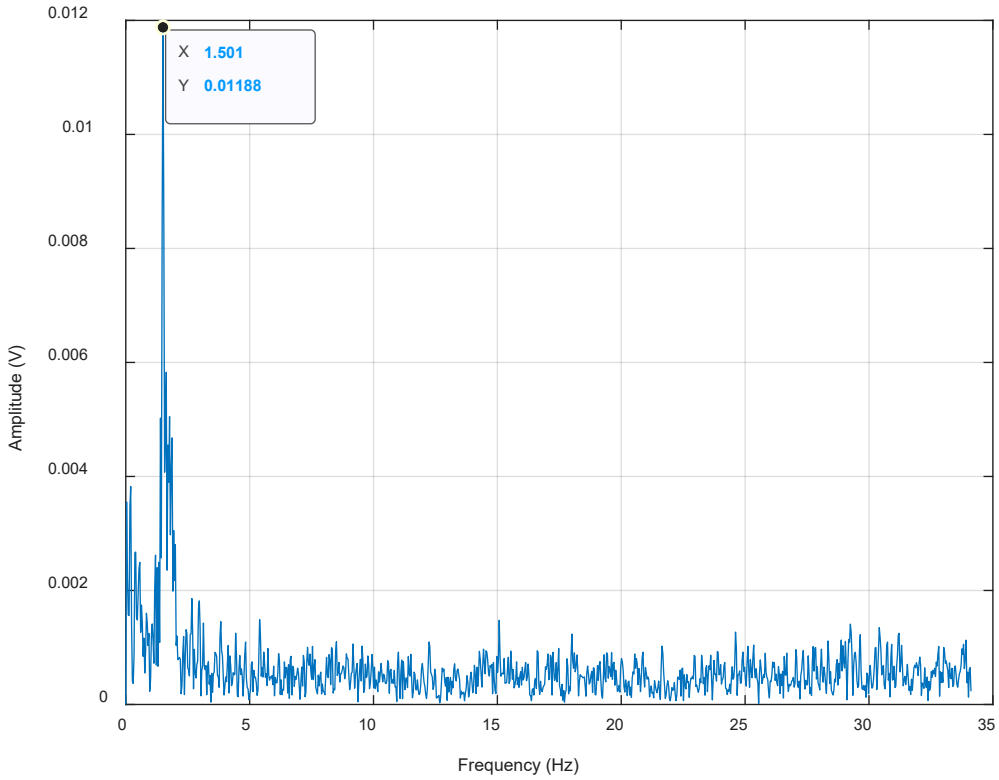

Figure 5.11 FFT of turbine thrust vibration at 91.5 *rpm* (© 1994-2022 The MathWorks, Inc.).

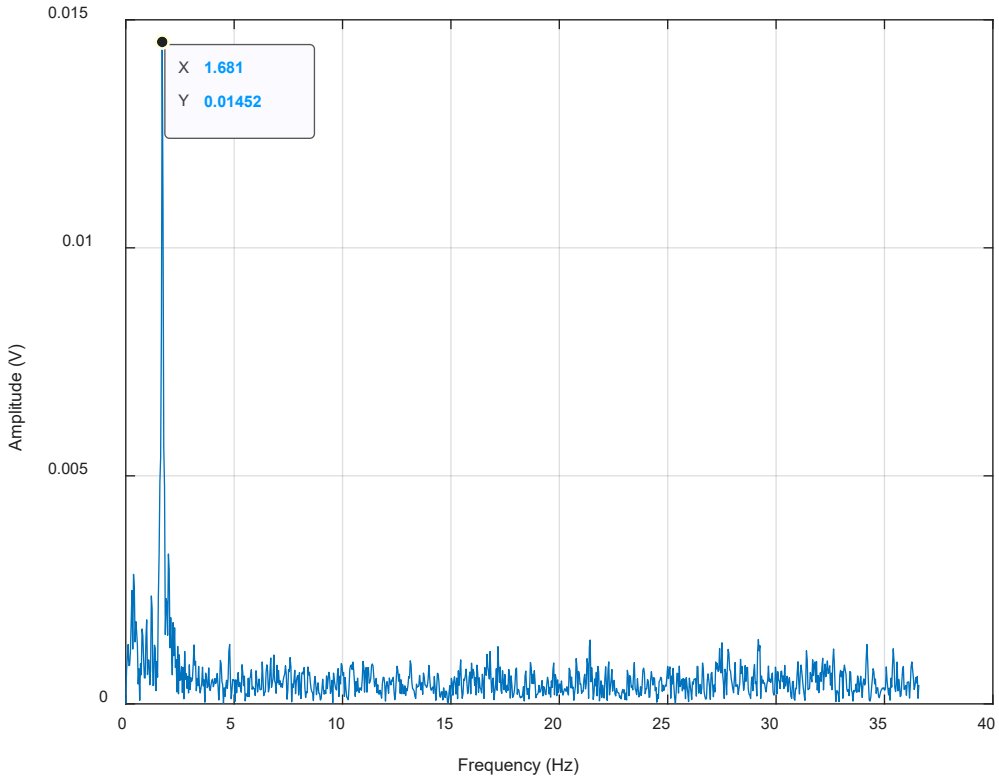

Figure 5.12 FFT of turbine thrust vibration at 101 *rpm* (© 1994-2022 The MathWorks, Inc.).

5.1.2 Torque vibration

The torque does not seem to follow the rotational speed as consistently as the thrust does, nor does there seem to be a vibrating frequency in the signal (Figure 5.13).

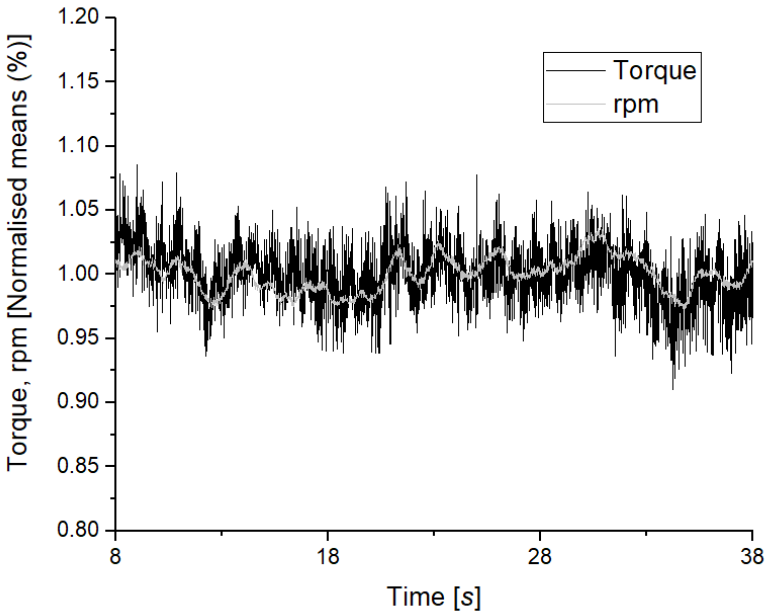

Figure 5.13 Normalised rotational speed superimposed to the normalised torque (8 to 38 *s*).

Applying the same procedure of eliminating rotational speed fluctuations and plotting the voltage variations, still there is no evident trend and it seems that the fluctuations are product of noise (Figure 5.14).

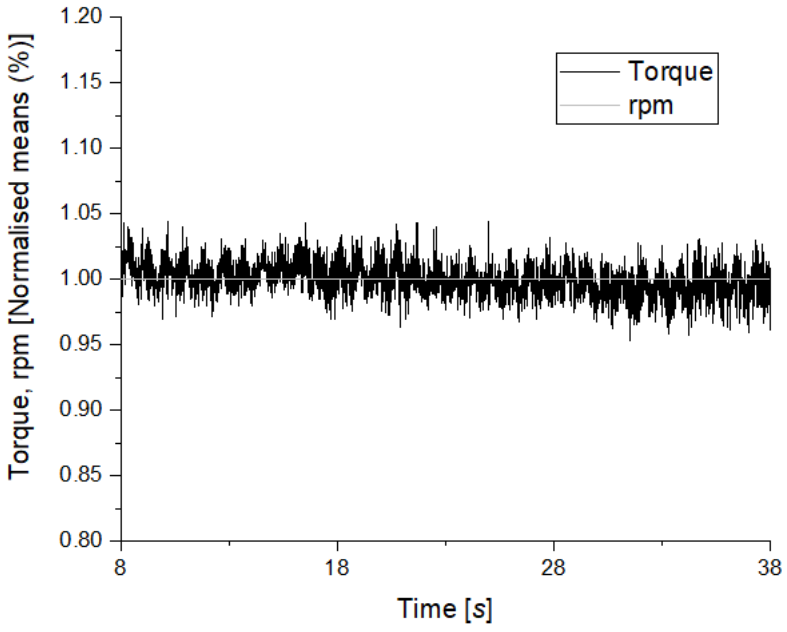

Figure 5.14 Variation of torque with respect to constant rpm, both normalised.

The average of the signal is 1+5.19E-16 *V* with a standard deviation of 14.2 *mV* (Figure 5.15).

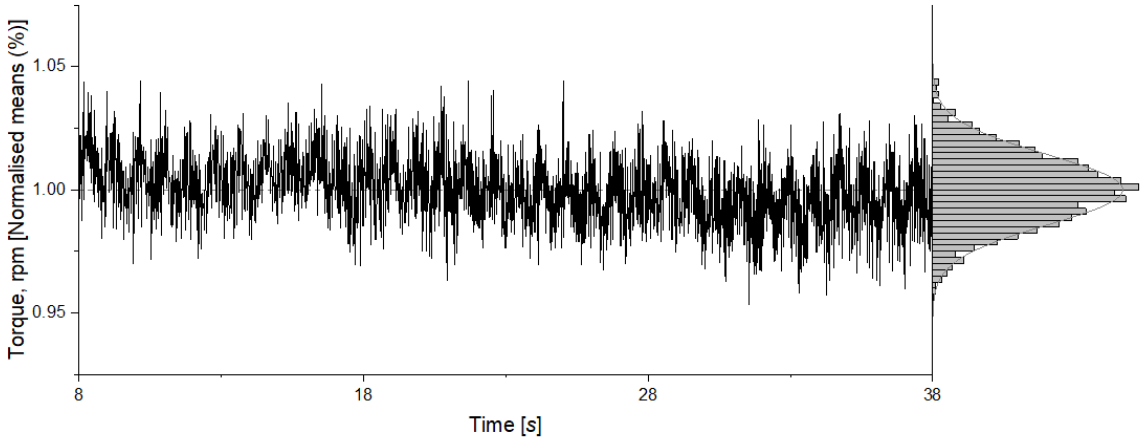

Figure 5.15 Distribution of torque oscillations around constant rpm.

The spectral analysis of the signal does show the synchronous frequency of 1.13 *Hz*, corresponding to the frequency of the rotational speed $\left(\frac{68\ rpm}{60\ sec}\right)$. More interestingly, it shows 3 additional frequencies, a lower one and two higher ones (Figure 5.16).

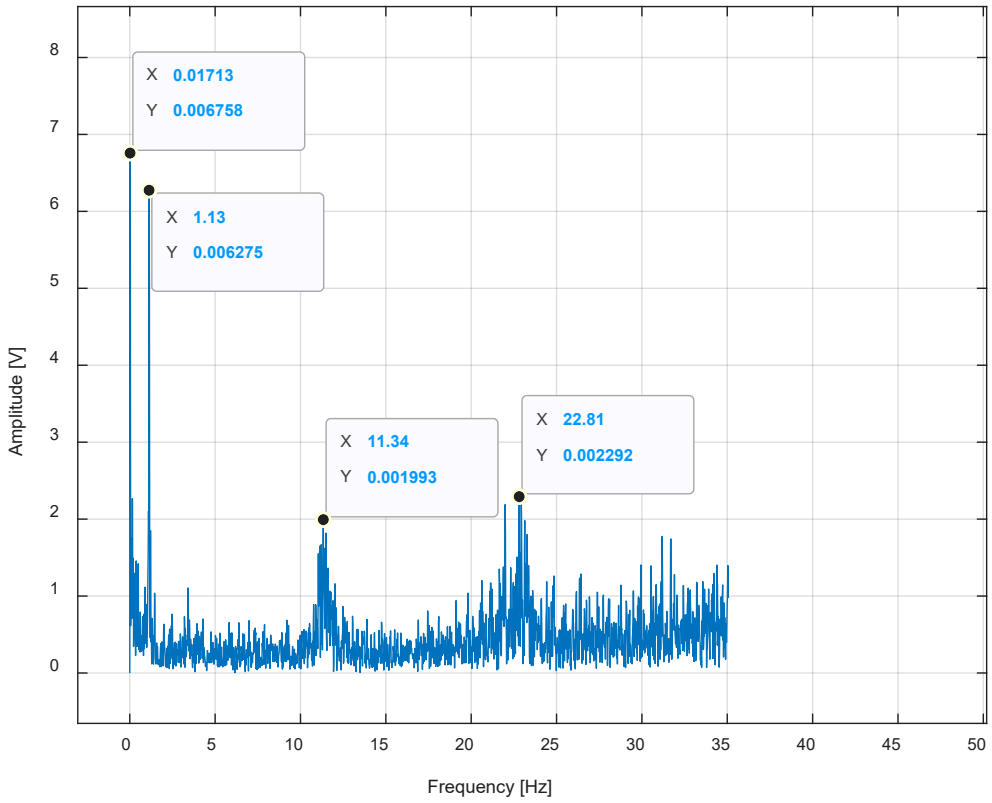

Figure 5.16 FFT of turbine torque vibration at 68 rpm (© 1994-2022 The MathWorks, Inc.).

The first frequency from left to right is a lower frequency than the turbine vibration, which suggests that it comes from a bigger system. Its period is around 58 *s* $\left(\frac{1}{0.01713}\right)$, so only half a wavelength would be seen in the 40 tow run (Figure 5.17).

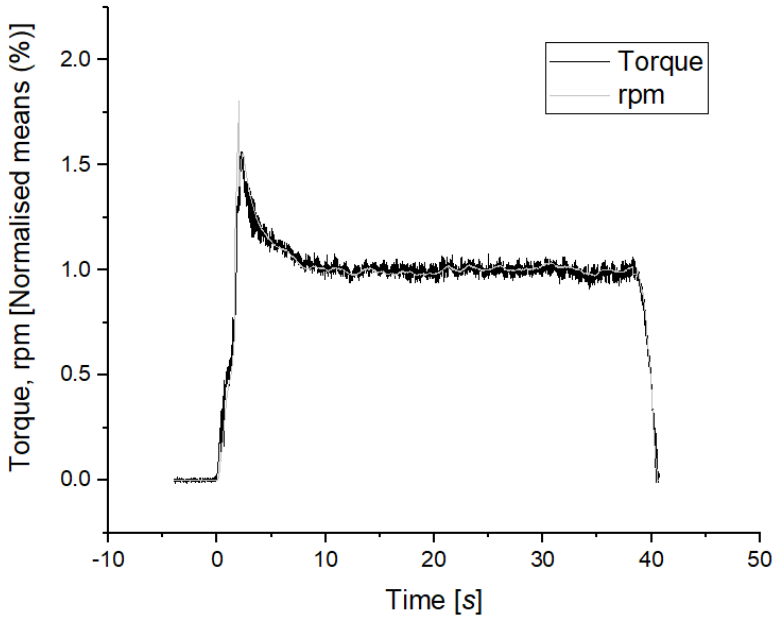

Figure 5.17 Superimposed torque and rpm measurements with normalised means from 8 to 38 *s*.

In a closer look at the run, it can be seen that before the 5 *s* mark, the torque signal seems to be slightly under the rpm one. From 5 to 25 *s* above, and again after the 25 *s* mark, the signal is below (Figure 5.18). This behaviour could be attributed to the carriage, because after acceleration, the load is connected, the turbine slows down, and the rpms stabilise, but the low frequency could have a damping behaviour rather than appearing as a cyclic load.

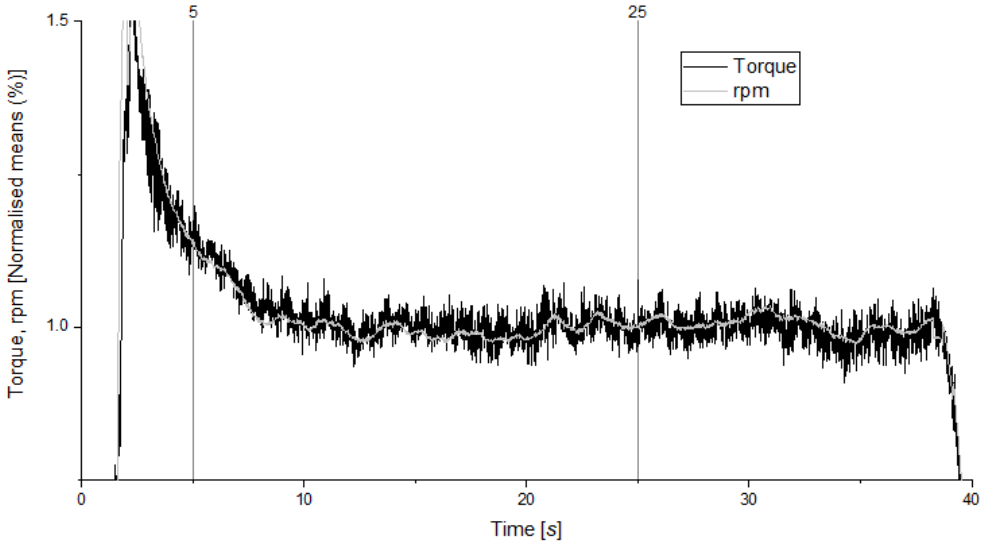

Figure 5.18 Close up of the normalised rotational speed superimposed to the normalised torque.

The higher frequencies to the right of the base frequency are in multiples of 10, and most likely a by-product of the synchronous frequency, because integer multiples from the original frequency also appear in unbalanced systems (Adams, 2010, p. 330). All are also present at 80.6 *rpm* (Figure 5.19), 91.5 *rpm* (Figure 5.20), and 101 *rpm* (Figure 5.21).

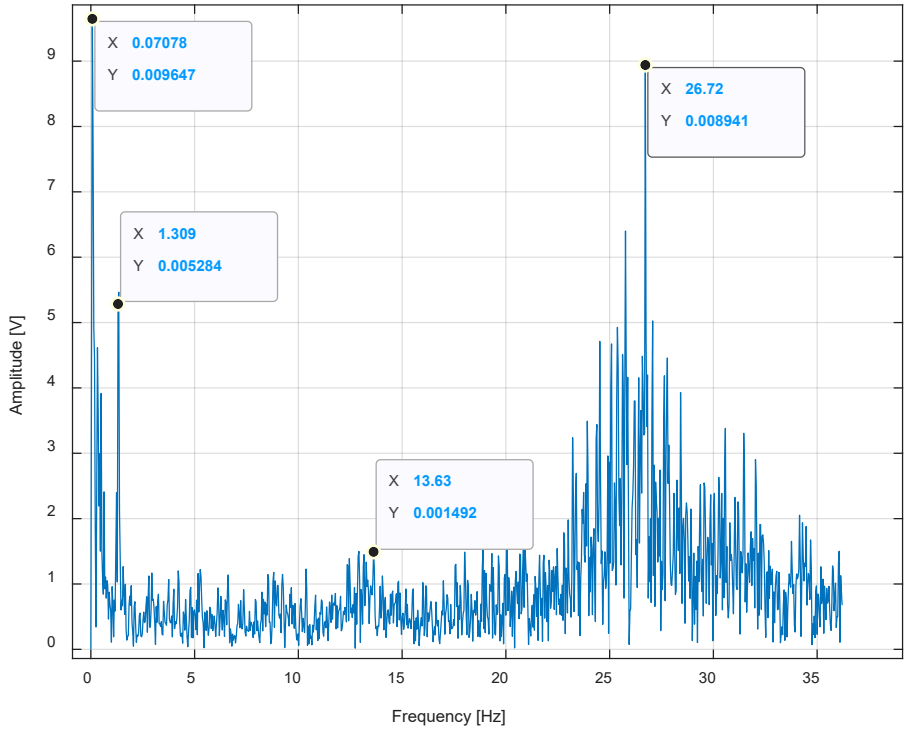

Figure 5.19 FFT of turbine torque vibration at 80.6 *rpm* (© 1994-2022 The MathWorks, Inc.).

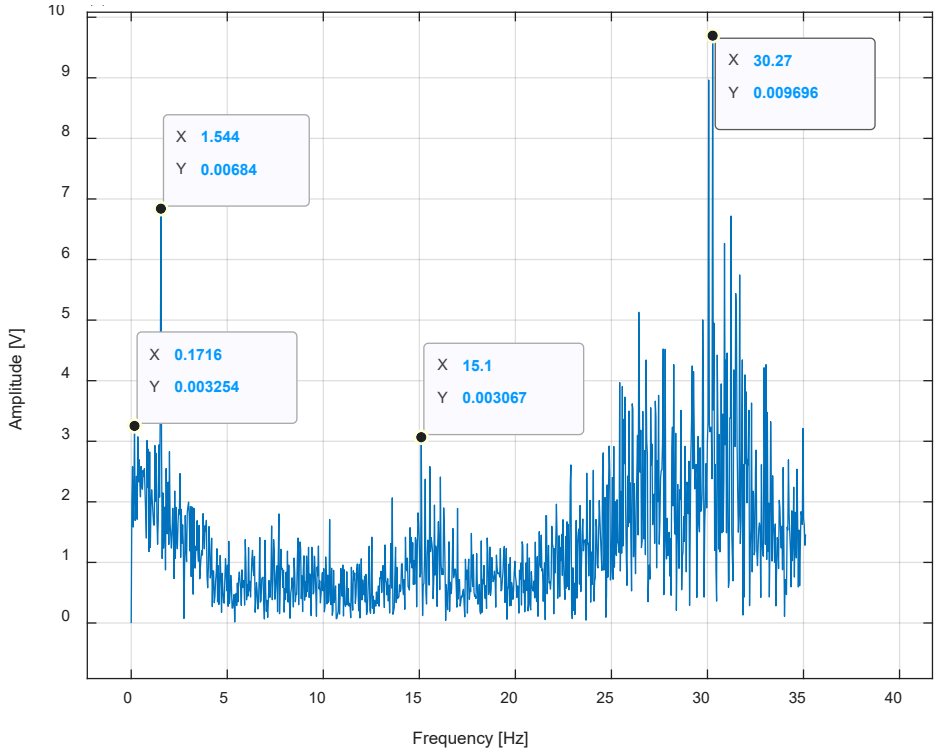

Figure 5.20 FFT of turbine torque vibration at 91.5 *rpm* (© 1994-2022 The MathWorks, Inc.).

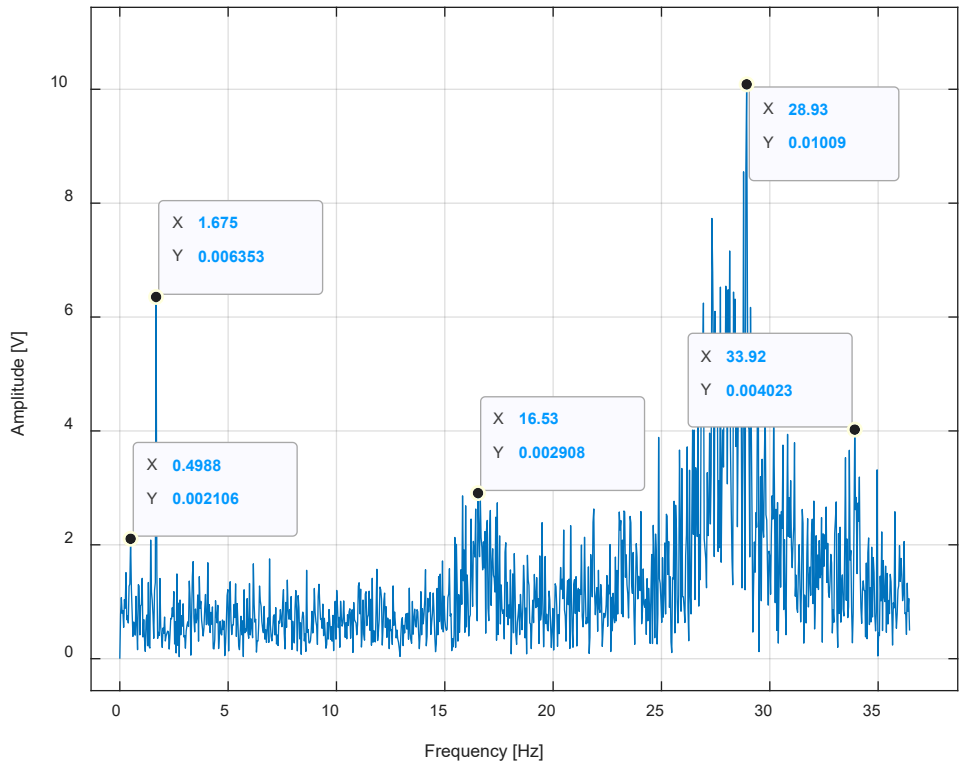

Figure 5.21 FFT of turbine torque vibration at 101 *rpm* (© 1994-2022 The MathWorks, Inc.).

5.2 Baseline C_P and C_T curves

The 1-m diameter turbine is a 1:20 scaled version of the 2-MW SIMEC Atlantis Energy AR2000. All other measurements are compared across groups of winglets, and eventually against the performance of the unmodified tidal turbine, with tips instead of winglets (T1). Figure 5.22 shows the thrust and power coefficient curves against tip speed ratio, at a towing speed of 0.76 *m/s*. The C_P reaches its peak above 0.45 at around a TSR of 5.0, according with the calculations for the maximum power transfer theorem (Section 4.5),with an average value of 0.42 for the range presented. Values for the CT go from 0.74 to 0.80, averaging 0.78.

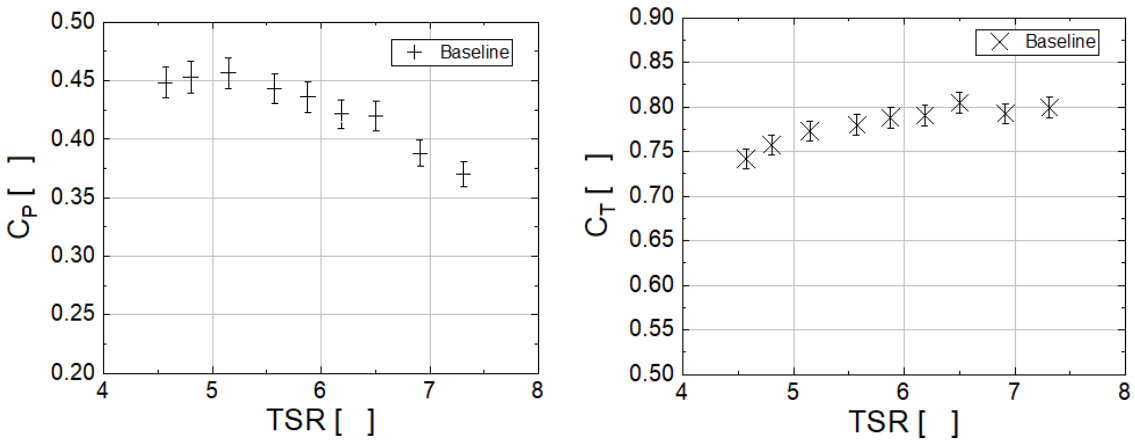

Figure 5.22 C_P and C_T curves for the unmodified blades (T1).

It can be seen in Figure 5.23 that the turbine performed better than predicted by the simulation. On average, the computer simulation underpredicted in 4% percent the power coefficient, and as much as 7% around the peak value, between tip speed ratios of 4.5 to 5.5. The thrust coefficient looks very similar. In fact, it was just under predicted by 1% on average.

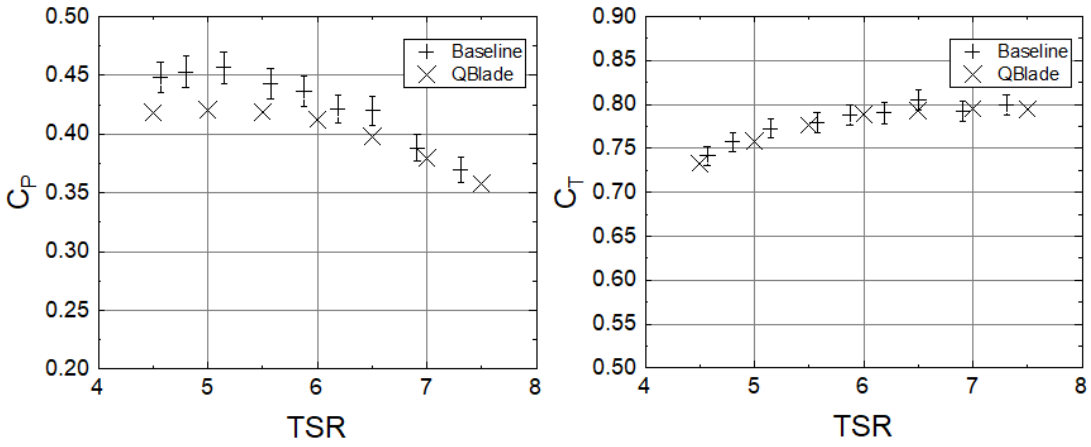

Figure 5.23 C_P and C_T curves vs TSR comparing the baseline versus the QBlade simulation

The 20 different winglets were designed changing the variables presented in subsection 2.6, which made possible to make the following main comparisons:

1. Height. Winglets W2, W3 and W4 vary in height keeping other variables the same.
2. Radius. W3, W5 and W6 have different curvature radius.
3. Cant angle. W5 and W7 are facing to opposite sides of the turbine.

Other comparisons were intended to be made, and will be examined later, while the variety of designs made possible to compare other details that emerged from unexpected results.

Winglets were designed at the end of 2017, and 3D printed in 2018. Most studies between 2006 and 2017 (Summarised in Table 2-2, page 40) suggested that winglets for wind and tidal turbines up to 10% height improve power output. Half of around 10 main authors studied in that same period do not include a curvature radius in their studies, *i.e.* a curvature radius of 0. The others use values of up to 50% curvature radius and only one suggests a value of around 100%, with a median of 25%. In terms of cant angle, most authors favour a cant angle of 90° (towards the suction side), one favours winglets facing both sides and just one predicts numerically that winglets facing the pressure side increase the overall power output.

For such reasons, the main winglet around which other winglet parameters are varied is W5 with a height of 5%, a curvature radius of 25% (relative to winglet height), and a cant angle of 90°, meaning that it is orientated in the same direction of the flow towards the suction side.

5.3 Height

The first three winglets were designed to compare the height effect in the power and thrust performance of the turbine. The chosen heights were 2.5%, 5% and 10%, all within the range of what previous literature suggested. They were distributed using a *'binary search'* approach where each value is double the previous, instead of an even distribution, to study if their effect was equally increased. The desired curvature radius for them was 25%, but W2 is so small that the radius would have been thinner than the airfoil width, so a fixed value of 50% was chosen. Figure 5.24 shows a side view of the three winglets. Cant angle is set at 90° (suction side), sweep, toe and twist are all at 0°. Blade length was always kept at 500 *mm*.

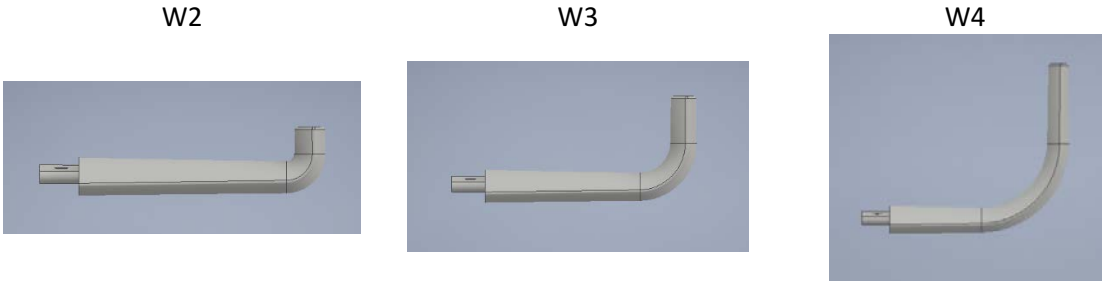

Figure 5.24 Side view of winglets with different height and same relative radius (Autodesk screen shots reprinted courtesy of Autodesk, Inc.).

Winglet 2 has the shortest height and it is expected to have the least impact on performance of the three. Figure 5.25 (Left) the C_P curve with an average value of 0.40 for W2 and 0.35 for W3, so it would be expected that W4 had the worst performance of the three, but it is not the case as it raises back to 0.38. W4 starts performing similarly to W3 from a TSR of 4.5 to slightly more than 5.0, between W2 and W3 after that and before a TSR of 6.0, then for two consecutive readings has the best performance of all between a TSR of 6.0 and 7.0, to end with a similar trend as W2 from a TSR of 7.0.

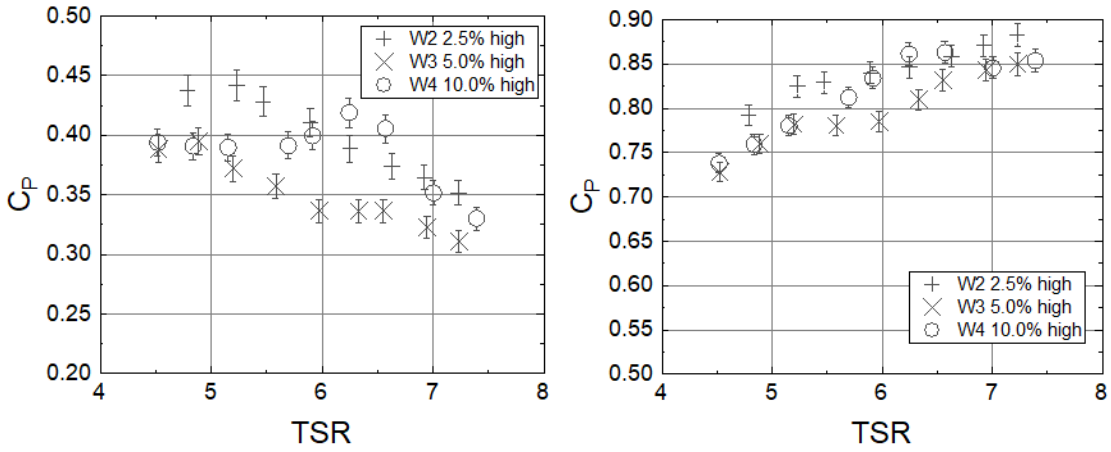

Figure 5.25 C_P and C_T curves vs TSR comparing height between W2, W3, and W4.

Thrust coefficient behaves differently, it increases together with the rotational speed, and it would be expected than taller winglets increased the value in proportion. It can be seen in Figure 5.25 (Right) that W2 induced the highest thrust coefficient with an average of 0.84, despite being the smallest winglet. Thrust from W3 is 0.80 on average, but a similar effect happened with W4 where there is no further reduction, rather it seems to go back up to 0.82, in the same way it happened with the power coefficient, with a peak between TSRs of 6.0 and 7.0.

As it was previously stated, the usual way of measuring the curvature radius is relative to the winglet height, which in practice makes two variables change at once. The varied designs of the winglets made possible to compare this trait alone. W5 has the same height as W3 and the same absolute curvature radius as W2 as can be seen in Figure 5.26.

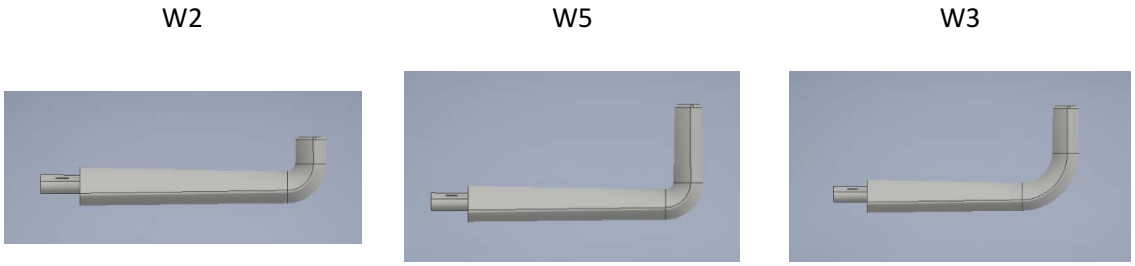

Figure 5.26 Winglets W2 and W5 with the same curvature radius and W3 and W5 same height (Autodesk screen shots reprinted courtesy of Autodesk, Inc.).

In Figure 5.27, performance of W3 and W5 is compared. Power and thrust coefficients are 0.35 and 0.79 for W3 respectively, and 0.36 and 0.80 for W5, which suggests that a smaller curvature radius makes the winglet perform better. Another point can be highlighted, comparing Figure 5.27 and Figure 5.25, it can be noted that winglets with more than 5% height and curvature radius of 50%, tend to reduce the turbine rotational speed for a set inflow velocity, reduce the power coefficient, and at the same time reduce the thrust, which suggests that the dominant force induced by them is not the drag resulting from skin friction. That is because each first reading was taken with the turbine in short-circuit, where power was dissipated internally by the generator.

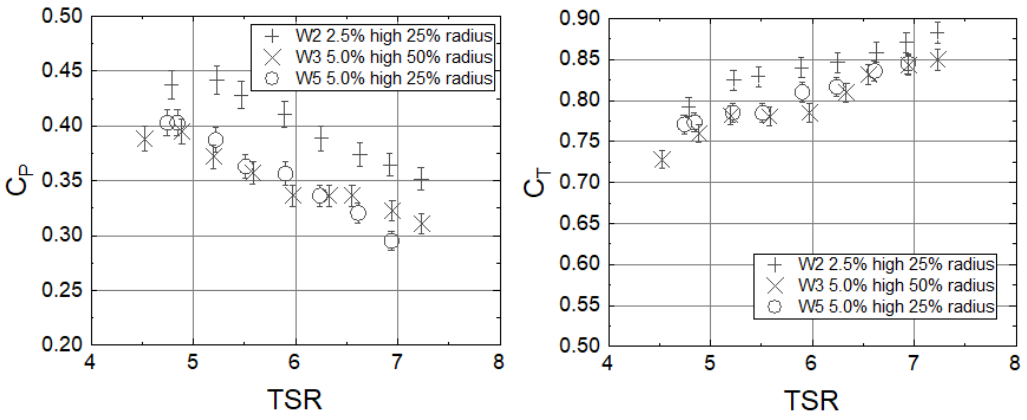

Figure 5.27 Power and thrust coefficients versus TSR to compare the effect of absolute radii.

Both, winglet 3 and winglet 4, reduce the first rotational speed compared to other winglets. The first point for each winglet is when the load is zero *Ohms* (short circuit). The baseline starts at a tsr of 4.6, other winglets start at 4.7 onwards, but the first rotational speed for winglets 3 and 4 is a tsr of 4.5. Such winglets have reduced power and less drag force. It will later be seen that such behaviour is not product of extra drag from skin friction, but from vortices formed behind the winglets causing lower performance due to flow detachment.

5.4 Curvature radius

Following the previous results, the second most important design variable was determined to be the curvature radius. W3, W5, and W6 compare this trait with values of 25%, 50% and 100% relative to a fixed winglet height of 5%, cant angle of 90°, and toe and sweep angles of 0°. Due to the constraint of W2 of curvature radius mentioned in the previous section, the ascending order goes from W5 with 25%, W3 50%, and W6 100% as shown in Figure 5.28.

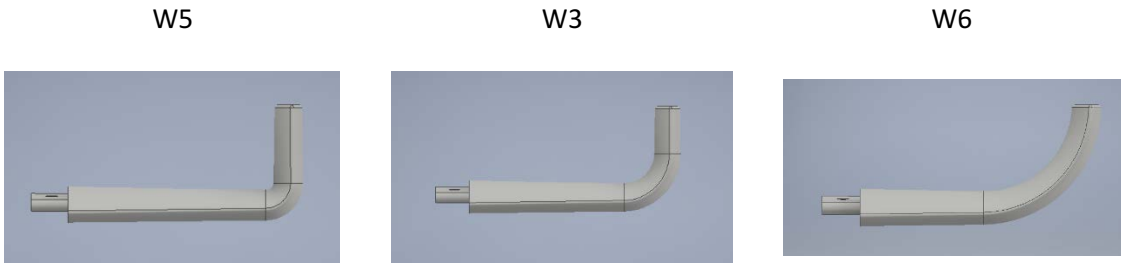

Figure 5.28 Side-view of W3, W5, and W6 comparing curvature radius (Autodesk screen shots reprinted courtesy of Autodesk, Inc.).

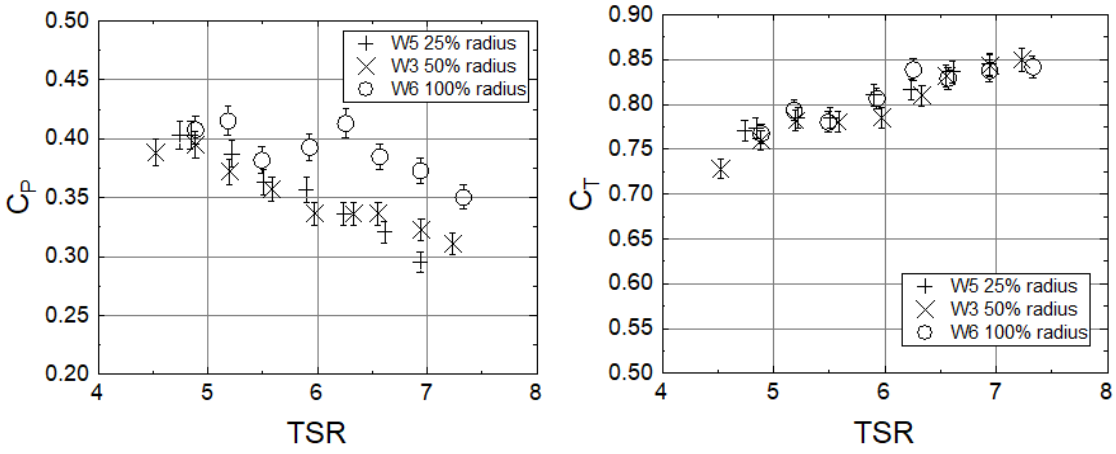

Figure 5.29 C_P and C_T curves versus TSR for winglets with fixed height and different radius.

Figure 5.29 shows same W3 and W5 seen previously in Figure 5.27 where they have a similar performance in power coefficient. It was also stated previously that a 50% curvature radius slowed down the turbine. Following that logic, it would have been expected that a 100% curvature radius would slow down further the turbine, but it can be observed that it was not the

case. In fact, W6 made the turbine perform at a higher power coefficient with an average of 0.39 for the range of TSRs presented, against 0.35 for W3 and 0.36 for W5. The average thrust coefficient for W3 was 0.79, 0.80 for W5 and 0.81 for W6. It is possible that the aforementioned vortical structures 'break' after getting to a certain size, just like a bubble would burst, particularly considering that the curvature radius in winglet 6 reaches the tip, so the flow from the tip could enter any suction area. These vortices are commented and presented visually in Section 5.7.3.

5.5 Cant angle

The results on previous two design parameters analysed were not conclusive as there did not seem to be a clear trend when varying them. The third most important design variable considered was the cant angle. Recalling, only one (Prof. Chattot) of the eleven main authors studied, in the period from 2006 to 2017, predicted numerically that winglets facing the suction side performed better than the ones faced to the pressure side, and most other CFD studies favoured the latter. This winglet was initially designed only to verify what was previously simulated. Figure 5.30 shows winglets W5 and W7 designed to face opposite directions, with a curvature radius of 25%, with sweep, toe and twist angles of 0°.

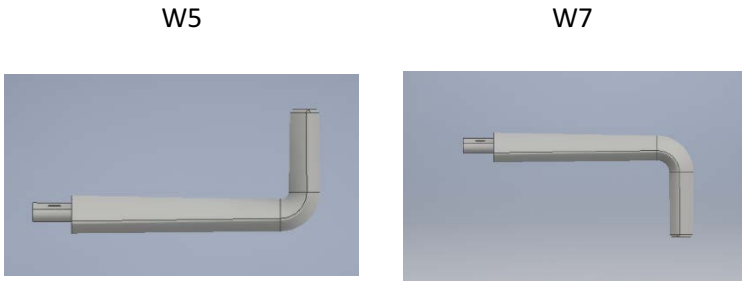

Figure 5.30 Winglets with opposite cant angles. W5 with 90° cant angle (Left) and W7 -90° (Right) (Autodesk screen shots reprinted courtesy of Autodesk, Inc.).

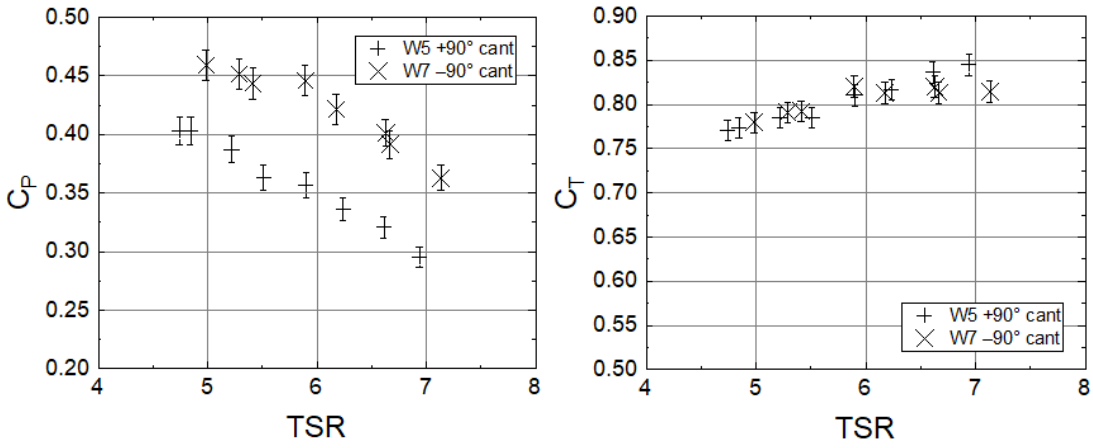

Figure 5.31 Power and thrust coefficient curves versus TSR for W5 and W7 comparing cant angles.

Surprisingly, and contrary to what was expected, winglet W7 has a peak power coefficient of 0.46 at around a TSR of 5.0, with an average value of 0.42, versus an average value of 0.36 for W5. That represents a 17% difference. More unexpectedly, both thrust coefficients have the same average value of 0.80. What would have been expected is a trade-off between power and thrust coefficients. If the power coefficient wants to be increased, usually the thrust coefficient would go up at the same time. For the case of winglets facing the suction side, it has been the case of reduction in power. In that sense, it is interesting to see how two winglets facing opposite directions can have such a different power coefficient, and yet maintain a similar thrust.

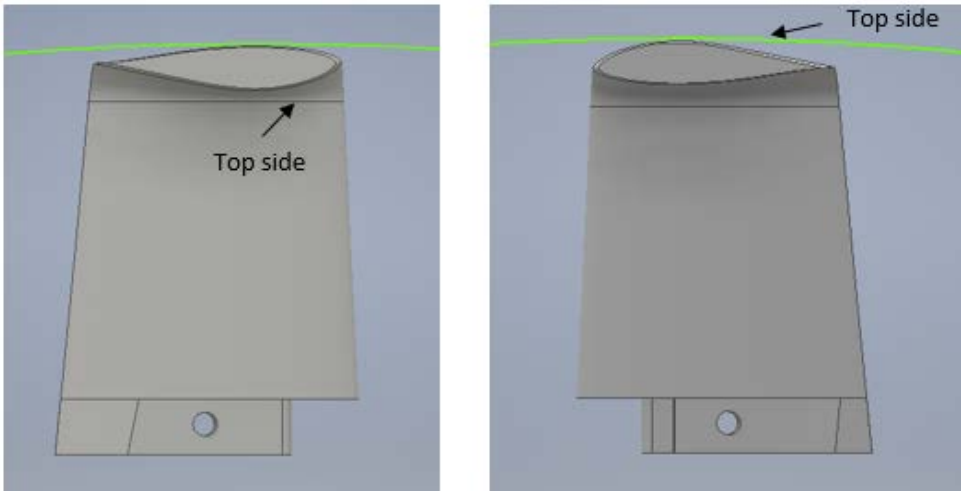

Figure 5.32 Airfoil orientation for opposite cant angles. W5 (Left), W7 (Right) (Autodesk screen shots reprinted courtesy of Autodesk, Inc.).

The first assumption to try to explain the observed behaviour, is that when winglets are bent towards the suction side, the airfoil ends up upside down as it can be seen in Figure 5.32 (Left). The green line represents the curvature radius of the rotation of the blade. Both winglets are facing different direction, but the direction of rotation is towards the leading edge. When the airfoil is upside down, like in the case of W5 and winglets faced towards the suction side, they seem to have a less hydrodynamic shape than those bent towards the pressure side like W7 Figure 5.32 (Right).

5.6 Mirrored winglet

As mentioned in Section 5.2, the varied designs of the winglets made possible more comparisons that were not intended to be done when winglets were designed. Figure 5.33 shows the same different orientation explained previously, where W18 has a mirrored profile with respect to W7, and that was originally designed to compare the airfoil orientation with W5.

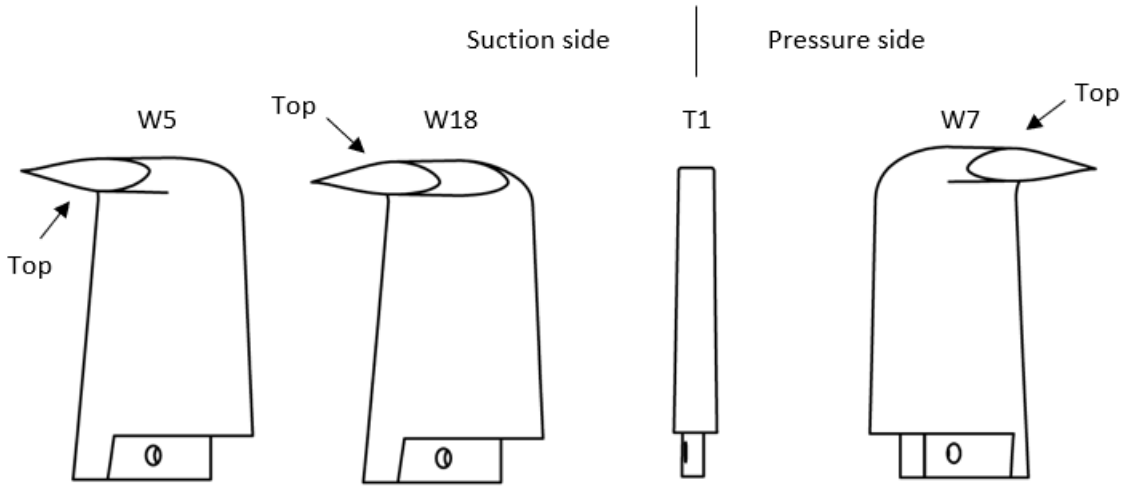

Figure 5.33 Airfoil orientation for W5, W7 and W18.

Figure 5.34 shows the power and thrust coefficients where it can be appreciated that indeed, W18 has a higher average power coefficient than W5, 0.370 versus 0.358 respectively. At the same time, the average thrust coefficient increases from 0.803 for W5 to 0.807 for W18.

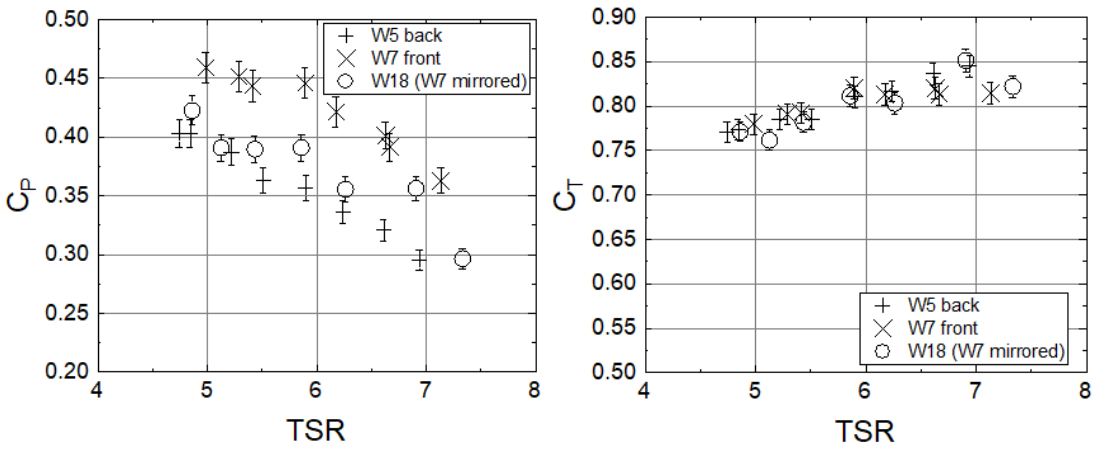

Figure 5.34 C_P and C_T curves versus TSR for W5, W7 and W18 comparing airfoil orientation.

The increased thrust coefficient could be explained by the change of apparent shape facing the flow. In the case of winglets facing the suction side, they resemble a section of a convex shape facing the flow, and the ones facing the pressure side appear as a concave shape towards the flow. The drag coefficient for a convex hollow half sphere is 0.38, and for a concave one is 1.38 (Hoerner, 1965, p. Chapter 3). The small difference in the actual C_T is marginal, compared to the difference in the drag coefficients for hollow half spheres, but the drag in a turbine is mainly determined by the Cd of each section. This means that only the tips of the blade would present this change in drag, and the chord of the three blades represent under 4% of the swept perimeter. The average power coefficient for W18 was 0.37 and there is still a significant gap versus the 0.42 for W7. Such difference cannot be attributed to geometrical differences.

5.7 Oil-based paint flow visualization

Modern flow visualization techniques include lasers and high-resolution cameras, but other techniques have been used in the past to determine the surface-flow interaction, such as turfs and paint. Setting up specialised equipment in a towing tank carriage is not an easy task, and the availability of these devices is scarce. In order to understand what was happening with the unexpected results, it was chosen to use an oil-based paint flow visualization technique.

Shimizu et al. (2003a, pp. 188–190) and Gertz, Johnson and Swytink-Binnema (2012, pp. 404–405) include section regarding surface oil flow visualisation in their experimental studies on winglets for wing turbines. Harwood, Young and Ceccio used surface-flow visualisaiton for a hydrofoil (2016, pp. 18–40). The technique consists on applying oil based paint to the surface of an airfoil, expose it to the desired flow speed, and let the paint follow (thus show) the path of the flow over the surface as it can be seen in Figure 5.35.

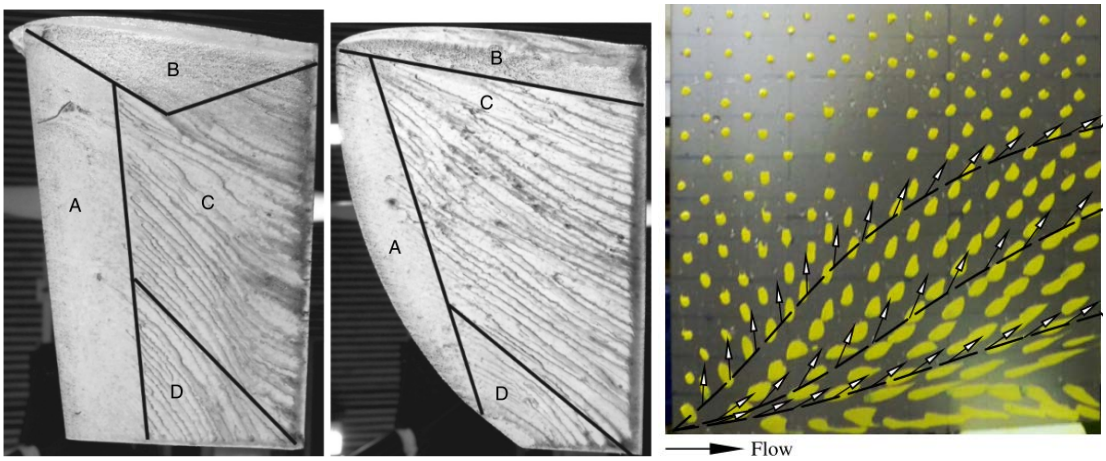

Figure 5.35 Surface oil flow visualisation on winglets [Left (Gertz, Johnson and Swytink-Binnema, 2012, p. 404)], and a hydrofoil [Right (Harwood, Young and Ceccio, 2016, p. 23)].

A 2:1 dilution ratio of oil-based paint combined with flaxseed oil was found by trial and error to have the right viscosity to leave the traits at the surface of the blade tips spinning at 75 *rpm*. The tip was painted in the same direction of rotation. The towing method was also modified to prevent the turbine over rotating above the desired speed. It involved starting with the turbine connected to a resistance of 0.07 Ω and a speed setting of 140, once the turbine started spinning, change the resistance to 0.1 Ω, and gradually changing the speed to 150, 160, 170, and 180 (0.76 *m/s*), then stopping. Figure 5.36 shows a 20 s average for 75 *rpm*.

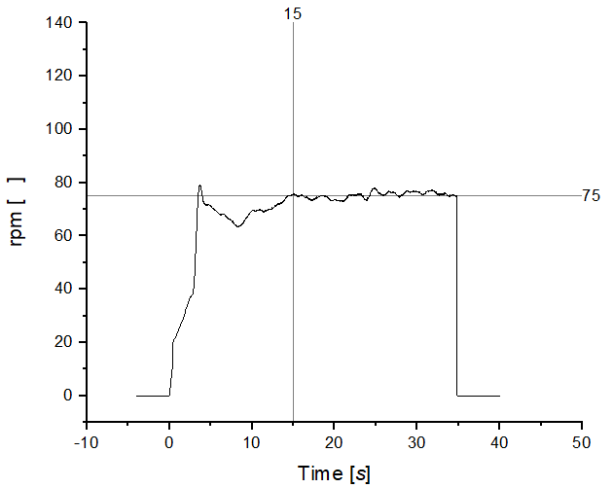

Figure 5.36 Example tow run for oil flow visualisation.

5.7.1 Winglet orientation

To make sense out of the patterns formed on the winglets, it is necessary to describe how flow detaches and recirculates over an airfoil as it can be seen in Figure 5.37. The flow goes from left to right, at low Reynolds numbers the boundary layer separates from the airfoil, recirculates and subsequently detaches from the back of the foil.

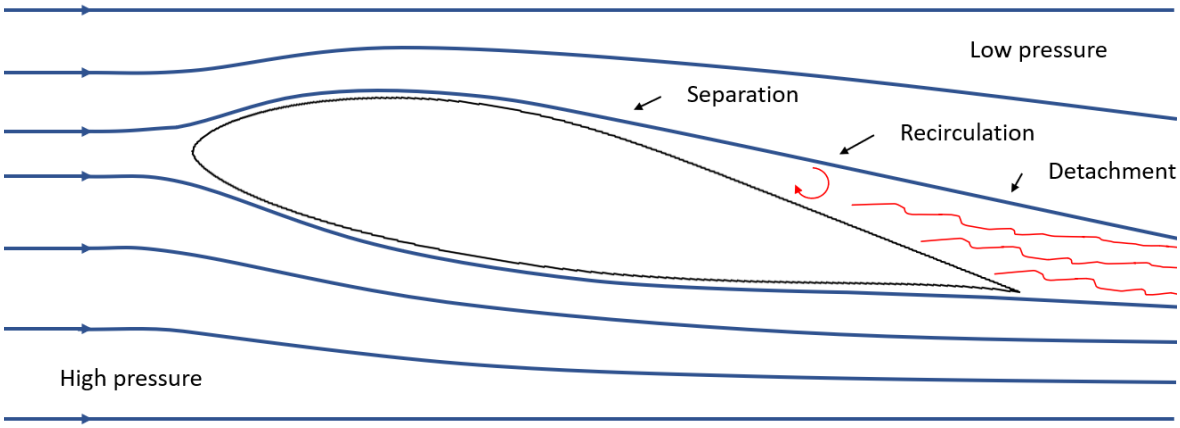

Figure 5.37 Flow recirculation after boundary layer detaches from the airfoil.

The previous effect can be observed in Figure 5.38, although the flow is coming from the right, so all sections are flipped. From right to left, the nose is first, flow separation can be observed, flow recirculation is appreciated, full detachment is shown. All winglets were painted from nose to back as shown by the picture on the left, because the idea was to find cross sectional disturbances in the flow. The picture on the right was painted from top to bottom and that help visualise more clearly how flow separates on an airfoil.

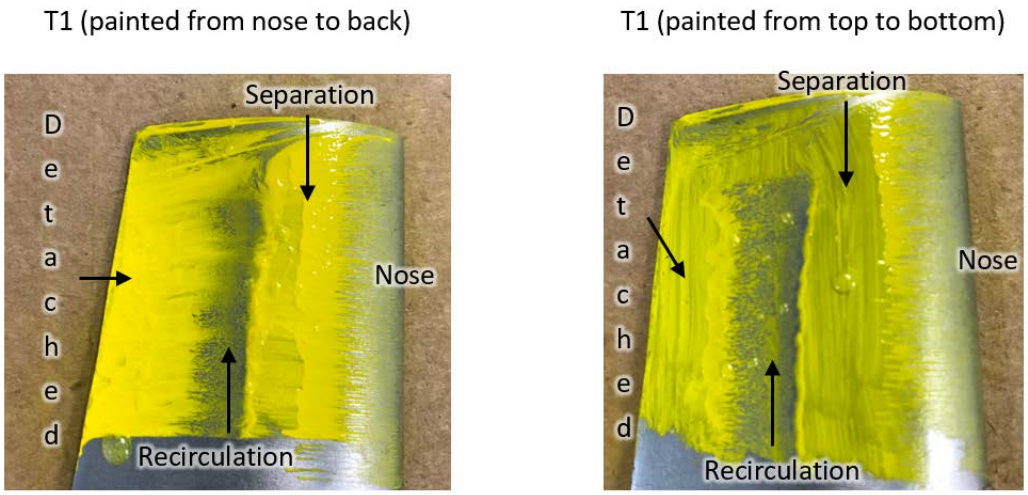

Figure 5.38 Tip vortex and flow recirculation in crossed painting.

The first comparison is made between W7 and W18 as shown in Figure 5.39. A vortex-shaped structure was found behind most winglets facing the suction side. Such vortex is created due to a low-pressure volume formed in that region. The recirculating flow from the blade meets the recirculating flow from the winglet to form a combined recirculating region that acts as a suction area. Analogically, this low-pressure volume is the same one found behind a moving object, which increases its drag force, like behind a lorry. In this scenario, the added drag force impacts the torque by reducing it, and the thrust by increasing it. Another interesting trait can be seen at the bottom of Figure 5.39 (Left). It is the vertical washed mark slightly to the left of the middle of the blade, which is the recirculating flow after it is detached from the airfoil (de Kat, 2019). W7 does not present such mark because it is facing the pressure side, thus the flow remains attached throughout the whole interaction with the blade. It does not show a vortex either, because it seems that the vortex is formed only behind the apparent flow.

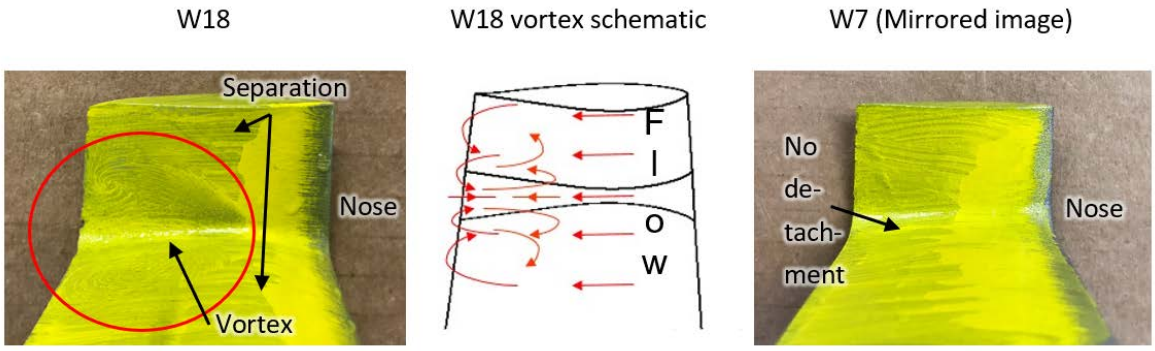

Figure 5.39 Vortex present at winglets facing suction side (Left), schematic (Centre), pressure side without vortex (Right).

5.7.2 Vortices in height comparison

In Section 5.3 W2 had the highest C_P value, followed by W4 and W3 was last. From Figure 5.40 it could be assumed that the small reduction in performance of W2 was caused by the vortex that extends towards the blade, but only covers the small height of the winglet. W4 does not seem to have a vortex, but the reduction in performance can be attributed to it being the highest. Finally, W3 had the worst performance, and the reason could be that the vortices occupied the largest region of them all.

W2 W3 W4

Figure 5.40 Vortices found in W2 and W3. W4 only has the one at the tip.

5.7.3 Vortices in the curvature radius

In Section 5.4 it was seen that W3 and W5 had a similar performance, and that W6 was expected to have a bigger decrease in performance than the previous two, but it was not the case. Figure 5.41 shows the vortices for curvature radius of 25%, 50% and 100%. W5, with 25% seems to have the clearest vortex of the three. In W3 it seems that the slightly bigger radius makes the vortex go further from the inner corner. W6 only seems to have a vortex at the very tip of it, which might explain why the C_P value went back up, instead of decreasing as it would have been expected.

W3 W5 W6

Figure 5.41 Vortices behind different curvature radii for W3, W5 and W6.

In addition to the height, curvature radius, and cant angle, the following are other differences that were intended to be compared across winglets found in Appendix A (section indicated):

- 50% Airfoil size (W8, sec. A.1). Same with ±45° sweep angle (W9 and W10, sec. A.2).
- 25% Airfoil size (W11), end point (12), edge end (14), and half edge end (W15). (Sec. A.3).
- W5 and W16 compare a 45° angle towards the suction side. (Section A.4).
- W17 is a wing extension. (Section A.5).
- W19 and W20 compare positive and negative toe angles. (Section A.6).
- W21 has an inverted profile and a negative toe angle. (Section A.7).

After realising that all winglets facing the suction side underperformed compared to the normal blade and having determined that a vortex was the cause for this underperformance, it was decided not to present all the results in the main body of the thesis. This is because some assumptions can be made, but they are not consistent due to the fact that the size of the vortex would have to be known at all times, and not only it might vary with each shape, but also with different rotational speeds. Each winglet and the simulation are compared versus the straight blade in Appendix A.8 with full C_P and C_T values, together with the percentage difference from the baseline.

5.8 Bending moment at the root

Combining the experimental results with the BEM simulations, it was possible to estimate the bending moment at the root. Since winglets are located at the tip of the blade, it can be considered that any change in the power and thrust coefficients are a consequence of the interaction between them and their surrounding at that point. The blades of the turbine are 500 *mm* from the centre of the shaft, but the actual span is 480 *mm*, and the weakest point affected by the bending moments is the thinnest most inner part of the blade, located 8 *mm* from the root (Figure 5.42). All estimations in this section have been calculated for that point. Installed wind turbines measure the moments at around 2-3% span from the root (Post, 2016, p. 4).

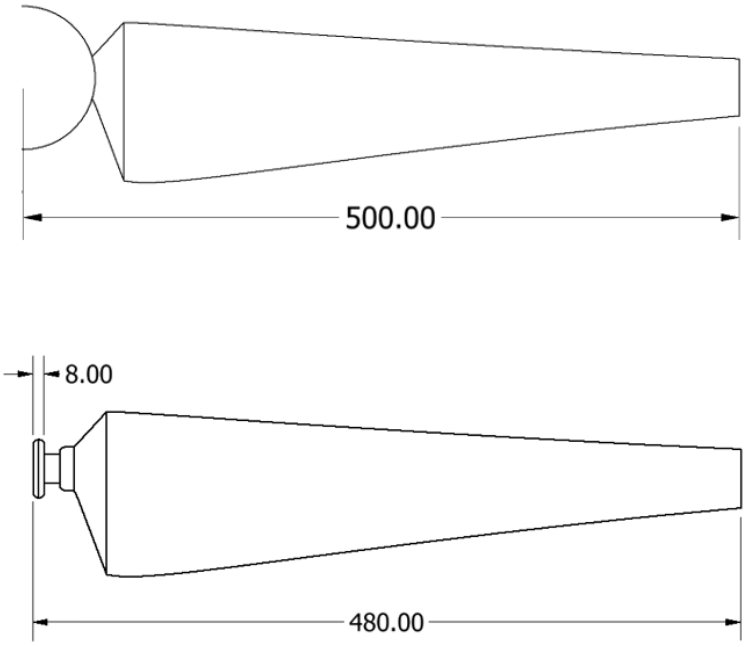

Figure 5.42 Blade from the centre of the axis (Top). Blade span (Bottom).

The Blade Element Momentum software gives the position of the element, the lift and drag coefficients, the local velocity and the inflow angle. With Equation 3.64 to Equation 3.68, the local thrust, torque, and their contribution to the overall moment was calculated. Appendix D contains an example of such calculations (deliberately blurred, as it contains information about the chord and drag and lift coefficients for each location and their local resultants).

The blade was divided into 40 sections. QBlade chooses a greater definition at the root and the top of the blade (to account for losses more accurately) and the position, chord, drag coefficient, lift coefficient, inflow angle, and local velocity were used to determine the force per unit of length applied at each one of those points (*N/m*) as can be seen in Figure 5.43 (Left).

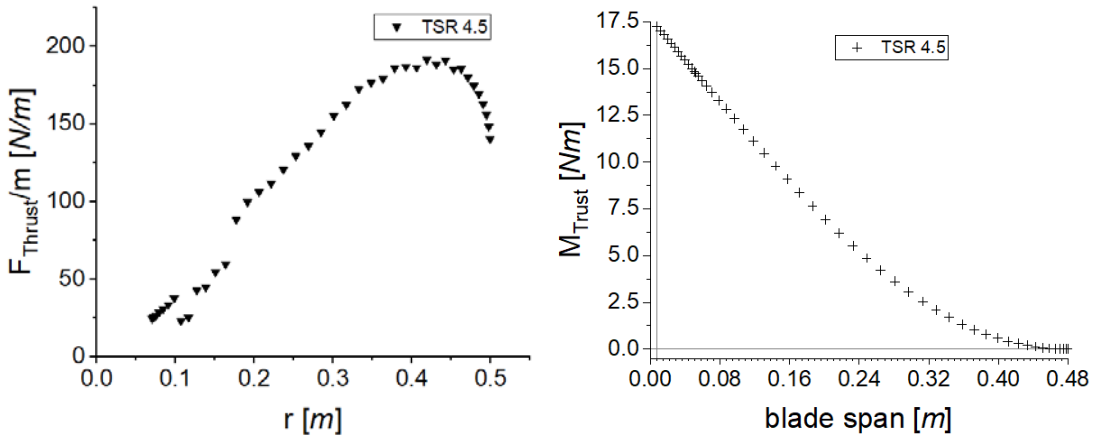

Figure 5.43 Force distribution per unit of length along the blade (Left). Moment at the blade (Right).

For this particular example, QBlade estimated a total force applied of 165.08 *N*, compared to the 168.28 *N* measured. To the previous, and other values at the same towing speed, 0.47 *N* were subtracted to eliminate the drag force at the hub with 0.05 *m* radius [using a drag coefficient of 0.42 (Hoerner, 1965, p. Chapter 3)]. The corrected value of 167.81 *N* is only 1.65% higher than what the program estimated. After increasing all forces proportionally to this adjustment, the bending moment at the root was calculated [Figure 5.43 (Right)] and the centre of pressure (CoP) is found at 0.336 *m* from the root. This means that any additional thrust increases the bending moment at the root by another 48.8%. In other words, for every 1% of extra thrust generated by the winglet, the bending moment at the root will be increased in almost 1.5%.

Similarly, the torque is calculated, with an estimated value of 10.48 *Nm* for the same case, versus the measured value of 11 *Nm*, a difference of around 5%, with a CoP located 0.296 *m* from the root. The centre of pressure for the torque is located around 10% lower than the centre of pressure for the thrust force, indicating that any added drag at the tip has a higher negative impact in the torque than the added bending moment at the root. Figure 5.44 shows the moment coefficients for the x and y axes. The trust generates a positive moment in the y axis. Conversely, as the turbine rotates counterclockwise, the torque generates a negative moment in the x axis according to the frame of reference.

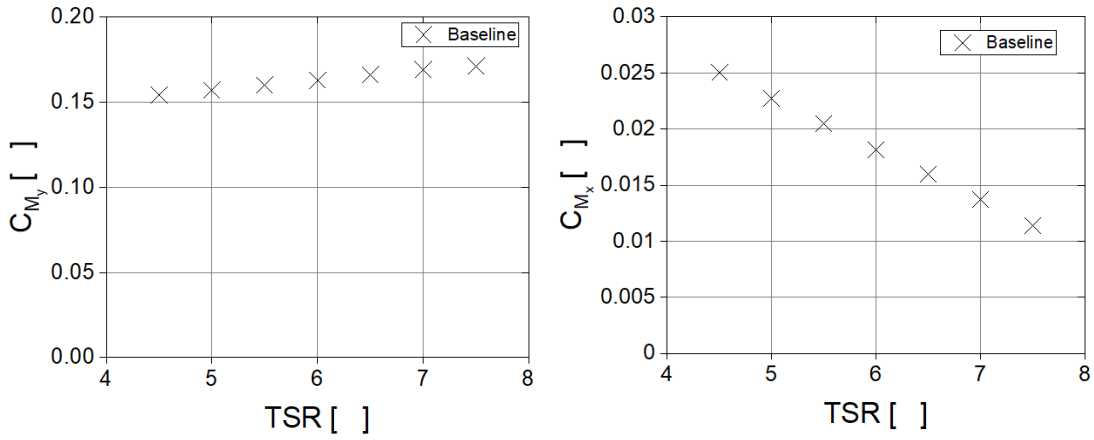

Figure 5.44 Moment coefficients on the *x* and *y* axes.

The bending moments were calculated for the thinnest innermost part of the root of the blade, located at 28 *mm* from the centre of the shaft. The values are presented in Figure 5.45, and it can be seen that as the turbine rotates faster, the thrust keeps dominating and switching the relative axis towards the *y* axis. The moment produced by the thrust force is on average 6 times larger for this tip speed configuration of 4.5. As the turbine rotates faster, the thrust force increases, the torque decreases, and the total bending moment moves towards the direction of the flow.

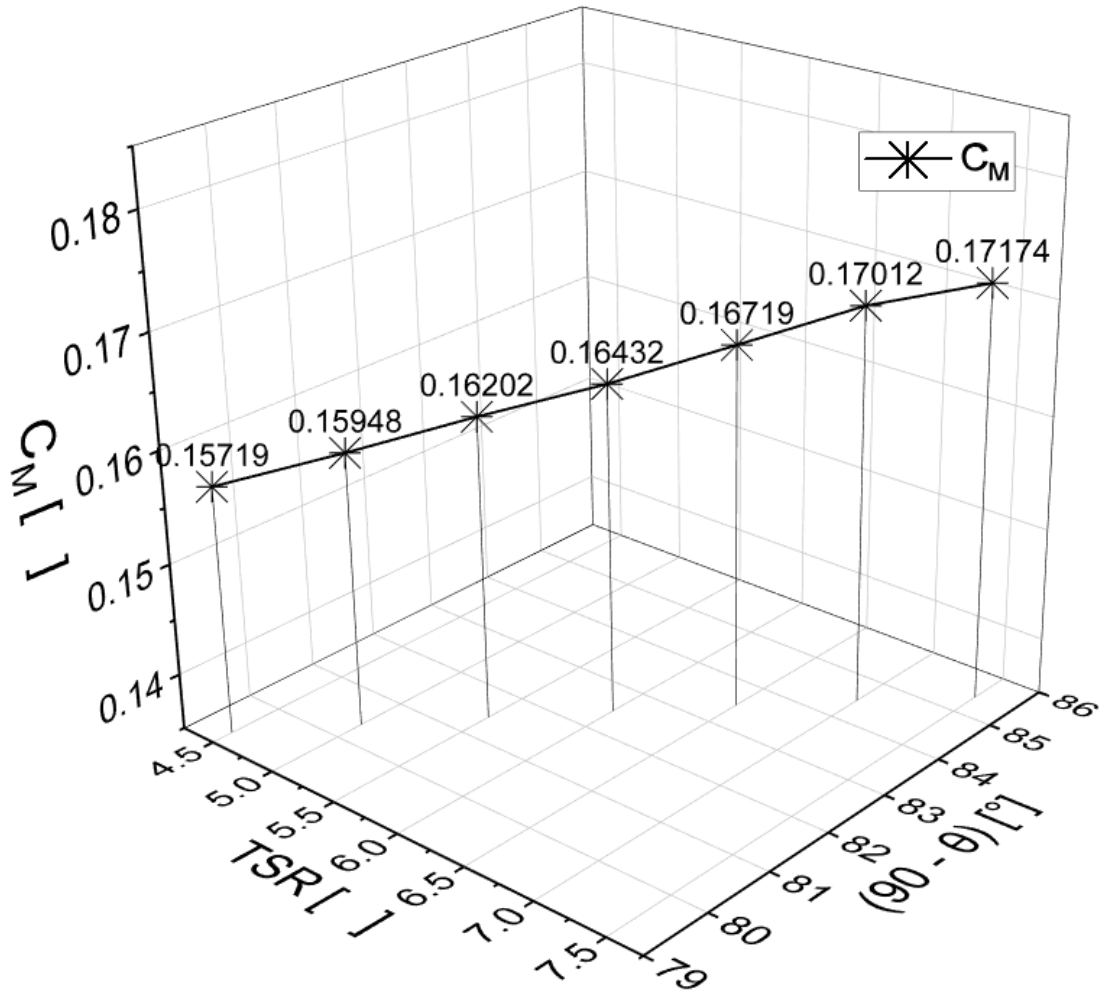

Figure 5.45 Combined coefficient of moment at different TSRs and its axis from the flow.

5.9 Reynolds effect

The turbine was scaled isometrically, speeds were Froude scaled. Ideally, the operational speed is such that the Re numbers are high enough to be compared to the full-scale device. In reality, this is impractical. In theory, because higher Reynolds numbers mean a more turbulent flow, when the turbine is operating at faster speeds, the flow should attach better to the surface. Two additional speeds were tested for the turbine with straight blades (T1). Figure 5.46 shows C_P and C_T curves for 3 different speeds. Re numbers for a TSR of 5.0 are 1.5, 1.6, and 1.7 x 10^5 at the tip of the blade for the low, middle, and high speed respectively. The average power coefficients for TSR from 5.0 to 7.0 are 0.44, 0.43 and 0.47, from low to high speed. It would have been expected that performance increased together with the speed, but it is not the case for the middle speed. The average thrust coefficients did show an increasing trend in average for TSR from 5.0 to 7.0 with values of 0.80, 0.82, and 0.85 for the low, middle, and high speed.

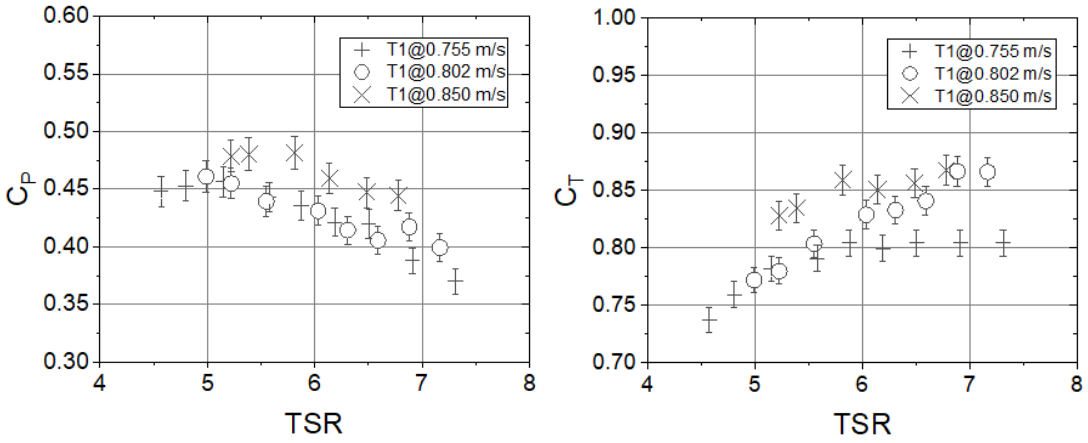

Figure 5.46 Power and thrust versus TSR at different towing speeds.

Figure 5.47 shows the same comparison for W7. In that case the variations were smaller. For averaged values from a TSR of 5.5 to 7.0 the C_P and C_T for 0.76, 0.80, and 0.85 *m/s* were 0.42, 0.43, 0.45, 0.82, 0.82, and 0.83. In this case, the power coefficient does seem to increase in relation with the speed, but even though the thrust coefficient has a close value for all speeds, the behaviour is not linear, as it can be seen in Figure 5.47 (Right). Figure 5.48 shows the comparison for different speeds between W7 and T1. The power coefficient of W7 increases for the middle speed but goes back down at the last speed. The thrust coefficient, following an opposite behaviour as what was seen with the straight blade, decreases, in comparison to the straight blade, as the speed increases. This last tendency could be related to a more energetic vortex at the tip of the blade that might be attenuated with the winglets facing to the front side.

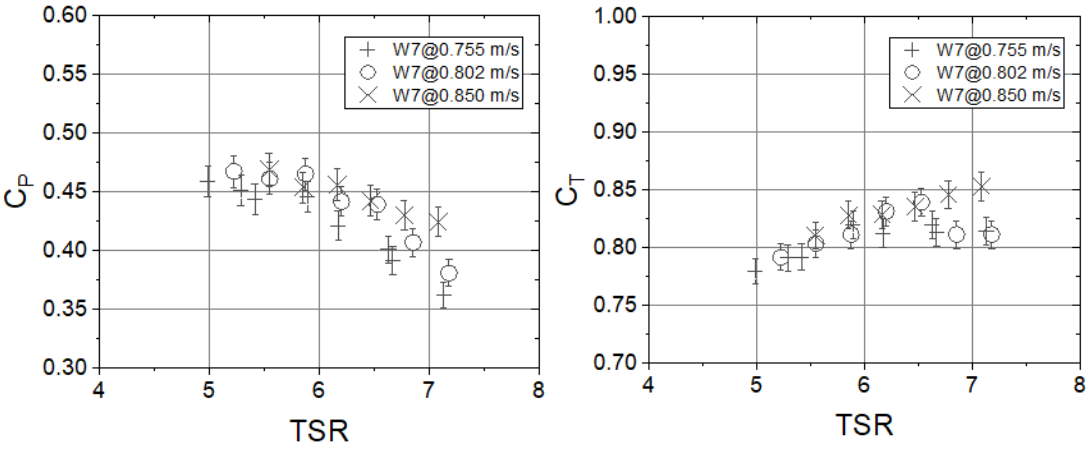

Figure 5.47 Power and thrust coefficients at different speeds for W7.

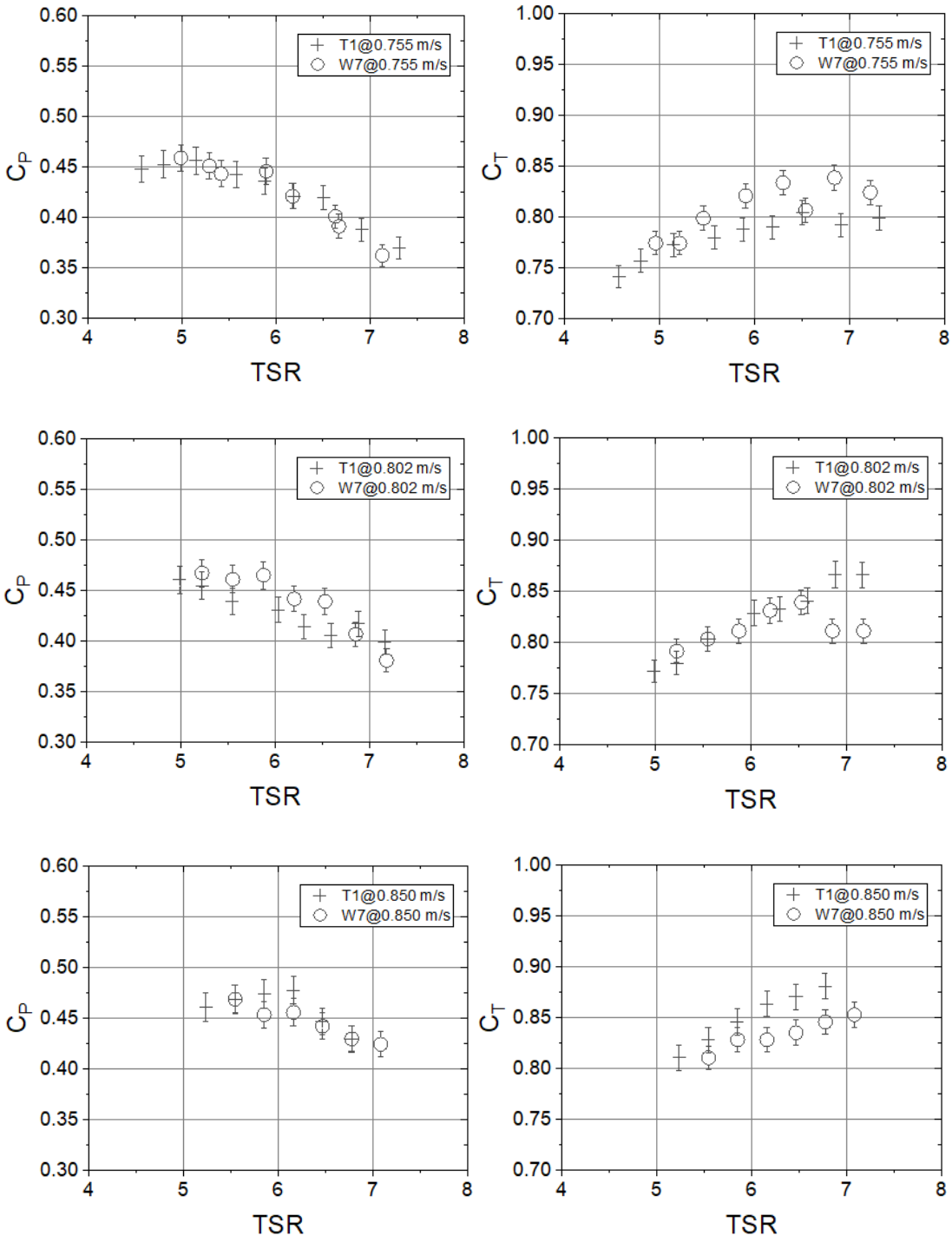

Figure 5.48 Comparison between T1 and W7 at the remaining speeds.

5.10 Overall performance of winglets on the turbine

Even though most of the studies summarised in Table 2-2 (page 40) predict that winglets positioned in any direction on a turbine increase the power output from a few percentages up to 10%, what was found through this study is that the only winglets that showed a slight improvement on the power output at some points, are the ones oriented towards the pressure side Figure 5.49.

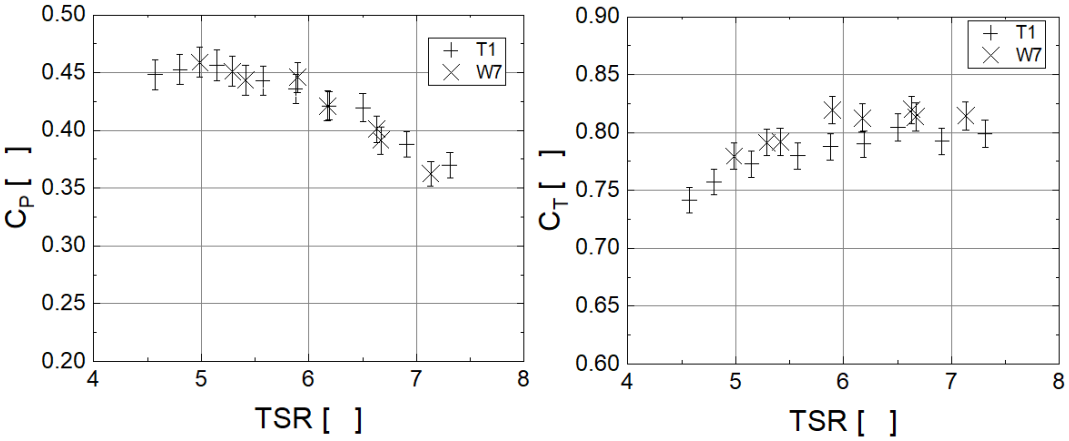

Figure 5.49 Power and thrust coefficients vs. tsr for winglet 7 (W7) towards the pressure side.

At tip speeds ratios of 5 and 6, winglet 7 has an increase in the power coefficient of 1.8% and 1.5%, respectively. Overall, the difference in power coefficient is on average -1.2% from the baseline, and the thrust coefficient increases by 3% on average.

The reason for the poor performance of the other winglets is due to the vortices formed behind them. An oil paint flow visualisation technique was useful to let the vortices leave their trace on the surface of the blade/winglet interface.

Chapter 6 Conclusions

Renewable energy is one of the fastest growing sources of primary energy as there is a world effort to decarbonise the grid. In line with directives focused on reducing greenhouse gas emissions, the UK has an incentive mechanism called Contracts for Difference that has run biannually and started on 2015. To date, the past 3 rounds have allocated contracts to more mature technologies with a lower LCOE like offshore wind. It is necessary to use as many renewable sources of energy to increase reliability, and tidal energy is an attractive choice as it can be predicted years in advance.

Tidal turbines are at a stage before being commercially viable at full scale. Reducing the LCOE would make this technology more competitive in the electricity market. One way of doing that is to increase the power coefficient, which is still behind those ones seen on wind turbines, by improving blade hydrodynamics. At this stage of technology development this is a lower risk method to reduce the LCOE compared to reducing device mass or capital cost. Winglets have been used successfully in the aircraft industry to reduce fuel consumption. Simulations have suggested that adding winglets to tidal turbines can have a beneficial effect too. Those predictions have not been verified with experiments.

BEMT is a fast and efficient numerical method to analyse the performance of a scaled turbine under ideal conditions. A towing tank gives an undisturbed environment to study the effect of adding winglets to the power and thrust coefficient of a scaled tidal turbine. In order to achieve Reynolds similarity model horizontal turbines need to be in excess of approximately 1/8th scale which is not achievable using normal experimental facilities, because they are too large. For this research a 1-m diameter model was used for test and verification which is towards the upper limit in size for experimental models used in indoor facilities.

SIMEC Atlantis Energy provided the design specifications for the blades of their AR2000 model. The scaled turbine was first evaluated using QBlade then manufactured. Around 90% of the scaled blade was machined in aluminium at the University of Southampton, with 20 different 3D-printed winglet designs, in aluminium as well, to explore their effect on the power and thrust coefficients.

Experiments carried out during this project were conducted at the towing tank at Solent University. The 60-m long tank towed at 0.75 *m/s* provided around 20 to 30 seconds of useful data. Turbulence is close to zero in a towing tank, for such reason it was possible to get very clear data that helped identify key aspects present in the experiments. The first of them was the turbine vibration that could be isolated and disregarded as noise. Secondly it helped identify small

variations in power and thrust coefficients, in the range of 1-2%. Lastly, it was possible to use a flow visualisation technique that consisted of covering the surface of interest with oil-based paint at the appropriate viscosity.

Most CFD studies found before this project stated that winglets facing the suction side had a better performance than if placed facing the pressure side. These studies did not predict the appearance of the vortices identified in this project, for such reason their predictions overestimated the benefits of winglets in reducing tip losses and the drag at that region. On the other hand, it could be possible to identify winglet shapes facing the pressure side that accomplish such purposes.

Winglets facing the suction side of the turbine reduce the power coefficient and, in some cases, they increase the thrust coefficient as well. This phenomenon is caused by some vortices that are formed behind the blade/winglet interface. These vortices were not present on the winglet facing the pressure side.

6.1 Findings on Research Objectives

- Winglets are the most widely technique used in aviation to improve a wing performance. In the case of horizontal axis turbines, other techniques include the use of micro-tabs, slots, tubercles, non-straight blades, passively adaptive blades, and ramps on the seabed to improve power capture.
- A blade extension bent into a winglet can be defined by 8 key parameters: airfoil, height, curvature radius, cant angle, chord distribution, sweep, toe and twist angles.
- The isometric scaling of the AR2000 turbine blades produced realistic results within design parameters when simulated using BEM theory software.
    - Blade/winglet interface was designed to allow fast accessible winglets swap.
- Each winglet effect on the power and thrust coefficient was measured and compared across groups and versus the straight blade.
- It was found that the most significant variable decreasing the power coefficient is the cant angle, by 12%. It is also suggested that other variable comparisons are made orienting winglets towards the pressure side where there was not found presence of vortices.
- With the use of a straightforward surface visualisation technique, it was possible to identify some vortices forming behind the blade at the junction with the winglets.
- From the experimental results, it is recommended that winglets are placed facing the pressure side, prevent the formation of vortices, and explore the advantages that varying the toe angle could bring.

- Previous literature cited in this work were unable to accurately predict the performance of winglets. This work, through experimental verification, has identified complex flow structures in the tip region that subsequent numerical modelling work should utilise that are capable of simulating this.

Throughout experiments, it was measured that most winglets facing the suction side decrease the power coefficient due to vortical structures formed behind the blade where winglets are joined. With the use of an oil-based paint flow visualisation, it was possible to identify their interaction with the blade surface. Power coefficient improvements of around 1-2% were recorded together with an increase in the thrust coefficient of around 3-4%. Analytically, with the aid of BEM theory, it is predicted that the structural cost of the increase in the thrust coefficient due to tip modifications, entails an extra bending moment at the root of the blade of 40% higher than the increase in thrust, i.e. 4.2-5.6% for this particular case.

6.2 Future work

The findings from this experimental work suggest that the effect of winglets facing the pressure side of tidal turbines should be explored. Alternatively, a geometric or flow alteration could be done to the suction-side facing winglets to avoid the appearance of the vortices that reduce their performance. CFD software capable to simulate these types of scenarios would be of great help for future studies. In the long run, feedback from the two techniques can be beneficial for both.

Appendix A Other winglet results

A.1 50% Airfoil

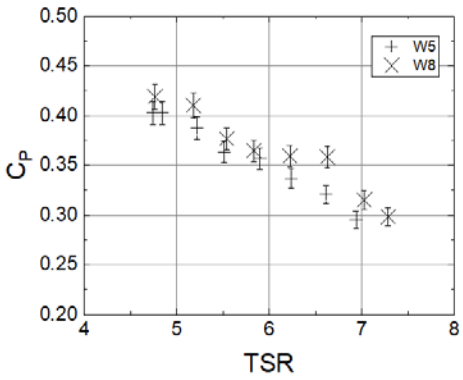

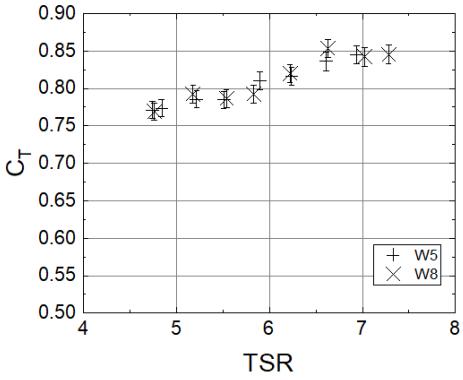

A.2 50% Airfoil with positive and negative 45° sweep angle.

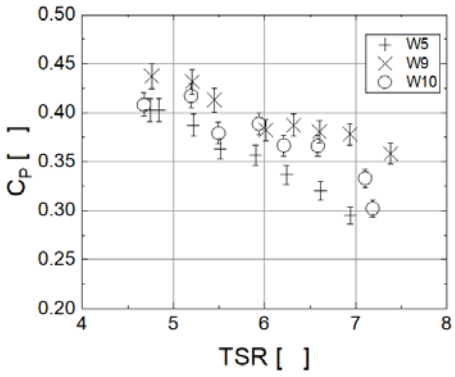

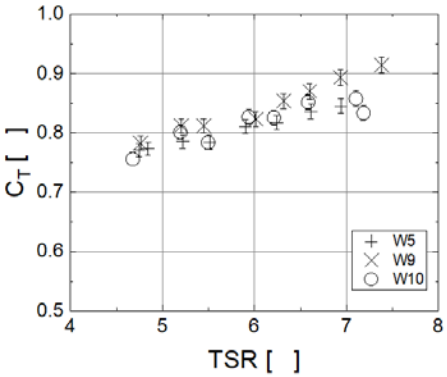

W9 W10

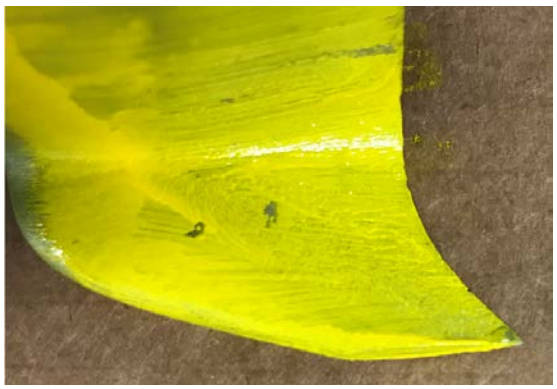

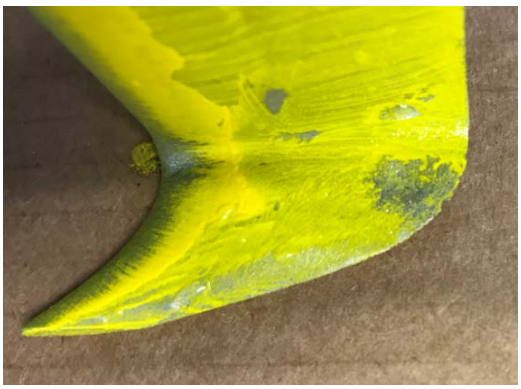

A.3 25% Airfoil size, end point, edge end, and half edge end.

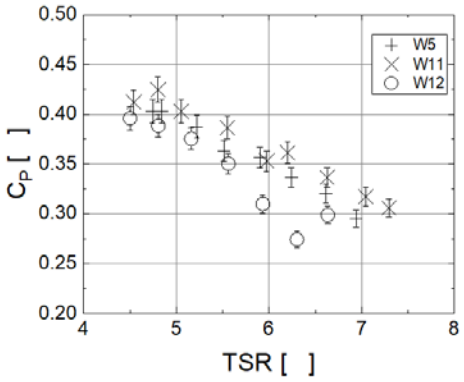

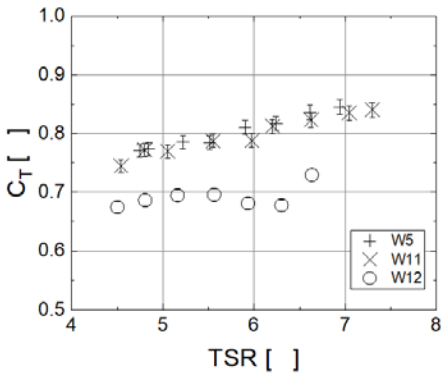

W11 W12

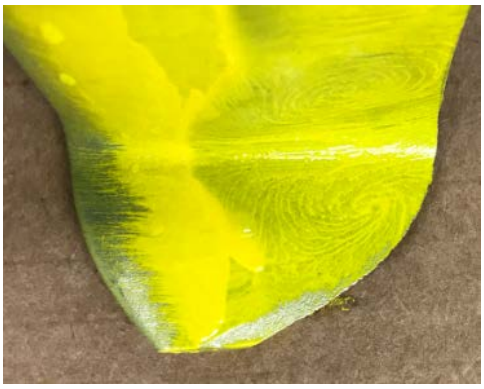

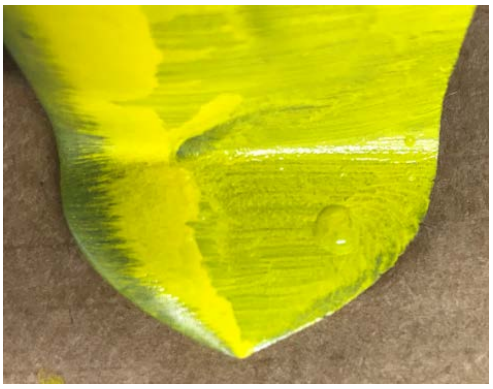

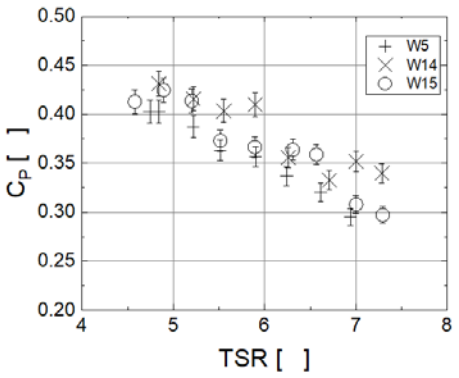

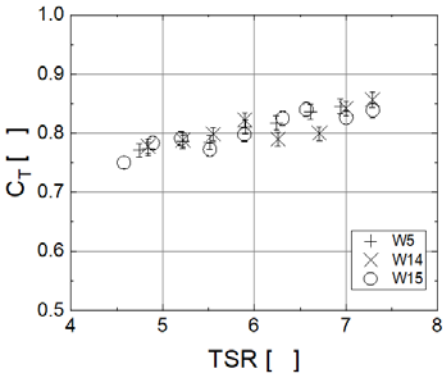

W14 W15

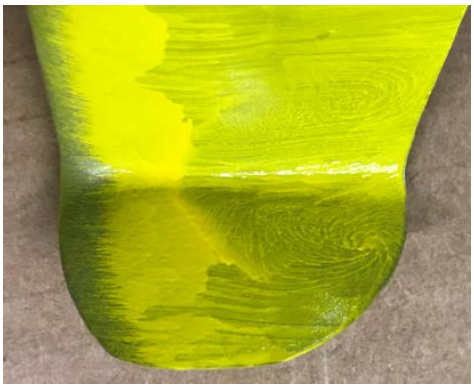

A.4 45° angle towards the suction side.

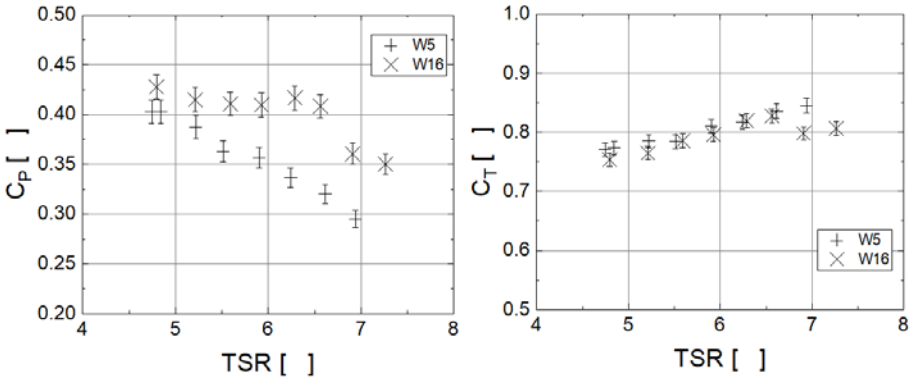

A.5 Wing extension

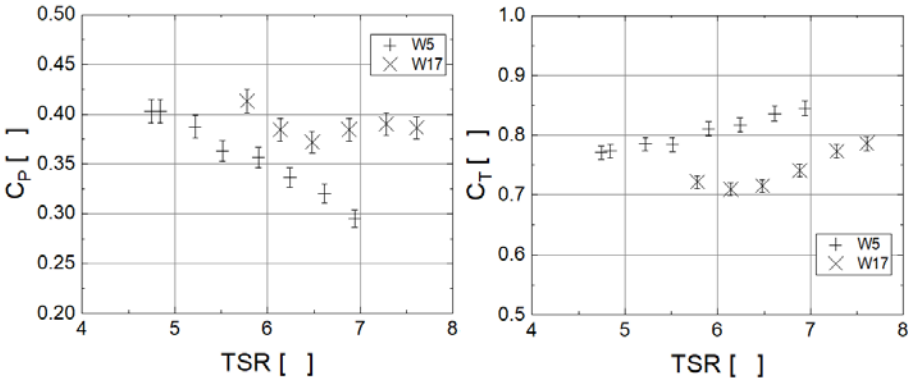

A.6 Toe angle

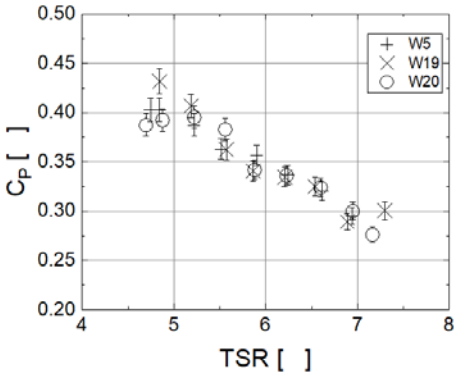

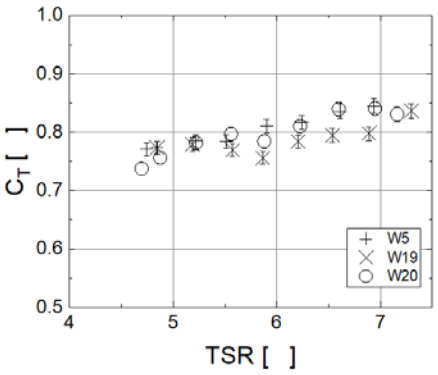

W19 W20

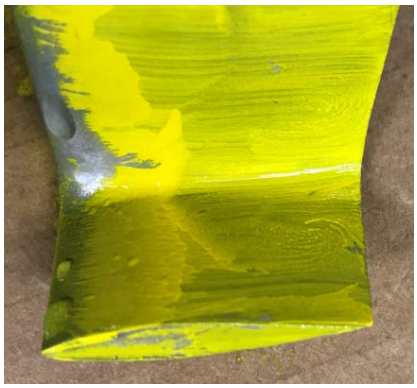

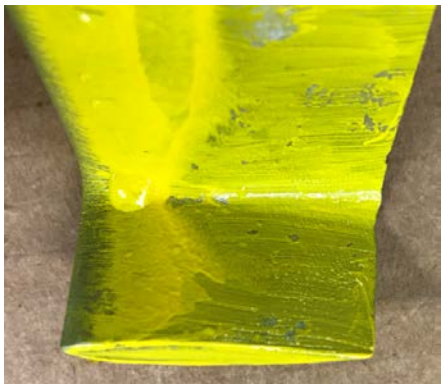

A.7 Inverted profile and negative toe angle.

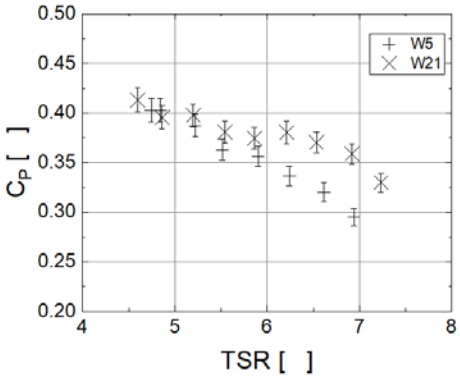

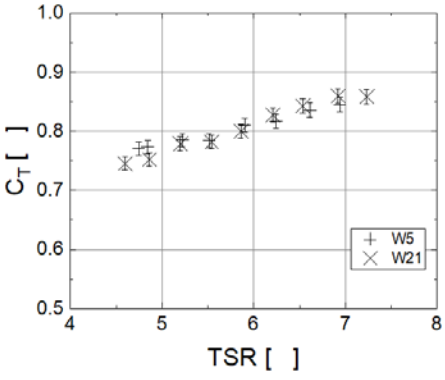

A.8 Each winglet and simulation compared to the baseline (T1)

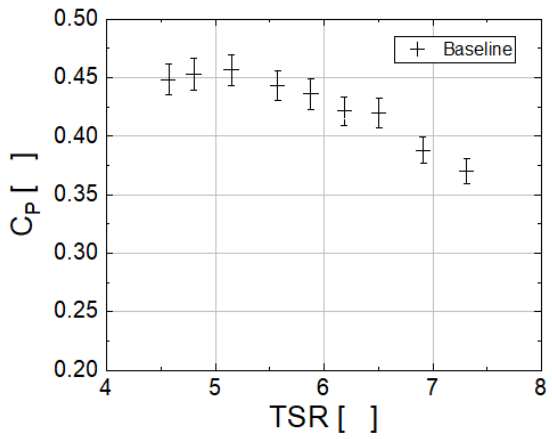

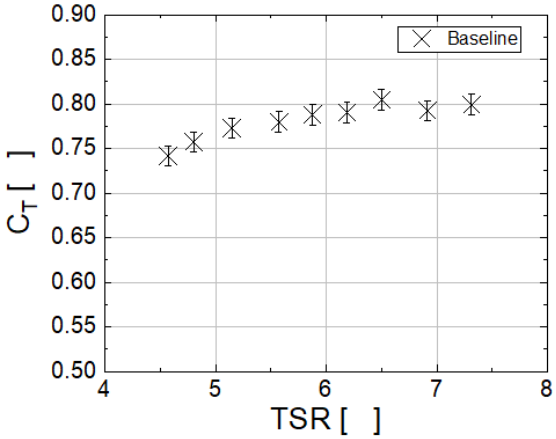

RPM	Torque	Thrust	TSR	omega	Cp T1	σ (Cp T1)	Ct T1	σ (Ct T1)
66	11.0	166	4.6	6.9	0.45	0.01311	0.74	0.01087
69	10.6	169	4.8	7.2	0.45	0.01325	0.76	0.01110
74	9.9	173	5.1	7.7	0.46	0.01336	0.77	0.01133
80	8.9	175	5.5	8.4	0.44	0.01296	0.78	0.01143
84	8.3	176	5.9	8.8	0.44	0.01275	0.79	0.01155
89	7.6	177	6.2	9.3	0.42	0.01232	0.79	0.01158
93	7.2	180	6.4	9.7	0.42	0.01228	0.80	0.01180
100	6.3	177	6.9	10.5	0.39	0.01135	0.79	0.01161
105	5.7	179	7.3	11.0	0.37	0.01082	0.80	0.01171

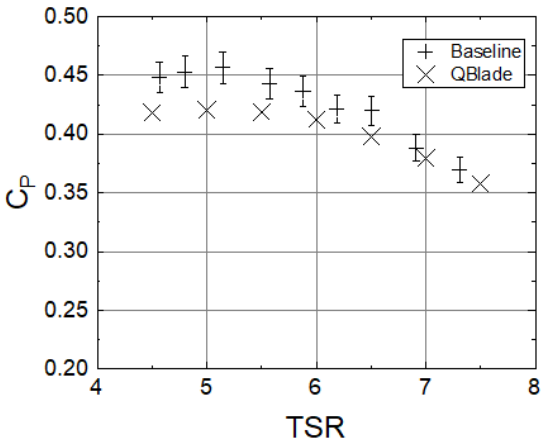

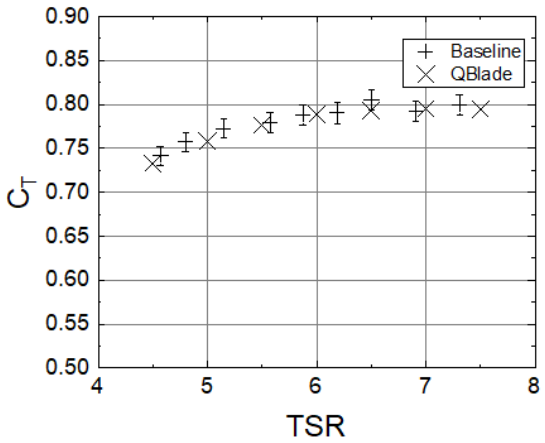

TSR	Cp QBlade	Ct Qblade	Cp T1	Ct T1	diff Cp (%)	diff Ct (%)
4.5	0.42	0.73	0.45	0.75	-6%	-3%
5	0.42	0.76	0.45	0.76	-7%	-1%
5.5	0.42	0.78	0.45	0.77	-7%	0%
6	0.41	0.79	0.44	0.78	-5%	1%
6.5	0.40	0.79	0.42	0.79	-4%	0%
7	0.38	0.79	0.39	0.80	-2%	-1%
7.5	0.36	0.79	0.35	0.81	3%	-2%
				Average	-4%	-1%

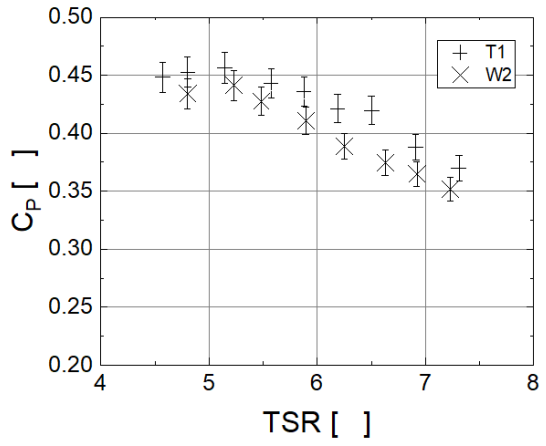

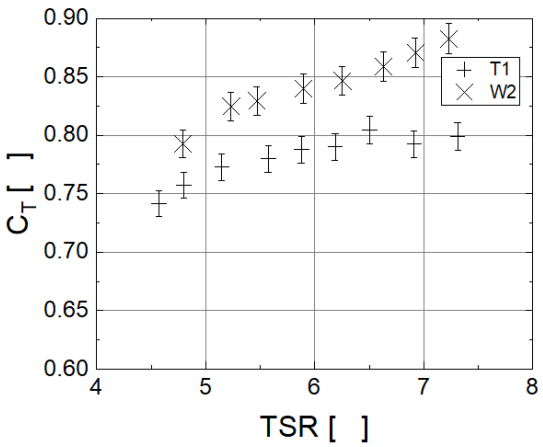

TSR	Cp W2	σ (Cp W2)	Ct W2	σ (Ct W2)	Cp T1	Ct T1	diff Cp (%)	diff Ct (%)
4.8	0.44	0.01269	0.79	0.01159	0.45	0.76	-3%	4%
5.2	0.44	0.01291	0.82	0.01209	0.45	0.77	-2%	7%
5.5	0.43	0.01251	0.83	0.01216	0.45	0.77	-5%	7%
5.9	0.41	0.01202	0.84	0.01231	0.44	0.78	-6%	8%
6.3	0.39	0.01137	0.85	0.01241	0.43	0.79	-9%	7%
6.6	0.37	0.01096	0.86	0.01258	0.41	0.80	-8%	8%
6.9	0.36	0.01067	0.87	0.01276	0.39	0.80	-7%	9%
7.2	0.35	0.01029	0.88	0.01294	0.37	0.81	-5%	9%
						Average	-6%	8%

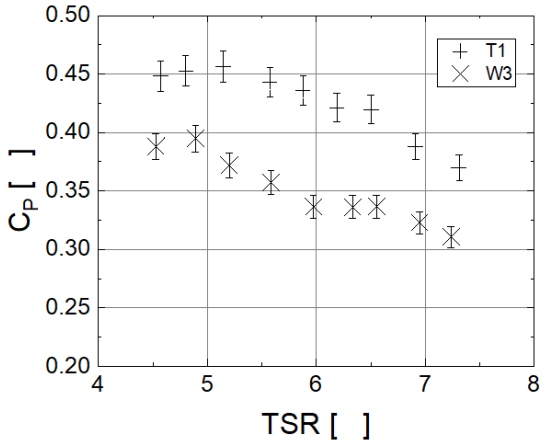

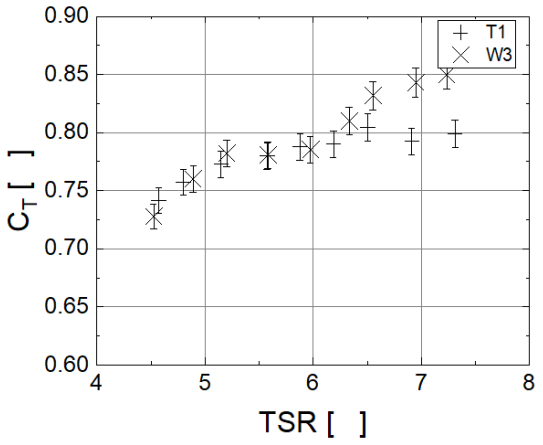

TSR	Cp W3	σ (Cp W3)	Ct W3	σ (Ct W3)	Cp T1	Ct T1	diff Cp (%)	diff Ct (%)
4.5	0.39	0.01135	0.73	0.01067	0.45	0.75	-13%	-3%
4.9	0.39	0.01155	0.76	0.01114	0.45	0.76	-12%	0%
5.2	0.37	0.01088	0.78	0.01146	0.45	0.77	-18%	2%
5.6	0.36	0.01045	0.78	0.01144	0.45	0.77	-20%	1%
6.0	0.34	0.00984	0.79	0.01151	0.44	0.78	-23%	0%
6.3	0.34	0.00983	0.81	0.01187	0.42	0.79	-21%	3%
6.6	0.34	0.00984	0.83	0.01219	0.41	0.79	-18%	5%
6.9	0.32	0.00944	0.84	0.01236	0.39	0.80	-17%	5%
7.2	0.31	0.00909	0.85	0.01245	0.37	0.81	-16%	5%
						Average	-18%	2%

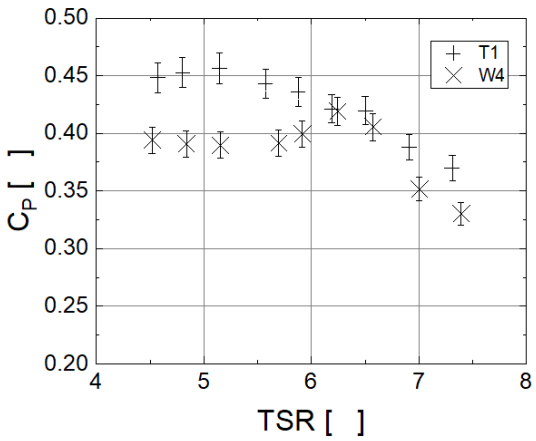

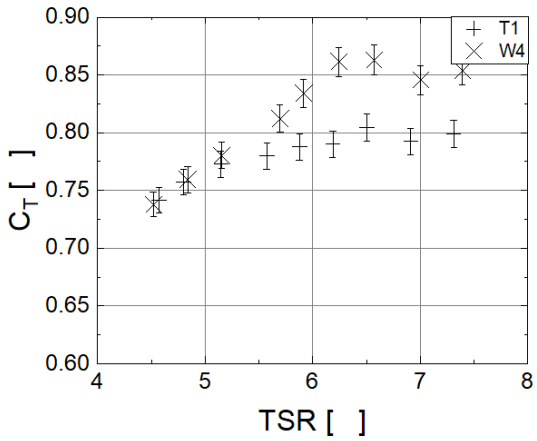

TSR	Cp W4	σ (Cp W4)	Ct W4	σ (Ct W4)	Cp T1	Ct T1	diff Cp (%)	diff Ct (%)
4.5	0.39	0.011522	0.74	0.01082	0.45	0.75	-12%	-2%
4.8	0.39	0.011432	0.76	0.01113	0.45	0.76	-13%	0%
5.2	0.39	0.011397	0.78	0.01144	0.45	0.77	-14%	2%
5.7	0.39	0.011446	0.81	0.01190	0.44	0.78	-12%	5%
5.9	0.40	0.011685	0.83	0.01222	0.44	0.78	-9%	7%
6.2	0.42	0.012251	0.86	0.01263	0.43	0.79	-2%	9%
6.6	0.41	0.011864	0.86	0.01265	0.41	0.79	-2%	9%
7.0	0.35	0.010285	0.85	0.01239	0.39	0.80	-9%	5%
7.4	0.33	0.009659	0.85	0.01252	0.36	0.81	-8%	5%
						Average	-9%	4%

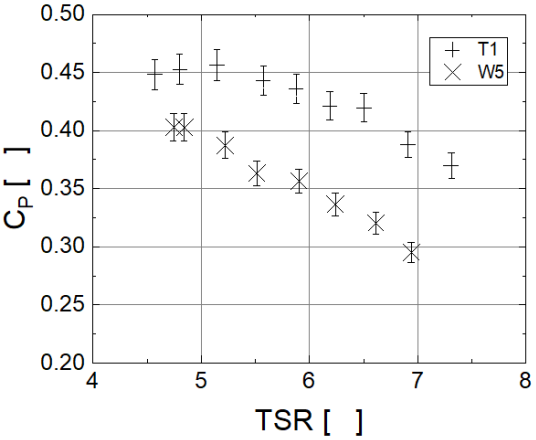

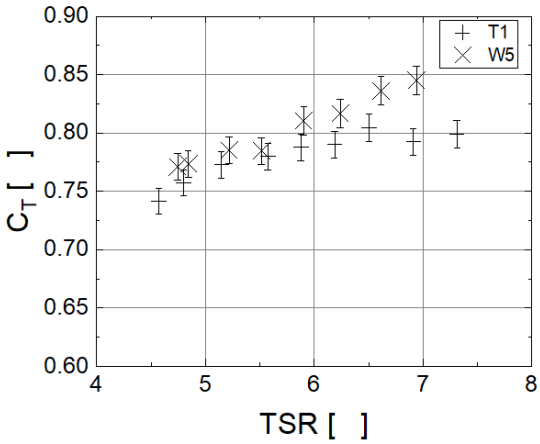

TSR	Cp W5	σ (Cp W5)	Ct W5	σ (Ct W5)	Cp T1	Ct T1	diff Cp (%)	diff Ct (%)
4.7	0.40	0.01178	0.77	0.01130	0.45	0.76	-10%	2%
4.8	0.40	0.01178	0.77	0.01134	0.45	0.76	-11%	2%
5.2	0.39	0.01133	0.79	0.01151	0.45	0.77	-14%	2%
5.5	0.36	0.01062	0.78	0.01150	0.45	0.77	-19%	1%
5.9	0.36	0.01043	0.81	0.01188	0.44	0.78	-19%	4%
6.2	0.34	0.00984	0.82	0.01197	0.43	0.79	-21%	4%
6.6	0.32	0.00938	0.84	0.01226	0.41	0.79	-22%	5%
6.9	0.30	0.00864	0.84	0.01239	0.39	0.80	-24%	5%
						Average	-18%	3%

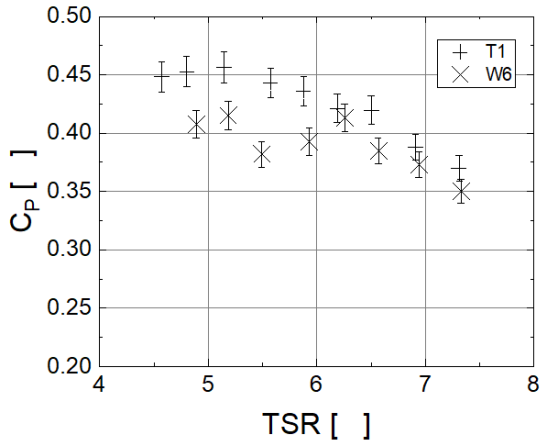

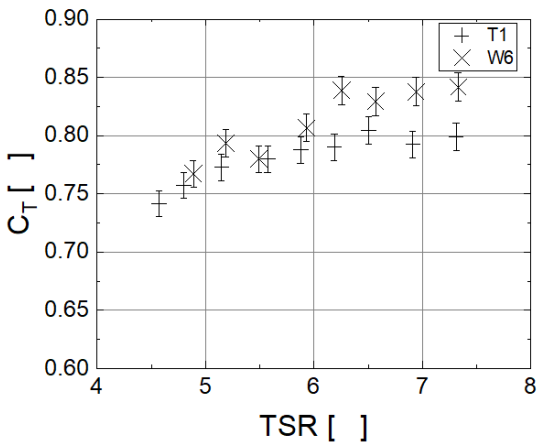

TSR	Cp W6	σ (Cp W6)	Ct W6	σ (Ct W6)	Cp T1	Ct T1	diff Cp (%)	diff Ct (%)
4.9	0.41	0.01192	0.77	0.01125	0.45	0.76	-10%	1%
5.2	0.42	0.01214	0.79	0.01163	0.45	0.77	-8%	3%
5.5	0.38	0.01117	0.78	0.01143	0.45	0.77	-15%	1%
5.9	0.39	0.01149	0.81	0.01182	0.44	0.78	-10%	3%
6.3	0.41	0.01208	0.84	0.01229	0.43	0.79	-3%	6%
6.6	0.38	0.01125	0.83	0.01215	0.41	0.79	-7%	4%
6.9	0.37	0.01091	0.84	0.01228	0.39	0.80	-4%	5%
7.3	0.35	0.01024	0.84	0.01234	0.36	0.81	-3%	4%
						Average	-8%	3%

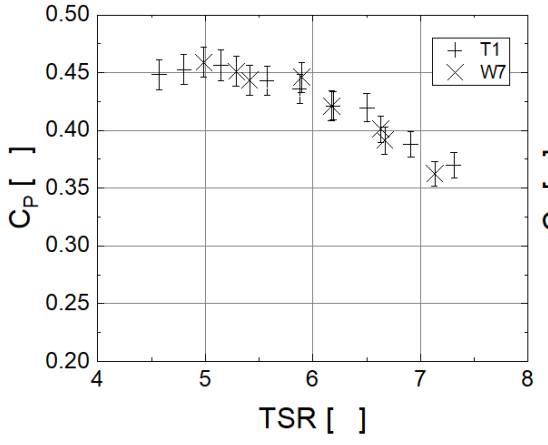

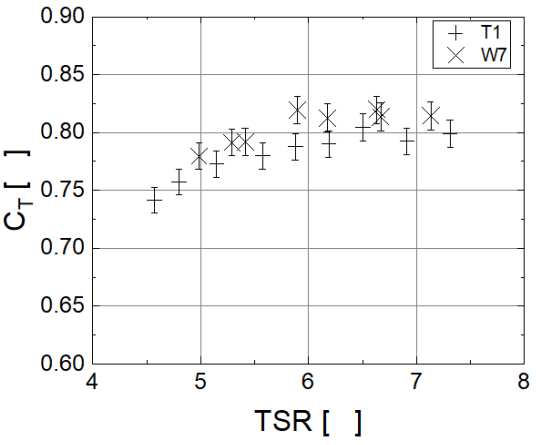

TSR	Cp W7	σ (Cp W7)	Ct W7	σ (Ct W7)	Cp T1	Ct T1	diff Cp (%)	diff Ct (%)
5.0	0.46	0.01331	0.78	0.01136	0.45	0.76	1.8%	2%
5.3	0.45	0.01283	0.79	0.01135	0.45	0.77	0.2%	3%
5.4	0.44	0.01311	0.79	0.01171	0.45	0.77	-1.3%	3%
5.9	0.45	0.01306	0.82	0.01204	0.44	0.78	1.5%	5%
6.2	0.42	0.01278	0.81	0.01222	0.43	0.79	-2.0%	3%
6.6	0.40	0.01148	0.82	0.01183	0.41	0.80	-1.8%	3%
6.7	0.39	0.01195	0.81	0.01230	0.41	0.80	-3.8%	2%
7.1	0.36	0.01074	0.81	0.01209	0.38	0.81	-3.8%	1%
						Average	-1.2%	3%

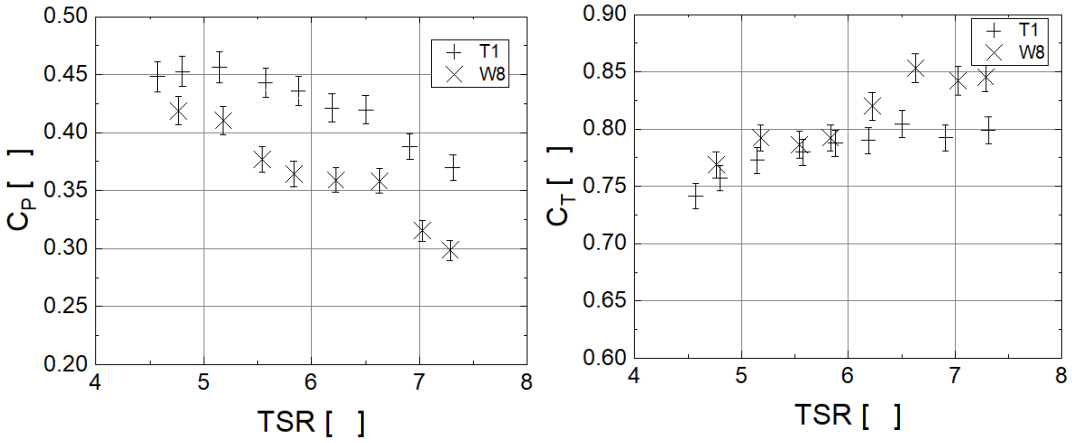

TSR	Cp W8	σ (Cp W8)	Ct W8	σ (Ct W8)	Cp T1	Ct T1	diff Cp (%)	diff Ct (%)
4.8	0.42	0.01225	0.77	0.01127	0.45	0.76	-7%	1%
5.2	0.41	0.01200	0.79	0.01161	0.45	0.77	-9%	3%
5.5	0.38	0.01102	0.79	0.01153	0.45	0.77	-16%	2%
5.8	0.36	0.01066	0.79	0.01162	0.44	0.78	-17%	2%
6.2	0.36	0.01051	0.82	0.01202	0.43	0.79	-16%	4%
6.6	0.36	0.01048	0.85	0.01251	0.41	0.80	-12%	7%
7.0	0.32	0.00922	0.84	0.01235	0.38	0.80	-18%	5%
7.3	0.30	0.00873	0.85	0.01239	0.37	0.81	-18%	5%
						Average	-14%	4%

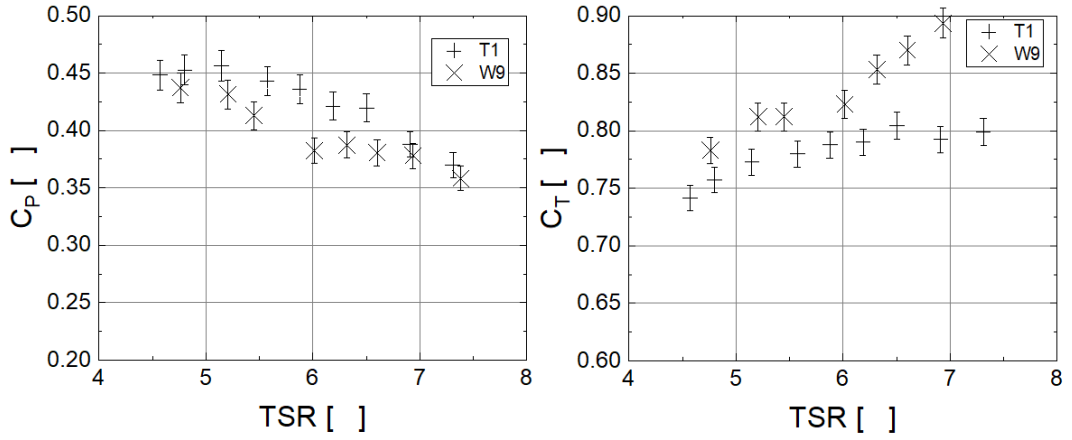

TSR	Cp W9	σ (Cp W9)	Ct W9	σ (Ct W9)	Cp T1	Ct T1	diff Cp (%)	diff Ct (%)
4.8	0.44	0.01279	0.78	0.01147	0.45	0.76	-3%	3%
5.2	0.43	0.01262	0.81	0.01190	0.45	0.77	-4%	6%
5.4	0.41	0.01207	0.81	0.01190	0.45	0.77	-8%	5%
6.0	0.38	0.01119	0.82	0.01206	0.44	0.78	-12%	5%
6.3	0.39	0.01133	0.85	0.01251	0.42	0.79	-9%	8%
6.6	0.38	0.01113	0.87	0.01275	0.41	0.79	-7%	9%
6.9	0.38	0.01106	0.89	0.01310	0.39	0.80	-3%	12%
7.4	0.36	0.01048	0.91	0.01340	0.36	0.81	0%	13%
						Average	-6%	8%

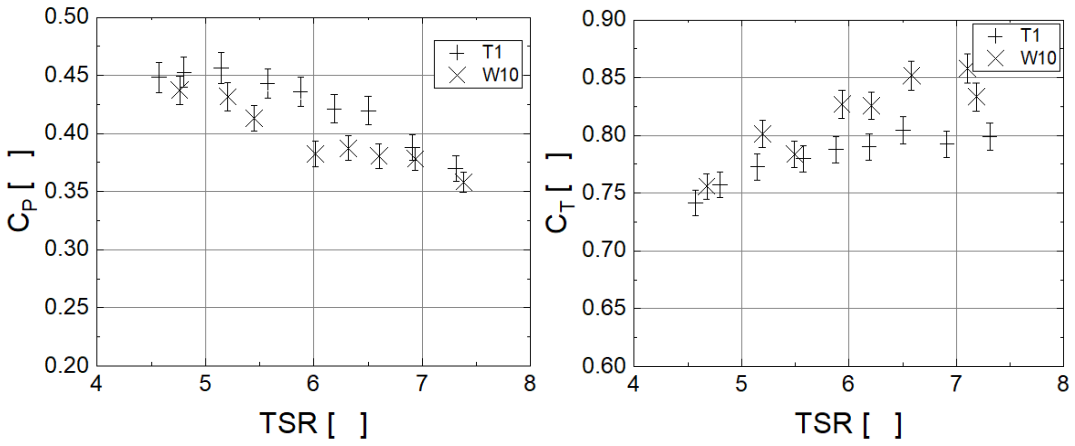

TSR	Cp W10	σ (Cp W10)	Ct W10	σ (Ct W10)	Cp T1	Ct T1	diff Cp (%)	diff Ct (%)
4.7	0.41	0.01194	0.76	0.01108	0.45	0.76	-9%	0%
5.2	0.42	0.01220	0.80	0.01174	0.45	0.77	-7%	4%
5.5	0.38	0.01109	0.78	0.01149	0.45	0.77	-15%	1%
5.9	0.39	0.01137	0.83	0.01212	0.44	0.78	-11%	6%
6.2	0.37	0.01072	0.83	0.01210	0.43	0.79	-14%	5%
6.6	0.37	0.01071	0.85	0.01249	0.41	0.79	-11%	7%
7.1	0.33	0.00974	0.86	0.01257	0.38	0.80	-12%	7%
7.2	0.30	0.00884	0.83	0.01222	0.37	0.81	-19%	3%
						Average	-12%	4%

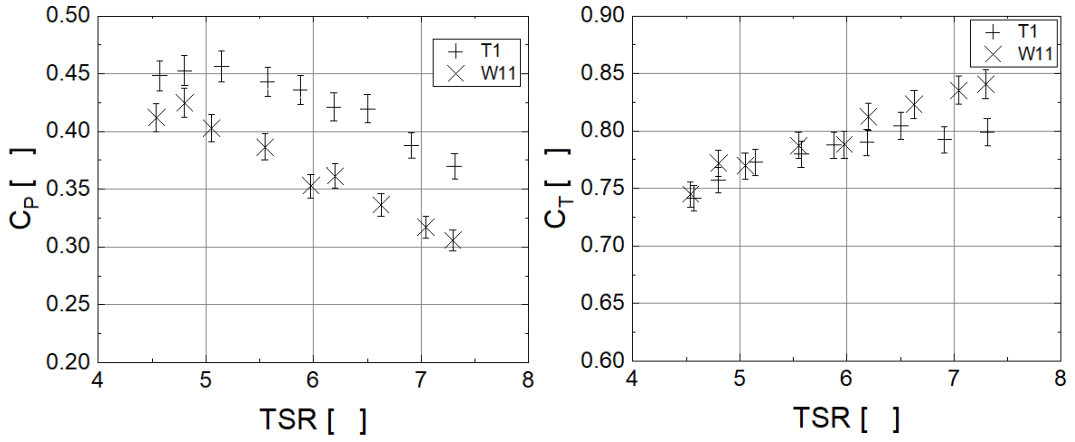

TSR	Cp W11	σ (Cp W11)	Ct W11	σ (Ct W11)	Cp T1	Ct T1	diff Cp (%)	diff Ct (%)
4.5	0.41	0.01205	0.74	0.01092	0.45	0.75	-8%	-1%
4.8	0.42	0.01242	0.77	0.01131	0.45	0.76	-6%	2%
5.1	0.40	0.01179	0.77	0.01128	0.45	0.76	-11%	1%
5.5	0.39	0.01131	0.79	0.01154	0.45	0.77	-14%	2%
6.0	0.35	0.01032	0.79	0.01155	0.44	0.78	-19%	1%
6.2	0.36	0.01057	0.81	0.01191	0.43	0.79	-16%	3%
6.6	0.34	0.00983	0.82	0.01206	0.41	0.80	-18%	3%
7.0	0.32	0.00928	0.84	0.01224	0.38	0.80	-17%	4%
7.3	0.31	0.00894	0.84	0.01232	0.36	0.81	-16%	4%
						Average	-14%	2%

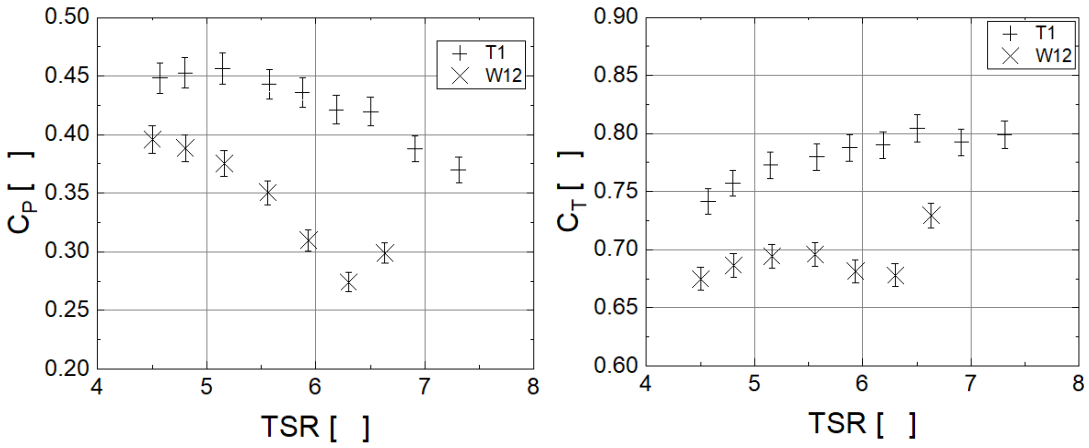

TSR	Cp W12	σ (Cp W12)	Ct W12	σ (Ct W12)	Cp T1	Ct T1	diff Cp (%)	diff Ct (%)
4.5	0.40	0.01158	0.67	0.00989	0.45	0.75	-11%	-10%
4.8	0.39	0.01136	0.69	0.01006	0.45	0.76	-14%	-10%
5.2	0.38	0.01098	0.69	0.01018	0.45	0.77	-17%	-9%
5.6	0.35	0.01025	0.70	0.01020	0.45	0.77	-22%	-10%
5.9	0.31	0.00906	0.68	0.00999	0.44	0.78	-29%	-13%
6.3	0.27	0.00802	0.68	0.00994	0.42	0.79	-35%	-14%
6.6	0.30	0.00874	0.73	0.01069	0.41	0.80	-27%	-8%
						Average	-22%	-11%

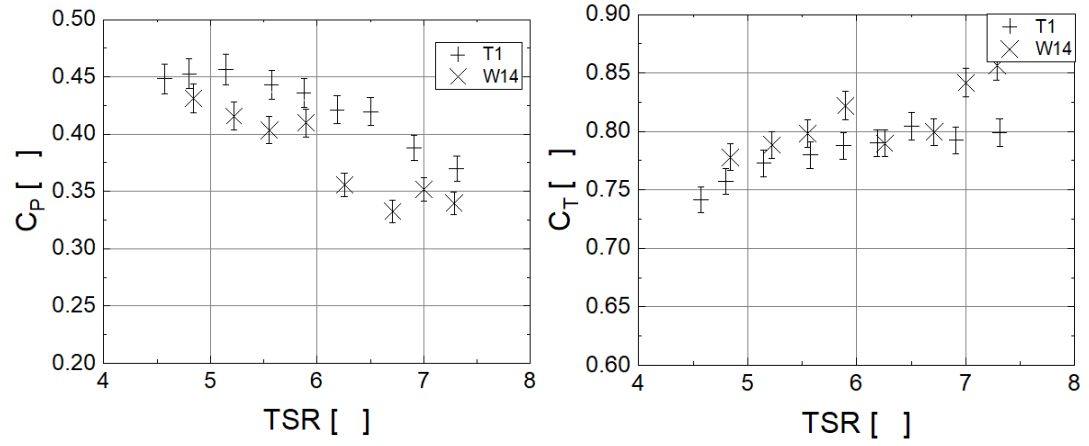

TSR	Cp W14	σ (Cp W14)	Ct W14	σ (Ct W14)	Cp T1	Ct T1	diff Cp (%)	diff Ct (%)
4.8	0.43	0.01261	0.78	0.01140	0.45	0.76	-4%	2%
5.2	0.42	0.01216	0.79	0.01156	0.45	0.77	-8%	3%
5.6	0.40	0.01180	0.80	0.01170	0.45	0.77	-10%	3%
5.9	0.41	0.01198	0.82	0.01205	0.44	0.78	-7%	5%
6.3	0.36	0.01041	0.79	0.01158	0.43	0.79	-17%	0%
6.7	0.33	0.00972	0.80	0.01172	0.40	0.80	-18%	0%
7.0	0.35	0.01029	0.84	0.01234	0.39	0.80	-9%	5%
7.3	0.34	0.00993	0.86	0.01255	0.37	0.81	-7%	6%
						Average	-10%	3%

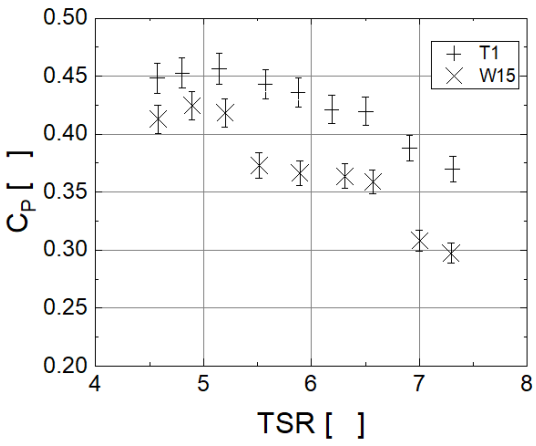

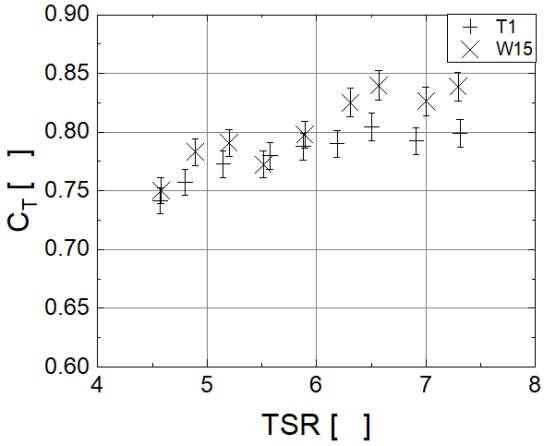

TSR	Cp W15	σ (Cp W15)	Ct W15	σ (Ct W15)	Cp T1	Ct T1	diff Cp (%)	diff Ct (%)
4.6	0.41	0.01208	0.75	0.01100	0.45	0.76	-8%	-1%
4.9	0.42	0.01242	0.78	0.01148	0.45	0.76	-6%	3%
5.2	0.42	0.01224	0.79	0.01159	0.45	0.77	-7%	3%
5.5	0.37	0.01091	0.77	0.01132	0.45	0.77	-17%	0%
5.9	0.37	0.01072	0.80	0.01169	0.44	0.78	-17%	2%
6.3	0.36	0.01064	0.83	0.01210	0.42	0.79	-14%	5%
6.6	0.36	0.01049	0.84	0.01231	0.41	0.79	-13%	6%
7.0	0.31	0.00901	0.83	0.01211	0.39	0.80	-20%	3%
7.3	0.30	0.00869	0.84	0.01229	0.36	0.81	-19%	4%
						Average	-13%	3%

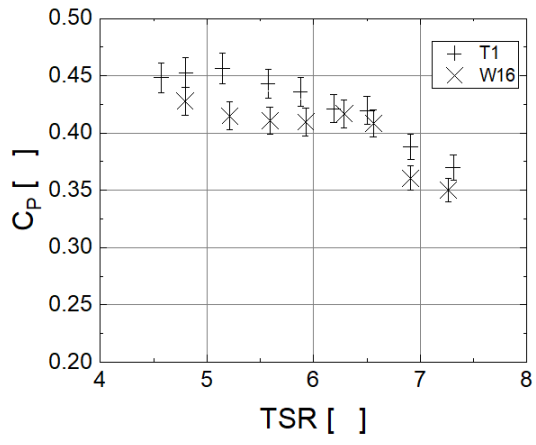

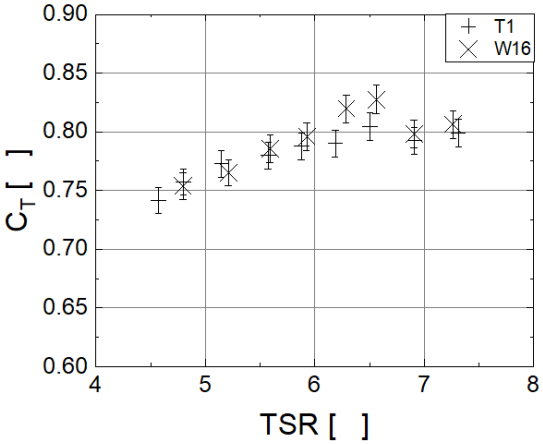

TSR	Cp W16	σ (Cp W16)	Ct W16	σ (Ct W16)	Cp T1	Ct T1	diff Cp (%)	diff Ct (%)
4.8	0.43	0.01251	0.75	0.01105	0.45	0.76	-5%	-1%
5.2	0.41	0.01214	0.77	0.01122	0.45	0.77	-8%	0%
5.6	0.41	0.01201	0.79	0.01151	0.45	0.77	-8%	1%
5.9	0.41	0.01198	0.80	0.01167	0.44	0.78	-7%	2%
6.3	0.42	0.01219	0.82	0.01201	0.43	0.79	-2%	4%
6.6	0.41	0.01195	0.83	0.01213	0.41	0.79	-1%	4%
6.9	0.36	0.01055	0.80	0.01170	0.39	0.80	-8%	0%
7.3	0.35	0.01024	0.81	0.01182	0.37	0.81	-5%	0%
						Average	-5%	1%

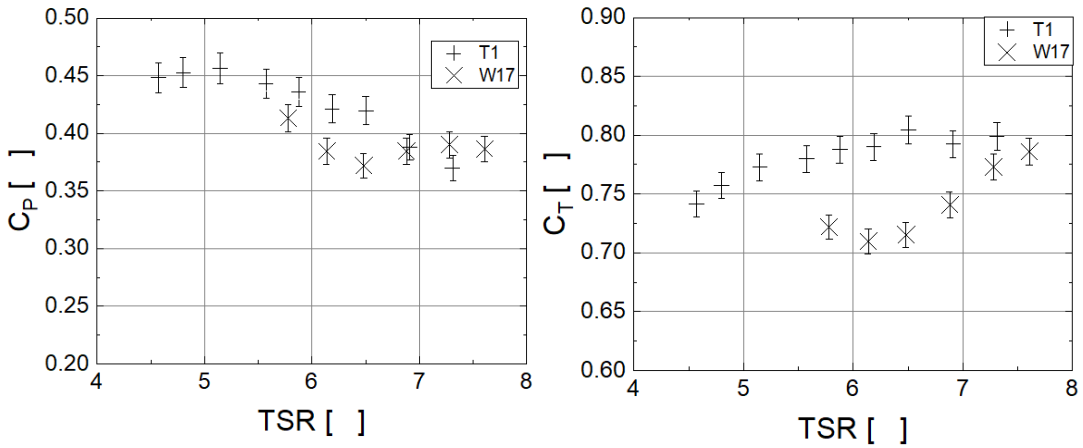

TSR	Cp W17	σ (Cp W17)	Ct W17	σ (Ct W17)	Cp T1	Ct T1	diff Cp (%)	diff Ct (%)
5.8	0.41	0.01209	0.72	0.01058	0.44	0.78	-7%	-7%
6.1	0.38	0.01124	0.71	0.01040	0.43	0.79	-11%	-10%
6.5	0.37	0.01087	0.72	0.01048	0.42	0.79	-11%	-10%
6.9	0.38	0.01125	0.74	0.01086	0.39	0.80	-2%	-7%
7.3	0.39	0.01141	0.77	0.01133	0.37	0.81	7%	-4%
7.6	0.39	0.01130	0.79	0.01152	0.34	0.81		
8.0	0.33	0.00978	0.76	0.01116	0.30	0.82		
						Average	-5%	-8%

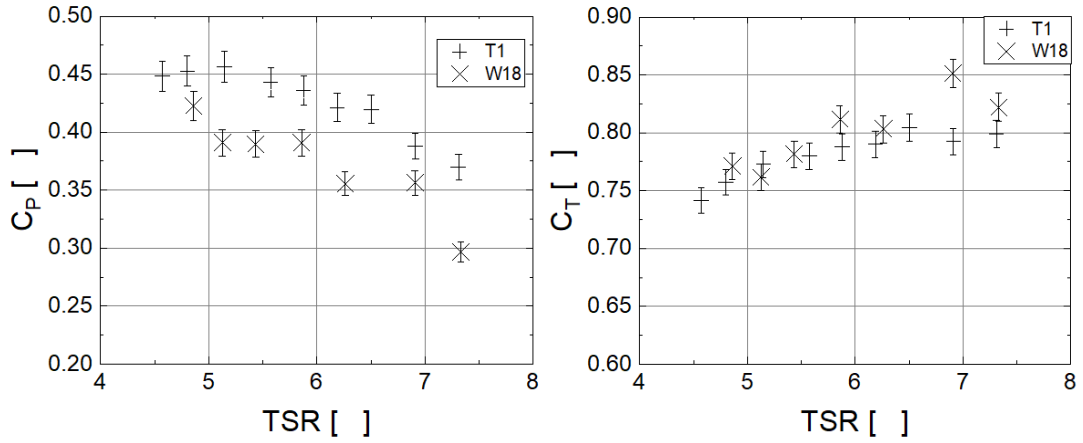

TSR	Cp W18	σ (Cp W18)	Ct W18	σ (Ct W18)	Cp T1	Ct T1	diff Cp (%)	diff Ct (%)
4.9	0.42	0.01236	0.77	0.01130	0.45	0.76	-6%	1%
5.1	0.39	0.01144	0.76	0.01116	0.45	0.77	-13%	-1%
5.4	0.39	0.01139	0.78	0.01146	0.45	0.77	-13%	1%
5.9	0.39	0.01144	0.81	0.01190	0.44	0.78	-11%	4%
6.3	0.36	0.01040	0.80	0.01177	0.43	0.79	-17%	2%
6.9	0.36	0.01042	0.85	0.01248	0.39	0.80	-9%	6%
6.9	0.36	0.01042	0.85	0.01248	0.39	0.80	-9%	6%
7.3	0.30	0.00868	0.82	0.01205	0.36	0.81	-18%	2%
						Average	-12%	3%

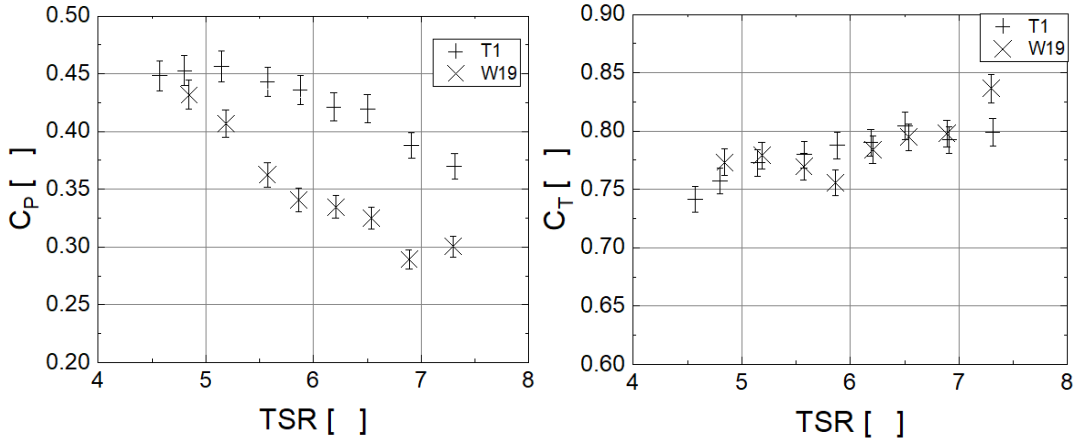

TSR	Cp W19	σ (Cp W19)	Ct W19	σ (Ct W19)	Cp T1	Ct T1	diff Cp (%)	diff Ct (%)
4.8	0.43	0.01263	0.77	0.01134	0.45	0.76	-4%	2%
5.2	0.41	0.01190	0.78	0.01142	0.45	0.77	-10%	2%
5.6	0.36	0.01061	0.77	0.01128	0.45	0.77	-19%	-1%
5.9	0.34	0.00996	0.76	0.01108	0.44	0.78	-23%	-3%
6.2	0.33	0.00979	0.78	0.01149	0.43	0.79	-22%	0%
6.5	0.33	0.00951	0.79	0.01165	0.41	0.79	-21%	0%
6.9	0.29	0.00846	0.80	0.01170	0.39	0.80	-27%	0%
7.3	0.30	0.00878	0.84	0.01226	0.36	0.81	-18%	3%
						Average	-18%	0%

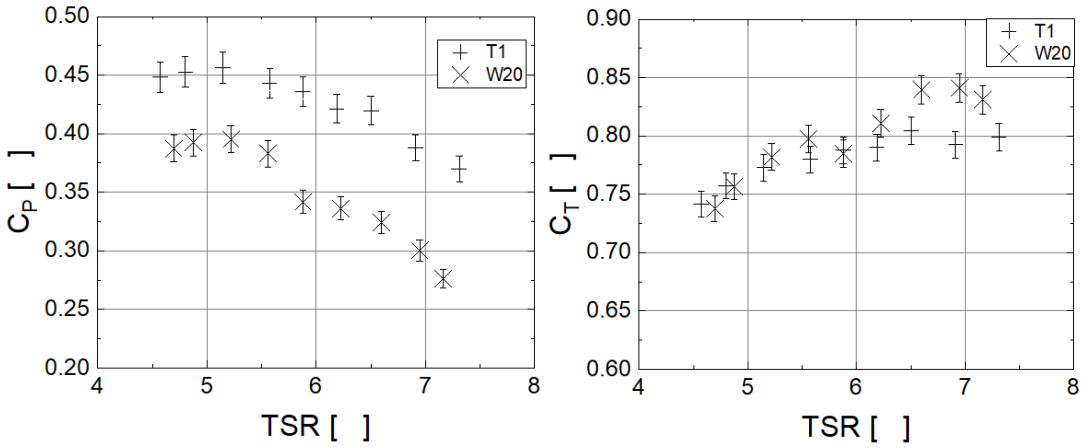

TSR	Cp W20	σ (Cp W20)	Ct W20	σ (Ct W20)	Cp T1	Ct T1	diff Cp (%)	diff Ct (%)
4.7	0.39	0.01133	0.74	0.01081	0.45	0.76	-14%	-3%
4.9	0.39	0.01148	0.76	0.01109	0.45	0.76	-13%	-1%
5.2	0.40	0.01156	0.78	0.01146	0.45	0.77	-12%	2%
5.6	0.38	0.01120	0.80	0.01168	0.45	0.77	-14%	3%
5.9	0.34	0.01000	0.78	0.01150	0.44	0.78	-22%	1%
6.2	0.34	0.00983	0.81	0.01188	0.43	0.79	-21%	3%
6.6	0.32	0.00948	0.84	0.01231	0.41	0.79	-21%	6%
6.9	0.30	0.00878	0.84	0.01233	0.39	0.80	-23%	5%
7.2	0.28	0.00808	0.83	0.01218	0.37	0.81	-26%	3%
						Average	-19%	2%

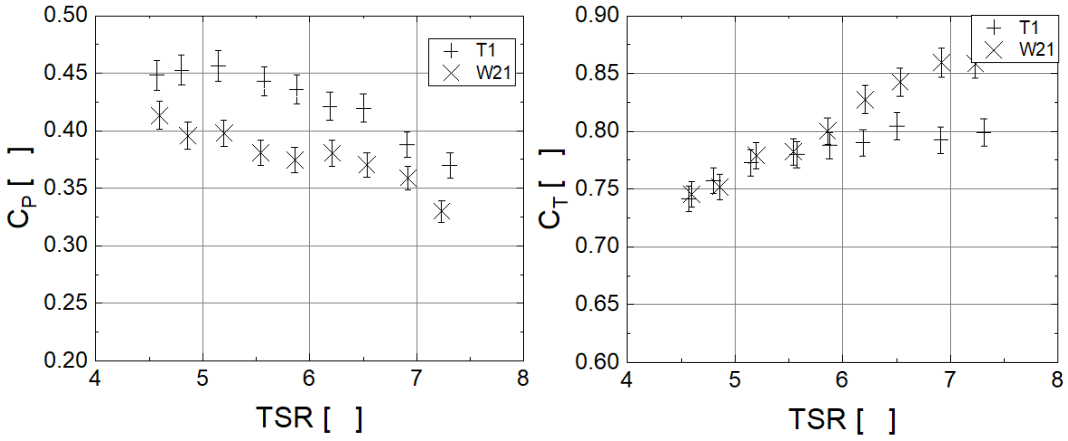

TSR	Cp W21	σ (Cp W21)	Ct W21	σ (Ct W21)	Cp T1	Ct T1	diff Cp (%)	diff Ct (%)
4.6	0.41	0.01209	0.75	0.01093	0.45	0.76	-8%	-1%
4.9	0.40	0.01157	0.75	0.01102	0.45	0.76	-12%	-1%
5.2	0.40	0.01163	0.78	0.01142	0.45	0.77	-12%	2%
5.5	0.38	0.01113	0.78	0.01147	0.45	0.77	-15%	1%
5.9	0.37	0.01096	0.80	0.01173	0.44	0.78	-15%	3%
6.2	0.38	0.01113	0.83	0.01213	0.43	0.79	-11%	5%
6.5	0.37	0.01083	0.84	0.01235	0.41	0.79	-11%	6%
6.9	0.36	0.01050	0.86	0.01260	0.39	0.80	-8%	7%
7.2	0.33	0.00965	0.86	0.01259	0.37	0.81	-11%	6%
						Average	-11%	3%

Appendix B Logbook

There were 5 main periods of experiments with the tidal turbine. Table 6-1 contains a daily summary, and more details can be found from Table 6-2 to Table 6-5. The first period was from the 17th to the 21st of September 2018. The second one from the 20th to the 24th of March 2019 at the University of Edinburgh for a joint project with Cardiff University and the University of Strathclyde. The third period included the 15th and the 17th of April 2019, the first day was dedicated to the Group Design Project 38 of Master's students. The last periods comprised from the 10th to the 14th of May and from the 8th to the 12th of July 2019. During that time, nearly 500 test runs were performed, the mounting time was halved to around 2-3 hours and the characterisation of winglets in the towing tank passed from lasting 1 hour to just half an hour. The slip-ring of the turbine got loose after all the tests, and the turbine had to be rewired due to an unidentified loose connection. One generator was burnt after towing the turbine at more than 1.4 *m/s* to test the clutch at the towing tank.

Table 6-1 Logbook Summary

Project	Date	Summary
UoS (1st Round)	13/09/2018	Thrust and torque pre-calibration.
	14/09/2018	Drop off turbine at Solent University Towing Tank.
	17/09/2018	First time turbine is mounted. Some pins needed to be cut to fit.
	18/09/2018	Deploy turbine, warm-up, repeatability test and Cp and Ct curves.
	19/09/2018	Retest T1 and test W2 - W4 and W6. W5 had a 3D printing defect.
	20/09/2018	Test W7 and W18 - half curves of W21.
	21/09/2018	Test 2nd half of W21, W15-W17, and W5. Retest T1, and W15.
	24/09/2018	Pick-up turbine at Solent University Towing Tank.
	03/10/2018	Torque and thrust calibration.
FloWave (Joint project)	15/03/2019	Ship 8 boxes with 200-300 kg of equipment to Edinburgh.
	18/03/2019	7 of 8 boxes arrived. A toolbox went missing.
	20/03/2019	Plug 10 *m* extension needed, mount turbine and take zeros when dry.
	21/03/2019	Take new zeros, zeros when wet and Run @ 0.85 *m/s and 85, 90 rpm*.
	22/03/2019	Recheck wires. Run @ 0.85 *m/s* and 95, 100 rpm.
	25/03/2019	Zeros for day 3. Run @ 0.85 *m/s* and 105, 110 rpm.
	26/03/2019	The experiment was stopped due to a leak in one of the other turbines.
	03/04/2019	Post-testing calibration.
Group Design Project 38	08/04/2019	Pre-testing calibration.
	11/04/2019	Drop-off turbine at Solent University Towing Tank.
	12/04/2019	Support GDP 38.
	15/04/2019	Mount turbine and run the turbine with the GDP38 set-up.
UoS (2nd round)	16/04/2019	It was determined that the turbine had a loose connection.
	17/04/2019	Easter Break.
	22/04/2019	
	24/04/2019	Pick-up turbine.

Appendix B

Project	Date	Summary
Turbine	25/04/2019	Source new cables and glands to rewire the turbine.
	29/04/2019 02/05/2019	Turbine re-wiring.
	07/05/2019	Zero readings, thrust and torque calibration.
UoS (3rd round)	09/05/2019	Drop off turbine at Solent University Towing Tank.
	10/05/2019	Turbine mounted, Dr. Myers blades tested. The slip ring is loose.
	11/05/2019	The slip ring is adjusted and other connections checked.
	13/05/2019	The turbine is working, the electronic load is used. Generator blows.
	14/05/2019	Change blown generator and test W5, W9, W12 and W15.
	17/05/2019	Pick up turbine.
UoS (4th round)	03/07/2019	Torque and thrust calibration.
	05/07/2019	Drop off turbine at Solent University Towing Tank.
	08/07/2019	Mount turbine and run at a 3rd speed to make analysis on Re effect.
	09/07/2019	Try Re test with W5. Complete T1 curves and run W2-4.
	10/07/2019	Test W6-W19.
	11/07/2019	Test W20, W21. Oil flow visualisation for T1, and W2-W4.
	12/07/2019	Oil flow visualisation for W5-W21 and the blade. Re effect on W7.
	15/07/2019	Pick up turbine.

Table 6-2 First set of experiments.

Place	Date	Time	Activity	Tip/ Winglet	Speed [m/s]	rpm [ ]
B21 UoS	13/09/2018	17:00-18:00	Pre-calibration	None		
Solent University	14/09/2018	16:00-17:00	Drop off turbine			
	17/09/2018	09:00-17:00	Mounting			
	18/09/2018	09:00-09:30	Deploy turbine			
		09:30-11:00	Setting-up	Tips		
		11:00-12:00	Test runs		Several	
		13:00-14:00	Repeatability tests			
		14:00-18:00	Characterisation		0.76	70-120
		18:00-18:30	Retrieve turbine			
	19/09/2018	09:00-09:30	Deploy turbine	Tips		
		09:30-10:30	Run 2		0.76	65-115
		10:30-12:00	Change tips	W2		
		12:00-13:00	Tests		0.76	65-115
		13:00-13:30	Change tips	W3		
		13:30-15:30	Tests		0.76	65-115
		15:30-16:00	Change tips	W4		
		16:00-17:00	Tests		0.76	65-115
		17:00-17:30	Change tips	W6		
		17:30-18:30	Tests		0.76	55-100
		18:30-19:00	Retrieve turbine			
	20/09/2018	09:00-09:30	Deploy turbine	W7		
		09:30-11:00	Tests		0.76	65-125
		11:30-12:00	Change tips	W18		
		12:00-13:00	Tests		0.76	60-120

Place	Date	Time	Activity	Tip/ Winglet	Speed [m/s]	rpm [ ]
		14:00-14:30	Change tips	W19		
		14:30-15:30	Tests		0.76	60-110
		15:30-16:00	Change tips	W20		
		16:00-17:00	Tests		0.76	60-115
		17:00-17:30	Change tips	W21		
		17:30-18:00	Tests		0.76	60-100
		18:00-18:30	Retrieve turbine			
	21/09/2018	08:30-09:00	Deploy turbine	W21		
		09:00-09:30	Tests		0.76	105-120
		10:00-10:30	Change tips	W15		
		10:30-11:30	Tests		0.76	60-120
		11:30-12:00	Change tips	W16		
		12:00-12:30	Tests		0.76	60-125
		12:30-13:00	Change tips	W17		
		13:00-14:00	Tests		0.76	65-125
		14:00-14:30	Change tips	W5		
		14:30-15:00	Tests		0.76	60-110
		15:00-15:30	Run 2		0.76	100-155
		15:30-16:00	Change tips	T1		
		16:00-16:30	Run 3		0.76	100-165
		16:30-17:00	Change tips	W15		
		17:00-17:30	Run 2		0.76	100-165
		17:30-18:00	Retrieve turbine			
		18:00-21:00	Unmounting			
	24/09/2018	16:00-17:00	Pick up turbine			
UoS	03/10/2020	16:00-17:00	Post-calibration			

Appendix B

Table 6-3 Joint projects.

Place	Date	Time	Activity	Tip/ Winglets	Speed [m/s]	rpm [ ]
Post room	15/03/2019		Ship equipment			
FloWave, Edinburgh (Joint project)	18/03/2019		7/8 boxes arrived			
	20/03/2019	09:00-13:00	Mounting			
		13:30-14:00	Lower platform			
		14:00-14:30	Zeros when dry			
		16:30-17:00	Lift platform			
	21/03/2019	09:00-12:00	Place turbine and lower platform			
		12:30-13:00	New zeros			
		13:00-14:00	Running the tank			
		14:00-15:00	Zeros when wet			
		15:00-16:00	Runs 1-4	Tips	0.85	85-90
		16:00-17:00	Lift platform			
	22/03/2019	09:00-12:00	Rewire turbine and lower platform			
		12:00-13:00	Zeros2 when wet			
		13:00-15:00	Runs 5-8		0.85	95-100
		15:00-	Lift platform			
	25/03/2019	09:00-09:30	Zeros dry day 3			
		09:30-10:30	Lower platform			
		10:30-13:00	Runs 9-12		0.85	105-110
	26/03/2019	09:00-12:00	Preparation and lowering platform			
		12:00-12:30	Zeros wet day 4			
		13:30-14:00	Last run		0.85	-
		14:00-17:00	Unmounting			
	28/03/2019		Equipment collection			
UoS	29/03/2019		Equipment arrived			
	03/04/2019	16:00-17:00	Post-testing calibration			
	08/04/2019	14:00-16:00	Pre-testing calibration			
Solent University (Group Design Project 38)	11/04/2019	16:00-17:00	Drop off turbine			
	12/04/2019	09:00-17:00	Support			
	15/04/2019	09:00-10:30	Mount turbine			
		10:30-11:00	Warm up and zero readings			
		11:00-12:00	Runs 1-2 Setting 1	Tips	0.7	60-70
		12:00-12:30	Zeros midday			
		12:30-13:00	Runs 3-6 Setting 1		0.7	75-90
		13:00-13:30	Zeros after lunchtime			
		13:30-14:30	Setting 2		0.7	55-95
		14:30-15:30	Setting 3		0.7	55-95
		16:00-16:30	Setting 4		0.7	55-95
		17:00-17:30	Setting 5		0.7	55-95
		17:30-18:00	Lift platform			
		19:00-19:30	Zeros after testing			

Table 6-4 Second and third round of experiments.

Place	Date	Time	Activity	Tip/ Winglets	Speed [m/s]	rpm [ ]
Solent University	16/04/2019	08:00-8:30	Lower turbine			
		08:30-09:00	Zeros			
		09:00-10:00	Baseline	Tips	0.7	60-
		10:00-11:00	Baseline 2		0.76	-120
		11:00-11:30	Baseline 3		0.76	
		11:30-12:00	Baseline 4th attempt		0.76	Loose c.
		12:00-12:30	Baseline 5		0.76	80-120
		12:30-13:00	Repeat baseline		0.76	80-120
		13:00-13:30	Re-repeat baseline		0.76	80-120
		13:30-14:00	Change tips	W5		
		14:30-16:00	Test		0.76	65-110
		16:00-16:30	Change tips	Tips		
		14:30-17:00	Test		0.76	70-120
		17:00-17:30	Re-test		0.76	70-130
		17:30-18:00	Lift turbine			
		18:00-20:00	Unmount turbine			
	17/04/2019		Easter Break			
	22/04/2019					
	24/04/2019	16:00-17:00	Pick-up turbine			
UoS	07/05/2019	16:00-16:15	Zero readings, thrust and torque calibration			
Solent University	09/05/2019	16:00-17:00	Drop off turbine			
	10/05/2019	08:00-11:00	Mount turbine			
		11:00-11:30	Warm up and zeros			
		11:30-12:00	Baseline	Tips	0.76	65-115
		12:00-12:30	Change blades	Dr. Myers	0.76	100-120
		12:30-13:00	Lift turbine			
	11/05/2019	12:00-15:00	Check connections			
	13/05/2019	08:30-09:00	Lower turbine	Tips		
		09:00-09:30	Warm up and zeros			
		09:30-10:00	Baseline		0.76	65-120
		10:00-10:30	Recheck connections			
		10:30-13:00	Recheck baseline		0.76	65-120
		14:00-14:30	Baseline speed 2		0.85	80-135
		15:00-16:00	Baseline*		0.76	65-100
		16:00-17:00	Repeatability		0.76	80
		17:00-17:30	Lift turbine			
	14/05/2019	09:00-11:30	Change blown generator			
		11:30-12:00	Baseline speed 2		0.85	85-110
		12:00-12:30	Change tips	W5		
		12:30-13:30	Test		0.76	65-110
		13:30-14:00	Change tips	W15		
		15:00-15:30	Recheck connections			
		15:30-16:00	Test		0.76	65-105
		16:00-16:30	Change tips	W12		
		16:30-17:00	Test		0.76	65-100
		17:00-17:30	Change tips	W9		

Appendix B

Place	Date	Time	Activity	Tip/ Winglets	Speed [m/s]	rpm [ ]
		17:30-18:00	Test		0.76	65-100
		18:00-18:30	Lift turbine			
		18:30-21:00	Unmount			
	17/05/2019	16:00-17:00	Pick up turbine			

Table 6-5 Last set of experiments.

Place	Date	Time	Activity	Tip/ Winglets	Speed [m/s]	rpm [ ]
UoS	03/07/2019	15:00-16:00	Torque and thrust calibration			
Solent	05/07/2019	14:00-17:00	Drop off turbine			
University	08/07/2019	09:00-12:30	Mount turbine	Tips		
		13:30-15:00	Warm-up and zeros with LD300		0.76	
		15:00-16:30	Baseline speed 3		0.80	75-110
		16:30-17:00	Lift turbine			
	09/07/2019	10:00-10:30	Lower turbine	W5		
		10:30-11:00	Test		0.76	65-100
		11:30-12:00			0.80	75-110
		12:00-12:30			0.85	80-105
		12:30-13:00	Change tips	T1		
		13:00-13:30	Retake 2 points		0.80	80, 85
		13:30-14:00	Change tips	W2		
		14:30-15:00	Test		0.76	70-105
		15:00-16:00	Change tips	W3, W4		
			Test		0.76	65-105
		17:00-17:30	Lift turbine			
	10/07/2019	09:00-12:00	Lower turbine	W6-W8		
			Test		0.76	70-105
		12:00-14:00	Change tips	W10, W11		
			Test		0.76	65-105
		14:00-16:30	Change tips	W14, W16		
			Test		0.76	70-105
		16:30-17:00	Change tips	W17		
		17:00-17:30	Test		0.76	75-105
		17:30-19:30	Change tips	W18, W19		
			Test		0.76	70-105
		19:30-20:00	Lift turbine			
	11/07/2019	10:00-10:30	Lower turbine	W20		
		10:30-11:00	Test		0.76	70-105
		11:00-14:30	Change tips	W21, T1		
			Test		0.76	65-105
		14:30-17:00	Prepare turbine for oil flow visualisation.			
		17:00-17:30	Test		0.76	75
		17:00-18:30	Change tips	W2-W4		
			Paint test		0.76	75
		18:30-19:00	Lift turbine			

Place	Date	Time	Activity	Tip/ Winglets	Speed [m/s]	rpm [ ]
	12/07/2019	09:00-09:30	Lower turbine	W5		
		09:30-10:00	Paint test		0.76	75
		10:00-13:00	Change tips	W6-W14		
			Paint test		0.76	75
		13:30-18:30	Change tips	W15-W21		
			Paint test		0.76	75
		18:30-19:00	Change tips	W7		
		19:00-19:30	Test		0.80	80-110
		19:30-20:00	Test		0.85	90-115
		20:00-20:30	Change tips	T1		
		20:30-21:00	Blade paint test		0.76	75
		21:00-24:00	Unmount turbine			
	15/07/2019	16:00-17:00	Pick up turbine			

Appendix C Example data of a run

The script in LabView indicated the DAQ box to sample at a frequency of 100 *Hz*. The row labelled 'Untitled' corresponds to the position of the blade in degrees, it is negative as the turbine rotates counter clockwise. 'Untitled 2' is the row where the signal of the torque is recorded as voltage, and 'Untitled 3' is the one of the thrust. From Table 6-6 it can be seen that one turn goes from -352.2 degrees to -356.4., that is 1.01167 revolutions. The time taken is 06.802361-6.182678=0.619683 *s*, 41 points are taken, so the effective sampling rate is around 67 *Hz*. In practice, it is inside the range of sampling rate which was from 66 to 67 *Hz*. The resolution is up to 15 μV, because the voltage range was 1 *V* and it is a 16-bit analogue to digital converter (1 *V*/1^16 *bit*) (National Instruments, 2009, p. Chapter 4-2). The last row titled 'Comment' is the timestamp of the sample in the format HH:MM:SS.

Table 6-6 Data for one revolution of W16 at 100 rpm.

Untitled	Untitled 1	Untitled 2	Untitled 3	Untitled 4	Comment
-352.200000	-0.109008	0.374269	-0.193113	-0.165845	10:09:06.182678
-3.225000	-0.340955	0.363099	-0.207897	-0.289046	10:09:06.201599
-9.675000	-0.519350	0.392996	-0.205269	-0.510808	10:09:06.211570
-22.950000	-0.604441	0.324989	-0.190156	-0.419475	10:09:06.234199
-32.100000	-0.165188	0.378540	-0.191142	-0.031473	10:09:06.249116
-37.725000	-0.295617	0.397595	-0.202312	-0.301859	10:09:06.258088
-49.425000	-0.358039	0.352586	-0.189499	-0.316643	10:09:06.277949
-59.700000	-0.397463	0.342073	-0.213154	-0.326499	10:09:06.294968
-69.975000	-0.196727	0.338459	-0.221039	-0.145804	10:09:06.310785
-77.775000	0.199488	0.420264	-0.239108	0.045733	10:09:06.324923
-90.375000	0.094356	0.369998	-0.224981	-0.135291	10:09:06.345831
-96.300000	-0.562060	0.387739	-0.209869	-0.601813	10:09:06.355764
-103.575000	-0.095538	0.318418	-0.223010	-0.010776	10:09:06.367729
-113.250000	-0.043629	0.391353	-0.230895	-0.126420	10:09:06.383718
-121.800000	-0.516393	0.357842	-0.236152	-0.524935	10:09:06.398103
-127.875000	-0.108351	0.324003	-0.235494	-0.033116	10:09:06.406684
-135.825000	-0.248636	0.379854	-0.239765	-0.335041	10:09:06.420601
-144.600000	-0.586372	0.354885	-0.236809	-0.499309	10:09:06.434736
-155.100000	-0.426046	0.368027	-0.239765	-0.294302	10:09:06.453135
-161.325000	-0.000591	0.392339	-0.218739	-0.016689	10:09:06.462625
-171.600000	-0.262434	0.309876	-0.225638	-0.331427	10:09:06.479575
-180.525000	-0.479926	0.426835	-0.231881	-0.414218	10:09:06.494606
-188.475000	0.013865	0.337473	-0.217753	0.010251	10:09:06.507542
-197.175000	-0.006176	0.398581	-0.229252	-0.123792	10:09:06.522461
-205.425000	-0.522307	0.384782	-0.211840	-0.571259	10:09:06.535426
-214.575000	-0.305801	0.328931	-0.218411	-0.130363	10:09:06.551383
-221.850000	0.003680	0.442933	-0.244365	-0.078783	10:09:06.562801
-235.425000	0.043104	0.353243	-0.218411	-0.118864	10:09:06.585741
-241.875000	-0.588343	0.406466	-0.229581	-0.595571	10:09:06.596709

Untitled	Untitled 1	Untitled 2	Untitled 3	Untitled 4	Comment
-250.425000	-0.335370	0.353900	-0.223010	-0.179315	10:09:06.609708
-259.950000	0.043762	0.375583	-0.217096	-0.046257	10:09:06.626546
-269.175000	-0.226953	0.405152	-0.216111	-0.321242	10:09:06.640270
-278.025000	-0.622839	0.315790	-0.182600	-0.492082	10:09:06.656417
-284.700000	-0.016032	0.385768	-0.211840	0.047375	10:09:06.667388
-294.675000	0.000723	0.369341	-0.203626	-0.132663	10:09:06.683374
-305.475000	-0.292988	0.402195	-0.176029	-0.322557	10:09:06.701297
-312.450000	-0.441487	0.376569	-0.205926	-0.421118	10:09:06.713267
-321.900000	-0.125763	0.332216	-0.198370	-0.045929	10:09:06.728261
-328.575000	-0.337341	0.445890	-0.174058	-0.351468	10:09:06.739528
-341.775000	-0.183586	0.335502	-0.199027	-0.156317	10:09:06.761469
-347.175000	-0.244693	0.408765	-0.184571	-0.218411	10:09:06.771445
-356.400000	0.063145	0.329917	-0.185228	0.019450	10:09:06.786452
-6.825000	-0.041986	0.403180	-0.195742	-0.189828	10:09:06.802361

Appendix D Bending moment calculation for a tsr of 4.5

pos	pos root	c	Cd	Cl	phi	vloc	F/(H*Cl,d)	Flx/H	Fdx/H	Fx/H	dH	Fx	Fxcorr	Fxr	Mofx	Fly/H	Fdy/H	Fy/H	Fy	Mofy	Mofyroot	Myrootcor	Fycorr	Mofyrootcorr
0.0280	0.0000														17.2402978									3.322362577
	0.0040														17.01664519									
	0.0080														16.79299259									
	0.0120														16.56933998									
	0.0160														16.34568738									
	0.0200														16.12203477									
	0.0240														15.89838217									
	0.0280														15.67472956									
	0.0320														15.45107696									
	0.0360														15.22742435									
	0.0400														15.00377175									
	0.0426	0.1244261	0.180006	0.565271	47.552	0.882593	48.46211	18.48893091	6.436963	24.92589	0.0009	0.0224358	0.022807	0.000972	14.85833046	20.21393	5.887651	14.32628	0.012895	0.00091	0.000549	0.000577	0.013542783	2.79584982
	0.0444	0.1239629	0.180638	0.572982	46.9043	0.888446	48.9242	19.15246172	6.453313	25.60577	0.0024	0.0613169	0.06233	0.002758	14.7576756	20.46985	6.037995	14.43185	0.034559	0.002502	0.001534	0.001612	0.036299092	2.773625337
	0.0474	0.1231958	0.181206	0.581099	45.7722	0.897684	49.63784	20.11941056	6.445335	26.56475	0.0036	0.0949743	0.096544	0.004575	14.59073191	20.66917	6.273902	14.39527	0.051466	0.00388	0.002439	0.002562	0.054051021	2.736831702
	0.0516	0.1221321	0.182774	0.605909	44.3119	0.913635	50.9736	22.09995114	6.508275	28.60823	0.0047	0.1354828	0.137722	0.0071	14.35872164	21.5754	6.666507	14.9089	0.070606	0.005617	0.00364	0.003823	0.074151959	2.685834066
	0.0559	0.1207818	0.182727	0.623732	42.7665	0.935011	52.79647	24.19882914	6.543242	30.74207	0.0059	0.1804544	0.183437	0.010431	14.06338105	22.33512	7.08923	15.24589	0.089493	0.007595	0.005089	0.005344	0.093987699	2.621148955
	0.0633	0.1191575	0.182231	0.645072	40.8933	0.963198	55.27419	26.95331586	6.594099	33.54741	0.0070	0.2338657	0.237731	0.015046	13.70696828	23.34218	7.614235	15.72794	0.109643	0.010009	0.006939	0.007288	0.11514983	2.54343388
	0.0708	0.1172742	0.183409	0.683004	38.9687	0.998531	58.46496	31.04656093	6.743649	37.79021	0.0080	0.3035933	0.308611	0.021851	13.29229638	25.11294	8.337021	16.77592	0.134772	0.013316	0.009542	0.010022	0.141541253	2.45349118
	0.0794	0.1151492	0.13892	0.366072	41.1118	1.04679	63.08846	17.40035791	5.76276	23.16312	0.0091	0.2096436	0.213109	0.016912	12.82276746	15.18561	6.60323	8.582381	0.077677	0.008339	0.006164	0.006474	0.081578589	2.352288138
	0.0889	0.1128019	0.13148	0.377767	38.9459	1.09314	67.39658	19.8014133	5.570135	25.37155	0.0100	0.2541595	0.25836	0.02297	12.30079797	16.00393	6.89184	9.112095	0.09128	0.010671	0.008115	0.008523	0.095865291	2.240122268
	0.0994	0.1102527	0.164664	0.610183	34.0729	1.14038	71.69	36.23428101	6.613585	42.84787	0.0109	0.4682629	0.476003	0.047312	11.73009024	24.50747	9.778184	14.72928	0.160969	0.020506	0.015999	0.016803	0.169054197	2.117906205
	0.1108	0.1075244	0.151354	0.587934	32.3965	1.20101	77.54796	38.49700357	6.288497	44.7855	0.0118	0.5274836	0.536202	0.059391	11.1168543	24.42764	9.910424	14.51722	0.170984	0.023726	0.018939	0.01989	0.179572065	1.987345876
	0.1230	0.1046402	0.142703	0.668594	29.6575	1.26538	83.77421	48.67343654	5.915421	54.58886	0.0126	0.6857179	0.697052	0.085703	10.46920071	27.71501	10.38873	17.32627	0.217644	0.032853	0.026759	0.028103	0.228575924	1.849580171
	0.1359	0.1016243	0.130336	0.671417	27.797	1.33754	90.90365	53.99123239	5.525209	59.51644	0.0133	0.7900808	0.80314	0.109135	9.784225251	28.46273	10.48082	17.98191	0.23871	0.039121	0.032437	0.034067	0.25069996	1.706304391
	0.1495	0.0985013	0.0412918	0.969223	22.9569	1.40523	97.25383	86.79506258	1.566311	88.36137	0.0139	1.2295043	1.249826	0.186849	9.077619038	36.76529	3.697729	33.06756	0.460119	0.081671	0.068788	0.072243	0.483229636	1.558932289
	0.1637	0.095296	0.0300387	1.0015	20.9522	1.48671	105.3166	98.50054304	1.13126	99.6318	0.0145	1.44227	1.466109	0.240024	8.357585457	37.71656	2.954397	34.76216	0.503217	0.096474	0.082384	0.086522	0.528492962	1.411923446
	0.1785	0.0920329	0.0292726	0.976254	19.7937	1.57576	114.2598	104.9561757	1.132624	106.0888	0.0150	1.5867171	1.612943	0.287833	7.632717009	37.77351	3.14707	34.62644	0.51789	0.10692	0.092419	0.097061	0.54390326	1.267304579
	0.1936	0.0887365	0.0248858	0.946243	18.8341	1.66919	123.6186	110.7102032	0.993135	111.7033	0.0154	1.7149813	1.743328	0.337557	6.910733507	37.76237	2.911633	34.85074	0.535063	0.118585	0.103603	0.108807	0.5619388	1.126631941
	0.2092	0.0854303	0.0227119	0.944135	17.6281	1.76459	133.0054	119.6783641	0.914813	120.5932	0.0157	1.8889715	1.920194	0.401624	6.198982674	38.02882	2.878956	35.14987	0.550588	0.130576	0.11516	0.120844	0.578242753	0.99140484
	0.2250	0.0821365	0.0214114	0.939883	16.569	1.86289	142.5216	128.3915168	0.870221	129.2617	0.0159	2.0536459	2.08759	0.469616	5.50528443	38.19955	2.924877	35.27467	0.569426	0.141763	0.126071	0.132404	0.588575697	0.862979214
	0.2409	0.0788769	0.0211942	0.922358	15.7724	1.96394	152.1164	135.0231603	0.876333	135.8995	0.0160	2.1775817	2.213371	0.533274	4.837079625	38.13746	3.1026	35.03486	0.561329	0.15096	0.135243	0.142606	0.589523285	0.742502129
	0.2570	0.0756712	0.0203505	0.922079	14.8509	2.06548	161.4146	143.8652728	0.841927	144.7072	0.0161	2.3250106	2.36344	0.607404	4.200672983	38.1476	3.17514	34.97246	0.561903	0.160142	0.144409	0.151662	0.590126133	0.630818256
	0.2731	0.0725382	0.0191453	0.933343	13.9456	2.1675	170.3942	154.3486745	0.786195	155.1349	0.0160	2.4855709	2.526654	0.689946	3.602239727	38.33783	3.166061	35.16176	0.563362	0.16961	0.153836	0.161562	0.591558639	0.52861594
	0.2890	0.0694947	0.0190732	0.927456	13.3031	2.27032	179.1	161.6501399	0.786032	162.4362	0.0159	2.5807047	2.62336	0.758266	3.047526968	38.22171	3.324347	34.89736	0.554432	0.175779	0.160255	0.168305	0.582280143	0.436439044
	0.3048	0.0665558	0.0182447	0.939817	12.5241	2.37163	187.1759	171.7252894	0.740537	172.4658	0.0157	2.7015047	2.746157	0.837144	2.540472834	38.14637	3.333759	34.81266	0.545306	0.181501	0.166232	0.174582	0.572695411	0.354493724
	0.3204	0.0637353	0.0178226	0.923608	12.1154	2.47299	194.8922	175.9947306	0.72902	176.7238	0.0154	2.7132397	2.758086	0.883633	2.084668267	37.77948	3.39612	34.38336	0.527888	0.183901	0.16912	0.177615	0.554402788	0.282832498
	0.3355	0.0610445	0.0174875	0.902697	11.7852	2.57251	201.9903	178.4924571	0.721449	179.2139	0.0150	2.6804128	2.724716	0.914273	1.681110287	37.2409	3.457846	33.78306	0.505276	0.183692	0.169544	0.17806	0.530655564	0.221218376
	0.3503	0.0584935	0.0175661	0.906991	11.252	2.66842	208.2506	185.2508286	0.713795	185.9646	0.0145	2.6930239	2.736519	0.958562	1.329380274	36.8554	3.587836	33.26757	0.481581	0.182175	0.168691	0.177164	0.505730438	0.169206854
	0.3645	0.0560908	0.017291	0.886197	10.9572	2.76199	213.9469	186.1425662	0.703157	186.8457	0.0139	2.5998648	2.642837	0.963314	1.029008527	36.03817	3.631914	32.40625	0.459917	0.176985	0.164359	0.172615	0.473565721	0.12622716
	0.3781	0.0538429	0.0170049	0.863188	10.6822	2.85173	218.9352	185.7072331	0.690095	186.3973	0.0133	2.4744245	2.515323	0.951079	0.777315863	35.03	3.658453	31.37154	0.416457	0.169129	0.157468	0.165378	0.437375275	0.091511741
	0.3911	0.0517553	0.017125	0.869109	10.1721	2.93609	223.0815	190.8546418	0.674681	191.5093	0.0126	2.4056444	2.445406	0.956276	0.570696136	34.24065	3.760223	30.48042	0.38288	0.160446	0.149725	0.157246	0.402111327	0.064183095
	0.4032	0.0498316	0.0168847	0.840517	9.91658	3.01656	226.7246	187.7187339	0.659266	188.378	0.0118	2.2187161	2.255388	0.909456	0.405861946	32.81814	3.770982	29.04716	0.342117	0.147534	0.137954	0.144884	0.359301517	0.043333732
	0.4146	0.0480746	0.0170159	0.841048	9.38769	3.09042	229.5732	190.4961414	0.637188	191.1333	0.0109	2.0888006	2.123325	0.880343	0.277694395	31.49438	3.854076	27.64031	0.302067	0.133697	0.125239	0.131529	0.317239485	0.027975627
	0.4251	0.0464861	0.0169707	0.8053	9.12211	3.15958	232.034	184.4937708	0.624292	185.1181	0.0100	1.8546202	1.885071	0.801332	0.181746617	29.62414	3.887978	25.73616	0.257812	0.116813	0.109594	0.115099	0.270761528	0.017131541
	0.4346	0.0450669	0.017062	0.799732	8.59231	3.22155	233.861	184.9270617	0.596137	185.5232	0.0091	1.6790777	1.70683	0.741858	0.1124042	27.9422	3.945354	23.99685	0.217183	0.100478	0.094397	0.099138	0.22809228	0.009845364
	0.4432	0.0438172	0.0169942	0.770871	7.84853	3.27495	234.9762	179.4395234	0.545295	179.9848	0.0080	1.445908	1.469807	0.651411	0.068874435	24.73501	3.955825	20.77919	0.16693	0.078656	0.073982	0.077698	0.175314241	0.005268136
	0.4507	0.0427365	0.016912	0.744594	7.15933	3.32156	235.7507	174.1699684	0.496898	174.6669	0.0070	1.2176901	1.237817	0.557894	0.03417158	21.87719	3.955931	17.92126	0.124938	0.059809	0.056311	0.059139	0.131213527	0.002565081
	0.4571	0.0418242	0.0168278	0.718947	6.53906	3.36099	236.2283	168.730725	0.452698	169.1834	0.0059	0.9931067	1.009521	0.461491	0.015853708	19.34097	3.949341	15.39163	0.090349	0.043832	0.041302	0.043376	0.094886942	0.001095375
	0.4624	0.0410795	0.0167235	0.690317	5.94598	3.39281	236.4366	162.3380914	0.409603	162.7477	0.0047	0.7707731	0.783513	0.362334	0.009087065	16.90769	3.932774	12.97491	0.061449	0.030138	0.028417	0.029844	0.064535698	0.000385517
	0.4666	0.0405014	0.0166014	0.660782	5.39207	3.41687	236.4271	155.5354976	0.368836	155.9043	0.0036	0.5574359	0.56665	0.264404	0.001692911	14.68071	3.907653	10.77306	0.038519	0.019052	0.017973	0.018876	0.040453837	9.77247E-05
	0.4696	0.0400893	0.0164743	0.628387	4.88652	3.43312	236.2523	147.9182995	0.331538	148.2498	0.0024	0.3549842	0.360852	0.169456	0.000230901	12.64602	3.877945	8.76807	0.020995	0.010447	0.009859	0.010355	0.0220497	1.19592E-05
	0.4714	0.0398423	0.0163281	0.594786	4.44242	3.44151	235.9457	139.9155994	0.298407	140.214	0.0009	0.1261926	0.128278	0.06047	0	10.87013	3.840971	7.029156	0.006326	0.003159	0.002982	0.003132	0.006643998	0
		Drag force	0.4700814	0.28%		thrust	168.278		Corrected	167.8079		55.02645	55.93596	CoP	0.308214938					3.492971		3.322363	12.35910625	
						torque	11.00525				x3	165.07935		Fyeq	10.77936909				x3	10.47891		CoP	0.2688 8999	
														Fr	56.96513128									
offset	0.0200										Scaled	1.0165286		theta	10.71524192	degree			Scaled	1.050229			1.755828274	
roottip	0.0080											1.5313988		Mr	17.55750441								2.329831614	
												0.3362149		CMx	0.154344241							CMy	0.025029922	

Glossary of Terms

accuracy	Degree of exactness when using a measuring device.
actuator disc	Permeable disc allowing the flow to pass through, at the same time it is influenced by the forces on its surface.
azimuth	Angular measurement in a spherical coordinate system. It is the angle between the projected vector and a reference one, in a reference plane.
baseline	Base standard used for comparisons.
blended	Smoothly joined.
cant	Angle measured perpendicular to the incoming flow, positive towards the direction of it, and negative against it.
carriage	Movable part of the tank where the turbine is attached for the tests.
cavitation	Formation of vapour bubbles in a region of low pressure.
chord	Length of an airfoil section from the leading to the trailing edge.
curvature radius	Absolute radius: measured with respect to the blade length.
	Relative radius: with respect to winglet height.
c-type	Winglets bent two times along its height, resembling a letter C.
dihedral	Comprising two planes.
downstream	In the direction of the current.
downwind	In the direction of the flow.
fins	Non-straight shape resembling fish fins.
height	Winglet height: measured with respect to the blade length.
micro-tabs	Small devices located around 90% chord length from the leading edge, parallel to the airfoil surface, to change the camber distribution of an airfoil.
mie	Related to Mie Univeristy in Japan.
multi-tip	More than one tip or winglet than can be facing upstream, downstream.
nacelle	Enclosed part of the turbine, where the main components are located.

passive-adaptive	Type of blades which geometry changes with different operating conditions due to the material and the way they are constructed.
pitch	Degree of tilt of the blade with respect to the plane of rotation.
precision	Exactness of a measuring device.
raked	A raked wingtip is a blade extension, either bent or not, that has a greater sweep than the rest of the blade.
slot	Slots are internal channels in the blade located in the lower part, intended to increase the pressure, thus increasing the lift.
span	Blade length.
spanwise	From the root to the tip of the blade.
spar	Internal components of a blade framework.
spiroid	Type of winglets in spiral shape.
sweep	Backward inclination of the blade or winglet, contrary to the direction of movement.
tip	Extreme outer edge of a blade.
toe	The toe angle is the angle of inclination of the base with respect to zero degrees.
tsr	Tip speed ratio, is the proportion of the tip speed versus the undisturbed
tubercle	Blades with tubercles are inspired by the flippers of a whale, that generate enough lift to help them steer in all directions. They are small rounded parts sticking behind the blade, out of the trailing edge.
upstream	Against the current direction.
upwind	Against the flow direction.
vortex	A whirling mass of water. In this context formed behind the blade due to the blade/winglet interaction, which produces a resisting force opposite to the rotation of the blade.
winglet fence	A winglet that is very similar to an endplate, facing both sides and backward sweep on both sides.

List of References

Adams, M. L. (2010) *Rotating Machinery Vibration: From Analysis to Troubleshooting, Second Edition*. Taylor \& Francis. Available at: https://books.google.co.uk/books?id=QW4IX6Odi3MC.

Afgan, I. *et al.* (2013) 'Turbulent flow and loading on a tidal stream turbine by LES and RANS', *International Journal of Heat and Fluid Flow*. Elsevier, 43, pp. 96–108. doi: 10.1016/J.IJHEATFLUIDFLOW.2013.03.010.

Agelin-Chaab, M. (2018) '1.11 Fluid Mechanics Aspects of Energy', in *Comprehensive Energy Systems*. Elsevier, pp. 478–520. doi: 10.1016/B978-0-12-809597-3.00110-3.

Ahmed, U. *et al.* (2017) 'Fluctuating loads on a tidal turbine due to velocity shear and turbulence: Comparison of CFD with field data', *Renewable Energy*. Pergamon, 112, pp. 235–246. doi: 10.1016/J.RENENE.2017.05.048.

Ali, A. *et al.* (2015) 'An Aerodynamic Study of a Domestic Scale Horizontal Axis Wind Turbine With Varied Tip Configurations', *Procedia Engineering*. Elsevier B.V., 105(Icte 2014), pp. 757–762. doi: 10.1016/j.proeng.2015.05.067.

Allmark, M., Ellis, R., *et al.* (2021) 'A detailed study of tidal turbine power production and dynamic loading under grid generated turbulence and turbine wake operation', *Renewable Energy*. Pergamon, 169, pp. 1422–1439. doi: 10.1016/J.RENENE.2020.12.052.

Allmark, M., Martinez, R., *et al.* (2021) 'A Phenomenological Study of Lab-Scale Tidal Turbine Loading under Combined Irregular Wave and Shear Flow Conditions', *Journal of Marine Science and Engineering 2021, Vol. 9, Page 593*. Multidisciplinary Digital Publishing Institute, 9(6), p. 593. doi: 10.3390/JMSE9060593.

Alonzo-García, A., Gutiérrez-Torres, C. del C. and Jiménez-Bernal, J. A. (2016) 'Computational Fluid Dynamics in Turbulent Flow Applications', *Numerical Simulation - From Brain Imaging to Turbulent Flows*. InTech. doi: 10.5772/63831.

ANDRITZ HYDRO Hammerfest (2012) 'Renewable energy from tidal currents', p. 12. Available at: https://www.andritz.com/resource/blob/61614/cf15d27bc23fd59db125229506ec87c7/hy-hammerfest--1--data.pdf (Accessed: 21 July 2020).

Anyi, M. and Kirke, B. (2010) 'Evaluation of small axial flow hydrokinetic turbines for remote communities', *Energy for Sustainable Development*. Elsevier, 14(2), pp. 110–116. doi: 10.1016/j.esd.2010.02.003.

Aqua-RET Project © (2012) *Download Images and Illustrations - Tidal Stream Technologies*, *Online*. Available at: http://aquaret.com/indexea3d.html?option=com_content&view=article&id=203&Itemid=344&lang=en (Accessed: 15 June 2021).

Aravindkumar, N. (2014) 'Analysis of the Small Wind Turbine Blade with and Without Winglet', *Int. Journal of Engineering Research and Applications*, 4(6), pp. 239–243.

Aßbrock, M.-A. (2013) *Rotor blade of an E-101 by Enercon*. Available at: https://commons.wikimedia.org/wiki/File:E-101,_Saerbeck_2.jpg (Accessed: 27 July 2020).

Atlantis Resources Ltd. (2015) *Acquisition of Marine Current Turbines Limited from Siemens*. Available at: https://simecatlantis.com/2015/04/29/acquisition-of-marine-current-turbines-limited-from-siemens/ (Accessed: 29 March 2015).

Bach, A. B. *et al.* (2014) 'Finite micro-tab system for load control on a wind turbine', *Journal of Physics: Conference Series*, 524, p. 012082. doi: 10.1088/1742-6596/524/1/012082.

Bahaj, A. S. *et al.* (2005) 'Experimental investigation into the hydrodynamic performance of marine current turbines', *Sustainable energy series, Report*, 3, pp. 544–1747.

Bahaj, A. S. (2011) 'Generating electricity from the oceans', *Renewable and Sustainable Energy Reviews*. Elsevier Ltd, 15(7), pp. 3399–3416. doi: 10.1016/j.rser.2011.04.032.

Bahaj, A. S. (2013) 'Marine current energy conversion: the dawn of a new era in electricity production', *Philosophical Transactions of the royal society*, 371(1985). doi: 10.1098/rsta.2012.0500.

Bahaj, A. S. and Myers, L. E. (2003) 'Fundamentals applicable to the utilisation of marine current turbines for energy production', *Renewable Energy*, 28(14), pp. 2205–2211. doi: 10.1016/S0960-1481(03)00103-4.

Bahaj, A. S. and Myers, L. E. (2013) 'Shaping array design of marine current energy converters through scaled experimental analysis', *Energy*. Elsevier Ltd, 59, pp. 83–94. doi: 10.1016/j.energy.2013.07.023.

Bahaj, A. S. S. *et al.* (2007) 'Power and thrust measurements of marine current turbines under various hydrodynamic flow conditions in a cavitation tunnel and a towing tank', *Renewable Energy*, 32(3), pp. 407–426. doi: 10.1016/j.renene.2006.01.012.

Baker, A. C. (1991) *Tidal Power*. P. Peregrinus (Energy Engineering Series). Available at:

https://books.google.co.uk/books?id=TAose4g7vjoC.

Batten, W. M. J., Harrison, M. E. and Bahaj, A. S. (2013) 'Accuracy of the actuator disc-RANS approach for predicting the performance and wake of tidal turbines', *Philosophical transactions. Series A, Mathematical, physical, and engineering sciences*, 371(1985), p. 20120293. doi: 10.1098/rsta.2012.0293.

BEIS (2020) *Digest of UK Energy Statistics (DUKES) 2020*. Available at: https://www.gov.uk/government/statistics/digest-of-uk-energy-statistics-dukes-2020.

BEIS (2021) *Digest of UK Energy Statistics (DUKES) 2021*. Available at: https://assets.publishing.service.gov.uk/government/uploads/system/uploads/attachment_data/file/1007132/DUKES_2021_Chapters_1_to_7.pdf.

Bertin, J. J. and Cummings, R. M. (2014) *Aerodynamics for Engineers*. Pearson (Always learning). Available at: https://books.google.co.uk/books?id=x2qjMgEACAAJ.

Blackmore, T., Batten, W. M. J. M. J. and Bahaj, A. S. (2014) 'Influence of turbulence on the wake of a marine current turbine simulator', *Proc. R. Soc. A*, 470(20140331), pp. 1–17. doi: 10.1098/rspa.2014.0331.

BP (2019) *Energy Outlook 2019 edition*. London, UK. Available at: https://www.bp.com/en/global/corporate/energy-economics/energy-outlook.html (Accessed: 28 July 2020).

BP (2020) *Statistical Review of World Energy*. London, UK. Available at: https://www.bp.com/en/global/corporate/energy-economics/statistical-review-of-world-energy.html (Accessed: 28 July 2020).

Bray, R. (2017) 'Conversation with Dr. Luke Myers and Rodolfo Olvera-Trejo'. University of Southampton: 24 July.

Breeze, P. (2014) *Power Generation Technologies*. Elsevier Science. Available at: https://books.google.co.uk/books?id=ZEZ1AgAAQBAJ.

Bryans, A. G. *et al.* (2005) 'Impact of Tidal Generation on Power System Operation in Ireland', *IEEE Transactions on Power Systems*, 20(4), pp. 2034–2040. doi: 10.1109/TPWRS.2005.857282.

Bryden, I. G. (2004) 'Tidal Energy', *Encyclopedia of Energy*. Elsevier, pp. 139–150. doi: 10.1016/B0-12-176480-X/00342-9.

Burton, Tony *et al.* (2011) 'Design Loads for Horizontal Axis Wind Turbines', in *Wind Energy*

Handbook. Chichester, UK: John Wiley & Sons, Ltd, pp. 193–323. doi: 10.1002/9781119992714.ch5.

Burton, T *et al.* (2011) *Wind Energy Handbook*. Wiley. Available at: https://books.google.co.uk/books?id=dip2LwCRCscC.

Burton, T. *et al.* (2021) 'Aerodynamics of horizontal axis wind turbines', in *Wind Energy Handbook 3e*. Wiley, pp. 39–152. doi: 10.1002/9781119451143.ch3.

Burton, T. L. *et al.* (2021) *Wind Energy Handbook*. Wiley. Available at: https://books.google.co.uk/books?id=ieklEAAAQBAJ.

van Bussel, G. J. W. (1990) 'A momentum theory for winglets on horizontal axis windturbine rotors and some comparison with experiments', *Fourth IEA Symposium on the Aerodynamics of Wind Turbines, November 19-20*.

Canet, H., Bortolotti, P. and Bottasso, C. L. (2020) 'On the scaling of wind turbine rotors'. doi: 10.5194/wes-2020-66.

Carlton, J. S. (2019) 'Chapter 2 - Propulsion Systems', in Carlton, J. S. (ed.) *Marine Propellers and Propulsion (Fourth Edition)*. Fourth Edi. Butterworth-Heinemann, pp. 11–28. doi: https://doi.org/10.1016/B978-0-08-100366-4.00002-X.

CATAPULT Offshore Renewable Energy (2018) *TIDAL STREAM AND WAVE ENERGY COST REDUCTION AND INDUSTRIAL BENEFIT*. Available at: https://ore.catapult.org.uk/app/uploads/2018/11/Tidal-Stream-and-Wave-Energy-Cost-Reduction-and-Industrial-Benefit.pdf.

Chattot, J.-J. (2006) 'Low Speed Design and Analysis of Wing/Winglet Combinations Including Viscous Effects', *Journal of Aircraft*, 43(2), pp. 386–389. doi: 10.2514/1.15349.

Chattot, J.-J. (2009) 'Effects of blade tip modifications on wind turbine performance using vortex model', *Computers & Fluids*, 38(7), pp. 1405–1410. doi: 10.1016/j.compfluid.2008.01.022.

Clean Energy Council (2020) *Renewable Energy Target*. Available at: https://www.cleanenergycouncil.org.au/advocacy-initiatives/renewable-energy-target (Accessed: 28 July 2020).

Clean Energy Council (2021) *Clean Energy Australia Report 2021*. Available at: https://assets.cleanenergycouncil.org.au/documents/resources/reports/clean-energy-australia/clean-energy-australia-report-2021.pdf.

Coles, D. *et al.* (2021) 'Cost modelling and design optimisation of tidal stream turbines', *Proceedings of the 14th European Wave and Tidal Energy Conference*, pp. 1–11.

Day, M. *et al.* (2012) 'A combined computational and experimental characterization of lean premixed turbulent low swirl laboratory flames: I. Methane flames', *Combustion and Flame*. Elsevier, 159(1), pp. 275–290.

Delucchi, M. A. and Jacobson, M. Z. (2011) 'Providing all global energy with wind, water, and solar power, Part II: Reliability, system and transmission costs, and policies', *Energy Policy*, 39(3), pp. 1170–1190. doi: 10.1016/j.enpol.2010.11.045.

Dixon, S. L. and Hall, C. (2013) *Fluid Mechanics and Thermodynamics of Turbomachinery*. Elsevier Science. Available at: https://books.google.co.uk/books?id=wZoTAAAAQBAJ.

Domenech, J., Eveleigh, T. and Tanju, B. (2018) 'Marine Hydrokinetic (MHK) systems: Using systems thinking in resource characterization and estimating costs for the practical harvest of electricity from tidal currents', *Renewable and Sustainable Energy Reviews*. Elsevier Ltd, pp. 723–730. doi: 10.1016/j.rser.2017.07.063.

Douglas, C. A., Harrison, G. P. and Chick, J. P. (2008) 'Life cycle assessment of the Seagen marine current turbine', *http://dx.doi.org/10.1243/14750902JEME94*. SAGE PublicationsSage UK: London, England. doi: 10.1243/14750902JEME94.

Drela, M. and Youngren, H. (2001) *XFOIL 6.9 User Primer*. Available at: https://web.mit.edu/drela/Public/web/xfoil/xfoil_doc.txt (Accessed: 25 August 2020).

Ebdon, T. *et al.* (2021) 'The impact of turbulence and turbine operating condition on the wakes of tidal turbines', *Renewable Energy*. Elsevier, 165, pp. 96–116.

Elfarra, M. A., Sezer-Uzol, N. and Akmandor, İ. S. (2014) 'NREL VI rotor blade: numerical investigation and winglet design and optimization using CFD', *Wind Energy*, 17(4), pp. 605–626. doi: 10.1002/we.1593.

Elfarra, M. A., Sezer-Uzol, N. and Akmandor, İ. S. (2015) 'Investigations on Blade Tip Tilting for Hawt Rotor Blades Using CFD', *International Journal of Green Energy*, 12(2), pp. 125–138. doi: 10.1080/15435075.2014.889007.

Ben Elghali, S. E. *et al.* (2007) 'A Simulation Model for the Evaluation of the Electrical Power Potential Harnessed by a Marine Current Turbine', *IEEE Journal of Oceanic Engineering*, 32(4), pp. 786–797. doi: 10.1109/JOE.2007.906381.

EMEC (2012) *Marine Energy*. Available at: http://www.emec.org.uk/marine-energy/ (Accessed: 24 May 2017).

EMEC (2016a) *Alstom (formerly TGL)*, *Online*. Available at: http://www.emec.org.uk/about-us/our-tidal-clients/alstom/ (Accessed: 29 July 2020).

EMEC (2016b) *Tocardo*, *Online*. Available at: http://www.emec.org.uk/about-us/our-tidal-clients/tocardo/ (Accessed: 29 July 2020).

EMEC (2017) *Nautricity*, *Online*. Available at: http://www.emec.org.uk/about-us/our-tidal-clients/nautricity/ (Accessed: 29 July 2020).

EMEC (2020) *Our Clients*. Available at: http://www.emec.org.uk/about-us/our-tidal-clients/ (Accessed: 29 July 2020).

EMEC (2022) *Open Hydro*. Available at: https://www.emec.org.uk/about-us/our-tidal-clients/open-hydro/ (Accessed: 9 February 2022).

Encarnacion, J. I., Johnstone, C. and Ordonez-Sanchez, S. (2019) 'Design of a Horizontal Axis Tidal Turbine for Less Energetic Current Velocity Profiles', *Journal of Marine Science and Engineering*. MDPI AG, 7(7), p. 197. doi: 10.3390/jmse7070197.

Fagan, E. *et al.* (2019) 'Design and testing of a full-scale 2 MW tidal turbine blade'. engrXiv. doi: 10.31224/OSF.IO/VMP3Y.

Finnegan, W. *et al.* (2020) 'Full-Scale Structural Testing of Wind and Tidal Turbine Blades', *Civil Engineering Research in Ireland 2020*. Available at: https://sword.cit.ie/ceri/2020/9/1 (Accessed: 17 October 2021).

Fraenkel, P. L. (2002) 'Power from marine currents', *Proceedings of the I MECH E Part A Journal of Power and Energy*, 216(1), pp. 1–14. doi: 10.1243/095765002760024791.

Gajardo Orellana, I. D. (2017) 'INVESTIGATION ON TIDAL TURBINE ARRAYS WITH A COUPLED DES-BEM MODEL'. Available at: https://repositorio.uc.cl/handle/11534/21376 (Accessed: 20 October 2021).

Galloway, P. W. (2013) *Performance quantification of tidal turbines subjected to dynamic loading*. University of Southampton.

Galloway, P. W., Myers, L. E. and Bahaj, A. B. S. (2014) 'Quantifying wave and yaw effects on a scale tidal stream turbine', *Renewable Energy*. Pergamon, 63, pp. 297–307. doi: 10.1016/j.renene.2013.09.030.

Gandhi, P. *et al.* (2019) 'PHYS1017: PHYSICS SKILLS 1'. Southampton: University of Southampton, p. 148.

Gaunaa, M. and Johansen, J. (2007a) 'Determination of the Maximum Aerodynamic Efficiency of Wind Turbine Rotors with Winglets', *Journal of Physics: Conference Series*, 75, p. 012006. doi: 10.1088/1742-6596/75/1/012006.

Gaunaa, M. and Johansen, J. (2007b) 'Estimation of possible increase in Cp by use of Winglets', in Bak, C. (ed.) *Research in aeroelasticity EFP-2006*. Risø National Laboratory, pp. 47–61. Available at: https://backend.orbit.dtu.dk/ws/portalfiles/portal/53754524/ris_r_1611.pdf.

Gaurier, B. *et al.* (2015) 'Tidal energy "Round Robin" tests comparisons between towing tank and circulating tank results', *International Journal of Marine Energy*. Elsevier, 12, pp. 87–109. doi: 10.1016/J.IJOME.2015.05.005.

Gaurier, B. *et al.* (2020) 'Experimental study of bathymetry generated turbulence on tidal turbine behaviour', *Renewable Energy*. Pergamon, 156, pp. 1158–1170. doi: 10.1016/J.RENENE.2020.04.102.

Ge, M., Tian, D. and Deng, Y. (2016) 'Reynolds Number Effect on the Optimization of a Wind Turbine Blade for Maximum Aerodynamic Efficiency', *Journal of Energy Engineering*. American Society of Civil Engineers (ASCE), 142(1), p. 04014056. doi: 10.1061/(asce)ey.1943-7897.0000254.

Gertz, D. and Johnson, D. A. (2011) 'An evaluation testbed for wind turbine blade tip designs-baseline case', *International Journal of Energy Research*, 35(15), pp. 1360–1370. doi: 10.1002/er.1897.

Gertz, D., Johnson, D. and Swytink-Binnema, N. (2012) 'An Evaluation Testbed for Wind Turbine Blade Tip Designs - Winglet Results', *Wind Engineering*. SAGE Publications, 36(4), pp. 389–410. doi: 10.1260/0309-524X.36.4.389.

Giles, J. W. (2013) *Energy extraction from shallow tidal flows*. Original typescript, 2013. Available at: https://eprints.soton.ac.uk/361703/.

Golfman, Y. (2016) *Hybrid anisotropic materials for wind power turbine blades*. CRC Press.

Le Guen-Geffroy, A. *et al.* (2020) 'Influence of Seawater Ageing on Fracture of Carbon Fiber Reinforced Epoxy Composites for Ocean Engineering', *Oceans*, 1(4), pp. 198–214. doi: 10.3390/oceans1040015.

Gyatt, G. W. and Lissaman, P. B. S. (1985) *Development and testing of tip devices for horizontal*

axis wind turbines. Available at: https://ntrs.nasa.gov/search.jsp?R=19860009304 (Accessed: 29 July 2020).

Hansen, T. (2017) *Aerodynamic Optimisation ofAirfoils and Winglets for WindTurbine Application*. Norwegian University of Science and Technology. Available at: https://www.researchgate.net/profile/Thomas_Hansen25/publication/329810096_Thomas_Hansen_Aerodynamic_Optimisation_of_Airfoils_and_Winglets_for_Wind_Turbine_Application/links/5c1bac0892851c22a338cc93/Thomas-Hansen-Aerodynamic-Optimisation-of-Airfoils-and-W.

Hardisty, J. (2009) *The Analysis of Tidal Stream Power*. Wiley. Available at: https://books.google.co.uk/books?id=SFUztwHVyHgC.

Harwood, C. M., Young, Y. L. and Ceccio, S. L. (2016) 'Ventilated cavities on a surface-piercing hydrofoil at moderate Froude numbers: cavity formation, elimination and stability', *Journal of Fluid Mechanics*. Cambridge University Press, 800, pp. 5–56.

Hau, E. (2013) 'Rotor Aerodynamics', in *Wind Turbines*. Berlin, Heidelberg: Springer Berlin Heidelberg, pp. 89–166. doi: 10.1007/978-3-642-27151-9_5.

Hoerner, S. F. (1965) *Fluid-dynamic Drag: Practical Information on Aerodynamic Drag and Hydrodynamic Resistance*. Hoerner Fluid Dynamics. Available at: https://books.google.co.uk/books?id=6K12uAAACAAJ.

Houde, J. (2012) 'Cost-benefit analysis of tidal energy generation in Nova Scotia: a scenario for a tidal farm with 300MW of installed capacity in the Minas Passage in 2020'. Halifax, Nova Scotia: Dalhousie University, p. 112. Available at: http://dalspace.library.dal.ca/bitstream/handle/10222/14578/Houde, Julie, MDE, ECON, April 2012.pdf?sequence=3.

Ibrahim, M. *et al.* (2015) 'Advances in Horizontal Axis Wind Turbine Blade Designs: Introduction of Slots and Tubercle', *Journal of Energy Resources Technology*, 137(5), p. 051205. doi: 10.1115/1.4030399.

IEA (2020) *Sustainable Recovery*, *IEA*. Paris. Available at: https://www.iea.org/reports/sustainable-recovery.

Imamura, H., Hasegawa, Y. and Kikuyama, K. (1998) 'Numerical Analysis of the Horizontal Axis Wind Turbine with Winglets.', *JSME International Journal Series B*, 41(1), pp. 170–176. doi: 10.1299/jsmeb.41.170.

Institute of Marine Engineering (2021) *Umberto Pugliese towing tank*. Available at:

http://www.inm.cnr.it/labs/umberto-pugliese-towing-tank/ (Accessed: 31 July 2021).

Jansen, M. *et al.* (no date) 'Offshore wind competitiveness in mature markets without subsidy', *Nature Energy*. doi: 10.1038/s41560-020-0661-2.

Jeffrey, W. (2020) '10 Smart Startups', *Mechanical Engineering*. American Society of Mechanical Engineers Digital Collection, 142(07), pp. 34–39. doi: 10.1115/1.2020-JUL1.

Jiang, Y., Fagan, E. and Goggins, J. (2019) 'Structural design and optimisation of a full-scale tidal turbine blade', in *Proceedings of the 13th European Wave and Tidal Energy Conference (EWTEC), Naples, Italy*, pp. 1–6.

Jing, Z., Ducoin, A. and Braud, C. (2020) 'Direct numerical simulation of transitional boundary layers on a horizontal axis wind turbine blade', *Journal of Physics: Conference Series*. IOP Publishing, 1618(5), p. 052042. doi: 10.1088/1742-6596/1618/5/052042.

Johansen, J. and Sørensen, N. (2006) 'Aerodynamic investigation of Winglets on Wind Turbine Blades using CFD', *Riso-R-1543(EN)*, 1543(February). Available at: https://backend.orbit.dtu.dk/ws/files/7703268/ris_r_1543.pdf.

Johansen, J. and Sørensen, N. (2007) 'Numerical analysis of winglets on wind turbine blades using CFD', *European Wind Energy Conference and Exhibition*. Available at: https://scholar.google.co.uk/scholar?hl=en&q=Numerical+Analysis+of+Winglets+on+Wind+Turbine+Blades+using+CFD&btnG=&as_sdt=1,5&as_sdtp=.

Johnson, N. *et al.* (2019) *Investigation of Innovative Rotor Concepts for the Big Adaptive Rotor Project*. Golden, CO (United States). Available at: https://www.nrel.gov/docs/fy19osti/73605.pdf.

Johnstone, C. (2021) 'Getting a 500kW Turbine into the Water [Talk at the PRIMaRE Summer School]'. University of Southampton: 13 September.

de Kat, R. (2019) 'Informal chat about Lecture 11: Flow Visualisation. Experimental Methods for Aerodynamics. Module code SESA6070'. University of Southampton, p. 35.

Khalafallah, M. G., Ahmed, A. M. and Emam, M. K. (2019) 'The effect of using winglets to enhance the performance of swept blades of a horizontal axis wind turbine', *Advances in Mechanical Engineering*, 11(9), p. 168781401987831. doi: 10.1177/1687814019878312.

Khaled, M. *et al.* (2019) 'Investigation of a small Horizontal–Axis wind turbine performance with and without winglet', *Energy*. Elsevier Ltd, 187, p. 115921. doi: 10.1016/j.energy.2019.115921.

Ko, D. H., Park, J. S. and Lee, K. S. (2018) 'Assessment of Tidal Current Energy Potential at

Uldolmok in the Southwestern Coast of Korea', *Journal of Coastal Research*. Coastal Education Research Foundation Inc., 85(85 (10085)), pp. 1301–1305. doi: 10.2112/SI85-261.1/201563/ASSESSMENT-OF-TIDAL-CURRENT-ENERGY-POTENTIAL-AT.

Korobenko, A. *et al.* (2018) 'Recent Advances in ALE-VMS and ST-VMS Computational Aerodynamic and FSI Analysis of Wind Turbines', in, pp. 253–336. doi: 10.1007/978-3-319-96469-0_7.

Kumar, Y. *et al.* (2016) 'Wind energy: Trends and enabling technologies', *Renewable and Sustainable Energy Reviews*, 53, pp. 209–224. doi: 10.1016/j.rser.2015.07.200.

Lacal Arantegui, R. *et al.* (2014) 'Energy Technology Reference Indicator (ETRI) projections for 2010--2050'. Petten, Netherlands: Publications Office of the European Union, p. 108. doi: 10.2790/057687.

Laß, A. *et al.* (2019) 'Rotor dynamic analysis of a tidal turbine considering fluid–structure interaction under shear flow and waves', *International Journal of Naval Architecture and Ocean Engineering*. Elsevier, 11(1), pp. 154–164. doi: 10.1016/j.ijnaoe.2018.03.002.

Lawton, S. and Crawford, C. (2014) 'Investigation and Optimization of Blade Tip Winglets Using an Implicit Free Wake Vortex Method', *Journal of Physics: Conference Series*, 524(1), p. 012033. doi: 10.1088/1742-6596/524/1/012033.

Li, H. *et al.* (2014) 'Reliability-based fatigue life investigation for a medium-scale composite hydrokinetic turbine blade', *Ocean Engineering*, 89, pp. 230–242. doi: 10.1016/j.oceaneng.2014.08.006.

Li, H. and Chandrashekhara, K. (2015) 'Particle swarm-based structural optimization of laminated composite hydrokinetic turbine blades', *Engineering Optimization*, 47(9), pp. 1191–1207. doi: 10.1080/0305215X.2014.954567.

Li, W. *et al.* (2016) 'Review on the blade design technologies of tidal current turbine', *Renewable and Sustainable Energy Reviews*, 63, pp. 414–422. doi: 10.1016/j.rser.2016.05.017.

Lin, T., Lee, J.-W. and Lwin, T. (2011) 'Integrated approach for rotor blade manufacturing cost estimate', *Aircraft Engineering and Aerospace Technology*. Emerald Group Publishing Limited, 83(4), pp. 235–244. doi: 10.1108/00022661111138657.

Lock, C. N. H., Bateman, H. and Townend, H. C. H. (1924) *Experiments to verify the independence of the elements of an airscrew blade*. HM Stationery Office.

Lockheed Martin (2017) *First Tidal Energy Turbine with Lockheed Martin Technology Deployed Off Scotland Coast*. Available at: https://news.lockheedmartin.com/2017-02-23-First-Tidal-Energy-Turbine-with-Lockheed-Martin-Technology-Deployed-Off-Scotland-Coast (Accessed: 29 July 2020).

Lothodé, C. *et al.* (2020) 'Investigation of blade-mast fluid-structure interaction of a tidal turbine'.

Low Carbon Innovation Coordination Group (2012) *Technology Innovation Needs Assessment (TINA)*. Available at: https://prod-drupal-files.storage.googleapis.com/documents/resource/public/TINAs - Examining the potential of low carbon technologies - MARINE ENERGY - PART F - REPORT.pdf.

MacGillivray, A. *et al.* (2014) 'Innovation and cost reduction for marine renewable energy: A learning investment sensitivity analysis', *Technological Forecasting and Social Change*, 87, pp. 108–124. doi: 10.1016/j.techfore.2013.11.005.

Magallanes Renovables (2020) *The Technology*. Available at: https://www.magallanesrenovables.com/ (Accessed: 29 July 2020).

Marten, D. and Wendler, J. (2013) *QBlade Guidelines*. Available at: http://q-blade.org/project_images/files/guidelines_v06(1).pdf (Accessed: 25 August 2020).

Mason-Jones, A. *et al.* (2013) 'Influence of a velocity profile & support structure on tidal stream turbine performance', *Renewable Energy*. Pergamon, 52, pp. 23–30. doi: 10.1016/j.renene.2012.10.022.

Maughmer, M. D. (2003) 'Design of Winglets for High-Performance Sailplanes', *Journal of Aircraft*, 40(6), pp. 1099–1106. doi: 10.2514/2.7220.

Metoc Ltd. for the Sustainable Development Commission (2007) *Tidal Power in the UK*. Available at: http://www.sd-commission.org.uk/data/files/publications/TidalPowerUK1-Tidal_resource_assessment.pdf (Accessed: 28 July 2021).

Moné, C. *et al.* (2015) *2015 Cost of Wind Energy Review*. Golden, CO (United States). Available at: https://www.nrel.gov/docs/fy17osti/66861.pdf.

Mourad, M. G. *et al.* (2020) 'Effect of winglet geometry on horizontal axis wind turbine performance', *Engineering Reports*. Wiley, 2(1). doi: 10.1002/eng2.12101.

Mühle, F. *et al.* (2020) 'An experimental study on the effects of winglets on the tip vortex interaction in the near wake of a model wind turbine', *Wind Energy*. Reston, Virginia: American Institute of Aeronautics and Astronautics, 23(5), pp. 1286–1300. doi: 10.1002/we.2486.

Muller, G. (2020) 'WEEG NEWSLETTER March 2020', *No. 34*, p. 2. Available at: https://generic.wordpress.soton.ac.uk/water/wp-content/uploads/sites/297/2020/06/WEEG-NEWSLETTER-Nr-34-03-2020.pdf.

Murdy, P. *et al.* (2021) 'Leveraging the Advantages of Additive Manufacturing to Produce Advanced Hybrid Composite Structures for Marine Energy Systems', *Applied Sciences*, 11(3), p. 1336. doi: 10.3390/app11031336.

Murray, R. E. *et al.* (2018) 'Towing tank testing of passively adaptive composite tidal turbine blades and comparison to design tool', *Renewable Energy*. Pergamon, 116, pp. 202–214. doi: 10.1016/j.renene.2017.09.062.

Myers, L. E. and Bahaj, A. S. (2010) 'Experimental analysis of the flow field around horizontal axis tidal turbines by use of scale mesh disk rotor simulators', *Ocean Engineering*. Elsevier, 37(2–3), pp. 218–227. doi: 10.1016/j.oceaneng.2009.11.004.

Myers, L. E. and Bahaj, B. (2008) 'Scale reproduction of the flow field for tidal energy converters', *10th World Renewable Energy Congress (WREC X)*, 44(0).

National Instruments (2009) *NI USB-621x User Manual*. Available at: https://www.ni.com/pdf/manuals/371931f.pdf (Accessed: 26 August 2020).

Naval Group (2016) *Cape Sharp Tidal turbine generates power*, *Online*. Available at: https://www.naval-group.com/en/news/cape-sharp-tidal-turbine-generates-power/ (Accessed: 28 July 2020).

Nicholls-Lee, R. F. and Turnock, S. R. (2007) 'The use of computational fluid dynamics in the optimisation of marine current turbines'.

Nicholls-Lee, R. F., Turnock, S. R. and Boyd, S. W. (2013) 'Application of bend-twist coupled blades for horizontal axis tidal turbines', *Renewable Energy*, 50, pp. 541–550. doi: 10.1016/j.renene.2012.06.043.

Ocean Energy Systems (2021) *GIS Map Tool*. Available at: https://www.ocean-energy-systems.org/ocean-energy/gis-map-tool/ (Accessed: 28 July 2021).

OES (2019) *Annual Report 2019*. Available at: https://tethys.pnnl.gov/publications/ocean-energy-systems-annual-report-2019.

Office of Energy Efficiency & Renewable Energy (2017) *How Do Wind Turbines Survive Severe Storms?* Available at: https://www.energy.gov/eere/articles/how-do-wind-turbines-survive-

severe-storms (Accessed: 20 July 2020).

Orbital Marine Power (2020) *The Concept*. Available at: https://orbitalmarine.com/ (Accessed: 29 July 2020).

Orbital Marine Power (2021) *Demystifying the Cost of Tidal Energy*. Available at: https://orbitalmarine.com/demystifying-the-cost-of-tidal-energy/ (Accessed: 29 July 2021).

Ostovan, Y. and Uzol, O. (2016) 'Experimental Study on the Effects of Winglets on the Performance of Two Interacting Horizontal Axis Model Wind Turbines', *Journal of Physics: Conference Series*, 753, p. 022015. doi: 10.1088/1742-6596/753/2/022015.

Peters, A. (2015) *This Funny Looking Nose-Doohickey Helps Wind Turbines Make More Power*. Available at: https://www.fastcompany.com/3047474/this-funny-looking-nose-doohickey-helps-wind-turbines-make-more-power (Accessed: 29 July 2020).

Porté-Agel, F., Bastankhah, M. and Shamsoddin, S. (2020) 'Wind-Turbine and Wind-Farm Flows: A Review', *Boundary-Layer Meteorology*. Springer, 174(1), pp. 1–59. doi: 10.1007/s10546-019-00473-0.

Porter, K. E. *et al.* (2020) 'Flume testing of passively adaptive composite tidal turbine blades under combined wave and current loading', *Journal of Fluids and Structures*. Academic Press, 93, p. 102825. doi: 10.1016/J.JFLUIDSTRUCTS.2019.102825.

Post, N. L. (2016) 'Improving Bending Moment Measurements on Wind Turbine Blades'. Available at: https://www.nrel.gov/docs/fy16osti/65996.pdf.

QBlade Team (2014) *About*. Available at: http://www.q-blade.org (Accessed: 25 August 2020).

del Razo, C. (2016) 'A Snapshot of the Mexican Clean Energy Obligations System', *Mexican Law Review*, 9(1), pp. 81–90. doi: 10.1016/j.mexlaw.2016.09.004.

Ren, Y. *et al.* (2017) 'Design and hydrodynamic analysis of horizontal axis tidal stream turbines with winglets', *Ocean Engineering*. Pergamon, 144, pp. 374–383. doi: 10.1016/j.oceaneng.2017.09.038.

Ren, Y., Liu, B. and Zhang, T. (2019) 'Influences of winglets on the hydrodynamic performance of horizontal axis current turbines', *Applied Ocean Research*. Elsevier, 92, p. 101931. doi: 10.1016/j.apor.2019.101931.

Rodriguez, S. (2019) *Applied Computational Fluid Dynamics and Turbulence Modeling: Practical Tools, Tips and Techniques*. Springer International Publishing. Available at:

https://books.google.co.uk/books?id=6T7CDwAAQBAJ.

Rosli, R. and Dimla, E. (2018) 'A review of tidal current energy resource assessment: Current status and trend', in *2018 5th International Conference on Renewable Energy: Generation and Applications (ICREGA)*. IEEE, pp. 34–40. doi: 10.1109/ICREGA.2018.8337585.

Saravanan, P., Parammasivam, K. M. and Rajan, S. (2012) 'Pressure distribution of rotating small wind turbine blades with winglet using wind tunnel', *Journal of Scientific & Industrial Research*, 71, pp. 425–429.

Saravanan, P., Parammasivam, K. M. and S, S. R. (2013) 'Experimental Investigation on Small Horizontal Axis Wind Turbine Rotor Using Winglets', 16(2), pp. 159–164. doi: 10.6180/jase.2013.16.2.07.

Secretaría de Energía (2020) 'PROGRAMA Sectorial de Energía 2020-2024', *Diario Oficial de la Federación*, 8 July, p. 210. Available at: http://www.dof.gob.mx/index_113.php?year=2020&month=07&day=08.

Shen, W. Z. *et al.* (2005) 'Tip loss corrections for wind turbine computations', *Wind Energy*. John Wiley & Sons, Ltd, 8(4), pp. 457–475. doi: 10.1002/we.153.

Shen, X. *et al.* (2016) 'Aerodynamic shape optimization of non-straight small wind turbine blades', *Energy Conversion and Management*. Elsevier Ltd, 119, pp. 266–278. doi: 10.1016/j.enconman.2016.04.008.

Shimizu, Y. *et al.* (1990) 'Studies on Horizontal Axis Wind Turbines With Tip Attachments', *Proc. ECWEC'90, Madrid, Spain*, pp. 279–283.

Shimizu, Y. *et al.* (1992) 'New technology of power augmentation on horizontal axis wind turbines using Mie vanes', *Journal of Wind Engineering and Industrial Aerodynamics*, 39(1–3), pp. 119–127. doi: 10.1016/0167-6105(92)90538-L.

Shimizu, Y. *et al.* (2003a) 'Power augmentation of a HAWT by Mie-type tip vanes, considering wind tunnel flow visualisation, blade-aspect ratios and Reynolds number', *Wind Engineering*, 27(3), pp. 183–194. doi: 10.1260/030952403769016663.

Shimizu, Y. *et al.* (2003b) 'Rotor configuration effects on the performance of a HAWT with tip-mounted mie-type vanes', *Journal of Solar Energy Engineering, Transactions of the ASME*, 125(4), pp. 441–447. doi: 10.1115/1.1621671.

SIMEC Atlantis Energy (2016) *SeaGen S*. Available at: https://simecatlantis.com/wp-

content/uploads/2016/08/SeaGen-Brochure.pdf (Accessed: 29 July 2020).

SIMEC Atlantis Energy (2018) *SIMEC Atlantis Energy Unveils World's Largest Single Rotor Tidal Turbine, the AR2000*. Available at: https://simecatlantis.com/2018/09/13/simec-atlantis-energy-unveils-worlds-largest-single-rotor-tidal-turbine-the-ar2000/ (Accessed: 25 June 2021).

SIMEC Atlantis Energy (2020a) *About SIMEC Atlantis Energy*. Available at: https://simecatlantis.com/about/atlantis/ (Accessed: 29 July 2020).

SIMEC Atlantis Energy (2020b) *MeyGen*. Available at: https://simecatlantis.com/projects/meygen/ (Accessed: 29 July 2020).

SIMEC Atlantis Energy (2020c) *Reporting Timetable Change and Company Update*. Available at: https://simecatlantis.com/2020/06/29/reporting-timetable-change-and-company-update/ (Accessed: 29 July 2020).

Simon, E. (2019) *Analysis: Record-low price for UK offshore wind cheaper than existing gas plants by 2023*, *Carbon Brief*. Available at: https://www.carbonbrief.org/analysis-record-low-uk-offshore-wind-cheaper-than-existing-gas-plants-by-2023 (Accessed: 17 July 2020).

Smyth, A. S. M. (2020) *Three-Dimensional Unsteady Hydrodynamics of Tidal Turbines (Doctoral thesis)*. doi: https://doi.org/10.17863/CAM.48853.

Solent University (2017) *We're filling up our newly-refurbished towing tank with 399 tonnes of fresh water - equivalent to the weight of 31 London buses! ? #FunFact [Twitter] 20 September*. Available at: https://twitter.com/solentuni/status/910509094376759301 (Accessed: 8 July 2021).

Sørensen, J. N. (2012) 'Aerodynamic Analysis of Wind Turbines', in *Comprehensive Renewable Energy*. Elsevier (Comprehensive Renewable Energy), pp. 225–241. doi: 10.1016/B978-0-08-087872-0.00209-2.

Stallard, T. *et al.* (2013) 'Interactions between tidal turbine wakes: experimental study of a group of three-bladed rotors', *Philosophical Transactions of the Royal Society A: Mathematical, Physical and Engineering Sciences*. The Royal Society Publishing, 371(1985). doi: 10.1098/RSTA.2012.0159.

Stehly, T. and Beiter, P. (2018) *2018 Cost of Wind Energy Review*. Golden, CO (United States). Available at: https://www.nrel.gov/docs/fy20osti/74598.pdf.

Sutherland, D. R. J. *et al.* (2017) 'Characterisation of current and turbulence in the FloWave Ocean Energy Research Facility', *Ocean Engineering*. Pergamon, 139, pp. 103–115. doi: 10.1016/J.OCEANENG.2017.02.028.

Sweety, M. *et al.* (2019) 'A Review of Winglets on Tip Vortex, Drag and Airfoil Geometry Review of Winglets on Tip Vortex, Drag and Airfoil Geometry', *Journal of Advanced Research in Fluid Mechanics and Thermal Sciences Journal homepage*, 63, pp. 218–237. Available at: www.akademiabaru.com/arfmts.html (Accessed: 9 December 2019).

Tobin, N., Hamed, A. and Chamorro, L. (2015) 'An Experimental Study on the Effects ofWinglets on the Wake and Performance of a ModelWind Turbine', *Energies*, 8(10), pp. 11955–11972. doi: 10.3390/en81011955.

Uihlein, A. and Magagna, D. (2016) 'Wave and tidal current energy – A review of the current state of research beyond technology', *Renewable and Sustainable Energy Reviews*, 58, pp. 1070–1081. doi: 10.1016/j.rser.2015.12.284.

UK Government (2010) 'National Renewable Energy Action Plan for the United Kingdom', pp. 1–160. Available at: https://www.gov.uk/government/uploads/system/uploads/attachment_data/file/47871/25-nat-ren-energy-action-plan.pdf (Accessed: 29 July 2020).

van Unen, A. (2020) *QED Naval and HydroWing acquire Tocardo Tidal Power*, *Tocardo Tidal Power*. Available at: https://www.tocardo.com/qed-naval-and-hydrowing-acquiring-tocardo-tidal-power/ (Accessed: 29 July 2020).

Vazquez, A. and Iglesias, G. (2016) 'Grid parity in tidal stream energy projects: An assessment of financial, technological and economic LCOE input parameters', *Technological Forecasting and Social Change*, 104, pp. 89–101. doi: 10.1016/j.techfore.2015.12.007.

de Vries, E. (2010) *Close up - Enercon, super turbines and beyond*, *Windpower Monthly*. Available at: https://www.windpowermonthly.com/article/1047013/close---enercon-super-turbines-beyond (Accessed: 8 June 2017).

Whitcomb, R. T. (1976) 'A design approach and selected wind tunnel results at high subsonic speeds for wing-tip mounted winglets', *Nasa Tn D-8260*, (July), pp. 1–33. Available at: https://ntrs.nasa.gov/archive/nasa/casi.ntrs.nasa.gov/19760019075.pdf.

WindEurope (2020) *Accelerating Wind Turbine Blade Circularity*. Available at: https://windeurope.org/wp-content/uploads/files/about-wind/reports/WindEurope-Accelerating-wind-turbine-blade-circularity.pdf.

Winslow, J. *et al.* (2017) 'Basic Understanding of Airfoil Characteristics at Low Reynolds Numbers (104–105)', *https://doi.org/10.2514/1.C034415*. American Institute of Aeronautics and

Astronautics, 55(3), pp. 1050–1061. doi: 10.2514/1.C034415.

Wood, D. H., Okulov, V. L. and Bhattacharjee, D. (2016) 'Direct calculation of wind turbine tip loss', *Renewable Energy*. Elsevier Ltd, 95, pp. 269–276. doi: 10.1016/j.renene.2016.04.017.

Young, A. *et al.* (2019) 'Improving tidal turbine efficiency using winglets', in. Available at: https://researchportal.bath.ac.uk/en/publications/improving-tidal-turbine-efficiency-using-winglets (Accessed: 23 September 2019).

Zhou, Z. *et al.* (2017) 'Developments in large marine current turbine technologies – A review', *Renewable and Sustainable Energy Reviews*, 71, pp. 852–858. doi: 10.1016/j.rser.2016.12.113.

Zhu, B. *et al.* (2017) 'Performance characteristics of a horizontal axis turbine with fusion winglet', *Energy*. Elsevier Ltd, 120, pp. 431–440. doi: 10.1016/j.energy.2016.11.094.